**Physics with Same-sign Dilepton and Multilepton Events**

by

Zhi Zheng

A dissertation submitted in partial fulfillment
of the requirements for the degree of
Doctor of Philosophy
(Physics)
in the University of Michigan
2020

Doctoral Committee:

Professor Jianming Qian, Chair
Professor James Wells
Associate Professor Gongjun Xu
Professor Bing Zhou
Professor Junjie Zhu

Zhi Zheng

zhengzhi@umich.edu

ORCID iD: 0000-0002-8323-7753

# ACKNOWLEDGMENTS

# TABLE OF CONTENTS

**Chapter**

# LIST OF FIGURES

FIGURE

# LIST OF TABLES

# LIST OF ABBREVIATIONS

**QED**  Quantum Electrodynamics

**QCD**  Quantum Chromodynamics

**SM**  Standard Model

**EW**  Electroweak

**SSML**  Same-sign Dilepton and Multilepton

**BSM**  Beyond Standard Model

**SUSY**  Supersymmetry

**LHC**  Large Hadron Collider

**QFT**  Quantum Field Theory

**EWSB**  Electroweak Symmetry Breaking

**VEV**  Vacuum Expectation Value

$pp$  Proton-proton

**PDF**  Parton Distribution Function

**NNLO**  Next-to-Next-to-Leading-Oder

**ISR**  Initial State Radiation

**FSR**  Final State Radiation

**UE**  Underlying Event

**ggF**  Gluon-Gluon Fusion

**VBF**  Vector-Boson Fusion

**VH**  Vector Boson Associated Production

$t\bar{t}H$  Top Associated Production

**2HDM**  2-Higgs Doublet Models

**NLO**  Next-to-Leading Order

**SMEFT**  Standard Model Effective Field Theory

**IP**  Interaction Point

**RMS**  Root Mean Square

**ID**  Inner Detector

**MS**  Muon Spectrometers

**TDAQ**  Trigger and Data Acquisition

**SCT**  Silicon Conductor Tracking

**TRT**  Transition-Radiation Tracker

**IBL**  Insertabel B-Layer

**MDT**  Monitored Drift Tube

**CSC**  Cathode Strip Chamber

**RPC**  Resistive Plate Chamber

**TGC**  Thin Gap Chamber

**MVA**  Multivariate Analysis

**WP**  Working Point

**BDT**  Boosted Decision Tree

**PV**  Primary Vertex

**MC**  Monte Carlo

**JES**  Jet Energy Scale

**JVT**  Jet Vertex Tagging

**NLO**  Next-to-Leading Order

**LO**  Leading Order

**NF**  Normalization Factor

**JER**  Jet Energy Resolusion

**NP**  Nuisance Parameter

**POI**  Parameter of Interest

# ABSTRACT

The Higgs boson was observed in 2012, completing the last missing piece in the Standard Model. While research that culminated with the LHC has established the Standard Model as a successful theory, there are still many unanswered questions. Studying events with same-sign dilepton and multilepton may help to gain insight into those questions. This dissertation reports on two searches for rare Standard Model processes, using proton-proton collisions data at a center-of-mass energy of $\sqrt{s} = 13$ TeV recorded by the ATLAS detector at CERN's Large Hadron Collider between years 2015-2018. Both searches are conducted with same-sign dilepton and multilepton final states, where leptons are considered to be either electrons or muons.

The first is a search for the associated production of the Higgs boson with a top quark pair ($t\bar{t}H$) in same sign dilepton and multilepton final states. A total of 6 final states, defined by the number and flavor of charged-lepton candidates in each event, and 25 event categories are defined to simultaneously search for the $t\bar{t}H$ signal and constrain several leading backgrounds. An excess of events consistent with $t\bar{t}H$ production, over the expected background from Standard Model processes, is found with an observed significance of 1.8 standard deviations, compared to an expectation of 3.1 standard deviations. Assuming Standard Model branching fractions, the measured $t\bar{t}H$ production cross section is $\sigma_{t\bar{t}H} = 294^{+182}_{-162}$ fb, consistent with the Standard Model prediction. The production rate of the $t\bar{t}W$ process is found to be higher than the theoretical prediction. The impact on the $t\bar{t}H$ cross section measurement of the assumptions made on the $t\bar{t}W$ background modeling is discussed.

The second is a search for four-top-quark production with same-sign dilepton and multilepton events. A multivariate discriminant using information based on jet multiplicity, jet flavor and event kinematics are used to separate signal from the background, and dedicated control regions are used to constrain dominant backgrounds. The four-top-quark production cross section is measured to be $24^{+7}_{-6}$ fb, assuming the Standard Model four-top-quark properties. This corresponds to an observed (expected) signal significance of 4.3 (2.4) standard deviations and provides the first evidence for this process.

# CHAPTER 1

# Introduction

Exploration of the unknown is the main driver of fundamental science. The goal of the particle physics is to unravel the fundamental rules of the universe. Researches in this field are to discover the most elementary constituents of matter, to reveal the inner workings of particle interactions and to explore the basic nature of space and time.

The notion that matter is built up from a set of elementary constituents dates back at least 2000 years to the time of ancient Greek philosophers. The ideas received a more quantitative basis in the late nineteenth century with the discovery of radioactivity and atom structures. In 1897, J.J Thomson discovered electrons from a study of cathode rays, which marked the start of the particle physics. With hints from Rutherford's scattering experiment, Niels Bohr constructed a 'planetary' model of the atom, in which electrons orbit around nucleus. It took 10 more years to understand the mysterious rules governing the atomic world: quantum mechanics. The quantum theory was introduced by Planck, Einstein and De Broglie, bringing a new idea of wave-particle duality. Wolfgang Pauli, Erwin Schrodinger, Werner Heisenberg and others constructed the quantum theory with the exclusion principle, the wave mechanics equation and the uncertainty principle. Then Paul Dirac combined quantum mechanics and special relativity in his theory and predicted that every particle has an antiparticle. This was confirmed with the discovery of the positron by Carl D Anderson in 1932. With the development from Richard Feynman, Shinichiro Tomonaga and Julian Schwinger, it was finally possible to formulate the perturbation theory of *Quantum Electrodynamics* (QED)[1–6].

The existence of the neutrino was postulated in 1930 by Wolfgang Pauli who was looking for an explanation for the fact that energy did not appear to be conserved in nuclear beta decays; and it was confirmed experimentally later in 1956. In the year of 1954, C.N. Yang and Robert Mills developed a new class of theories called 'gauge theories'[7, 8]. Weak interaction was included into the gauge theory by Julian Schwinger, Sidney Bludman, and Sheldon Glashow. During 1964 to 1968, Higgs, Kibble, Guralnik, Hegen, Brout and Englert from three independent groups developed the Higgs mechanism which gives the mass of elementary particles[9–11].

By the early 1960s, as accelerators reached higher energies, a hundred or more types of particles were found and the complex connections between particles made it hard to make sense of what was going on. Things began to become clearer when in 1961 Murray Gell-Mann and Yuval Ne'eman independently came up with a scheme that brought some order to the chaos of the particle zoo[12, 13]. Dubbed the eightfold way, Gell-Mann and George Zweig independently used this scheme to propose the existence of a new type of particles that makes up bigger particles such as neutrons and protons in 1964[14, 15]. Naming them quarks, their existence was confirmed at the Stanford Linear Accelerator Center (SLAC) just four years later. The discovery of quarks ultimately led to *Quantum Chromodynamics* (QCD) – the quantum theory of the atomic nucleus, and particles within it.

It took a collective worldwide effort combining theory and experiment for a more complete picture to form. This effort culminated in the theory of the electromagnetic and weak forces (electroweak theory) being combined with the theory of the strong force (QCD), and then the *Standard Model* (SM) was formed. The SM reduced all of the known particles down to just a few elementary ones, placing them into lists and groups, much like the periodic table of elements. In the late 1970s and early 80s, many of SM predictions were verified experimentally. In 1984, the $W^\pm$ and Z bosons predicted by the *Electroweak* (EW) theory were observed by two experiments at the European Organization for Nuclear Research (CERN) [16–19]. The last and the heaviest quark in the SM, top quark, was discovered in 1995 by the CDF and D∅ experiments at Tevatron $p\bar{p}$ collider at Fermilab[20, 21]. In 2012, the Higgs boson was discovered by the ATLAS and CMS experiment at CERN, completing the last piece of the SM[22, 23]. While research that culminated with the LHC has established the SM as a successful theory, there are still many unanswered questions, for example, why the Higgs boson mass is small given the very large top-quark induced radiative correction. New physics is needed to tackle these questions.

Many theoretical models for new physics produce the *Same-sign Dilepton and Multilepton* (SSML) final states. Some of the *Beyond Standard Model* (BSM) theories predict new heavy particles with large coupling to heavy SM particles such as the top quark, W/Z and Higgs boson. SSML final states are often produced in the cascade decays of these new particles. Examples of *Same-sign Dilepton and Multilepton* (SSML) produced in the BSMs include the production of *Supersymmetry* (SUSY) particles[24], Majorana neutrinos[25], the vector-like quarks[26], and the dark matter[27]. For example, gluino pair production can yield the same-sign top quarks which may decay to the same-sign dilepton final state. Any deviation from the SM in this final state will indicate new physics. Many rare SM processes that are not yet observed also share SSML signature, e.g. the $t\bar{t}t\bar{t}$ production. As more LHC data become available, studies of these rare processes provide more stringent test of the SM while increasing the likelihood of revealing new physics.

Looking into SSML phase space, SM processes are few and have low cross sections, e.g. $t\bar{t}W/Z$, $t\bar{t}H$, di- and multi-boson and multi-top ($t\bar{t}t$,$t\bar{t}t\bar{t}$) processes. However, many SM processes with this signature have been recently observed by ATLAS and CMS, e.g. the $t\bar{t}H$ process which was observed in 2018. The kinematics of these processes are not extensively studied. On the other hand, there are large background contributions coming from instrumental effects. These backgrounds can often only be reliably estimated using data-driven method. This makes the analyses of SSML events quite challenging.

This dissertation will focus on the studies of $t\bar{t}H$ and $t\bar{t}t\bar{t}$ processes in the SSML final states, and is organized as follows. Chapter 2 gives a brief summary of the SM of particle physics and the phenomenology of the physics at the LHC. Chapter 3 presents an overview of the LHC machine and the ATLAS detector. Chapter 4 introduces the general information on the ATLAS event reconstruction. In Chapter 5, common tools used in the SSML analyses are introduced. Chapter 6 presents the search for the associated production of the Higgs boson and a top quark pair in the SSML final states (referred to as $t\bar{t}H$ analysis). In Chapter 7, evidence for $t\bar{t}t\bar{t}$ production in the SSML final states (referred to as $t\bar{t}t\bar{t}$ analysis) is presented. Finally, a summary and outlook of physics with SSML events are given in Chapter 8.

# CHAPTER 2

# Standard Model

The SM of particle physics is a theory describing the elementary particles and their interactions, and has been very successful in explaining and predicting a wide variety of experimental results[28, 29]. The SM was cobbled together by many brilliant minds over the course of nearly the whole of the twentieth century, sometimes driven forward by new experimental discoveries, sometimes by theoretical advances. It was a collaborative effort in the largest sense, spanning continents and decades.

To put the formulation of the SM in a nutshell, all matter in nature is composed of fermions, forces between particles are mediated by force carrying gauge bosons, and masses of particles are generated by the Higgs mechanism which predicts a scalar Higgs boson. The particles in the SM are presented schematically in Figure 2.1.
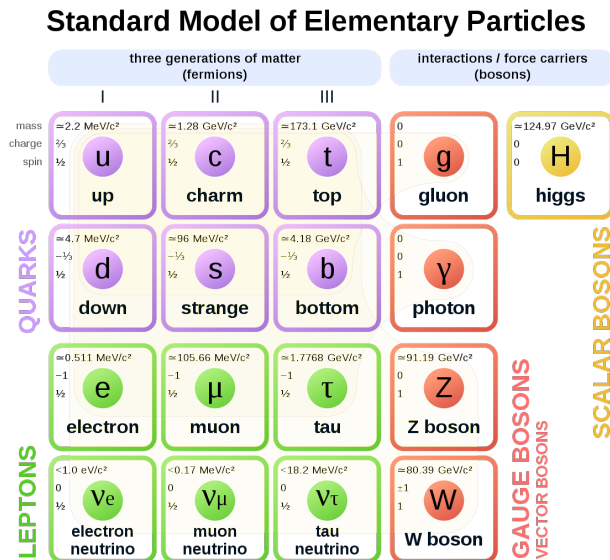


Figure 2.1: SM of elementary particles: the 12 fundamental fermions and 5 fundamental bosons. [29].

Fermions are spin $1/2$ particles and obey Fermi-Dirac statistics. They consist of quarks and leptons which form the basic building blocks of matter. There are six types, known as flavors, of quarks: up ($u$), down ($d$), strange ($s$), charm ($c$), bottom ($b$) and top ($t$), and they are grouped into three generations of doublets. Up, charm and top quarks have electric charge of $2/3$ e, and others have electric charge of $-1/3$ e. Here e is the magnitude of the electron's electric charge. Each quark flavor comes in three colors. All quarks carry a baryon number (B) of $+1/3$, while their anti-particles carry a baryon number of $-1/3$. This baryon number is experimentally found to be conserved. Leptons also come with six flavors organized in three generations of doublets. Electron ($e$), muon ($\mu$) and tau ($\tau$) all have electric charge of $-e$, while their corresponding neutrinos are charge neutral. A lepton number (L) of $+1$ is assigned to each generation, and $-1$ is assigned to the corresponding anti-particles. Lepton number is experimentally found to be conserved.

There are four known fundamental forces in nature: gravitational and electromagnetic interactions, which produce significant long-range forces whose effects can be experienced in everyday life, and the weak and strong interactions, which produce short-distance forces and govern nuclear interactions. The SM describes all of these forces except for gravity, which cannot yet be described by a quantum theory. In the SM, the matter particles interact with each other through the exchange of force carrier particles. These force carriers, listed below, are vector gauge bosons possessing a spin quantum number of 1 and obeying Bose-Einstein statistics:

- $W^+$, $W^-$ and $Z^0$ bosons: massive, the force carriers of the weak nuclear force;

- Photon ($\gamma$): massless, the force carrier of the electromagnetic force;

- Eight gluons (g): massless, eight force carriers of the strong force.

## 2.1   The Lagrangian and Symmetries of the Standard Model

The dynamics of the SM is described by a Lagrangian based on the formalism of relativistic *Quantum Field Theory* (QFT), and the Lagrangian is the action integrated over all space-time ($x$) of the Lagrangian density $\mathcal{L}_{\mathrm{SM}}(x)$. Symmetries are transformations under which the Lagrangian is invariant and they play important roles in the SM because of the implications of Noether's theorem[30]. As the theorem states, if an action is invariant under some group of transformations (symmetries), there exist one or more quantities that are invariant under these transformations. Poincare symmetry, which includes translations, rotations and Lorentz boosts, is a global continuous symmetry of the SM, associated with three conserved quantities: energy, momentum and angular momentum.

Before digging into the local symmetries of the SM, notations of fermions in the SM under QFT framework are introduced. Fermions can be divided into left-handed weak-isospin doublets

(L) with isospin $I = 1/2$, which are arranged as

$$\begin{pmatrix} u_L \\ d_L \end{pmatrix}, \begin{pmatrix} c_L \\ s_L \end{pmatrix}, \begin{pmatrix} t_L \\ b_L \end{pmatrix}, \tag{2.1}$$

$$\begin{pmatrix} v_e \\ e_L \end{pmatrix}, \begin{pmatrix} v_\mu \\ \mu_L \end{pmatrix}, \begin{pmatrix} v_\tau \\ \tau_L \end{pmatrix} \tag{2.2}$$

and the right-handed weak-isospin singlets ($R$) with isospin $I = 0$, which are written as:

$$e_R, \ \mu_R, \ \tau_R, \ u_R, \ c_R, \ t_R, \ d_R, \ s_R, \ b_R. \tag{2.3}$$

In the SM, only left-handed neutrinos exist.

The SM Lagrangian is formulated by the local gauge symmetry of the group $SU(3)_C \times SU(2)_L \times U(1)_Y$, which governs the electromagnetism, weak and strong interactions. The transformations under this group are gauge transformations, and gauge fields are introduced in order to preserve the symmetry under given transformations. Only then is the Lagrangian gauge invariant under these transformations.

Electromagnetic and weak interactions are unified by the Glashow-Weinberg-Salam theory, also known as the EW theory[31–33], which respects the $SU(2)_L \times U(1)_Y$ gauge invariance.

The gauge field of the $U(1)_Y$ transformation is $B_\mu$, which transforms as

$$B_\mu \to B_\mu + \frac{1}{g_1} \partial_\mu \alpha(x). \tag{2.4}$$

Here $\alpha(x)$ is the phase applied as part of the symmetry and $g_1$ is the coupling constant between $B_\mu$ and fermions. Fermions transform under the $U(1)$ phase shift as $(L, R) \to e^{iY\alpha(x)/2}(L, R)$. The quantity Y, called weak hypercharge, takes a value of -1 for the doublets and -2 for the singlets, i.e.:

$$L = \begin{pmatrix} \nu_e \\ e_L \end{pmatrix} \to e^{-i\alpha(x)/2} \begin{pmatrix} \nu_e \\ e_L \end{pmatrix}, \ R = e_R \to e^{-i\alpha(x)} e_R, \tag{2.5}$$

The $SU(2)_L$ symmetry is preserved only by the left-handed particles (leptons or quarks), with the right-handed chiral particles not participating, and requires three additional gauge fields, $W_\mu^a (a = 1, 2, 3)$, which transform as:

$$W_\mu^a \to W_\mu^a + \frac{2}{g_2} \partial_\mu \alpha^a(x) + \epsilon^{abc} \alpha^b(x) W_\mu^c, \tag{2.6}$$

where $\vec{\alpha}(x)$ is the phase applied as part of the symmetry, $g_2$ is the coupling constant between

$W_\mu^a$ and fermions, and $\epsilon^{abc}$, which is totally antisymmetric, is the structure constant for $SU(2)$. Similar as the $U(1)$ transformation, the fields themselves will transform under the symmetry as $(L, R) \to e^{iI^3 \vec{\alpha}(x) \cdot \vec{\tau}/2}(L, R)$, where $\vec{\tau}$ are the Pauli matrices. $I^3$ is the projection of the isospin: $I^3 = +1/2 \ (-1/2)$ for the upper (lower) components of the doublets and $I^3 = 0$ for the singlets. Thus, the $SU(2)$ transformation, which treats left- and right-handed particles differently, breaks chiral symmetry. Therefore, the left-handed doublet and right-handed singlet transform as:

$$L = \begin{pmatrix} \nu_e \\ e_L \end{pmatrix} \to e^{i\vec{\alpha}(x) \cdot \vec{\tau}/2} \begin{pmatrix} \nu_e \\ e_L \end{pmatrix}, \quad R = e_R \to e_R. \tag{2.7}$$

The local $SU(3)$ symmetry is associated with strong force, which acts only on the particles (quarks) that have color charges. The strong force, described by a QFT called *Quantum Chromodynamics* (QCD), is mediated by eight gluons $G_\mu^a$ ($a = 1, 2, 3, .., 8$), which transform as

$$G_\mu^a \to G_\mu^a - \frac{1}{g_3}\partial_\mu \alpha^a(x) + f^{abc}\alpha^b(x)G_\mu^c, \tag{2.8}$$

where $\alpha^a(x)$ is the phase applied as part of the symmetry, $g_3$ is the coupling constant for strong interaction, and $f^{abc}$ which are totally antisymmetric, are the structure constant for $SU(3)$. The quarks have three basic color-charge states, which are labeled as red (r), green (g) and blue (b). The three color states form a basis in a 3-dimensional complex vector space. The quarks transform under the $SU(3)$ transformation as

$$q \to e^{i\sum_a \alpha(x)^a \lambda^a/2}q, \tag{2.9}$$

where $\lambda^b/2$ are $3 \times 3$ hermitian matrices and are the generators of $SU(3)$ rotations.

Under the $SU(3)_C \times SU(2)_L \times U(1)_Y$ symmetry, taking all introduced gauge fields and the corresponding conserved quantities, a gauge covariant derivative is introduced:

$$D_\mu = \partial_\mu - ig_1\frac{Y}{2}B_\mu - ig_2\frac{\tau^i}{2}W_\mu^i - ig_3\frac{\lambda^a}{2}G_\mu^a. \tag{2.10}$$

Summations is applied for the repeating indices[1], and in the subsequent discussion, this rule also applies unless specified. Under the theoretical framework based on gauge invariance, all the particles must be massless, which is in contradiction to observations. The Higgs Mechanism which predicts the existence of a neutral scalar, the Higgs boson, is introduced to explain the generation of mass through the *Electroweak Symmetry Breaking* (EWSB).

---

[1]The Einstein summation convention still applies, even if the color index i and j are not in an upper and lower position. This exception extends also to the color indices a, b, ... of the gauge fields to be introduced.

Combining all the components above, the Lagrangian of the SM can be summarized as:

$$\mathcal{L}_{\text{SM}} = \mathcal{L}_{\text{EW}} + \mathcal{L}_{\text{QCD}}. \tag{2.11}$$

Concerning the EW Lagrangian $\mathcal{L}_{\text{EW}}$, this can be summarized as

$$\mathcal{L}_{\text{EW}} = \mathcal{L}_{\text{gauge}} + \mathcal{L}_{\text{fermion}} + \mathcal{L}_{\text{Higgs}} + \mathcal{L}_{\text{Yukawa}}. \tag{2.12}$$

The $\mathcal{L}_{\text{gauge}}$ in Equation 2.12 describes the gauge field tensor of the force carrier vector-bosons and their kinematics, which is written as:

$$\mathcal{L}_{\text{gauge}} = -\frac{1}{4} B_{\mu\nu} B^{\mu\nu} - \frac{1}{4} W^a_{\mu\nu} W^{a\mu\nu}, \tag{2.13}$$

where:

$$W^a_{\mu\nu} = \partial_\mu W^a_\nu - \partial_\nu W^a_\mu - g_2 \epsilon^{abc} W^b_\mu W^c_\nu \ (a = 1, 2, 3), \tag{2.14}$$

$$B_{\mu\nu} = \partial_\mu B_\nu - \partial_\nu B_\mu, \tag{2.15}$$

are the $SU(2)_L$ and $U(1)_Y$ field strength.

The fermion term $\mathcal{L}_{\text{fermion}}$ in Equation 2.12 , describes the fermion (f) kinematics and interactions with the gauge bosons and is written as:

$$\mathcal{L}_{\text{fermion}} = \sum_{f=L_L, L_R, Q_L, u_R, d_R} \bar{f} i \gamma^\mu \partial_\mu f$$
$$\underbrace{- \sum_{f=L_L, L_R, Q_L, u_R, d_R} \bar{f} i \gamma^\mu (ig_1 \frac{Y}{2} B_\mu) f - \sum_{f=L_L, Q_L} \bar{f} i \gamma^\mu (ig_2 \frac{\tau^i}{2} W^i_\mu) f,}_{\text{EW interaction term}} \tag{2.16}$$

where $\gamma^\mu$ is the Dirac matrix. In Equation 2.16, $L_L$ and $Q_L$ denote the left-handed doublets of each family leptons and quarks, $L_R$ represents the singlets of the leptons; $u_R$ and $d_R$ denote the singlets of the up-type and down-type quarks, respectively. In Equation 2.16, the EW term describes the interaction between fermions and W, Z and $\gamma$ bosons. However, the $W^a_\mu$ and $B_\mu$ for the $SU(2)_L \times U(1)_Y$ group do not directly correspond to the physical $W^\pm$ , Z and $\gamma$ bosons, which are generated as a result of the spontaneous symmetry breaking of $SU(2)_L \times U(1)_L$.

The charge vector boson, $W^\pm_\mu$ is defined as the linear combinations of $W^1_\mu$ and $W^2_\mu$:

$$W^\pm_\mu = \frac{1}{\sqrt{2}} (-W^1_\mu \pm i W^2_\mu). \tag{2.17}$$

The two remaining neutral fields $W_\mu^3$ and $B_\mu$ mix to form $Z_\mu$ and $A_\mu$ (the field of photon $\gamma$):

$$A_\mu \equiv \frac{1}{\sqrt{g_1^2 + g_2^2}}(g_1 W_\mu^3 + g_2 B_\mu), \tag{2.18}$$

$$Z_\mu \equiv \frac{1}{\sqrt{g_1^2 + g_2^2}}(g_1 W_\mu^3 - g_2 B_\mu). \tag{2.19}$$

The couplings can be grouped in the following way:

$$
\begin{aligned}
e &= \frac{g_1 g_2}{\sqrt{g_1^2 + g_2^2}}, \\
\cos\theta_W &= \frac{g_1}{\sqrt{g_1^2 + g_2^2}}, \\
\sin\theta_W &= \frac{g_2}{\sqrt{g_1^2 + g_2^2}}.
\end{aligned}
\tag{2.20}
$$

Here, the angle $\theta_W$ is the weak mixing angle.

With the redefinition of $W_\mu^a$ and $B_\mu$ in terms of $W_\mu^\pm$, $Z_\mu$ and $A_\mu$, the EW interaction term in Equation 2.16 for first generation leptons (for simplification) can be specified as

$$
\begin{aligned}
\mathcal{L}_{\nu_e, e} = &\underbrace{\sum_{f \in e, \nu_e} e Q_f (\bar{f}\gamma^\mu f) A_\mu}_{\text{Electromagnetic interaction}} \\
&+ \underbrace{\frac{g_2}{\cos\theta_W} \sum_{f \in e, \nu_e} \left[ \bar{f}_L \gamma^\mu f_L (I_f^3 - Q_f \sin^2\theta_W) + \bar{f}_R \gamma^\mu f_R (-Q_f \sin^2\theta_W) \right] Z_\mu}_{\text{Neutral weak interaction}} \\
&+ \underbrace{\frac{g_2}{\sqrt{2}} \left[ \bar{\nu}_e \gamma^\mu e_L W_\mu^+ + \bar{e}_L \gamma^\mu \nu_e W_\mu^- \right]}_{\text{Charge weak interaction}},
\end{aligned}
\tag{2.21}
$$

where $I_f^3$ is the fermion field's quantum number associated with the third component of weak-isospin. In the EW theory, the electric charge $Q_f$ is related to $SU(2)$ and $U(1)$ gauge symmetries via Gell-Mann-Nishijima relation [34]

$$Q_f = I_f^3 + \frac{1}{2}Y \tag{2.22}$$

In the Equation 2.21, the first term describes the electromagnetic interactions between fermions and the photon, the second term describes the neutral weak interaction of the Z boson coupling with both left- and right-handed fermions, and the third term describes the charged weak interactions of the $W^\pm$ bosons transforming the up- and down-type fields of the left-handed $SU(2)$ doublets into

each other.

The Lagrangian of the Higgs section $\mathcal{L}_{\text{Higgs}}$, which describes the Higgs field kinematics and potential energies, is given by:

$$\mathcal{L}_{\text{Higgs}} = (D_\mu \phi)^\dagger D_\mu \phi - V(\phi), \tag{2.23}$$

where $\phi$ is the scalar Higgs field. In the Equation 2.23, only the EW part is considered in the derivative $D_\mu$, which can be written as,

$$D_\mu = \partial_\mu - ig_1 \frac{Y}{2} B_\mu - ig_2 \frac{\tau^i}{2} W. \tag{2.24}$$

The $\mathcal{L}_{\text{Yukawa}}$, the interaction term of matter particles with the Higgs field, is given by

$$\mathcal{L}_{\text{Yukawa}} = \sum_f \frac{y_f}{2} \phi \bar{f} f + h.c, \tag{2.25}$$

which is associated with the Higgs mechanism to be discussed in Section 2.2.

The QCD Lagrangian $\mathcal{L}_{\text{QCD}}$ can be easily written down as

$$\mathcal{L}_{\text{QCD}} = -\frac{1}{4} G^a_{\mu\nu} G^{a\mu\nu} + \sum_{f=quarks} \bar{f}(i\gamma^\mu \partial_\mu - m_f)f + \bar{f}_\alpha \gamma^\mu g_3 \frac{\lambda^a_{\alpha\beta}}{2} G^a_\mu f_\beta \tag{2.26}$$

where:

$$G^a_{\mu\nu} = \partial_\mu G^a_\nu - \partial_\nu G^a_\mu - g_3 f^{abc} G^b_\mu G^c_\nu \ (a = 1, 2, ..., 8), \tag{2.27}$$

is the $SU(3)_C$ gauge field strength. In the Equation 2.26, $\alpha$ and $\beta$ is the color index ($\alpha$ = 1,2,3 and $\beta$ = 1,2,3). This equation defines the strong interaction, and contains the quark-gluon interaction terms as well as the gluon self-coupling terms.

## 2.2 The Higgs Mechanism

The Brout-Englert-Higgs mechanism (Higgs mechanism)[9–11] is introduced to provide mass-term in $\mathcal{L}_{\text{SM}}$, since the mass terms for fermions or gauge bosons are not allowed under the $SU(2)_L \times U(1)_Y$ symmetries. Adding the simple mass term for fermions like $m f \bar{f}$ will break the $SU(2)_L$ invariance of the $\mathcal{L}_{\text{SM}}$, as the $SU(2)_L$ breaks chiral symmetry. On the other hand, the mass term for the gauge bosons like $m B_\mu B^\mu$ is not invariant under $U(1)$ transformation stated in Equation 2.4. In the Higgs mechanism, a complex scalar doublet field (called Higgs field) is introduced and gauge bosons and fermions gain their masses by interacting with the Higgs field.

The Higgs field $\phi$ is a $SU(2)_L$ doublet and is traditionally expressed as:

$$\phi = \frac{1}{\sqrt{2}} \begin{pmatrix} \phi_1 + i\phi_2 \\ \phi_3 + i\phi_4 \end{pmatrix}, \tag{2.28}$$

It has a weak hypercharge $Y_\phi = 1$ and a self-potential:

$$V(\phi) = -\mu^2 \phi^\dagger \phi - \lambda(\phi^\dagger\phi)^2. \tag{2.29}$$

As shown in Figure 2.2, if $\mu^2 > 0$, Equation 2.29 describes a self-interacting complex scalar filed;
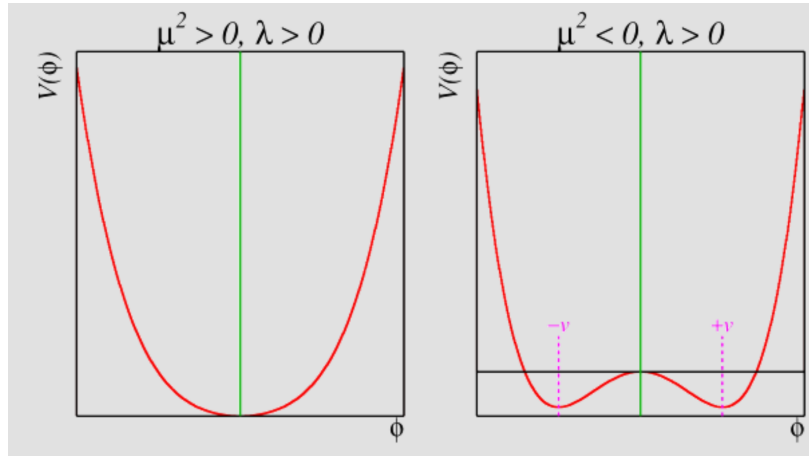


Figure 2.2: Illustration of the Higgs potential with different parameters, (left) Higgs potential with $\mu^2 > 0$ with stable equilibrium at $\phi = 0$, (right) Higgs potential with $\mu^2 < 0$, $\phi = 0$ is no longer a stable equilibrium and the Higgs attains a non-zero vacuum expectation value at $\pm\nu$ - breaking the $SU(2)_L \times U(1)_Y$ gauge symmetry of the EW sector of the SM.

if $\mu^2 < 0$, the potential described by Equation 2.29 has non-zero minima located at

$$\phi^\dagger \phi = \frac{-\mu^2}{2\lambda} = \frac{\nu^2}{2}. \tag{2.30}$$

The stable equilibrium point $\phi_0$ of the Higgs potential, also called as the Higgs *Vacuum Expectation Value* (VEV), is not at $\phi = 0$ but at $\nu$,

$$\phi_0 = \frac{1}{\sqrt{2}} \begin{pmatrix} 0 \\ \nu \end{pmatrix}. \tag{2.31}$$

Owing to the conservation of electric charge and the neutral vacuum requirement for a VEV, in the choice of $\phi_0$ in Equation 2.31, the up-type $SU(2)$ component of the Higgs field is chosen to be zero. With one component of $\phi_0$ attaining a non-zero VEV, the $SU(2)$ gauge symmetry is not

respected by the vacuum state and the $SU(2)_L \times U(1)_Y$ symmetry is spontaneously broken[2]. The Higgs field with a non-zero VEV is therefore referred to as the EWSB in the SM. The scalar VEV of Equation 2.31 hence yields the breaking scheme,

$$SU(2)_L \times U(1)_Y \rightarrow U(1)_Q, \tag{2.32}$$

where $U(1)_Q$ is the symmetry that conserves the electric charge and is by construction still a true vacuum symmetry. Thus, the $U(1)_Q$ symmetry of the electromagnetic interaction is unbroken by the scalar VEV.

To set up a perturbation expansion around the VEV, $\phi$ in Equation 2.28 can be expressed as:

$$\phi(x) = \begin{pmatrix} 0 \\ \frac{1}{\sqrt{2}}(\nu + h(x)) \end{pmatrix}, \tag{2.33}$$

where $h(x)$ corresponds to a variable field that is small for perturbations around the VEV and is the excitation of the Higgs field that represents the physically observable Higgs boson. The Higgs potential $V(\phi)$ can be rewritten as

$$V(\phi) = -\frac{\mu^4}{4\lambda} - \mu^2 h(x)^2 + \lambda\nu h(x)^3 + \frac{\lambda}{4}h(x)^4. \tag{2.34}$$

The second term in Equation 2.34 represents the mass (at the tree level) of the physical Higgs boson $m_h = \sqrt{-2\mu^2} = \sqrt{2\lambda}\nu$. The third term and fourth terms are the Higgs boson self-interaction terms.

Similarly, the kinematic term $T(\phi)$ of Higgs in Equation 2.23 can be written as:

$$\begin{aligned} T(\phi) =& (D_\mu\phi)^\dagger D_\mu\phi \\ =& \underbrace{\frac{1}{2}(\partial_\mu h(x))^2}_{\text{First: kinematic term}} + \underbrace{\frac{g_1^2}{8}(W_\mu^1 + iW_\mu^2)(W^{1\mu} - iW^{2\mu})(v + h(x))^2}_{\text{Second: W term}} \\ & + \underbrace{\frac{1}{8}(g_1 W_\mu^3 - g_2 B_\mu)(g_1 W^{3\mu} - g_2 B^\mu)(v + h(x))^2}_{\text{Third: Z and photon term}}, \end{aligned} \tag{2.35}$$

In the Equation 2.35, only the EW part is considered in $D_\mu$ which is shown in Equation 2.24.

Based on the definition in Equation 2.17, the second term in Equation 2.35 becomes

$$\left(\frac{g_1}{2}(v + h(x))\right)^2 W_\mu^+ W^{-\mu}, \tag{2.36}$$

---

[2]Spontaneous symmetry breaking can describe systems whose Lagrangian obeys symmetries, but the lowest energy vacuum solution does not exhibit that same symmetry

yielding the W boson mass: $m_W = \frac{g_1 \nu}{2}$.

With the two remaining neutral fields $W^3$ and B mixed to form the mass eigenstates as shown in Equation 2.18 and 2.19, the third term in Equation 2.35 can be rewritten as

$$\frac{1}{2} \left( \frac{\sqrt{g_1^2 + g_2^2}}{2} (v + h(x)) \right)^2 Z_\mu Z^\mu + 0^2 A_\mu A^\mu, \tag{2.37}$$

The Z boson acquires a mass of $m_Z = \frac{\sqrt{g_1^2 + g_2^2} \nu}{2}$ and the photon remains massless.

The Equation 2.36 and 2.37 also have terms describing the triple ($hW_\mu^\dagger W^\mu$ and $hZ_\mu^\dagger Z^\mu$) and quartic ($h^2 W_\mu^\dagger W^\mu$ and $h^2 Z_\mu^\dagger Z^\mu$) boson interactions of the $W^\pm/Z$ boson and the Higgs boson, with the coupling proportional to the mass of the gauge boson squared. Such coupling is referred to as gauge coupling of the Higgs boson.

The degrees of freedom before and after the Higgs mechanism stay the same, therefore one can say that the scalar degrees of freedom have been eaten by the $W^\pm$ and Z bosons to become their longitudinal components.

To explain how the fermions obtain mass, one must consider the last term $\mathcal{L}_{\text{Yukawa}}$ (Equation 2.25) in the SM, which describes the interaction of fermions with the Higgs field and is invariant under the $SU(2)_L \times U(1)_Y$ transformation. Further expanding $\phi$ around its minimum by substituting Equation 2.33 into Equation 2.25, the Yukawa term is rewritten as:

$$\mathcal{L}_{\text{Yukawa}} = \sum_f \frac{y_f}{2} (\nu + h(x)) \overline{f} f, \tag{2.38}$$

yielding the fermion masses as $m_f = \frac{y_f \nu}{2}$, where $y_f$'s are the fermion Yukawa couplings and are free parameters of the SM that need to be measured. Equation 2.38 also describes the interaction between fermions and the Higgs boson with the coupling $\frac{y_f}{2} = \frac{m_f}{\nu}$ proportional to the fermion mass.

## 2.3 Success of Standard Model and Open Questions

On July 4th, 2012, a Higgs like particle with a mass around 125 GeV was discovered by the ATLAS[22] and CMS [23] collaboration at CERN, completing the last piece of the SM. Sequential measurements[35–41] confirmed that the particle is indeed very likely the SM Higgs boson. Figure 2.3 shows the measured values of the Higgs fermion and the gauge-boson coupling parameters as a function of the fermion and the gauge-boson masses. These measurements are in good agreement with the SM predictions for a $m_h = 125$ GeV Higgs boson. With a handful of additional experimentally determined parameters, the SM specifies all of interactions between the particles.
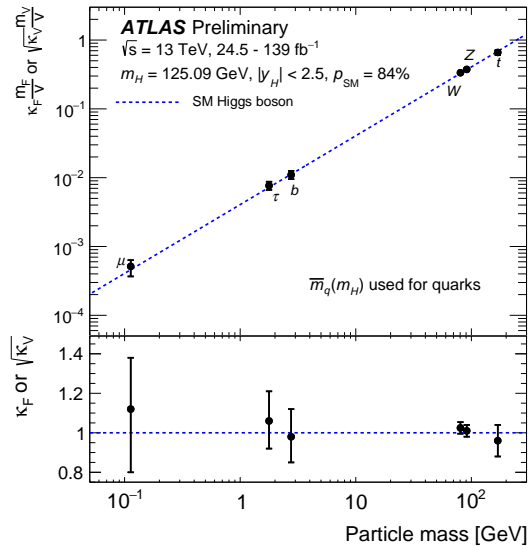
Figure 2.3: Measured values of the Higgs fermion and the gauge-boson coupling parameters as a function of the fermion and the gauge-boson masses. The blue dashed line shows the SM prediction (see Equation 2.36, 2.37 and 2.38)[42].

Figure 2.4 shows a summary of cross section measurements for many SM processes, compared to their corresponding theoretical expectations. The excellent agreement of all these measurements with their SM predictions is a great triumph of the SM.

Despite the success, there are many unanswered experimental and theoretical questions in the SM. Several open questions are:

- Dark Matter and dark energy from the astrophysical observations [44] are not presented in the SM.

- Non-zero neutrino mass, suggested from the observation of neutrino oscillation between different flavors[45], contradicts the SM predictions.

- The matter-antimatter asymmetry[46] observed can not be explained by the SM.

- The ultraviolet radiative corrections from the top quark give rise to the large loop corrections on the small Higgs boson mass, and this makes the EW sector sensitive to high energy cut-off scales near the Planck Mass $M_p \approx 10^{18} - 10^{19}$ GeV.
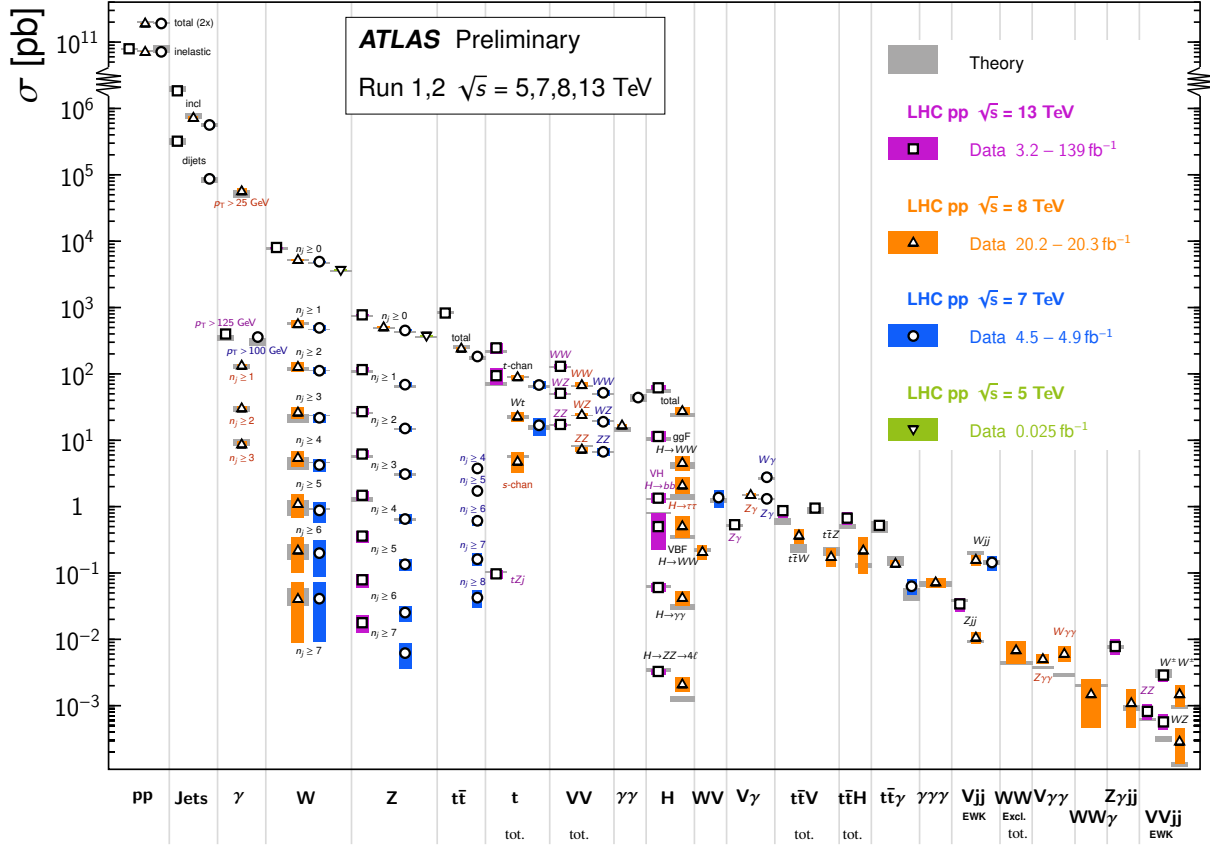
Figure 2.4: A summary of some Standard Model total and fiducial production cross section measurements, corrected for branching fractions, compared to their corresponding theoretical expectations[43].

## 2.4 Phenomenology of Proton-Proton Collisions

The basic approach for studying physics of interests at colliders is to measure the cross sections of the corresponding processes using the information recorded in particle detectors and compare the measurements with theoretical predictions. The cross section of a process produced at the LHC can be expressed as

$$\sigma_{pp \to X} = \sum_{A,B} \int_0^1 dx_A dx_B f_A(x_A, \mu_F^2) f_B(x_B, \mu_F^2) \times \hat{\sigma}_{AB \to X}(x_A p_A, x_B p_B, \mu_F^2, \mu_R^2). \qquad (2.39)$$

In the Equation 2.39, the sum runs over the parton A and B that exist in the incident protons and contribute to the hard-scatter process. $\mu_F$ is the factorization scale and $\mu_R$ is the renormalization

scale, $f_i(x_i, \mu_F^2)$ is the *Parton Distribution Function* (PDF) and $\hat{\sigma}_{AB \to X}$ is the parton-level cross section with parton A having momentum $p_A$ and parton B having momentum $p_B$. Figure 2.5 shows and illustration of *Proton-proton* ($pp$) collision. The main theoretical components can be described
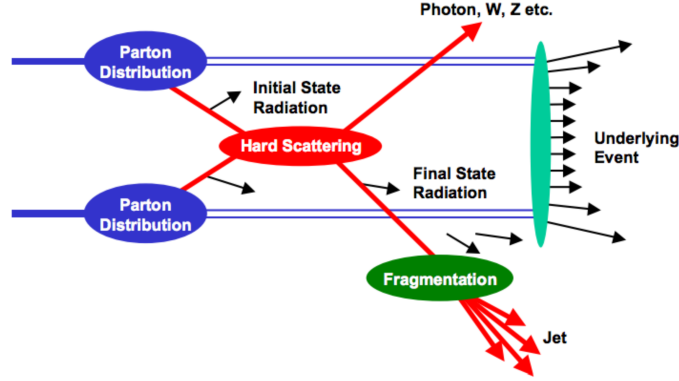


Figure 2.5: Schematic view of a proton-proton collision

as:

- ***Parton Distribution Function*** (**PDF**): Protons are composite particles comprised of quarks and gluons (partons). PDF, $f_i(x_i, \mu_F^2)$, defines the probability to find a parton of a particular flavor with momentum fraction $x_i$ at some energy scale $Q^2 = \mu_F^2$. Figure 2.6 shows the measured PDFs of gluons and quarks in NNPDF3.0 which is accurate in perturbation QCD at *Next-to-Next-to-Leading-Oder* (NNLO)[47];

- **Hard Scattering**: Hard scattering, which is typically characterized by large momentum transfer (i.e large 4-momentum transfer $Q^2$), large transverse momentum ($p_T$) or a large mass scale, represents the event produced by parton interaction, and $\sigma_{AB \to X}$, describing the rate and properties of hard-scattering interaction, can be predicted with some precision from perturbative EW and QCD calculations;

- ***Initial and Final State Radiation*** (**ISR and FSR**): ISR and FSR comes from the QCD and QED radiations from the incoming and outgoing partons;

- **Fragmentation and Hadronization**: Parton Fragmentation and Hadronization produces the hadronic jets in the final state from the partons which are produced in the hard scattering;

- ***Underlying Event*** (**UE**): UE includes particles produced by proton remnants.

As presented in Equation 2.39, both PDFs and parton level cross sections depend on the $\mu_F$. The $\mu_F$ defines the cut-off scale to separate short-distance hard interactions, which are included in

16
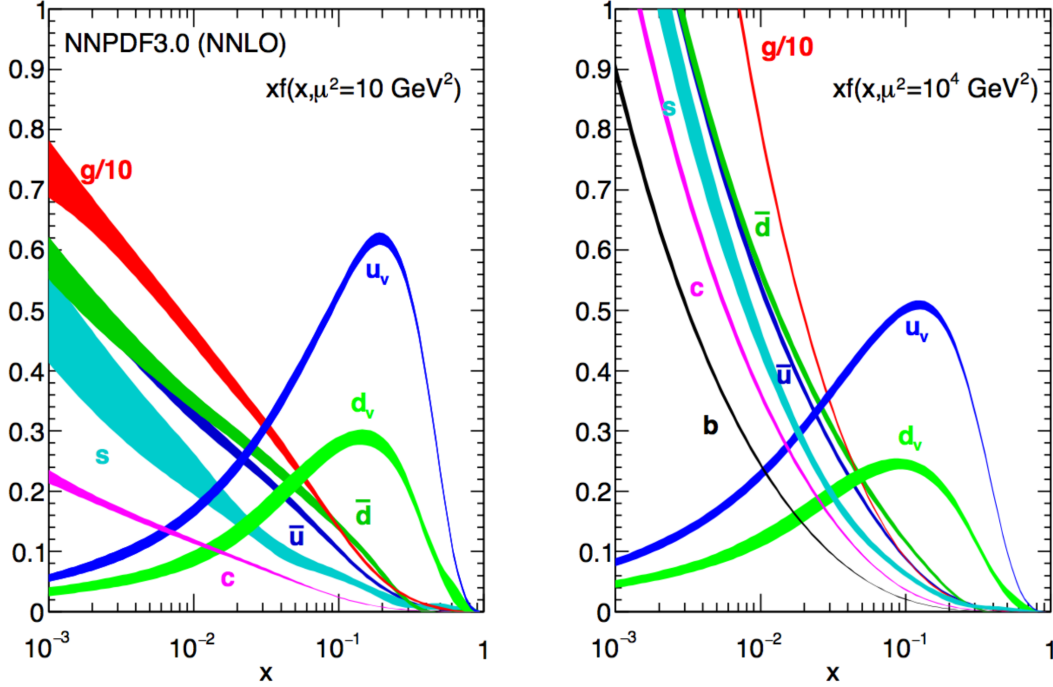
Figure 2.6: NNPDF3.0 NNLO PDF set for $Q^2 = 10\text{GeV}^2$ and $Q^2 = 10^4\text{GeV}^2$[47].

the parton level cross sections, and the long-distance physics, which cannot be described with perturbative QCD due to soft and collinear singularities and is absorbed in the PDFs. $\mu_R$ defines the ultraviolet cut-off scale, which impacts the calculation with the perturbation theory of QFT.

## 2.5    Higgs Boson Phenomenology at the LHC

The SM Higgs boson can be produced at the LHC mainly via the following four processes: *Gluon-Gluon Fusion* (ggF), *Vector-Boson Fusion* (VBF), *Vector Boson Associated Production* (VH) and *Top Associated Production* ($t\bar{t}H$). The Feynman diagrams of these production processes are shown in Figure 2.7. The production cross sections of different processes as a function of the Higgs boson mass at a center-of-mass energy of $\sqrt{s} = 13$ TeV, and as a function of the center-of-mass energy for a Higgs boson mass of 125 GeV are shown in Figure 2.8, respectively.

The ggF process is the dominant Higgs boson production process at LHC, accounting for around 90% of the total production cross section at $m_H = 125$ GeV. Since gluon is massless, its interaction with the Higgs boson involves a fermion loop, dominated by the top-quark loop. Hence the ggF process can be used to indirectly probe the Higgs boson coupling with the top quark. The VBF process has the second largest cross section and is featured by two forward jets. It can be used to probe the Higgs boson coupling with the W/Z bosons. The VH process can also

(a) Gluon-Gluon Fusion

(b) Vector-Boson Fusion

(c) Vector-Boson Associated

(d) Top Associated
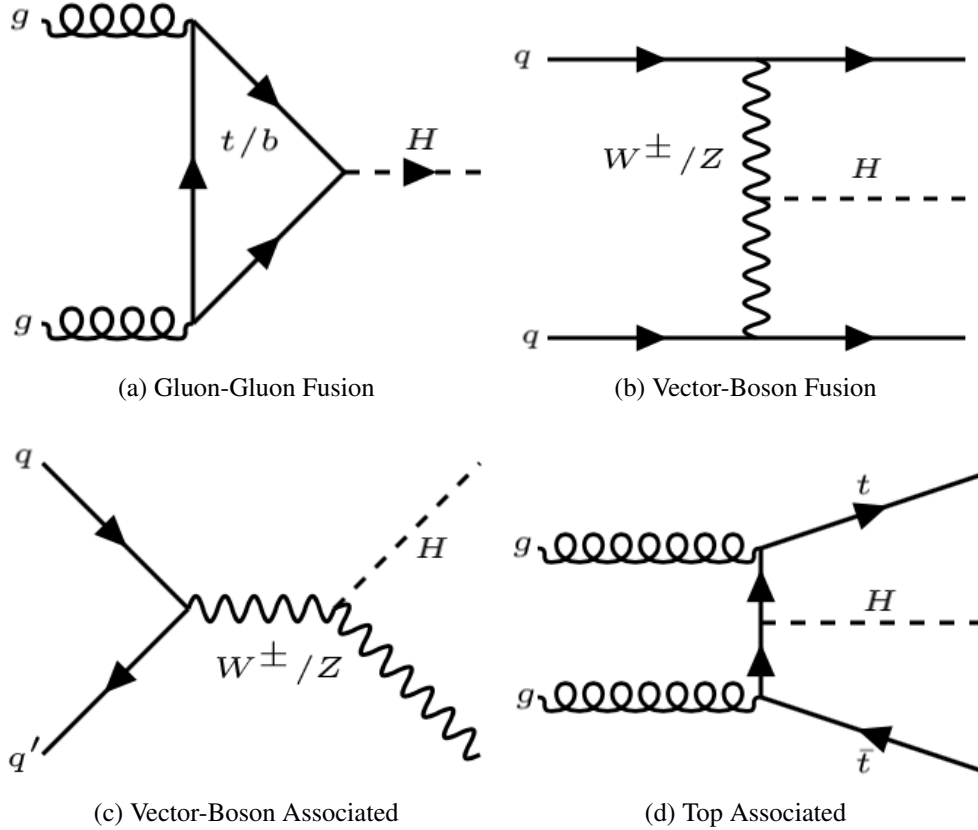
Figure 2.7:  The four main production processes of the Higgs boson at proton-proton collider.

provide probes to the coupling of the Higgs boson to the W/Z bosons and can be captured with the presence of W/Z decay products (leptons, quarks, or missing transverse momentum) in the final states. Since producing a $t\bar{t}$ pair and a Higgs boson requires a significant amount of energy from the incoming gluons, the $t\bar{t}H$ production has small cross section and will be discussed later in details.

Higgs boson decays are of great interest as they define the approach for identifying the Higgs boson. The branching fractions for different decay modes as a function of the Higgs boson mass are summarized in Figure 2.9. The dominant decay mode is the Higgs boson to a $b\bar{b}$ quark pair. However, searches for $H \rightarrow b\bar{b}$ are complicated by poor resolution of di-$b$-jets (from the fragmentation of $b$ quark, described in Chapter 4) mass spectrum and difficulties of identifying $b$-jets with sufficient accuracy and precision. Besides, the decay is difficult to distinguish from the overwhelming background of $b$-quark pairs produced via the QCD processes. The $H \rightarrow WW^*$ decay has the second largest branching fraction. With $W \rightarrow \ell\nu$, the reconstruction of a Higgs boson mass is difficult with the presence of neutrino. The $H \rightarrow \gamma\gamma$ and $H \rightarrow ZZ^* \rightarrow 4\ell$ decays, despite their small branching fractions, are most suited for the precision measurements of the Higgs boson properties, since they have many advantages such as the good mass resolutions and the excellent
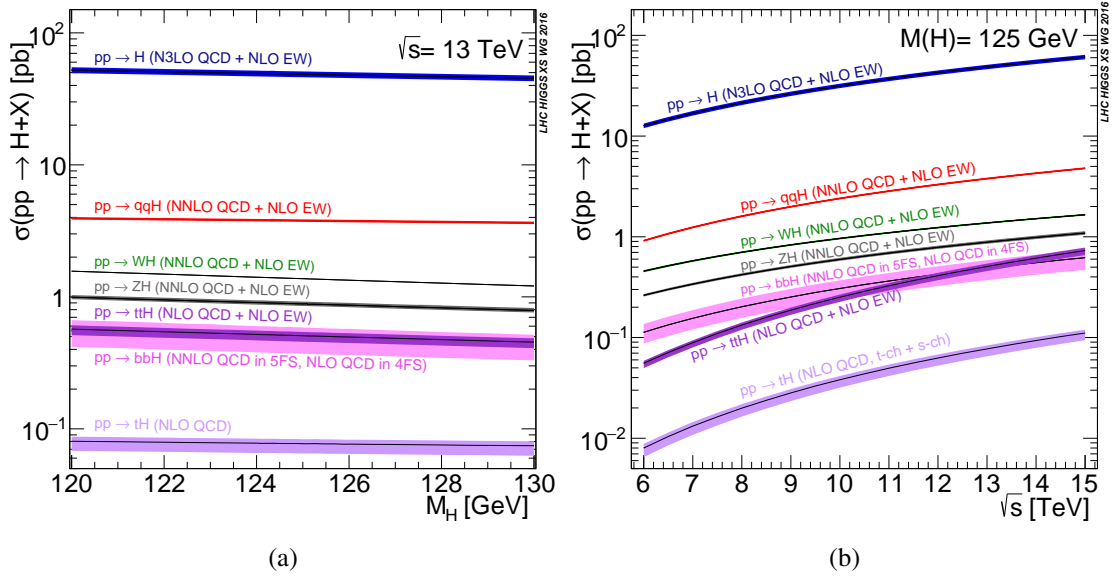
Figure 2.8: (a) The production cross sections of different processes as a function of Higgs boson mass at the center-of-mass energy $\sqrt{s} = 13$ TeV and (b) as a function of the center-of-mass energy with hypothesized Higgs boson mass of 125 GeV[48].

signal over background ratios.
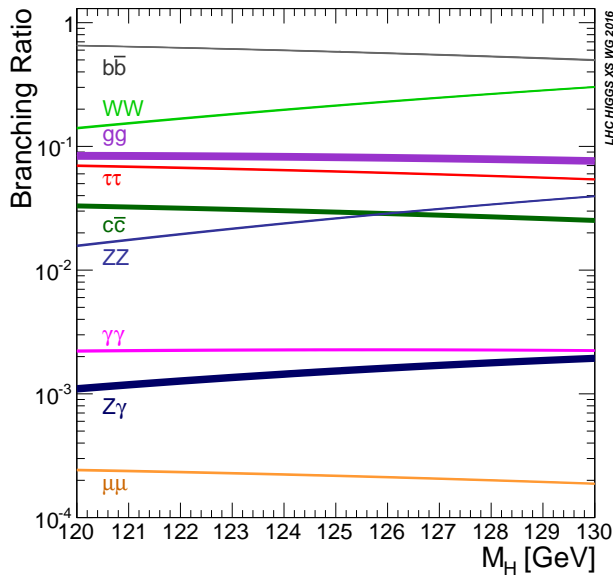


Figure 2.9: SM Higgs decay branching fractions[48].

### 2.5.1 Associated Production of a Higgs Boson with a Top Quark Pair

The Yukawa coupling of the Higgs boson with the top quark ($y_t$) is of special interests. Top quark is the heaviest fermion in the SM, with the largest Yukawa coupling around 1, and it impacts the stability of the potential for the Higgs field through radiative corrections. As shown in Figure 2.10, a small variation in $y_t$ turns the monotonic behavior of the effective potential for the Higgs field to one with an extra minimum at large values of the Higgs field. This suggests that $y_t$ might play a special role in the EWSB and can be sensitive to new physics[49].
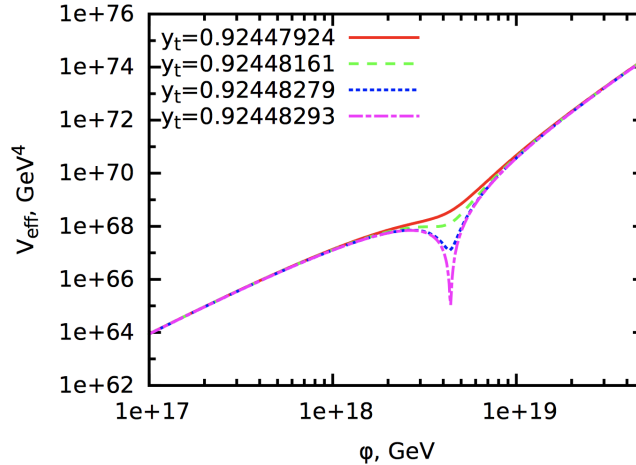


Figure 2.10: Different Higg potentials for Higgs fields corresponding to the different input values of top Yukawa coupling[49].

The $t\bar{t}H$ production can provide a direct way to measure $y_t$ at the tree-level. The SM predicts the Higgs boson to be a scalar particle ($J^{CP} = 0^{++}$), however the presence of a $J^{CP} = 0^{+-}$ pseudoscalar-scalar admixture is still allowed in many extensions beyond BSM, such as SUSY and *2-Higgs Doublet Models* (2HDM)[50], and $t\bar{t}H$ can be a good process to disentangle the BSM components[51].

The $t\bar{t}H$ cross section at $\sqrt{s} = 13$ TeV is $507^{+35}_{-50}$ fb, which is computed at the NLO in QCD with the leading NLO EW corrections (i.e. $\mathcal{O}(\alpha_s^2\alpha^2)$) [52–57].

However, searching for the $t\bar{t}H$ production can be difficult as $t\bar{t}H$ accounts for only around 1% of the total Higgs cross section. There are three different analyses designed to look for the $t\bar{t}H$ production based on Higgs boson decays:

- $t\bar{t}H$ ($H \to \gamma\gamma$) which has a very tiny cross section but a clean signature;

- $t\bar{t}H$ ($H \to b\bar{b}$) which is the dominant mode but has large background from $t\bar{t}$ production with associated $b$-jets.

- $t\bar{t}H$ ($H \to WW^*/ZZ^*/\tau^\pm\tau^\mp$) which will result in the SSML final states with sensitivity in between $t\bar{t}H$ ($H \to \gamma\gamma$) and $t\bar{t}H$ ($H \to b\bar{b}$).

The $t\bar{t}H$ process has been observed by both ATLAS[37] and CMS[40] in 2018 from the combination of $H \to b\bar{b}$, $\gamma\gamma$ and multilepton channels. Searches for $t\bar{t}H$ in SSML final states will be presented in Chapter 6.

## 2.6   Top Quark Phenomenology at the LHC

The top quark is the heaviest known elementary particle, and was discovered in 1995 by the CDF and DØ collaborations[20, 21]. After its discovery, the top quark has been scrutinized at the Tevatron and the LHC collider for many of its properties, ranging from measurements of top quark mass, to spin correlations in $t\bar{t}$ production, and to measurements of the Yukawa coupling of the top quark in $t\bar{t}H$ . The last is part of a class of processes, denoted as $t\bar{t} + X$ and $t + X$, where top-quark pairs or single top quark are produced in association with other elementary particles, and this type of processes provide access to some of top quark's most interesting properties: the Yukawa coupling in measurements involving the $t\bar{t}H$ vertex, and the weak coupling of the top quark to a vector boson in measurements with top interacting with a vector boson. These processes are of great interests because many BSM theories introduce modifications to the top-quark sector and to the couplings of the top quark. Any deviations from the SM predictions due to BSM effects can be parametrized in a model-independent way using the framework of the *Standard Model Effective Field Theory*  (SMEFT)[58–60].

### 2.6.1   Associated Production of a Top Quark Pair with a W Boson

Measurements of top-quark pairs in associated with a W boson, $t\bar{t}W$, directly probe the weak coupling of the top quark to a W boson. The $t\bar{t}W$ process is often an important background in searches involving final states with SSML and $b$-quarks, i.e measurements of the $t\bar{t}H$ production and the four top quarks production.

The $t\bar{t}W$ cross section at $\sqrt{s} = 13$ TeV is $601 \pm 76$ fb, which is computed at NLO in QCD with the leading NLO EW corrections (i.e. $\mathcal{O}(\alpha_s^2\alpha^2)$) [48, 61, 62]. An overview of all measurements in comparison with the theoretical prediction is shown in Figure 2.11. Higher cross section for the $t\bar{t}W$ process has been observed in different analyses. This points to the limited understanding of the $t\bar{t}W$ process.

Recent work [63, 64] have shown that sub-leading NLO EW corrections for the $t\bar{t}W$ production are larger than expected, primarily because of the large NLO$_3$ term ($\alpha_s\alpha^3$) driven by the $t\bar{t}W + q$
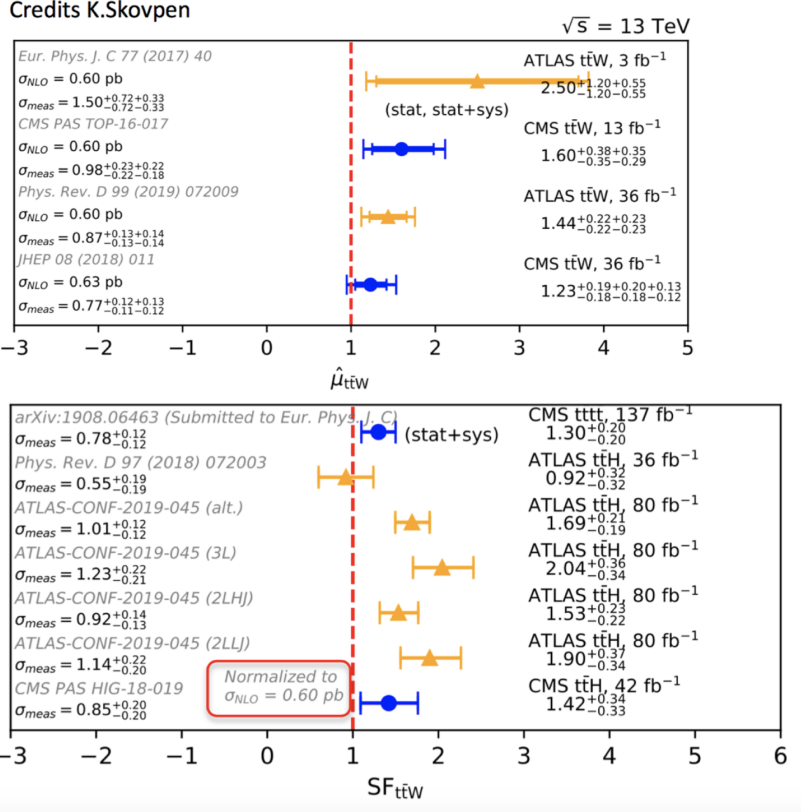
Figure 2.11: Measurements of $t\bar{t}W$ cross sections in different analyses (up) and scale factors for $t\bar{t}W$ measured in different phase spaces (bottom) compared with the theory calculation in Ref.[48].

diagrams with a Higgs boson exchanged in the $t$-channel (Feynman diagram for this NLO contribution is shown in Figure 2.12a). These subleading NLO EW corrections result in a 9% increase in the total cross section. Their effects on the jet-multiplicity distribution for $t\bar{t}W$ are not flat, as shown in Figure 2.12b. Besides, offshell effects at the decay level[65] and spin correlations of the decay products[64] can also affect $t\bar{t}W$ differential distributions. Further studies from both theories and experiments are needed to understand the $t\bar{t}W$ process.

## 2.6.2 Production of Four Top Quarks

The production of four top quarks ($t\bar{t}t\bar{t}$) is a rare process predicted by the SM, but has not been observed yet. The cross section of the SM production of the four top quarks in $pp$ collisions at $\sqrt{s} = 13$ TeV is predicted to be $\sigma_{t\bar{t}t\bar{t}} = 12$ fb with a relative scale uncertainty of $\pm 20\%$, computed at complete NLO [63]. Example of Feynman diagrams for $t\bar{t}t\bar{t}$ production in the SM is shown in Figure 2.13. The $t\bar{t}t\bar{t}$ cross section is sensitive to the magnitude and CP properties of the Yukawa coupling of the top quark to the Higgs boson since four top quarks can be produced via an offshell SM Higgs boson[66, 67], as shown in Figure 2.13b.
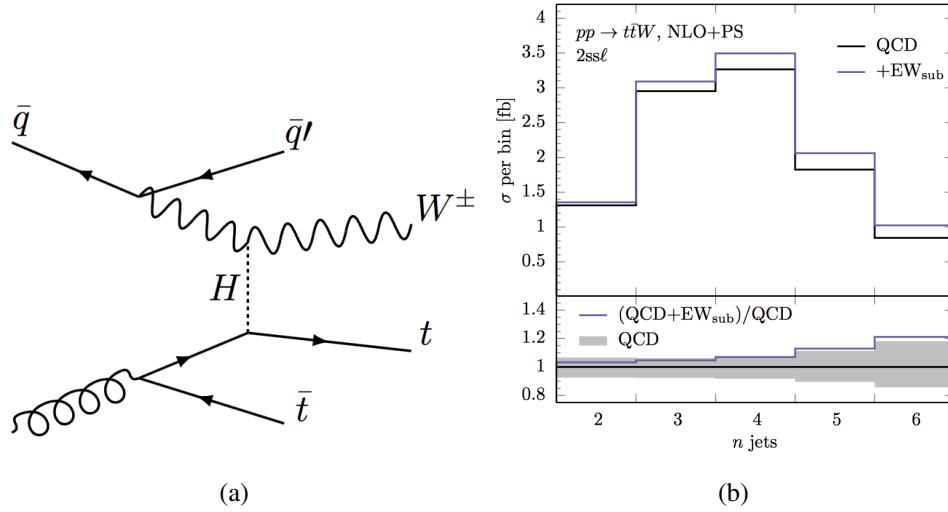
Figure 2.12: (a)The Feynman diagram for $\bar{q}g \to t\bar{t}W^{\pm}q'$ with a Higgs boson exchanged in the $t$-channel [63] and (b) the effect of the this EW contributions on the jet multiplicities [64].
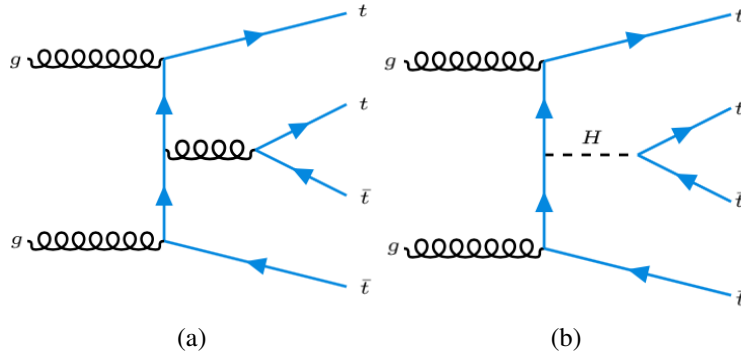


Figure 2.13: (a)Example of Feynman diagrams for SM $t\bar{t}t\bar{t}$ production at leading order in QCD and (b) Feynman diagrams for $t\bar{t}t\bar{t}$ coming from offshell SM Higgs boson.

Enhancements of the $t\bar{t}t\bar{t}$ cross section are expected in many BSM scenarios, such as gluino pair production in SUSY theories [68, 69](shown in Figure 2.14a), pair production of scalar gluons [70, 71], or the production of a heavy pseudoscalar or scalar boson in association with a top-quark pair ($t\bar{t}$) in Type II 2HDM [72–74](shown in Figure 2.14b). Within the effective field theory framework, the BSM contribution to $t\bar{t}t\bar{t}$ production can be parametrized by nonrenormalizable effective couplings and can be represented for instance via a $t\bar{t}t\bar{t}$ contact interaction (shown in Figure 2.14c).

ATLAS and CMS previously searched for the $t\bar{t}t\bar{t}$ production in 13 TeV $pp$ collisions. The ATLAS search combined the results in the SSML and in the channel selecting single-lepton or
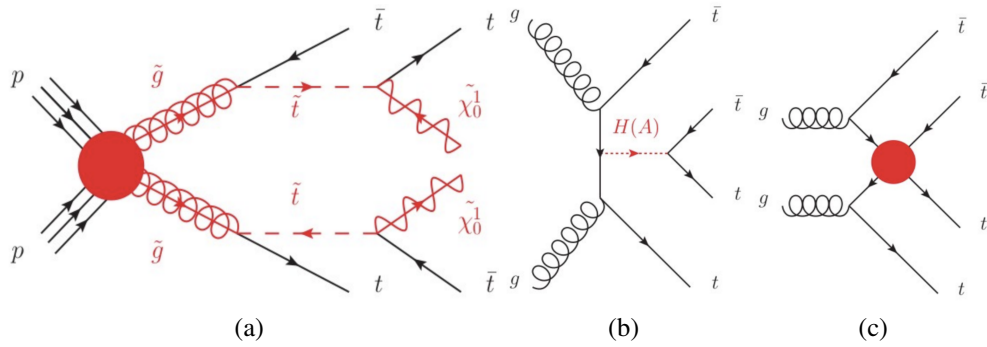
Figure 2.14: The Feynman diagrams for $t\bar{t}t\bar{t}$ production from (a) gluino pair production in SUSY, (b) the production of a heavy pseudoscalar or scalar boson in association with a top-quark pair, and (c) a $t\bar{t}t\bar{t}$ contact interaction.

dilepton events with two opposite-sign charged leptons (called 1L/2LOS) using 36 fb$^{-1}$ of data leading to an observed (expected) significance of 2.8 (1.0) standard deviations [75, 76]. The CMS combination of the 1L/2LOS and SSML channels using 36 fb$^{-1}$ quotes an observed (expected) significance of 1.4 (1.1) standard deviations [77]. The latest CMS search using 137 fb$^{-1}$ in the SSML channel leads to an observed (expected) significance for the $t\bar{t}t\bar{t}$ signal of 2.6 (2.7) standard deviations [78]. Evidence for $t\bar{t}t\bar{t}$ production is achieved in the SSML channel by ATLAS using an integrated luminosity of $139$fb$^{-1}$[79] and this analysis will be presented in Chapter 7.

# CHAPTER 3

# Large Hadron Collider and ATLAS Detector

## 3.1 Large Hadron Collider

The *Large Hadron Collider* (LHC) [80], straddling the border between France and Switzerland at the CERN[1] laboratory, is the world's largest and most powerful particle accelerator with a circumference of 27 kilometers and is designed to probe energy frontier at the TeV scale.
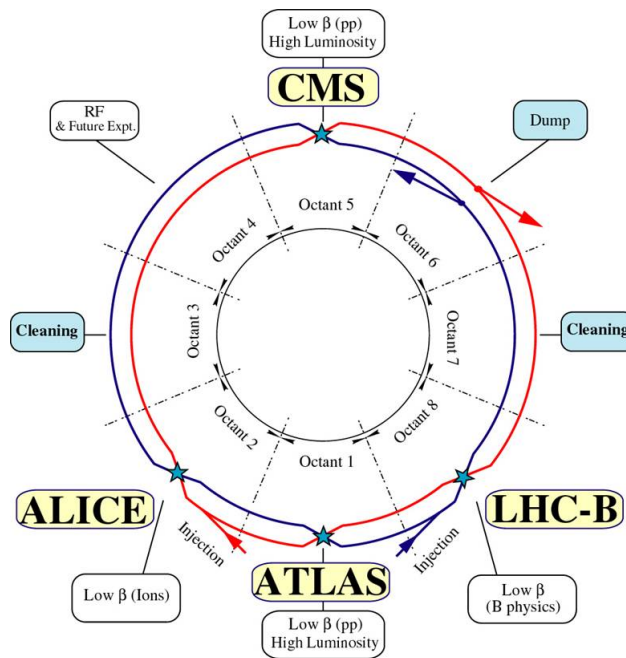


Figure 3.1: Overview schematic for the four main experiments and the two ring structures of the LHC.

The basic layout of the LHC is shown in Figure 3.1. Unlike a particle-antiparticle collider that can have both beams in the same phase space in a single ring, LHC is a particle-particle collider

---

[1]The European Organization for Nuclear Research (French: Organisation europenne pour la recherche nuclaire), known as CERN is a European research organization that operates the largest particle physics laboratory in the world.

where two counter rotating beams are made to collide head-on at specific Interaction Points (IPs). It operates at *Proton-proton* ($pp$), lead-lead (*Pb-Pb*) and proton-lead (*p-Pb*) collision modes. There are four IPs, and each IPs is instrumented with a detector. The four detector and their main physics goals are summarized below:

- **ALICE** (A Large Ion Collider Experiment) [81]: A heavy-ion detector to study physics of strongly interacting matter at extreme energy densities, where a phase of matter called quark-gluon plasma forms;

- **ATLAS** (A Toroidal LHC Apparatus)[82]: One of the two general purpose detectors to probe a wide range of physics including testing the predictions of the SM and searching for BSM physics;

- **CMS** (Compact Muon Solenoid )[83]: The other general purpose detector;

- **LHCb** (Large Hadron Collider beauty) [84]: A $b$-physics detector to investigate the properties of $b$-hadrons, particularly the slight differences between matter and antimatter in the interactions of $b$-hadrons.

The LHC has been in stable operation since 2009, and it operates in so-called 'runs', multi-year periods for roughly continuous data-taking[2]. There have been two runs of the LHC so far, Run I and Run II: the Run I (2010-2012) operation of the LHC at a center-of-mass energy of $\sqrt{s} = 7 - 8$ TeV, the Run II (2015-2018) operation recently finished at a center-of-mass energy of $\sqrt{s} = 13$ TeV. The schedule of the LHC and its high-luminosity(HL) upgrade are illustrated in Figure 3.2.
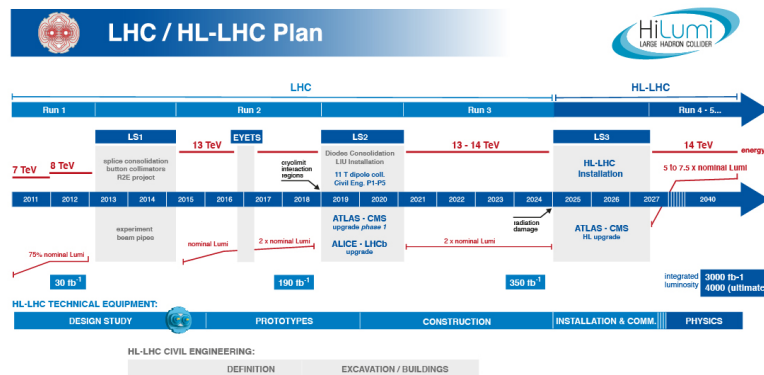


Figure 3.2: Schedule of the LHC operation[80].

---

[2]CERN shuts down during the winter months, each run is segmented each year with a several month long shutdown in the winter and a ramp-up period in the spring.

### 3.1.1 Injection Chain

The LHC is designed to accelerate protons to an energy of 7 TeV. To achieve such a high energy scale, the LHC is supplied with protons from injection chain Linac2 - Proton Synchrotron Booster (PSB) - Proton Synchrotron (PS) - Super Proton Synchrotron (SPS) as shown in Figure 3.3. Pro-
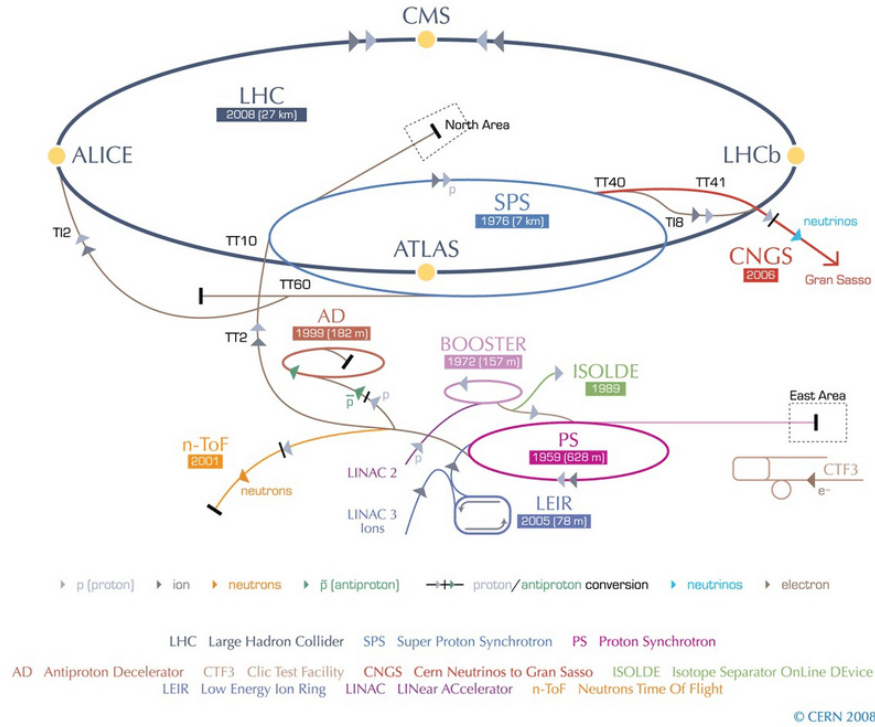


Figure 3.3: The schematic layout of the accelerator complex at CERN. The protons are accelerated through Linac 2, PSB, PS and SPS before injected into the LHC[85].

tons are initially produced from Hydrogen atoms using a metal cylinder called a Duoplasmatron, in an electric field. In the next stage, the protons pass through Linac 2, a linear accelerator, with the kinematic energy accelerated to 50 MeV. They then enter the PSB, a circular storage ring composed of four stacked rings which accelerate the protons further to 1.4 GeV. The protons are then transformed into the PS, which accelerates them to 25 GeV. Before extraction from PS, proton bunches with 25 ns spacing are produced by debunching and rebunching the beam. Afterwards, the SPS receives the protons from the PS and accelerates them up to 450 GeV. At this point, the protons have sufficient energy to be injected into the LHC. After being injected into the main LHC ring, they are accelerated by 16 radio-frequency cavities up to the maximum velocities, and in Run-II, beams are ramped up to 6.5 TeV. The two beams travel in opposite directions before collision.

### 3.1.2 Luminosity

Luminosity (L) is also an important parameter to characterize the performance of a collider, and it is defined as the ratio of event rate ($\frac{dN}{dt}$) over the cross section ($\sigma$) of a process in which the event is produced,

$$L = \frac{1}{\sigma} \frac{dN}{dt} \tag{3.1}$$

The luminosity has the unit of $cm^{-2}s^{-1}$. It depends only on the beam parameters and can be written as:

$$L = \frac{N_b^2 n_b f_{\text{rev}} \gamma_r}{4\pi \varepsilon_n \beta^*} F, \tag{3.2}$$

where $N_b$ is the number of particles per bunch, $n_b$ is the number of bunches per beam, $f_{\text{rev}}$ is the revolution frequency, $\gamma_r$ is the relativistic gamma factor, $\varepsilon_n$ is the normalized transverse beam emittance, $\beta^*$ is the beta function at the collision point, and F is the geometry luminosity reduction factor due to the crossing angle at the IP, which can be expressed as:

$$F = \left(1 + (\frac{\theta_c \sigma_z}{2\sigma^*})^2\right)^{-1/2}, \tag{3.3}$$

where $\theta_c$ is the full crossing angle at the IP, $\sigma_z$ is the *Root Mean Square* (RMS) bunch length, and $\sigma^*$ is the transverse RMS beam size at the IP.

The integral of the luminosity over time ($L_{int}$):

$$L_{int} = \int L dt \tag{3.4}$$

called as the integrated luminosity, represents the data size in a data-taking period. It is expressed in terms of an inverse cross section (typically in $fb^{-1}$).

At the LHC, multiple $pp$ interactions occur within each bunch crossing. The mean number of $pp$ inelastic interactions per bunch crossing is often referred to as pile-up parameter ($\mu$), and characterizes the instantaneous luminosity at any give time. These additional collisions are uncorrelated with the hard-scattering process and can contribute as a background of soft energy depositions which have particular adverse and complex effects on jet reconstruction [86]. $\mu$ averaged over all colliding bunch pairs is denoted as $\langle \mu \rangle$. Figure 3.4 (a) shows the luminosity-weighted distribution of the $\mu$ value in $pp$ collision data at the LHC in years of 2015, 2016, 2017 and 2018 [87]. The data used in this dissertation were collected during the Run II operation of the LHC (Figure 3.4). Table 3.1 highlights the typical values of representative beam parameters of the LHC in $pp$ collision mode during the Run II operation. From 2016 to 2018, the peak luminosity surpassed the designed value.

28
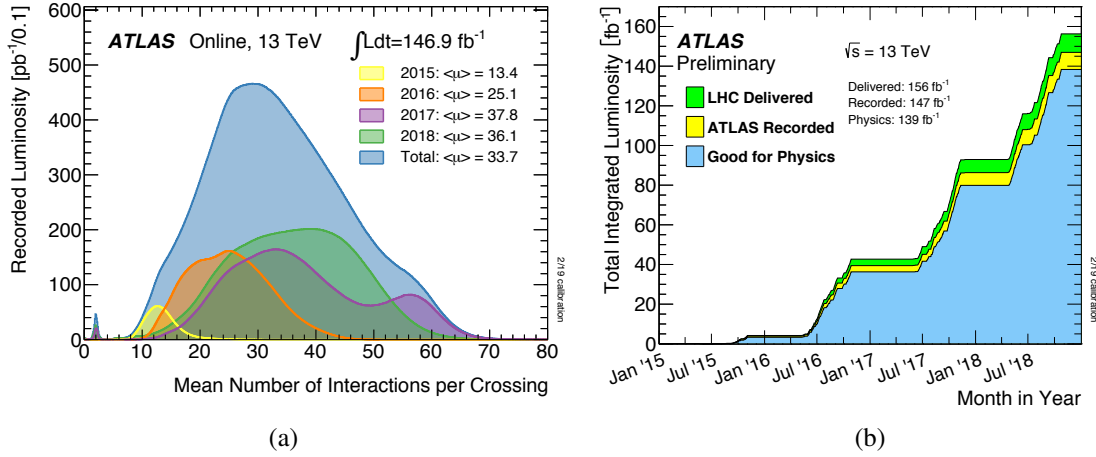
Figure 3.4: (a) The luminosity-weighted distribution of the mean number of interactions per crossing for 2015 - 2018 $pp$ collision data at $\sqrt{s} = 13$ TeV; (b)Cumulative luminosity versus time delivered to ATLAS (green), recorded by ATLAS (yellow), and certified to be good quality data (blue) during stable beams for $pp$ collisions at $\sqrt{s} = 13$ TeV in 2015-2018[87].

Table 3.1: Selected proton running condition in the LHC operation in Run II and the corresponding design parameters.

| Parameter | Design | 2015 | 2016 | 2017 | 2018 |
|---|---|---|---|---|---|
| Beam energy [TeV] | 7.0 | 6.5 | 6.5 | 6.5 | 6.5 |
| Bunches/beam $n_b$ | 2808 | 2232 | 2208 | 2544/1909 | 2544 |
| Bunch spacing (ns) | 25 | 25 | 25 | 25 | 25 |
| Typical bunch population ($10^{11}$ protons) | 1.15 | 1.1 | 1.1 | 1.1/1.2 | 1.1 |
| $\beta^*$ (m) | 0.55 | 0.8 | 0.4 | 0.3 | 0.3-0.25 |
| Peak Luminosity $L_{peak}$ ($10^{33}$cm$^{-2}$s$^{-1}$) | 10 | 5 | 13 | 16 | 19 |
| $\langle \mu \rangle$ | 25 | 13 | 25 | 38 | 36 |

## 3.2 ATLAS Detector

The ATLAS detector is a symmetric cylindrical detector that probes both $pp$ and heavy ion collisions, and it is designed to be sensitive to a wide range of physics, including tests of the SM and searches for new phenomena. Located at Point 1 of the LHC ring (see Figure 3.3), the ATLAS detector is 44m long and 25m in diameter, weighs about 7000 tons, and is the largest volume detector ever built for a particle collider. Being general purpose in scope, the ATLAS detector is hermetic and has nearly $4\pi$ solid angle coverage around the $pp$ collision point. A schematic view of the detector is shown in Figure 3.5. There are four sub-detectors including the *Inner Detector* (ID), the electromagnetic and hadronic calorimeters, and the *Muon Spectrometers* (MS). The
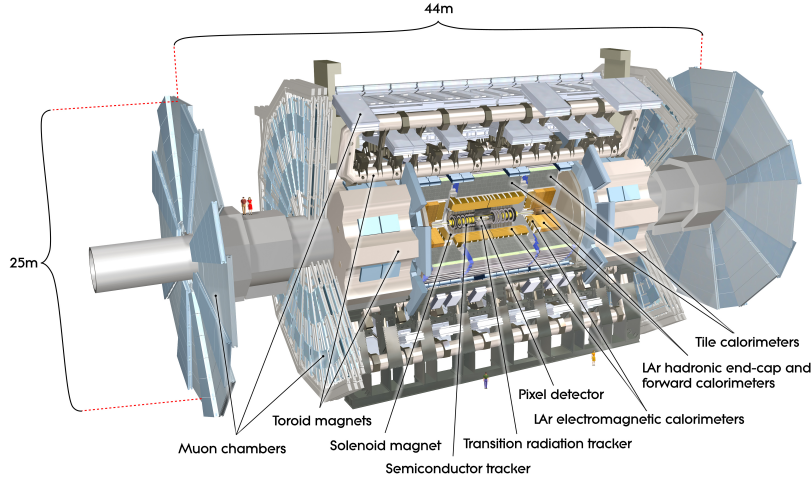
Figure 3.5: Cut-away view of the ATLAS detector[82].

*Trigger and Data Acquisition* (TDAQ) system, which selects events with distinguishing signatures from the collision, is integrated with the detectors. The general performance parameters for the sub-detectors are summarized in Table 3.2. In the following, each subsystem will be briefly introduced.

Table 3.2: Summary of general performance parameters of the sub-detectors.

| Subsystem | Resolution | $\eta$ coverage | Trigger coverage |
|---|---|---|---|
| Inner detector | $\sigma_{p_T}/p_T = 0.05\%p_T \oplus 1\%$ | $\pm 2.5$ | |
| EM calorimeter | $\sigma_E/E = 10\%/\sqrt{E} \oplus 0.7\%$ | $\pm 3.2$ | $\pm 2.5$ |
| Hadronic calorimeter | | | |
| Barrel and end-cap | $\sigma_E/E = 50\%/\sqrt{E} \oplus 3\%$ | $\pm 3.2$ | $\pm 3.2$ |
| Forward | $\sigma_E/E = 100\%/\sqrt{E} \oplus 10\%$ | $3.1 < \lvert\eta\rvert < 4.9$ | $3.1 < \lvert\eta\rvert < 4.9$ |
| Muon spectrometer | $\sigma_{p_T}/p_T = 10\%, p_T = 1\,\mathrm{TeV}$ | $\pm 2.7$ | $\pm 2.4$ |

### 3.2.1 ATLAS Coordinate System

The ATLAS experiment utilizes a right-handed Cartesian coordinate system with the interaction point at the origin, while the $z$-axis lies along the beam and the $x$-$y$ plane is transverse to the beam direction. The positive $x$-axis points from the IP to the center of the LHC rings, while the positive $y$-axis points upwards in the transverse plane. The side-A and side-C of the detector[3] is

---

[3]'A' for 'airport', since this is the side pointing towards Geneva International Airport, and 'C' for either 'Crozet' or 'Charly's' since this is the side pointing to two of Crozet and Charly's Pub in the town of Saint-Genis-Pouilly.

with positive and negative $z$, respectively. ATLAS also uses spherical coordinates, $(r, \phi, \theta)$ with the azimuthal angle $\phi$ measured as usual around the beam axis and the polar angle $\theta$ defined as the angle from the beam axis.

The nomenclatures normally used to describe the characteristics of the particles detected by the ATLAS detector are briefly introduced below. The pseudorapidity, $\eta$, is commonly used when describing systems of particles or locations within the detector and is defined as $\eta = -\ln[\tan(\theta/2)] = \frac{1}{2}\ln\left(\frac{|\mathbf{p}|+p_z}{|\mathbf{p}|-p_z}\right)$. In case of a massive object, the rapidity $y = \frac{1}{2}\ln\left(\frac{E+p_z}{E-p_z}\right)$ is used instead. The rapidity as a function of pseudorapidity can be approximately expressed as $y \approx \eta - \frac{\cos\theta}{2}(\frac{m}{p_T})^2$, so the pseudorapidity of a particle traversing the detector is equal to its rapidity if the particle is massless or ultra-relativistic. The component of the particle momentum in the transverse ($x$-$y$) plane is called as the transverse momentum $p_T$ ($p_T = p \cdot \sin(\theta)$). The transverse energy is defined as $E_T = \sqrt{p_T^2 + m^2}$ for an object with mass $m$ and transverse momentum $p_T$. The distance $\Delta R$, describing the angular distance in the $\eta$-$\phi$ space, is defined as $\Delta R = \sqrt{\Delta\eta^2 + \Delta\phi^2}$.

### 3.2.2 Inner Detector

The ATLAS *Inner Detector* (ID)[88][89], the innermost sub-detector as shown in Figure 3.6, provides precise particle tracking measurements while bombarded with intense radiation created at
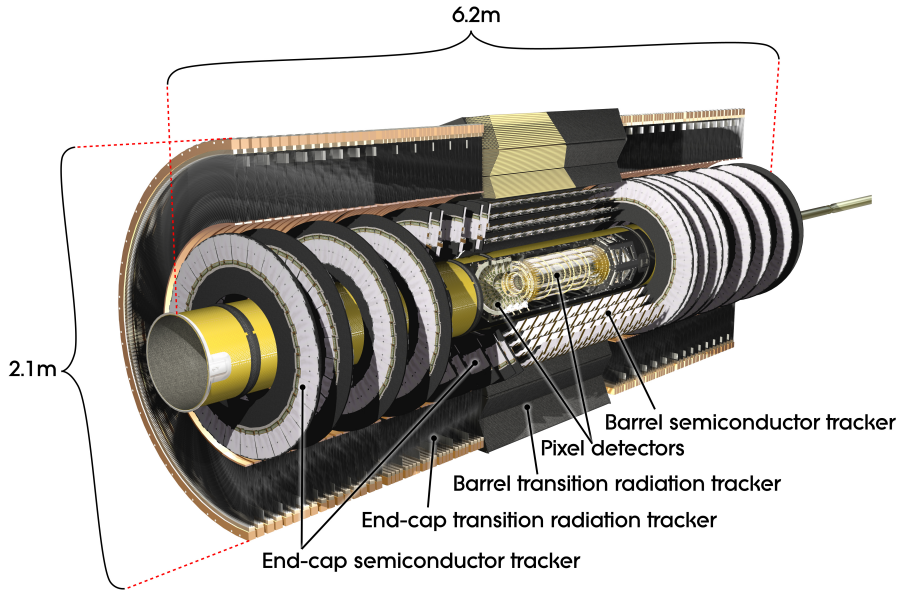


Figure 3.6: Schemtic view of the ATLAS Inner Detector[82].

high rates during collisions. It combines high-resolution detectors at inner radii (pixel and silicon detectors) with continuous tracking elements at outer radii (the transition-radiation tracker), all

contained in a thin superconducting solenoid magnet with a central field of 2T, which is parallel to the beam pipe. The ID is capable of providing hermetic and robust pattern recognition and excellent momentum resolution, as well as both primary and secondary vertex measurements for charged tracks above a given $p_T$ threshold (about 5 GeV) in $|\eta| < 2.5$. As shown in Figure 3.7, the ID consists of three sub-detectors: a semiconductor pixel detector offering the highest granularity around the vertex region, a *Silicon Conductor Tracking* (SCT) using silicon microstrip and pixel technology to provide the fine granularity, and a gas-filled straw tube *Transition-Radiation Tracker* (TRT) complementing the silicon tracker at larger radii. A summary of the main parameters is shown in Table 3.3.
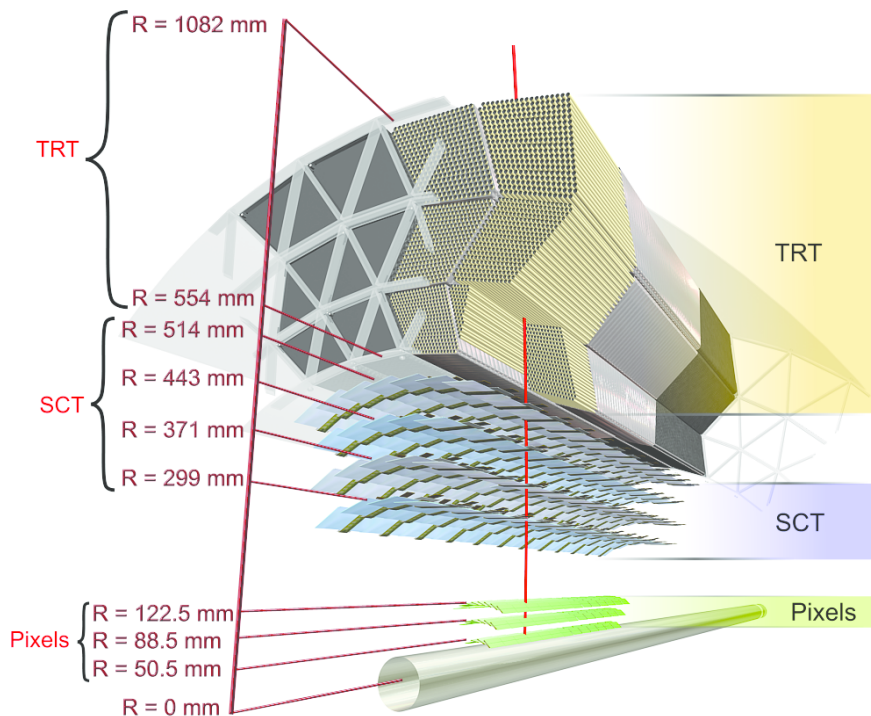


Figure 3.7: A schematic drawing of the Inner Detector showing the sensors and structural elements traversed by a charge track of 10 GeV $p_T$ in the barrel detector ($\eta = 0.3$)[90].

### 3.2.2.1 Pixel Detector and Insertable B-Layer

Being the innermost sub-detector of the ID, the pixel detector is designed to provide high-precision measurements per track as close to the IP as possible. It plays a vital role in determining the impact parameter resolution, vertex identification and identification of short-lived particles such as $b$ hadrons and $\tau$ leptons.

During LHC Run I, the pixel detector consisted of three cylindrical layers (B-layer, layer 1, layer 2) in the barrel, and three disk layers in the end-cap regions perpendicular to the beam pipe

Table 3.3: Parameters of the Inner Detector. The resolutions quoted are typical values (the actual resolution in each detector depends on $|\eta|$).

| System | Position | Area (m$^2$) | Resolution $\sigma(\mu$m$)$ | Channels ($10^6$) | $|\eta|$ coverage |
|---|---|---|---|---|---|
| Pixels | IBL | 0.2 | $R_\phi = 12$, $z = 66$ | 16 | $\pm 2.5$ |
| | 3 barrel layers | 1.4 | $R_\phi = 12$, $z = 66$ | 81 | $\pm 1.7$ |
| | 3 end-cap disks | 0.7 | $R_\phi = 12$, $z = 77$ | 43 | 1.7-2.5 |
| Silicon strips | 4 barrel layers | 34.4 | $R_\phi = 16$, $z = 580$ | 3.2 | $\pm 1.4$ |
| | 9 end-cap wheels | 26.7 | $R_\phi = 16$, $z = 580$ | 0.3 | 1.4-2.5 |
| TRT | Axial barrel straws | | 170 (per straw) | 0.1 | $\pm 0.7$ |
| | Radial end-cap straws | | 170 (per straw) | 0.32 | 0.7-2.0 |
| | 36 straws per track | | | | |

to guarantee at least three space points over the full tracking pseudorapidity range of $|\eta| < 2.5$. The active parts of the pixel detector consist of a module composed of silicon sensors, front-end electronics and flex-hybrids with control circuits. The nominal pixel size is 50 $\mu$m in the $\phi$ direction and 400 $\mu$m in $z$ (barrel region, along the beam axis) or $r$ (disk region). In total, there are approximately 80 million readout channels from the pixel detector alone. This results in fine spatial hit resolution of 12$\mu$m in $(r - \phi)$ and 66$\mu$m along $z$.

In Run II, a fourth layer, the *Insertabel B-Layer* (IBL)[91], was added to the pixel detector between a new beam pipe and the first pixel layer, at a radius of 33 mm. It alone accounts for 8 million readout channels of the pixel detector, resulting in a precise spatial hit resolution of 8$\mu$m in $(r - \phi)$ and 40$\mu$m along $z$. The addition of the IBL is aimed at improving both b-tagging efficiency and vertex resolution even in case of a complete B-layer failure, as well as, fulfilling the increasing bandwidth requirements resulting from the expected Phase-I LHC[4] peak instantaneous luminosity.

### 3.2.2.2 Semiconductor Tracker

The *Silicon Conductor Tracking* (SCT), using silicon-conductor-based sensing elements, surrounds the pixel detector, as illustrated in Figure 3.6. The SCT system is designed to provide four precision measurements per track in the intermediate radial range, contributing to the measurements of momentum, impact parameter and vertex position, as well as providing good pattern recognition by the use of high granularity. The barrel SCT uses eight layers of silicon microstrip

---

[4]In order to achieve the requirement for the High Luminosity of LHC (HL-LHC), the LHC accelerator plans a series of upgrades that will substantially increase the instantaneous luminosity. It is anticipated that the peak luminosity could reach $2 \times 10^{34}$/cm$^2$/s in the first phase of the LHC program (Phase-I LHC), providing an integrated luminosity of over 300 fb by 2023. In the second phase of the LHC physics program (Phase-II LHC), the accelerator will provide an additional integrated luminosity of about 2500 fb over 10 years of operation.

detectors to provide precision points in $(r - \phi)$ and $z$ coordinates. The barrel section of the SCT is composed of 4 cylindrical layers and the end-caps consist of 9 disks to ensure pseudorapidity coverage out to $|\eta| <2.5$. The spatial hit resolution of the SCT is 16 $\mu$m in $(r - \phi)$ and 580 $\mu$m along $z$.

### 3.2.2.3   Transition Radiation Tracker

The outermost component of the ID is the *Transition-Radiation Tracker* (TRT), based on the use of straw detectors. The TRT is intrinsically radiation hard, and allows on average 36 $(r - \phi)$ two-dimensional space-point measurements with a resolution of approximately 120 $\mu$m. In addition to tracking, electron identification capability is added by employing xenon gas to detect transition-radiation photons created in a radiator between the straws.

## 3.2.3   Calorimeters

The ATLAS calorimeter system[92, 93], situated outside of the ID and central solenoid, comprises both electromagnetic and hadronic calorimeters. It provides measurement and containment of showers from electrically charged and neutral particles. A view of the calorimeter system is provided by Figure 3.8. The calorimeters are split into two classes based on detector technology: either adopting liquid argon[93] or scintillator tiles[92] as the detector medium.
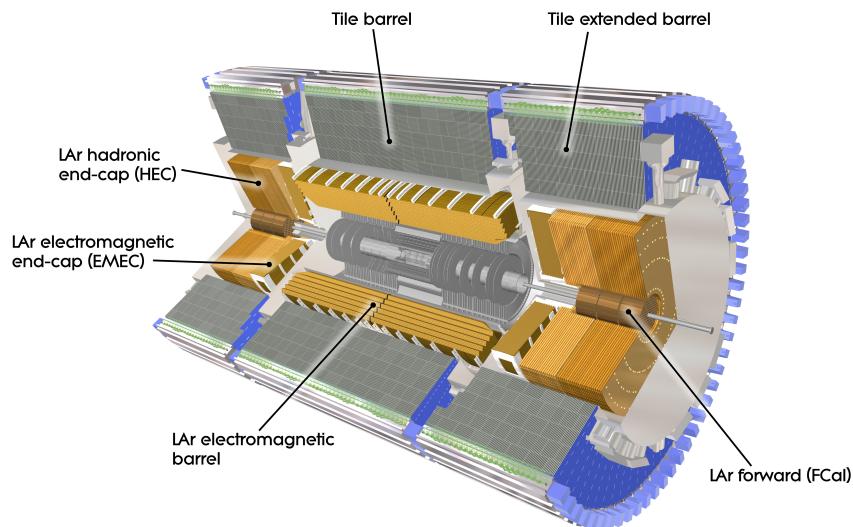


Figure 3.8: Cut-away view of the ATLAS calorimeter system[82].

The electromagnetic calorimeter is a high-granularity lead/liquid-argon (LAr) sampling calorimeter with an accordion geometry, providing complete $\phi$ symmetry without azimuthal cracks. It con-

tains a barrel part, covering regions $|\eta| < 1.475$, and two end-cap parts, covering regions $1.375 < |\eta| < 3.2$. The transition region between the barrel and the end-caps, $1.375 < |\eta| < 1.52$, has a large amount of material upstream of the first active calorimeter layer. Over the region $|\eta| < 2.5$, the electromagnetic calorimeter is divided into three layers in depth, which are finely segmented in $\eta$ and $\phi$. In the region $2.5 < |\eta| < 3.2$, electromagnetic calorimeter is segmented in two sections in depth. In front of the accordion calorimeter, an additional thin presampler layer, covering the $|\eta| < 1.8$, is used to correct energy loss upstream of the calorimeter.

The electromagnetic calorimeter is designed to measure the total energy of electrons and photons. Incoming electron or photon initiates a cascade of electromagnetic interactions where the pair production and bremsstrahlung dominate. The shower development is complex, and can be split into longitudinal profile and angular profile. The longitudinal distribution of energy deposition as a function of depth $t$ is reasonably described by

$$\frac{dE}{dt} = E_0 t^\alpha e^{-\beta t}, \tag{3.5}$$

where $\alpha$ and $\beta$ are model parameters and $E_0$ is the energy of the incident particle. The angular distribution of the produced particles by electromagnetic interactions is very narrow, and the lateral width can be characterized by Morliere radius

$$R_M = X_0 \frac{21.2\text{MeV}}{E_c}, \tag{3.6}$$

where $X_0$ is the radiation length and $E_c$ is the critical value below which absorption processes like ionization for electrons, Compton and photon-electric effects start to dominate. To ensure that the majority of electrons and photons are contained within the electromagnetic calorimeter, the electromagnetic calorimeter has a total thickness of $> 22X_0$ in the barrel and $> 24X_0$ in the end-cap.

The hardonic calorimeter includes the tile calorimeter, the liquid-argon hadronic calorimeter (HEC) and the liquid-argon forward calorimeter (FCal). The tile calorimeter is located in the barrel region, and it is split into three layers in depth.

The hadronic showering is dominated by a succession of inelastic hadronic interactions which are characterized by multi-particle production and particle emission originating from nuclear decay of excited nuclei. The longitudinal development of hadronic showering is determined by the average nuclear interaction length $\lambda$ which is much larger than $X_0$. Apart from the large longitudinal development of hadron cascades, their lateral width is also largely increased compared to electromagnetic cascades. This is caused by the large transverse momentum transfers in the nuclear interactions. The hadronic calorimeter has a total thickness of approximately $7\,\lambda$ in the barrel

region and around 12 $\lambda$ in the end-cap region. Together with the electromagnetic calorimeter, it can effectively contain the majority of the particle showers and limit the punch-through into the muon system.

The total energy resolution of a calorimeter can be parameterized with three terms

$$\frac{\sigma_E}{E} = \frac{a}{\sqrt{E}} \oplus \frac{b}{E} \oplus c, \tag{3.7}$$

where a, b, c are constants, and the three terms are due to energy fluctuations, electric noise and shower leakage, respectively. The electromagnetic calorimeter offers good energy resolution with the sampling term of the energy resolution at the level of $10\%/\sqrt{E}$ and a global constant term less than $0.7\%$. For the hadronic calorimeter, the response to charge pions, electrons and muons is quite different. Using charge pions as a benchmark, the hadronic calorimeter provides energy resolution around $50\%/\sqrt{E} \oplus 3\%$ in the barrel and end-cap region. On the other hand, the forward calorimeter gives much worse energy resolution around $100\%/\sqrt{E} \oplus 10\%$.

### 3.2.4 Muon Spectrometer

The *Muon Spectrometers* (MS) [94] is the outermost system of the ATLAS detector. The layout of the MS is illustrated in Figure 3.9. As shown in Figure 3.10, in the barrel region, tracks are
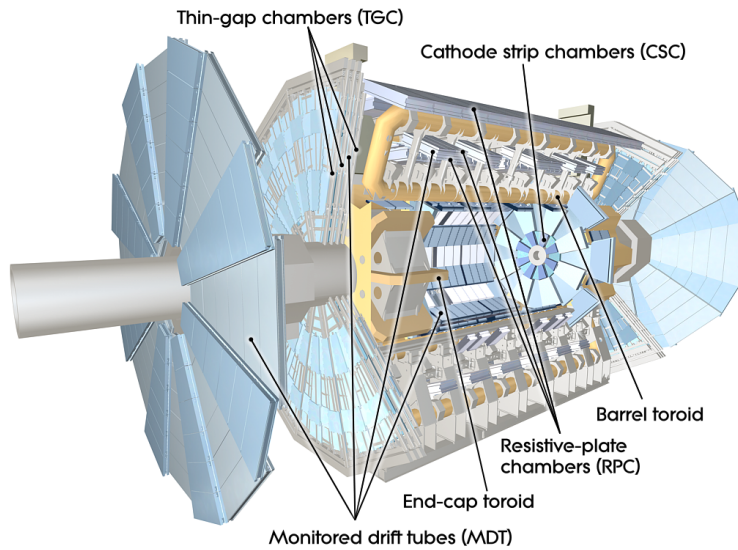


Figure 3.9: Schematic illustration of the muon spectrometer system composed of the detector panels and the toroid magnets[82].

measured in chambers arranged in three cylindrical layers around the beam axis; in the transition and end-cap regions, the chambers are installed vertically, also in three layers.
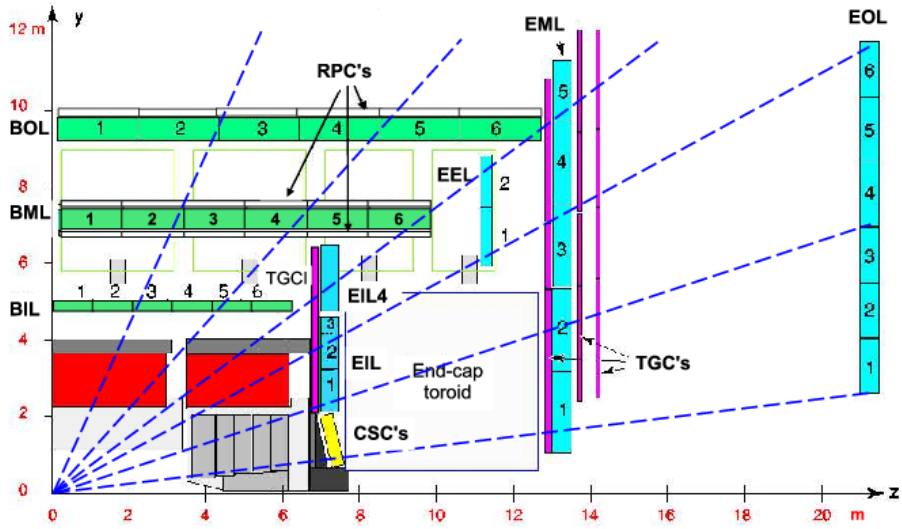
Figure 3.10: Cross-sectional view of the ATLAS detector in the $r - z$ projection of a quadrant of muon spectrometer.

The MS is housed in large superconducting air-core toroid magnets. The magnet system[95] consists of three toroids, with barrel toroid (BT) covering $|\eta| < 1.4$ and two end-cap toroids (ECTs) inserted at each end covering 1.6< $|\eta|$ <2.7 (as shown in Figure 3.11). The bending power
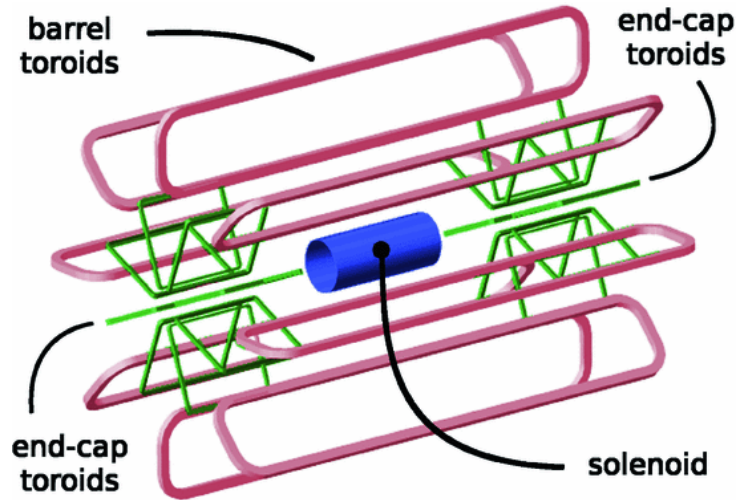


Figure 3.11: Magnet system of the ATLAS detector[95].

as function of $\eta$ is shown in Figure 3.12a. The magnetic field provides typical bending powers of 3 T in the barrel and 6 T in the end-cap regions. Owing to the finite number of coils, the

field configuration is not perfectly toroidal and presents a regularly rippled profile (Figure 3.12b). These effects are most visible in the transition region between the BT and the ECT, where there exist significant radial field components, as well as small regions with degraded bending power.



(a)                                          (b)
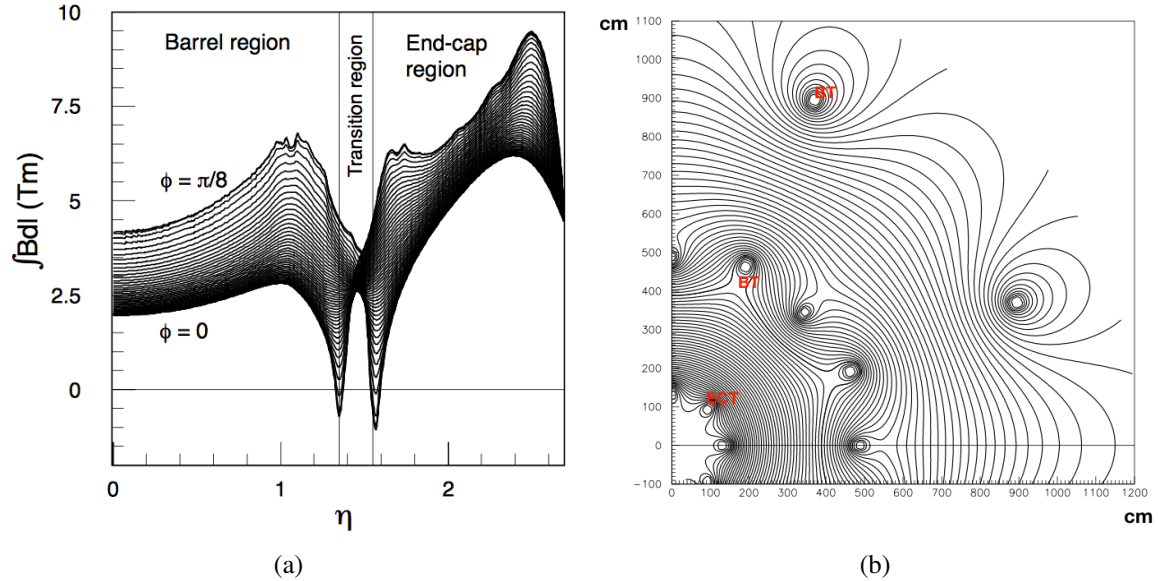
Figure 3.12: (a) Toroid bending power $\int B dl$ of the azimuthal field component, integrated between the first and the last muon chamber, as a function of pseudorapidity. The curves correspond to azimuthal angles equally spaced between the barrel toroid and end-cap toroid. (b)Magnetic field map in the transition region. The field lines are shown in a plane perpendicular to the beam axis and located in the middle of an end-cap toroid. The interval separating consecutive lines is 0.1 T. Individual barrel and end-cap coils are visible[94].

The MS consists of precision-tracking chambers, which is responsible for precisely measuring the transverse momenta of the muons and the trigger chambers with fast response to trigger on the muons. The precision-tracking chambers are composed of the Monitored Drift Tubes (MDTs), which are used over most of the $\eta$ range, and the Cathode Strip Chambers (CSCs) with higher granularity to fulfill the demanding rate and background conditions, which cover the large $\eta$ region and close to the beam line. The trigger chambers include three concentric cylindrical stations of the Resistive Plate Chambers (RPCs) in the barrel region and the Thin Gap Chambers (TGCs) in the end-cap region. The precision-tracking chambers provide precise measurement of muon tracks in the bending plane, while the trigger chambers provide measurement of track coordinates orthogonal to the precision measurement, in a direction approximately parallel to the magnetic field line. Selected parameters characterizing the performance of muon sub-systems are summarized in Table 3.4.

The MS has a momentum resolution as a function of $\eta$ and $\phi$. For a given value of $\eta$, the muon

Table 3.4: Parameters of the sub-system of the MS.

| Detector Type | Chamber Resolution (RMS) | | | Number of | |
|---|---|---|---|---|---|
| | $z/R$ | $\phi$ | time | chambers | channels |
| MDT | 35 $\mu$m | - | - | 1194 | 370k |
| CSC | 40 $\mu$m | 5 mm | 7 ns | 32 | 67k |
| RPC | 10 mm | 10 mm | 1.5 ns | 596 | 355k |
| TGC | 2-6 mm | 3-7 mm | 4 ns | 192 | 440k |

momentum resolution can be parameterized as a function of $p_T$ :

$$\frac{\sigma_{p_T}}{p_T} = \frac{p_0^{MS}}{p_T} \oplus p_1^{MS} \oplus p_2^{MS} \cdot p_T, \tag{3.8}$$

where $p_0^{MS}$, $p_1^{MS}$ and $p_2^{MS}$ are coefficients related to the energy loss in the calorimeter material, multiple scattering and intrinsic resolution term, respectively. The MS is optimized to provide a relative resolution better than $3\%$ over a wide $p_T$ range, and $10\%$ at $p_T = 1$ TeV.

### 3.2.5 Trigger and Data Acquisition

The *Trigger and Data Acquisition* (TDAQ) system[96–98] plays an essential role in ATLAS data taking. With the size of a raw event being approximately $\mathcal{O}(1)$ MB, the rate of collision data at the designed LHC bunch crossings of 40 MHz is nearly $\mathcal{O}(10)$ TB/s. It is impractical to both respond and record every one of these events, due to the limitation in both processing power and data storage capacity. On the other hand, the rate of events with the interesting physics phenomena is only a small fraction of total event rates. For this reason, a competent trigger system is employed to select potential interesting candidate events to be further processed and considered for permanent storage. The trigger system is usually complemented by a data acquisition system which efficiently gather and process the data from the readout architecture.

A schematic layout of the ATLAS TDAQ system is shown in Figure 3.13. In Run II, the trigger system consists of two levels of event selections: a hardware-based Level-1 trigger (L1) reducing rate to 100 kHz and a software-based high-level trigger (HLT) further reducing event rate to 1 kHz. The L1 trigger uses relative coarse-grained measurements from calorimeters and MS to rapidly identify relatively high-$p_T$ objects like muons, electrons, photons, jets and $\tau$-leptons decaying into hadrons, as well as large missing and total transverse energy. The L1 calorimeter (L1Calo) triggers make use of information from both electromagnetic and hadronic calorimeters with a reduced granularity of approximately $\Delta\eta \times \Delta\phi = 0.1 \times 0.1$. The L1 Muon (L1Muon)
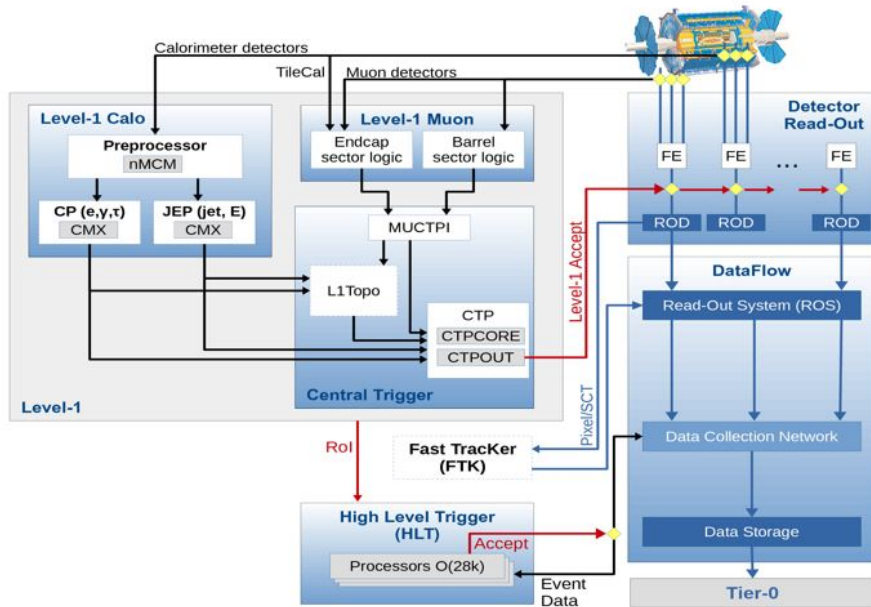
Figure 3.13: The ATLAS TDAQ system in Run II[82].

triggers provide fast trigger decision after collecting track information from RPC and TGC. A topological trigger processor (L1Topo) is capable to apply topological selections on the L1 trigger objects from both L1Calo and L1Muon triggers. Results from L1Calo, L1Muon and L1Topo are processed by the Central Trigger Processor (CTP), which implements a trigger 'menu' with the logical combinations of L1 trigger items. The CTP finally forms a trigger decision within 2.5 $\mu$s by processing logical combination. Pre-scaling of trigger menu items is implemented to allow optimal use of the bandwidth as luminosity and background conditions change. The L1 identifies Regions-of-Interests (ROIs), which are the regions of detector where the selected event has identified interesting features.

The candidate events selected by the L1 trigger system are forwarded to the HLT, which includes a level 2 (L2) trigger and the event filter (EF). The L2 selection is seeded by the RoI information provided by the L1 trigger, using all available detector data within the RoIs at full granularity and precision. The EF uses the ATLAS Athena[99] reconstruction framework to perform high level object reconstruction and identification.

# CHAPTER 4

# Particle Reconstruction and Identification

In order to transform raw information gathered in the ATLAS detector into well-defined and meaningful representations of the underlying physics processes, all physics analyses start with reconstructing and identifying physics objects, such as electron, muon, jets, ect.. The physics analyses presented in this dissertation involve use of leptons, photons, jets, and missing transverse momentum ($\mathbf{p}_T^{\text{miss}}$, the $p_T$ of undetectable particles, e.g. neutrinos). This chapter describes the reconstruction algorithms that are used to reconstruct and identify these physics objects.

## 4.1 Charged-Particle Tracks

The reconstruction of charged-particle tracks ('tracking') is based on information provided by the ID or the MS[100] which are introduced in Section 3.2. While the ID track reconstruction has to deal with the high track density imposes a large amount of combinatorial track candidates, the MS track reconstruction is mainly limited by huge amount of inert material, the cavern background and the highly inhomogeneous magnetic field. In the following, tracking in the ID and the MS will be introduced.

### 4.1.1 Tracking in the Inner Detector

Tracking in the ID is based on fitting a trajectory model to a set of measurements using a sequence of algorithms[100]. The inside-out algorithm starts from 3-point seeds in the silicon detectors and adds hits moving away from the interaction points using a combinatorial Kalman filter[1], and then tracks are extended into the TRT. This is the baseline algorithm designed for efficiently reconstructing the primary charged particles. In a second stage, a track search, referred to as back-tracking, starts from segments reconstructed in the TRT and extends inwards to include silicon

---

[1]Iterative algorithm that provides best estimation of the state based on projection of earlier measurements and current measurement.

hits. The back-tracking is designed to reconstruct secondary particles produced in the interactions or decays of the primary particles. Finally tracks with a TRT segment but no extension into the silicon detectors are referred to as TRT-standalone tracks.

Within the solenoidal magnetic field of the ID, charged-particle tracks follow helical trajectories and can be fully characterized by five track parameters:

$$(d_0, z_0, \phi, \theta, q/p), \tag{4.1}$$

where $d_0$ ($z_0$) is the transverse (longitudinal) impact parameter relative to the center of the beam spot, $\phi$ and $\theta$ are the azimuthal and polar coordinate, respectively, of the track at the point where $d_0$ and $z_0$ are defined, $q/p$ is the ratio of the particle charge to the magnitude of its momentum. An illustration describing the track parameters is shown in Figure 4.1.
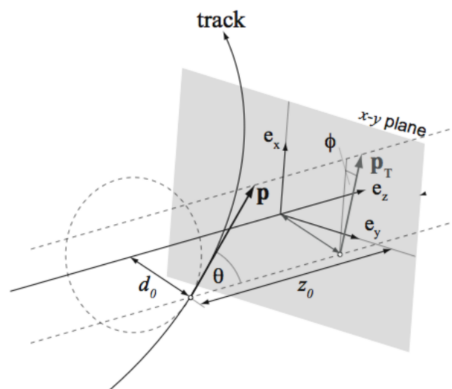


Figure 4.1: Illustration of the relationship between the track parameters and associated track.

## 4.1.2 Tracking in the Muon Spectrometer

Tracking in the MS start from segments reconstructed within each muon chamber[101]. In each MDT chamber and the nearby trigger chamber, a Hough transform is used to search for hits aligned on a trajectory in the bending plane. The segments are reconstructed by performing a straight-line fit to the hits found in each MDT layer. The RPC or TGC hits measure the coordinate orthogonal to the bending plane. Segments in the CSC detectors are built using a separated combinatorial search in the $\eta$ and $\phi$ detector planes, which includes a loose requirement on the compatibility of the segment with the luminous region.

The MS track candidates are then built by fitting hits from segments in different layers with a segment-seed combinatorial search. The search starts with segments generated in the middle layers of the detector where more trigger hits are available, then extends to use segments in outer

and inner layers as seeds. The segments are selected based on hit multiplicity and fit quality, and are matched using their relative positions and angles. At least two matching segments are required to build a track, except in the barrel-end-cap transition region where a single high-quality segment with $\eta$ and $\phi$ information can be used to build a track. Once a MS track candidate is formed from the combined segments, a global $\chi^2$ fit is performed to improve the association of hits to each muon candidate. A track candidate is accepted if the $\chi^2$ fit satisfies the pre-defined criteria. The $\chi^2$ fit is repeated to remove outlying hits as necessary, until a threshold is met for all associated hits.

## 4.2   Primary Vertex

*Primary Vertices* (PVs), the points where $pp$ interactions have occurred, are directly relevant to the reconstruction of hard-scatter interactions and are essential in reconstructing the full kinematic properties of the event. Reconstruction of PVs follows the adaptive vertex fitting (AVF)[102, 103] using the collection of the reconstructed tracks. The procedure of PV reconstruction is divided into two stages: vertex finding, which is a pattern recognition process where reconstructed tracks are associated to vertex candidates, and vertex fitting, which deals with reconstruction of the actual vertex position and its covariance matrix. The strategy is briefly outlined in the following steps:

- A set of tracks satisfying the track selection criteria is defined.

- A seed position for the first vertex is selected.

- The tracks and the seed are used to estimate the best vertex position with a fit following an iterative procedure. In each iteration, less compatible tracks are down-weighted and the vertex position is recomputed.

- The tracks incompatible with the vertex determined in the previous step are removed and allowed to be used in the determination of another vertex.

- The whole procedure is repeated with remaining tracks in the event to fit another vertex.

All vertices with at least two associated tracks are retrained as valid PV candidates. The presence of so-called secondary, tertiary and so on .. vertices are also important especially for flavor tagging described in Section 4.4.1 and photon conversion tagging discussed in Section 4.3.1.

## 4.3   Electron and Muons

In analyses, electrons and muons (light leptons) can be produced from the decay of heavy particles, such as W, Z, or Higgs boson, originating from hard interaction vertices. These leptons are

denoted as 'prompt leptons', and are of interest in most situations. Hence, the ability to efficiently reconstruct, identify and isolate them are essential steps in physics analyses.

Electrons and muons, being charged particles, leave identifiable tracks in the ID. As a result, their reconstruction involves the tracks and vertices as the initial seed. Electron reconstruction and identification, described in Section 4.3.1, are preformed based on the track information from the ID and calorimetric information from the electromagnetic calorimeter. Muon reconstruction and identification, described in Section 4.3.2, revolves around stitching together the tracks in the ID and MS.

Light leptons produced in $b/c$ hadron decays or photon conversion processes, denoted as 'non-prompt leptons', can become significant sources of background, especially in the SSML analyses, for example the $t\bar{t}H$ analysis presented in Chapter 6 and the $t\bar{t}t\bar{t}$ analysis presented in Chapter 7. Lepton isolation, which reduces contribution of non-prompt leptons, is described in Section 4.3.3.

### 4.3.1 Electron

#### 4.3.1.1 Electron Reconstruction

The reconstruction of electron candidates is based on three fundamental components characterizing the signatures of electrons: localized clusters of energy deposits found in the electromagnetic calorimeter (see Section 3.2.3), tracks in the ID, and close matching in $\eta \times \phi$ space of the tracks to the clusters which form the final electron candidates[104]. Figure 4.2 provides a schematic illustration of the elements that enter into the reconstruction of an electron. Electromagnetic-energy
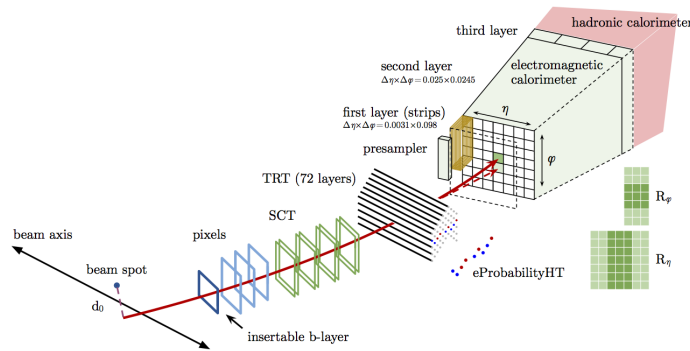


Figure 4.2: A schematic illustration of the path of an electron through the detector. The red trajectory shows the hypothetical path of an electron, and the dashed red trajectory indicates the path of a photon produced by the interaction of the electron with the material in the tracking system[104].

cluster candidates are selected from localized energy deposits in the electromagnetic calorimeter with a sliding-window algorithm[105] of size 3×5 towers in $\eta \times \phi$. The electromagnetic clusters are then seeded from towers of energy deposits with total transverse energy above $2.5$ GeV. The ID

tracks are refitted using a Gaussian Sum Filter (GSF) method[106] which takes into account of the non-linear effect of the bremsstrahlung radiation and improves estimation of the electron tracks. The GSF tracks are matched to the electromagnetic cluster seed using the cluster barycenter as the point of reference to match in $\eta - \phi$. If the electromagnetic cluster has an associated GSF-track with no association with a vertex from photon conversion[107], it is considered as an electron candidate; if the matched GSF candidate is not associated with the primary hard-scatter vertex but to a secondary vertex, the cluster is marked as a converted photon; if there is no GSF-track candidate matching to the electromagnetic cluster, the cluster is labeled as an unconverted photon.

#### 4.3.1.2 Electron Identification

Once an electron candidate is reconstructed, a likelihood-based (LH) identification is preformed to suppress background objects such as hadronic jets or converted photons[104]. The LH is a *Multivariate Analysis* (MVA) that makes a decision based on simultaneously evaluating several properties of the electron candidate, including measurements from the tracking system and the calorimeter system, as well as quantities that combine both tracking and calorimeter information. To meet the needs of different physics analyses, different WPs, including 'Loose', 'Medium' and 'Tight', are defined based on the values of the final LH discriminant to make the trade-off between signal efficiency and background rejection. Both 'Tight' and 'Loose' WPs are used in the $t\bar{t}H$ analysis (see Section 6.1), and only 'Tight' WP is used in the $t\bar{t}t\bar{t}$ analysis (see Section 7.1). The effi-
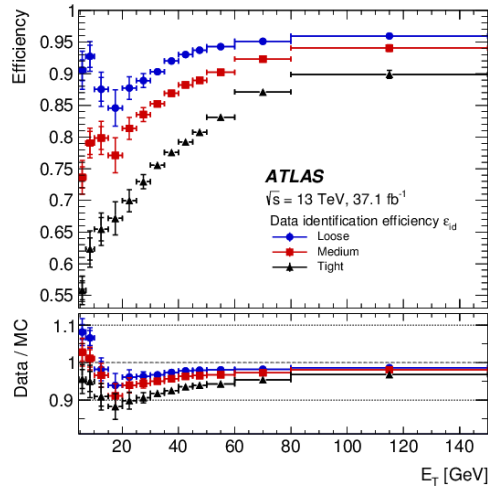


Figure 4.3: Measured LH electron-identification efficiencies in $Z \rightarrow e^+e^-$ events for Loose (blue), Medium (red) and Tight (black) WP as a function of $E_T$[104].

ciencies to identify prompt electron candidates with different WPs for data and the corresponding

45

data-to-simulation ratios are summarized in Figure 4.3. They are extracted from $J/\psi \to ee$ and $Z \to ee$ sample using tag-and-probe methods[104]. For the 'Tight' WP, the identification efficiencies for electrons and backgrounds are in a range of $85\% - 95\%$ and $0.2\% - 0.4\%$, respectively.

### 4.3.1.3 Electron Charge Identification

The electric charge of an electron is determined from the curvature of the associated track reconstructed in the ID. The mis-identification of the electron charge (referred to as Q-MisID) can occur through two mechanisms. The first is the 'trident' process in which an electron (positron) emits a hard bremsstrahlung photon that subsequently converts to an electron-positron pair. This can result in a track of the incorrect charge being associated with the electron. The second is the mismeasurement of the curvature of the electron track, and this typically happens for electrons with high momentum. The Q-MisID can be rejected with an additional selection criterion based on the output discriminant of a *Boosted Decision Tree* (BDT)[104] trained using TMVA toolkit[108]. The BDT parameters are optimized to achieve the best possible rejection of electrons reconstructed with the wrong charge given an efficiency loss of $3\%$ for electrons with correctly reconstructed charge. The probability of electron to have its charge mis-identified is measured using a sample of $Z \to ee$ events (described in Section 5.2.1). The comparison between the measured probability for Medium identified electrons with and without BDT selection is presented in Figure 4.4. This Q-MisID BDT is used in both the $t\bar{t}H$ analysis (see Section 6.1) and $t\bar{t}t\bar{t}$ analysis (see Section 7.1).
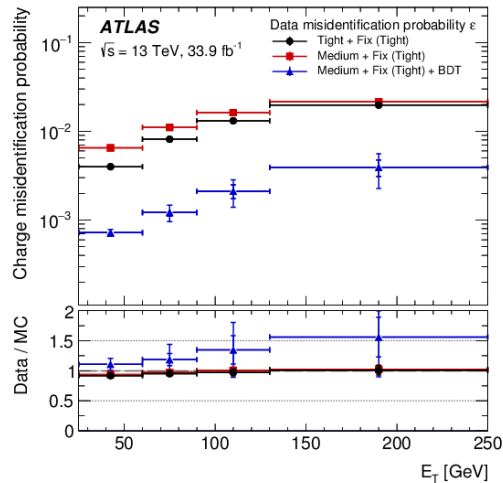


Figure 4.4: Charge-misidentification rates in 2016 data and simulated $Z \to ee$ events as a function of $E_T$ showing the impact of applying the BDT requirement to suppress charge mis-identification (red vs. blue)[104].

46

### 4.3.1.4  Photon Conversion Tagger

Electrons from photon conversion processes (referred to as conversions) can become non-negligible background in some analyses, especially in the $t\bar{t}H$ analysis and the $t\bar{t}t\bar{t}$ analysis. Conversion electrons can originate from the QED processes $\gamma* \to e^+e^-$, and are referred to as internal conversions. For internal conversions, a photon produced at the hard scattering level will immediately decay into a $e^+e^-$ pair and has conversion radius less than 20 mm (inside the beam pipe). Conversion electrons can also originate from photon interactions with the detector material, and are referred to as material conversions. Material conversions have conversion radius larger than 20 mm. Conversion electrons are reconstructed and identified due to two features of the ATLAS photon conversion reconstruction[107]:

- A conversion vertex is only reconstructed from a pair of silicon tracks when it has a radius larger than 20 mm with respect to the beam-line. As a result, conversions with radius less than 20 mm are considered as electrons.

- Conversion candidates with two tracks which have one track with a hit on the innermost silicon layer and the other without a hit on the innermost silicon layer are considered as electrons.

Rejection of conversions can be achieved with the reconstruction of the converted photons by relaxing the reconstruction requirements described above. Conversions tend to have more than one tracks associated to the cluster. To reconstruct converted photons, the best-matched track for the electron is paired with its closest track with opposite electric charge and the invariant mass of the pair ($m_{trk-trk,PV}$) is reconstructed (shown in Figure 4.5a). However, this can only correctly reconstruct mass for photon whose conversion vertex is close to the PV, thus can be used to capture



(a) $m_{trk-trk,PV}$      (b) $m_{trk-trk,CV}$      (c) $R_{CO}$
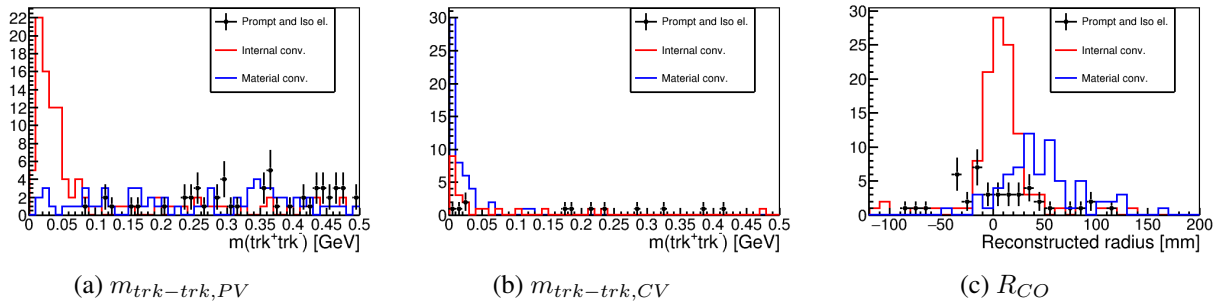
Figure 4.5: (a) Mass for the two associated tracks at the PV when no conversion vertex with $r > 20$ mm, (b) mass of two associated tracks at the conversion vertex for candidates with radius $r > 20$ mm and (c) Reconstructed radius for prompt internal conversions and material conversions.

internal conversions. To reconstruct material conversions, the correct conversion vertex is built by finding a point at which the momenta of the two tracks are parallel in the transverse plane. The reconstructed mass at the conversion vertex referred to as $m_{trk-trk,CV}$ is shown in Figure 4.5b. The $m_{trk-trk,PV}$ and $m_{trk-trk,CV}$ are used in the $t\bar{t}t\bar{t}$ analysis to constrain internal and material conversions (see Section 7.2). The reconstructed radius for the conversion vertex ($R_{CO}$), shown in Figure 4.5c, can provide good separation between internal and material conversions.

Photon conversion taggers is built based on variables described above ($R_{CO}$, $m_{trk-trk,CV}$ and $m_{trk-trk,PV}$ ). If a conversion vertex is found with radius $R_{CO} > 20mm$ and $m_{trk-trk,CV} < 100$ MeV, a material conversion candidate is defined. If the electron candidate is not from material conversion and has $m_{trk-trk,PV} < 100$ MeV, an internal conversion candidate is defined. By requiring the electron candidate to fail both material and internal conversion requirements, a very tight electron candidate is defined and conversions can be rejected around 40%. These three categories – material conversions, internal conversions and very tight electrons – are used in the $t\bar{t}H$ analysis (see Section 6.1).

### 4.3.2   Muon

#### 4.3.2.1   Muon Reconstruction

Muon reconstruction is performed based on the information from ID, MS and calorimeter. There are four types depending on different reconstruction methods and sub-detectors used[101].

- Combined (CB) muons: CB muons are reconstructed by combining hits from both the ID and MS sub-detectors. Most muons are reconstructed following an outside-in method in which muon is first reconstructed in the MS and then extrapolated inward and matched to an ID track. An inside-out combined reconstruction is used as a complementary approach.

- Segment-tagged (ST) muons: ST muons are built with ID tracks matched to at least one track segment in the MDT or CSC chambers. They are used when muons cross only one layer of MS chambers because of their low $p_T$.

- Calorimeter-tagged (CT) muons: a CT muon is reconstructed when an ID track is matched to energy deposit in calorimeter compatible with a minimum-ionizing particle, without having corresponding measurements in the MS. CT muons have the lowest purity, but they recover acceptance in the regions of MS that are only partially instrumented allowing for cabling and services to calorimeter and ID systems, particularly in the region $|\eta| < 0.1$.

- Extrapolated (ME) muons: ME muons are reconstructed solely using MS tracks and a loose requirement that the corresponding track is compatible with originating from the IP.

### 4.3.2.2 Muon Identification

Muon identification is implemented to suppress background, mainly from pion and kaon decays, and to select prompt muons with high efficiency and/or guaranteeing a robust momentum measurement. Reconstructed muons from in-flight decays of charged hadrons are often characterized by the presence of a distinctive "kink" topology in the reconstructed tracks, hence independent momentum measurements in the ID and MS may not be compatible for those muons. The muon identification makes use of quantities related to track qualities in the ID and MS, which are summarized below.

- $q/p$ significance, defined as

$$q/p = \frac{|q/p_{T,\text{ID}} - q/p_{T,\text{MS}}|}{\sqrt{\sigma^2_{p_T,\text{ID}} + \sigma^2_{p_T,\text{MS}}}}, \tag{4.2}$$

  is the absolute value of the difference between the ratio of the charge and transverse momentum of the muons measured in the ID and in the MS divided by the quadrature sum of the corresponding uncertainties.

- $\rho'$, defined as

$$\rho' = \frac{p_{T,\text{ID}} - p_{T,\text{MS}}}{p_{T,\text{CB}}}, \tag{4.3}$$

  is the absolute value of the difference between the transverse momentum measurements in the ID and MS divided by the $p_T$ of the combined track.

- normalized $\chi^2$ of the combined track fit.

- number of hits in the ID and the MS.

Several WPs are designed to suit the needs of a wide variety of physics analyses. Three standard WPs are designed to cover the needs of the majority of physics analyses: the *Medium* WP which provides an efficiency and purity suitable for a wide range of analyses and keeps the systematic uncertainties on prompt-muon efficiency and background rejection small, the *Loose* WP which offers a higher efficiency at the cost of less purity and larger systematic uncertainty and is designed for high muon multiplicity analyses like the Higgs boson decay in the four-muon final state, and the *Tight* WP which limits the non-prompt muon background. The *Medium* WP is used in both the $t\bar{t}H$ analysis (see Section 6.1) and the $t\bar{t}t\bar{t}$ analysis (see Section 7.1). Two additional WPs are designed for analyses targeting the extremes of the phase space. The *HighPt* WP ensures an optimal momentum measurement for muons with $p_T$ above 100 GeV, while the *LowPt* WP targets muons with $p_T$ below 5 GeV, which will be discussed in details.

### 4.3.2.3 Low-$p_T$ Muon Working Points

For muons with $p_T < 5$ GeV, the non-prompt muon background can be large, and the *LowPt* WP exploits a dedicated set of variables providing a good separation between prompt and non-prompt muons to obtain an optimal background rejection while maintaining high efficiency. Momentum balance significance (MBS) is defined as MBS $= (p_{ID} - p_{MS} - E_{loss})/\sigma(E_{loss})$, where $p_{ID}$ and $p_{MS}$ are respectively the momentum measured in the ID and in the MS, $E_{loss}$ is the energy lost measured in the calorimeter system, and $\sigma(E_{loss})$ is the uncertainty on $E_{loss}$. For muons with no momentum measured in the MS, MBS is set to 0. The scattering neighbor significance (SNS) is a variable estimating the significance of a change in trajectory (kink) along the track, expected in the presence of a hadron decaying to a muon. The SNS is defined as the largest value of scattering angle significances over the entire track. Scattering angle significance is computed considering pairs of adjacent hits along the track, and evaluated as the significance of the angular distance in the bending plane between the two half tracks ending/starting at each of the hits. The scattering curvature significance (SCS) is computed as the change of the normalized integral of the scattering angle significances in the track bending plane, sensitive to large kinks along the trajectory. It is a variable used to capture the presence of a significant discontinuity in the track direction, which is a characteristic of in-flight hadron decays. Figure 4.6 shows the distributions of the described variables for prompt muons and for fakes in simulated $t\bar{t}$ events.
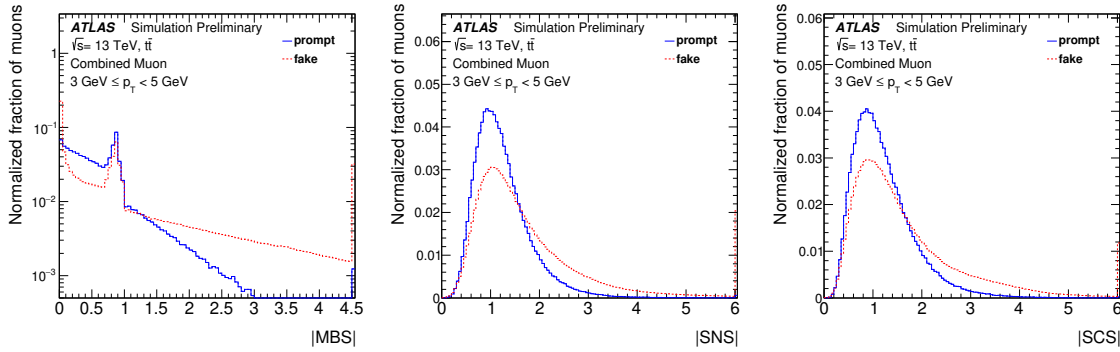


Figure 4.6: Simulated distributions, in $t\bar{t}$ events, of the MBS (left), SNS (centre) and SCS (right) for tracks associated to prompt muons (blue) and tracks associated to hadron fakes (red).

For the *LowPt* WP, only CB tracks are used. Two versions of the WP have been developed, referred to in the following as the cut-based and multivariate WPs respectively.

For cut-based WP, in $|\eta| < 1.3$, at least one MS station is required; in $1.3 < |\eta| < 1.55$, at least two MS stations are required; in $|\eta| > 1.55$, the *Medium* WP requirements are applied. Moreover, a very loose selection on the variables described above is used to suppress fakes: $|\text{MBS}| < 3.0$, $|\text{SNS}| < 3.0$ and $|\text{SCS}| < 3.0$.

The multivariate WP further exploits by combining several discriminating variables in a BDT, which is trained on separate samples from $t\bar{t}$ events containing prompt muons from W boson decays and non-prompt muons from light hadron decays respectively. The training is performed separately for muons reconstructed by the inside-out algorithm and outside-in CB muons with the same set of discriminating variables. The variables used include the same three that are used for the cut-based WP, as well as additional ones related to the MS segments associated with the muon, the energy loss in the calorimeters, and the number of missing precision hits in the middle MS layer.

The modeling of all variables in simulation is verified by comparing to data in dedicated control regions with a high purity of low-$p_T$ prompt muons and muons from hadron decays respectively. The modeling for prompt muons is evaluated using a tag-and-probe selection targeting the $J/\psi$ resonance. The modeling for muons from hadron decays is evaluated using a selection targeting the decay $B_s^0 \to J/\psi\phi$ with subsequent decays $J/\psi \to \mu^+\mu^-$ and $\phi \to K^+K^-$. A $B_s^0$ candidate is reconstructed by matching a pair of muons, which satisfy the *Medium* WP requirements and have an invariant mass close to the $J/\psi$ mass, to a common vertex with two ID tracks that have an invariant mass close to the $\phi$ mass. A high purity of $B_s^0$ events is attained by selecting candidates where four-particle invariant mass is close to $B_s^0$ mass. The modeling is checked for muon candidates matched to the ID tracks forming the $\phi$ candidates. Figure 4.7 shows the distributions for three variables used in the BDT in the $B_s^0$ region.
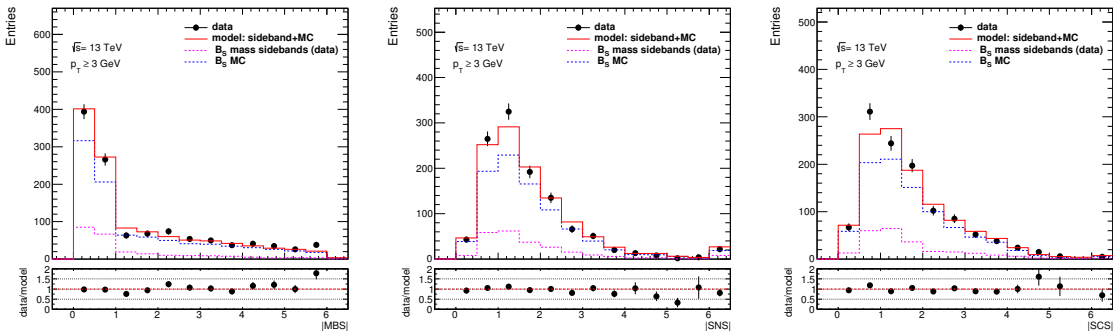


Figure 4.7: Distributions of the kinematic variables, MBS (left), SNS (center) and SCS (right), used in the *LowPt* WP for data and estimated background in the control sample for kaon decays.

In the construction of the multivariate *LowPt* WP, 8 variables are used which provide good discriminating power between prompt and fake muons and are well modeled in the *Monte Carlo* (MC). The distributions of the gradient BDT score for prompt and fake muons are shown in Figure 4.8, where a good separation between the two categories is observed. Good agreement is observed between the distributions obtained from the sample used for the BDT training and a statistically independent sample, indicating that there is no over-training of the BDT.

51
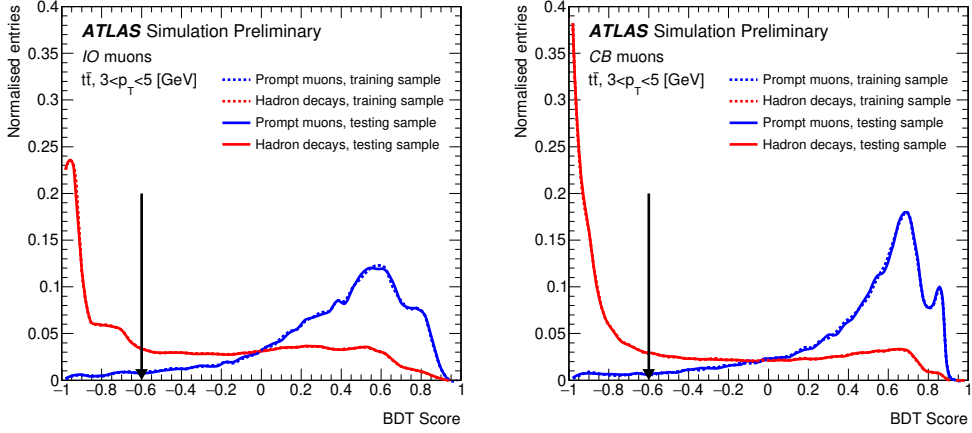
Figure 4.8: Distributions of the gradient BDT score for CB muons reconstructed with the inside-out (IO) algorithm(left) and other CB muons (right) in the simulated $t\bar{t}$ events. The distributions are shown for the event sample used to train the multivariate discriminant (dash line), and a statistically independent sample (full lines). The black arrows indicate the values of the requirements that define the multivariate *LowPt* selection.

The performance of the cut-based and multivariate *LowPt* WPs in simulation is compared to that of the Medium WP in Figure 4.9. Relative to *Medium* WP, the cut-based *LowPt* WP achieves a substantial increase in the prompt-muon efficiency in the barrel region while retaining good rejection of fake muons. In the end-cap regions, an improved rejection of fake muons is obtained at the cost of a small prompt-muon efficiency loss. Relative to the cut-based *LowPt* WP, the
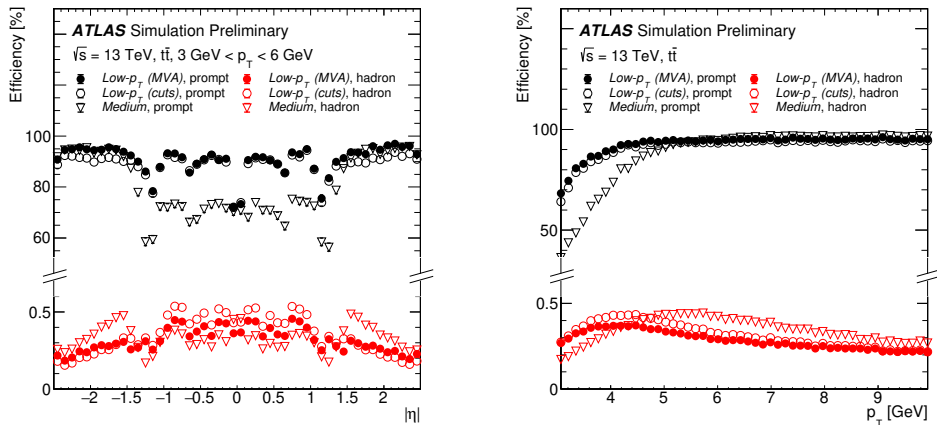


Figure 4.9: Efficiency as a function of $|\eta|$ (left) and $p_T$ (right) for *LowPt* and *Medium* requirements in simulated $t\bar{t}$ events, shown separately for prompt muons and muons from hadron decays. Both the cut-based and multivariate *LowPt* WPs are included.

multivariate WP achieves a better rejection of non-prompt muons in the barrel region and a higher prompt-muon efficiency in the end-cap region.

### 4.3.3 Lepton Isolation

Lepton isolation criteria are based on track- and calorimeter-based isolation variables. The track-based isolation variables, $p_T^{\text{varconeXX}}$ are defined as the sum of $p_T$ of the selected tracks within a cone centered around the lepton, excluding the lepton itself, where the surrounding cone has a variable radius defined as,

$$\Delta R = \min\left(\frac{10}{p_T[\text{GeV}]}, \Delta R_{\max}\right), \tag{4.4}$$

where $\Delta R_{\max}$ is the maximum cone size. The variable radius compensates for the fact that leptons produced in the decay of high-momentum heavy particles tend to have other decay products very close to the lepton's direction of travel. The isolation variable $p_T^{\text{varcone20}}$ ($p_T^{\text{varcone30}}$) has $\Delta R_{\max} = 0.2$ (0.3). Track-based isolation variables are largely pileup-independent, due to the rejection of tracks originating from pileup vertices or with large transverse impact parameters relative to the PV. The calorimeter-based isolation variable, $E_T^{\text{topocone20}}$, is defined as the sum of the transverse energies of topological cell clusters in the cone around the lepton, extrapolated to the calorimeter, after subtracting the contribution from energy deposit of lepton itself and correcting for pileup effects. Calorimeter-based isolation tends to be less reliable and more pileup dependent than the track-based isolation. Combining selections on track-based and calorimeter-based isolation, different isolation WPs are formed to fulfill the needs of a wide variety of physics analyses. In the $t\bar{t}H$ analysis (see Section 6.1), 'FixedCutLoose' WP is used; in the $t\bar{t}t\bar{t}$ analysis (see Section 7.1), 'FCTight' WP is used for electrons and 'FCTightTrackOnly' WP is used for muon. Table 4.1 lists these three WPs with the discriminating variables and the criteria used in their definitions.

Table 4.1: Definition of three isolation WPs used in the analyses presented in Chapter 6 and 7. The discriminating variables are listed in the second column and the criteria used in the definition are reported in the third column.

| Isolation WP | Discriminating variable(s) | Definition |
|---|---|---|
| FixedCutLoose | $p_T^{\text{varcone30}}/p_T, E_T^{\text{topocone20}}/p_T$ | $p_T^{\text{varcone30}}/p_T < 0.15, E_T^{\text{topocone20}}/p_T < 0.30$ |
| FixedCutTight | $p_T^{\text{varcone20}}/p_T, E_T^{\text{topocone20}}/p_T$ | $p_T^{\text{varcone30}}/p_T < 0.06, E_T^{\text{topocone20}}/p_T < 0.06$ |
| FixedCutTightTrackOnly | $p_T^{\text{varcone30}}/p_T$ | $p_T^{\text{varcone30}}/p_T < 0.06$ |

A multivariate discriminant 'non-prompt lepton BDT' [109] is developed for physics analyses that need the highest rejection of non-prompt leptons such as the $t\bar{t}H$ multilepton analysis (See

Section 6.1 ). This discriminant is based on a BDT taking 8 input variables related to isolation and b-tagging (see in Section 4.4.1), shown in Table 4.2. The training is performed using the simulated $t\bar{t}$ sample with two separated ranges of lepton transverse momentum, $3 < p_T < 10$ GeV and $p_T > 10$ GeV, to account for the strong $p_T$ dependency of the input variables. The distributions of the BDT score for prompt leptons and non-prompt leptons are shown in Figure 4.10.

Table 4.2: Variables used as input to construct the non-prompt lepton BDT.

| Variable | Description |
| --- | --- |
| $N_{\text{track}}$ in track jet | Number of tracks collected by the track jet |
| $RRN_{ip}$ | Recurrent Neural Network with additional impact parameter information of tracks inside the track-jet |
| DL1mu | DL1 (deep learning tagger) extended with Soft Muon Tagging information |
| $p_T^{rel}$ | The lepton $p_T$ projected on the track jet direction |
| $p_T^{tracklepton}/p_T^{trackjet}$ | The ratio of the track lepton $p_T$ and the track jet $p_T$ |
| $\Delta R(lepton.trackjet)$ | $\Delta R$ between the lepton and the track jet axis |
| $p_T^{\text{varcone30}}/p_T$ | Lepton track isolation, with track collecting radius of $\Delta R < 0.3$ |
| $E_T^{\text{topocone30}}/p_T$ | Lepton calorimeter isolation, with topological cluster collecting radius of $\Delta R < 0.3$ |
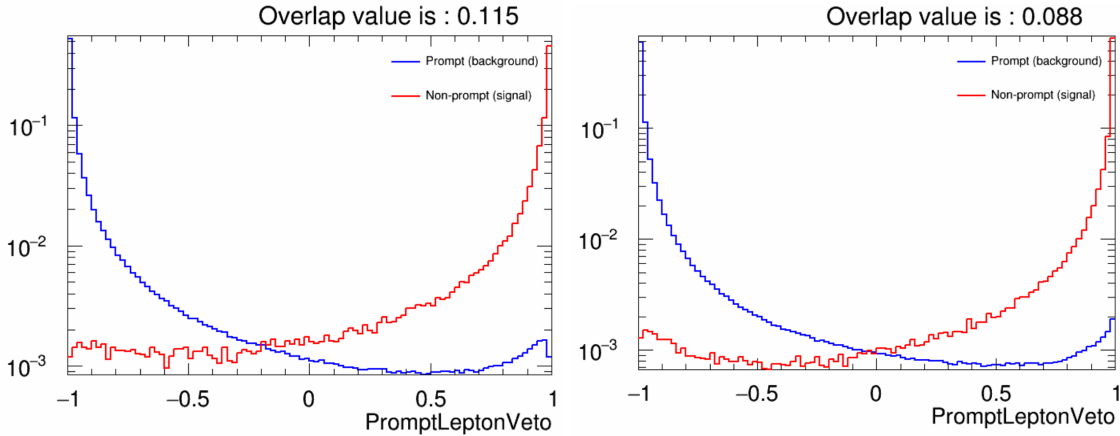


Figure 4.10: Distributions of the ''non-prompt lepton BDT'' score for electrons (left) and muons (right) in the simulated $t\bar{t}$ events. This BDT is used to distinguish the prompt leptons from the non-prompt leptons.

## 4.4 Jets

Due to the confining nature of QCD, color-charged quarks and gluons produced in collisions are not observable as isolated and stable partons. Instead, their production is characterized by the radiation of additional quarks and gluons roughly collinear with the initiating colored partons. The

radiation pattern of these colored objects is dictated by the color field that binds them and eventually results in the production of color-neutral hadrons. The collimated sprays of hadrons as a result of this hadronization process lead to the phenomenology of jets, which are the macroscopically observable signature of produced quarks and gluons and whose kinematic properties reflect those of an initiating parton. Jets are reconstructed by clustering nearby calorimeter cells using the anti-$k_t$ algorithm [110, 111] and matching the clustered object with ID tracks. Specifically, topo-clusters, with their energies at either electromagnetic scale or hadronic scale, form the basic constituents of a jet[112]. Jets used in this work are reconstructed at the electromagnetic energy scale with the anti-$k_t$ with a distance parameter R = 0.4. Reconstructed jets have the energy of electromagnetic showers measured correctly, while the energy deposition characteristic of hadronic particle decays and interactions are not accurately accounted for. To correctly assign meaningful energy and momentum measurements to the reconstructed jets that correspond to the energies and momenta of the initiating, underlying particle-level jets, several *Jet Energy Scale* (JES) calibration[111] are taken, including an origin correction which changes the jet direction to point to the hard-scatter vertex, a pileup correction which consists of jet area-based and residual correction, an absolute MC-based calibration which corrects jet 4-momentum to the particle level energy scale, a global sequential calibration which reduces flavor dependence and energy leakage effects, and residual a in site calibration which is derived using in situ measurements and is applied only on data. These steps are shown in the flowchart in Figure 4.11.
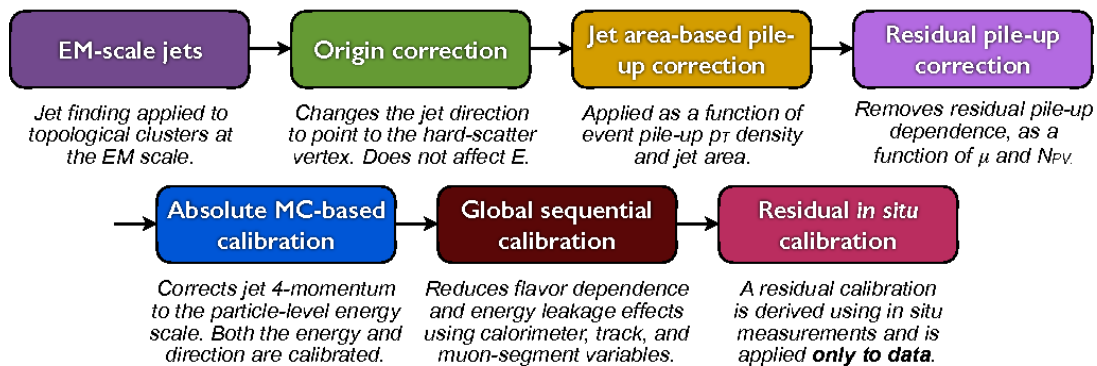


Figure 4.11: Flowchart representing the sequence of steps taken in the jet calibration.

Pileup interactions often result in reconstructed jets in the final state that are not associated with the primary hard-scatter vertex, and the suppression of pileup jets has been a crucial component for the analyses presented in Chapter 6 and 7. A multivariate algorithm requirement has been defined to discriminate between these pileup jets and the hard-scatter jets. This algorithm is called the *Jet Vertex Tagging* (JVT) and it relies on using the tracks associated with reconstructed jets in order to give an indication of the probability that a jet is a pileup jet[113]. The JVT is applied to the jets in

the analyses presented in Chapter 6 and 7 with $p_\mathrm{T} < 60\,\mathrm{GeV}$ and $|\eta| < 2.4$, in order to suppress jets which originate from pile-up collisions.

### 4.4.1 Flavor Tagging

Identifying jets containing heavy-flavored hadrons, i.e. jets containing $b$- and $c$- flavored hadrons, referred as 'flavor tagging', is an important aspect for physics programs, especially for analyses with the top quark which decays to a W-boson and a $b$-quark nearly $100\%$ of the time. Jets tagged, which are arisen likely from the hadronization of initiating $b$-($c$-) quarks, are referred to as '$b$-tagged jets' ('$c$-tagged jets') or simply as '$b$-jets'('$c$-jets'). All other jets then are assumed to have arisen from light-flavor quarks and referred to as 'light-flavor jets' ('light-jets').

Heavy-flavor tagging of jets relies on the fact that the b- and c-hadrons have relatively long lifetime. The typical b-hadron lifetime is 1.6 ps ($c\tau \approx 450\mu$m), which leads to b-hadrons traveling away from the PV and results in a reconstructable secondary vertex in the Pixel detector. A specialized multivariate algorithm called 'MV2', which utilizes the BDT classifier with input from the outputs of several other b-tagging algorithms based on impact parameters, secondary vertex reconstruction, and reconstruction of the full decay chains[114]. Three variants of the MV2 algorithm exist, MV2c00, MV2c10 and MV2c20, where the name of the taggers indicates the $c$-jet fraction used in the training samples, e.g. in MV2c10 which is used in this work, the background sample is composed of $10\%(90\%)$ $c$-(light-) jets. The BDT output for the MV2c10 tagger can be seen in Figure 4.12[115]. WPs, defined with different target efficiency for accepting $b$-tagged jets,
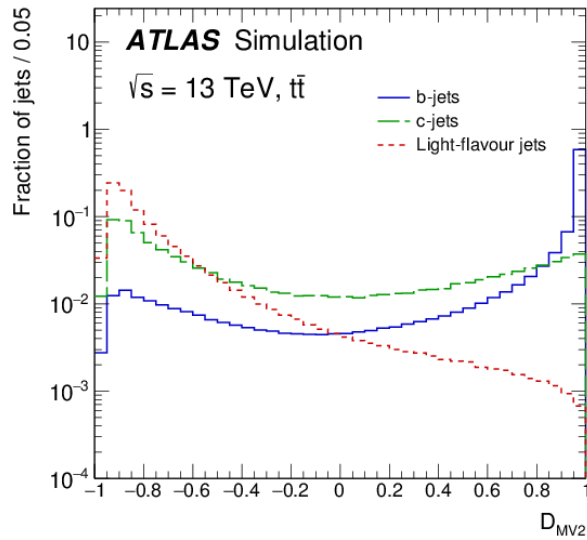


Figure 4.12:  MV2c10 BDT output for $b$- (solid blue), $c$- (dashed green) and light-flavor (dotted red) jets evaluated with $t\bar{t}$ events[115].

are defined by selection thresholds on the MV2 discriminant. The standard ATLAS $b$-tagging WPs are defined for accepting $b$-jets with $p_T > 20$ GeV with average efficiency of 60%, 70%, 77%, and 85%. The WPs are based on selections made on the MV2 output score and are defined in Table 4.3 , along with the rejection factors[2] for $c$-jets, $\tau$-jets[3] and light-flavor jets. In the $t\bar{t}H$ analysis (see Section 6.1), the 70% WP is chosen to identify $b$-jets, while in the $t\bar{t}t\bar{t}$ analysis (see Section 7.1), a jet is considered $b$-tagged if it passes the 77% WP. In some analysis e.g. the $t\bar{t}t\bar{t}$ analysis (see Section 7.3), in order to use the full $b$-tagging information of an event, a jet is given a pseudo-continuous $b$-tagging score that defines if the jet pass the $b$-tagging operating points of 85%, 77%, 70% and 60%, giving respectively a score of five, four, three and two, or if the jet does not pass any of the previous WPs, giving a score of one.

Table 4.3: WPs defined for the MV2c10 $b$-jet identification algorithm. The cut thresholds on the MV2 discriminant associated with a given $b$-jet efficiency, referred as WPs, are given in the second column. The rejection factors for $c$-, $\tau$-, and light-flavor jets are shown in the three right- most columns.

| WPs (efficiency) | MV2 selection | Rejection factor | | |
|---|---|---|---|---|
| | | $c$-jet | $\tau$-jet | light-jet |
| 60% | > 0.94 | 23 | 140 | 1200 |
| 70% | > 0.83 | 8.9 | 36 | 300 |
| 77% | > 0.64 | 4.9 | 15 | 110 |
| 80% | > 0.11 | 2.7 | 6.1 | 25 |

Due to the imperfect description of the detector response and physics modeling effects in MC simulation, a calibration procedure[115] is performed to correct the MC-based efficiencies to those observed in data. A sample of events enriched in $t\bar{t}$ dileptonic decays is selected to evaluate the performance of the $b$-tagging algorithm in data. To extract $b$-jet tagging efficiency, the selected events are classified into different bins according to the $p_T$ of the two jets, $m_{j_i,\ell}$ (i is the index of the jets) and $b$-tagging discriminant. Once events have been selected and classified, a log-likelihood function is built, allowing the simultaneous estimation of the $b$-jet tagging probabilities and flavor compositions. The result of the calibration is a correction scale factor, applied on a per-jet basis, that is defined as the ratio of the measured efficiencies in data and efficiencies calculated in MC (SF $= \varepsilon_{\text{data}}/\varepsilon_{\text{MC}}$), measured as a function of the jet $p_T$ and $\eta$. The $b$-jet tagging efficiency measurement for the $\varepsilon_b = 70\%$ of the MV2 algorithm and corresponding $b$-jet tagging efficiency scale factors are shown in Figure 4.13.

---

[2]The rejection factor is defined as the inverse of the efficiency.
[3]Hadronically decaying $\tau$ leptons are accepted by the b-tagging algorithms at rates higher than light-flavor jets, due to the non-negligible decay length of the $\tau$ lepton.
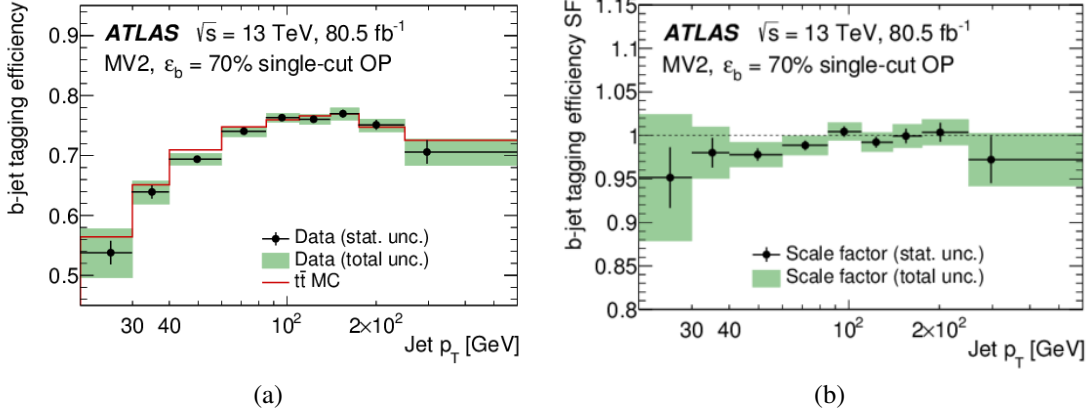
Figure 4.13: (a) $b$-jet tagging efficiency as a function of jet $p_T$ for the $70\%$ WP of the MV2 $b$-jet tagging algorithm in MC and (b) $b$-jet tagging efficiency correction scale-factors for the $70\%$ WP of the MV2 $b$-jet tagging algorithm as a function of jet $p_T$ [115].

## 4.5  The Missing Transverse Momentum

The missing transverse momentum ($\mathbf{p}_T^{miss}$) is defined as the momentum imbalance in the plane transverse to the beam axis. The missing transverse energy, $E_T^{\mathrm{miss}}$ , is the magnitude of the $\mathbf{p}_T^{miss}$. $\mathbf{p}_T^{miss}$ is calculated as the negative vectorial sum of the reconstructed objects associated with the event[116],

$$\mathbf{p}_T^{\mathrm{miss}} = \sum \mathbf{p}_T^{e} + \sum \mathbf{p}_T^{\gamma} + \sum \mathbf{p}_T^{\tau} + \sum \mathbf{p}_T^{jets} + \sum \mathbf{p}_T^{\mu} + \sum \mathbf{p}_T^{soft}, \tag{4.5}$$

where $\mathbf{p}_T^{soft}$ is the transverse momentum of reconstructed tracks originating from the primary hard-scatter vertex but not associated with any of the hard objects indicated in the other terms appearing in Equation 4.5. For the component $E_{x(y)}^{miss}$, the magnitude $E_T^{\mathrm{miss}}$ and azimuthal angle $\phi^{\mathrm{miss}}$ are calculated as:

$$E_T^{\mathrm{miss}} = \sqrt{(E_x^{\mathrm{miss}})^2 + (E_y^{\mathrm{miss}})^2}, \tag{4.6}$$

$$\phi^{\mathrm{miss}} = \arctan\left(E_y^{\mathrm{miss}}/E_x^{\mathrm{miss}}\right). \tag{4.7}$$

Large momentum imbalance may suggest the presence of particles which escape the detector, such as neutrinos or stable, weakly-interacting particles. Additionally, detector mismodeling, noise, limited coverage, or miscalibration of the reconstructed objects used in the reconstruction of $E_T^{\mathrm{miss}}$ can also contribute nonzero values of $E_T^{\mathrm{miss}}$ .

# CHAPTER 5

# Common Elements in the Analyses of the Same-Sign Dilepton and Multilepton Final States

There are many ways to study and analyze the data to test hypotheses or perform measurements of fundamental quantities. In this dissertation, two analyses are presented in searching for rare processes using the SSML events: search for the associated production of the Higgs boson with a top-quark pair (referred to as the $t\bar{t}H$ analysis) in Chapter 6 and evidence for the $t\bar{t}t\bar{t}$ production (referred to as the $t\bar{t}t\bar{t}$ analysis) in Chapter 7. Although details are different, the two analyses follow the same general strategy. Since there are a large number of processes produced at the same time at the LHC, selection criteria are applied on physics objects (introduced in Chapter 4) to filter the set of recorded events into a small sample, in which the physics process of interest targeted in each analysis dominates or at least is preferred. The physics process of interest is treated as 'signal', and other contributions are referred to as 'backgrounds'. MC simulation, discussed in Section 5.1, is extensively used to model both signal and background processes, and serves as the bridge between theoretical calculations and complex detector signatures. The data-driven methods are also used, especially for estimations of background contributions caused by instrumental effects, e.g. leptons from mis-reconstruction and mis-identification. As introduced in Chapter 1, these instrumental backgrounds are sizable in the SSML final states. In Section 5.2, the origin and properties of the instrumental backgrounds are presented along with several methods that have been explored to estimate their contributions. There are many sources of systematic uncertainties (systematics), which come along with the background estimations and signal modelings that affect the final results. These systematics are introduced in Section 5.3. Finally, to quantify the consistency between theoretical predictions and experimental observations, statistical analyses are preformed. Statistical methods employed in these analyses are discussed in Section 5.4.

# 5.1 Monte Carlo Simulation

MC simulations are, in general, based on the concept of random samplings for the possible outputs of a process, which is probabilistic in nature. A distribution of those values should converge to a statistical sample that accurately describes the expected results of the studied process. These simulations are deeply related to the phenomenology of the parton-parton collision presented in Section 2.4. They can usually be split into matrix element MC generators calculating the hard-scattering processes, parton shower MC generators dealing with radiations (ISR and FSR) as well as jet fragmentation and hadronization, and the simulation of the detector response. Besides, the process of the UE introduced in Section 2.4 is simulated using tunable phenomenological models provided by specific MC generators[117].

Matrix element MC generators use full matrix element of given parton numbers and generally offer reliable descriptions far from soft collinear limits. The generators used in this dissertation are MADGRAPH5_AMC@NLO[118] and POWHEGBOX[119, 120]. On the other hand, parton shower MC generators simulate QCD radiations in the soft-collinear limits by successive emissions, and they can be tunned to fit data. Matrix element MC generators are usually interfaced with separate parton shower MC generators to perform a full description of a given process, and a proper jet matching algorithm is needed to avoid double counting of multi-jets phase space. There are general-purpose MC event generators capable of performing matrix-element calculation as well as handling the parton shower and UE modeling. PYTHIA [121] HERWIG [122] and SHERPA [123–127] are three such generators. However, PYTHIA and HERWIG are used only as parton shower generators, while SHERPA is used as both matrix element and parton shower generators in this dissertation.

In order to compare with data collected in ATLAS, the generated events are processed through a simulation of the ATLAS detector geometry and response using GEANT4 [128, 129], and through the same reconstruction software as the data. Corrections are applied to the simulated events so that the object candidates' selection efficiencies, energy scales and energy resolutions match those measured from data control samples (see Chapter 4). The simulated samples are normalized to their theoretical cross sections. Additional normalization factors are applied for some samples, as appropriate, to correct for the difference in the event yields between the simulations and data (see Section 5.2.2.2).

Generator programs and configurations used for simulating the signal and background processes in the $t\bar{t}H$ analysis and the $t\bar{t}t\bar{t}$ analysis are summarized in Table 5.1.

Table 5.1: The configurations used for the event generation of signal and background processes. The samples used to estimate the systematic uncertainties are indicated in parentheses. $V$ refers to production of an electroweak boson ($W$ or $Z/\gamma^*$). The matrix element (ME) order refers to the order in the strong coupling constant of the perturbative calculation. If only one parton distribution function (PDF) is shown, the same one is used for both the ME and parton shower generators; if two are shown, the first is used for the ME calculation and the second for the parton shower. Tune refers to the underlying-event tune of the parton shower generator. MG5_AMC refers to MAD-GRAPH5_AMC@NLO 2.2.X or 2.3.X [118]; PYTHIA 6 refers to version 6.427 [130]; PYTHIA 8 refers to version 8.2 [131]; HERWIG++ refers to version 2.7 [132]; HERWIG7 refers to version 7.0.4 [122]; MEPS@NLO refers to the method used in SHERPA [123–127] to match the matrix element to the parton shower. Samples using PYTHIA 6 or PYTHIA 8 have heavy flavor hadron decays modeled by EVTGEN 1.2.0 [133]. All samples include leading-logarithm photon emission, either modeled by the parton shower generator or by PHOTOS [134]. The masses of the top quark and the SM Higgs boson were set to $172.5$ GeV and $125$ GeV. The column 'Analysis' shows where the Monte Carlo is used. If the sample is used only in $t\bar{t}t\bar{t}$ analysis, it will be labeled as '$t\bar{t}t\bar{t}$', if it is used only in $t\bar{t}H$ analysis, it will be labeled as '$t\bar{t}H$', and if it is used in both analyses, it will be labeled as 'both'.

| Process | Generator | ME order | Parton shower | PDF | Tune | Analysis |
|---|---|---|---|---|---|---|
| $t\bar{t}H$ | POWHEG-BOX [119, 120] | NLO | PYTHIA 8 | NNPDF3.0 NLO [47]/ NNPDF2.3 LO [135] | A14 | both |
| | (POWHEG-BOX) | (NLO) | (HERWIG7) | (NNPDF3.0 NLO/ MMHT2014 LO [136]) | (H7-UE-MMHT) | both |
| $t\bar{t}t\bar{t}$ | MG5_AMC | NLO | PYTHIA 8 | NNPDF3.1 NLO [47] | A14 | $t\bar{t}t\bar{t}$ |
| | MG5_AMC | LO | PYTHIA 8 | NNPDF2.3 LO | A14 | both |
| | (MG5_AMC) | (NLO) | (HERWIG7) | (MMHT2014 LO) | (H7-UE-MMHT) | $t\bar{t}t\bar{t}$ |
| $t\bar{t}W$ | SHERPA 2.2.1 | MEPS@NLO | SHERPA | NNPDF3.0 NNLO | SHERPA default | both |
| | (MG5_AMC) | (NLO) | (PYTHIA 8) | (NNPDF3.0 NLO/ NNPDF2.3 LO) | (A14) | both |
| $t\bar{t}(Z/\gamma^*)$ | MG5_AMC | NLO | PYTHIA 8 | NNPDF3.0 NLO/ NNPDF2.3 LO | A14 | |
| | | | | | | both |
| | (SHERPA 2.2.0) | (LO multileg) | (SHERPA) | (NNPDF3.0 NLO) | (SHERPA default) | both |
| $tHqb$ | MG5_AMC | LO | PYTHIA 8 | CT10 [137] | A14 | |
| $tHW$ | MG5_AMC | NLO | HERWIG++ | CT10/ CTEQ6L1 [138, 139] | UE-EE-5 | $t\bar{t}H$ |
| $t\bar{t}$ | POWHEG-BOX | NLO | PYTHIA 8 | NNPDF3.0 NLO/ NNPDF2.3 LO | A14 | both |
| $t\bar{t}$ $\to W^+bW^-\bar{b}\ell^+\ell^-$ | MG5_AMC | LO | PYTHIA 8 | NNPDF3.0 LO | A14 | $t\bar{t}H$ |
| $tZ$ | MG5_AMC | LO | PYTHIA 6 | CTEQ6L1 | Perugia2012 | both |
| $tWZ$ | MG5_AMC | NLO | PYTHIA 8 | NNPDF2.3 LO | A14 | both |
| $t\bar{t}t$ | MG5_AMC | LO | PYTHIA 8 | NNPDF2.3 LO | A14 | both |
| $t\bar{t}W^+W^-$ | MG5_AMC | LO | PYTHIA 8 | NNPDF2.3 LO | A14 | both |
| Single top ($t$-, $Wt$-, $s$-channel) | POWHEG-BOX [140–142] | NLO | PYTHIA 8 | NNPDF3.0 NLO/ NNPDF2.3 LO | A14 | both |
| $VV$, $VVV$ | SHERPA 2.2.2 | MEPS@NLO | SHERPA | NNPDF3.0 NNLO | SHERPA default | both |
| $Z\to\ell^+\ell^-$ | SHERPA 2.2.1 | MEPS@NLO | SHERPA | NNPDF3.0 NLO | SHERPA default | both |
| $W\to\ell\nu$ | SHERPA 2.2.1 | MEPS@NLO | SHERPA | CT10 | SHERPA default | $t\bar{t}t\bar{t}$ |
| $t\bar{t}ZZ$,$t\bar{t}WZ$ $t\bar{t}HH$,$t\bar{t}WH$ | MG5_AMC | LO | PYTHIA 8 | NNPDF2.3 LO | A14 | $t\bar{t}t\bar{t}$ |

### 5.1.1 $t\bar{t}H$ Production

The nominal sample used to model the $t\bar{t}H$ process is generated using the *Next-to-Leading Order* (NLO) generator POWHEG-BOX v2 [119, 120] with the NNPDF3.0 NLO [47] PDF set. The renormalization and factorization scales, $\mu_R$ and $\mu_F$, are set to equal to the geometric mean of the transverse energies of the top quark, the antitop quark, and the Higgs boson. The POWHEG-BOX model parameter $h_{\text{damp}}$, which controls matrix element to parton shower matching and effectively regulates the high-$p_\text{T}$ radiation, is set to be $1.5 \times (2m_t + m_H)/2 = 352.5$ GeV. The parton shower and hadronization are modeled using PYTHIA 8.2 [131] and the A14 tune [143], and the Higgs boson decay branching fractions are calculated using HDECAY [48, 144]. An additional $t\bar{t}H$ sample is generated with POWHEG-BOX interfaced to HERWIG7 [122, 132] to evaluate the impact of the parton shower and hadronization model (see Section 6.4.1.1).

### 5.1.2 $t\bar{t}t\bar{t}$ Production

In the $t\bar{t}t\bar{t}$ analysis, the production of $t\bar{t}t\bar{t}$ events is modeled using the MADGRAPH5_AMC@NLO v2.6.2 generator which provides matrix elements at NLO in the strong coupling constant $\alpha_s$ with the NNPDF3.1NLO PDF. The renormalization and factorization scales are set to be $0.25 \times \sum_i \sqrt{m_i^2 + p_{T,i}^2}$, where the sum runs over all the particles generated from the matrix-element calculation, following Ref. [63]. Top quarks are decayed at the *Leading Order* (LO) using MADSPIN [145, 146] to preserve spin correlations. The generated events are interfaced with PYTHIA8.2 for the parton shower and hadronization, using the A14 set of tuned parameters and the NNPDF23LO [47] PDF set. Another $t\bar{t}t\bar{t}$ sample is produced at LO with the same MC settings used for the NLO sample. It is used for multivariate signal extraction in the $t\bar{t}t\bar{t}$ analysis (see Section 7.3) and also used as the nominal sample in the $t\bar{t}H$ analysis. A comparison of the different generation order on the $t\bar{t}t\bar{t}$ predictions is shown in Figure 5.1. The NLO generation gives similar kinematic predictions as the LO generation. In the $t\bar{t}t\bar{t}$ analysis, an additional $t\bar{t}t\bar{t}$ sample is also produced at NLO replacing the parton shower of the nominal samples with HERWIG7.04 [122, 132] to evaluate the impact of the parton shower and hadronization model (see Section 7.4.1.1).

### 5.1.3 $t\bar{t}W$ Background

Simulated sample for $t\bar{t}W$ production is generated using the SHERPA 2.2.1 [123] generator with the NNPDF3.0 NLO PDF set. The matrix element includes calculations for up to one additional parton at NLO and up to two partons at LO using COMIX [125] and OPENLOOPS [124], and is merged with the SHERPA parton shower [126] using the MEPS@NLO prescription [127] with a merging scale of 30 GeV. The choice of renormalization and factorization scales is $\mu_R = \mu_F = H_\text{T}/2$, where
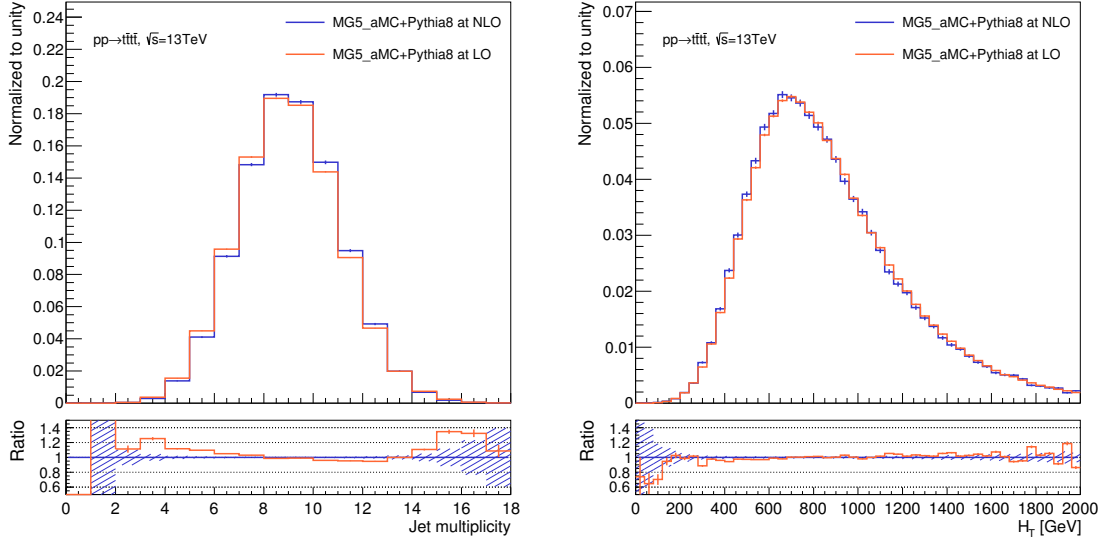
Figure 5.1: Truth-level distributions of the jet multiplicity and the scalar sum of jet $p_T$ ($H_T$) from MC@NLO+PYTHIA $t\bar{t}t\bar{t}$ generation at NLO and at LO. All distributions are normalized to one. The ratios of the LO calculations relative to the NLO calculations are shown in the bottom panel.

$H_T$ is defined as the scalar sum of the transverse masses $\sqrt{p_T^2 + m^2}$ of all final-state particles.

In the $t\bar{t}t\bar{t}$ analysis, nominal cross section used for the simulated $t\bar{t}W$ sample is $601 \pm 76$ fb (see Section 2.6.1). However, in the $t\bar{t}H$ analysis, additional scaling factors to this cross section are applied to account for the missing higher order QCD and EW corrections described in Section 2.6.1. Previous work [118] has shown that NLO QCD corrections to $t\bar{t}W$+1-jet production can be large. An inclusive scaling factor of 1.11 has been estimated using dedicated samples generated with SHERPA 2.2.5 using the MEPS@NLO [127] prescription, and cross-checked with the NLO generator MADGRAPH5_AMC@NLO 2.2.1 [118] using the FxFx prescription [147]. In addition, a scale factor of 1.09 has been estimated from the sub-leading NLO EW corrections. Therefore, after applying these two scaling factors, the inclusive cross section, used to normalize the $t\bar{t}W$ sample in the $t\bar{t}H$ analysis, becomes $727 \pm 92$ fb.[1][2]

An alternative sample is generated at NLO (thus at the lower order than the nominal sample) with the MADGRAPH5_AMC@NLO 2.2.1 generator using the same scale choice and PDF set as the nominal sample, and interfaced to PYTHIA 8.2 in combination with the A14 tune. This sample is used to estimate the uncertainties associated with the modeling of additional QCD radiations (see Section 5.3.2.1).

---

[1]The theoretical uncertainties are not revised based on the additional corrections considered, but are scaled proportionally to the scaling factors applied.

[2]Different theoretical $t\bar{t}W$ cross sections are considered in the $t\bar{t}H$ analysis and $t\bar{t}t\bar{t}$ analysis. Because the simplication is needed for publication of the $t\bar{t}t\bar{t}$ analysis, the cross section from Yellow Report is used.

### 5.1.4 Other Backgrounds

The simulation of $t\bar{t}$, $t\bar{t}Z/\gamma^*$ and $VV$ production follows Ref. [148–150]. The production of $t\bar{t}$ events is modeled using the POWHEGBOX v2 generator at NLO with the NNPDF3.0NLO PDF set and the $h_{\mathrm{damp}}$ parameter. set to $1.5\,m_{\mathrm{top}}$ [151]. The events are interfaced with PYTHIA8.2 using the A14 tune and the NNPDF23LO PDF set. For the $t\bar{t}Z/\gamma^*$ sample, the inclusive $t\bar{t}\ell^+\ell^-$ matrix element is computed at NLO, including the off-shell $Z$ and $\gamma^*$ contributions with $m(\ell^+\ell^-) > 1$ GeV. In addition, a dedicated $t\bar{t}$ sample including rare $t \to Wb\gamma^*(\to \ell^+\ell^-)$ radiative decays, $t\bar{t} \to W^+bW^-\bar{b}\ell^+\ell^-$, is generated using a LO matrix element and requiring $m(\ell^+\ell^-) > 1$ GeV. In this sample the photon can be radiated from the top quark, the $W$ boson, or the $b$-quark. The $t\bar{t}Z/\gamma^*$ and $t\bar{t} \to W^+bW^-\bar{b}\ell^+\ell^-$ samples are combined together to form the "$t\bar{t}Z/\gamma^*$ (high mass)" sample. The contribution from internal photon conversions ($\gamma^* \to \ell^+\ell^-$) with $m(\ell^+\ell^-) < 1$ GeV are modeled by QED multiphoton radiation via the parton shower in the inclusive $t\bar{t}$ sample and is referred to as "$t\bar{t}\,\gamma^*$ (low mass)". Further details on the generation settings for these samples can be found in Table 5.1. Special treatment has been taken to avoid double-counting of contributions when combining different simulated samples. The cross section for inclusive $t\bar{t}\ell^+\ell^-$ production, with $m(\ell^+\ell^-) > 1$ GeV, is $162 \pm 21$ fb. This cross section is computed at NLO in QCD and electroweak corrections [48, 62, 118]. The LO cross section for the $t\bar{t} \to W^+bW^-\bar{b}\ell^+\ell^-$ sample is scaled by a factor of 1.54, based on comparisons between the NNLO+NLL [152–156] and LO cross sections for $t\bar{t}$ production. Diboson backgrounds are normalized using the cross sections computed at NLO in QCD by SHERPA 2.2.2. Rare background contributions ($tZ$, $ttWW$, $WtZ$, $VVV$, $t\bar{t}t$, $tHjb$ and $WtH$) are normalized using their NLO theoretical cross sections[48, 118, 150, 157].

In the $t\bar{t}t\bar{t}$ analysis, rare backgrounds from $t\bar{t}$ productions in association with dibosons ($t\bar{t}ZZ$, $t\bar{t}WZ$, $t\bar{t}HH$ and $t\bar{t}WH$) are generated using the LO MADGRAPH5_AMC@NLO generator interfaced to PYTHIA8 using the A14 tune and scaled to NLO cross sections [48]. A summary of these rare processes' cross sections used in the analysis is shown in Table 5.2.

Table 5.2: Summary of the rare processes' cross sections (LO) and their k-factor to NLO. All the cross sections used for the normalization here are NLO.

| Process | cross section (fb) | k-factor |
|---------|--------------------|----------|
| $t\bar{t}ZZ$ | 1.49 | 1.23 |
| $t\bar{t}WW$ | 8.10 | 1.22 |
| $t\bar{t}WZ$ | 2.47 | 1.58 |
| $t\bar{t}HH$ | 0.74 | 1.02 |
| $t\bar{t}WH$ | 1.14 | 1.39 |

## 5.2  Instrumental Background

Despite the high levels of accuracy achieved by the ATLAS lepton reconstruction and identification algorithm described in Chapter 4, leptons from misidentification and mis-reconstruction (instrumental backgrounds) can be quite important in the SSML analyses. These background sources of leptons are divided into three categories:

- Fake leptons are objects which are not real leptons, for example pions and kaons misidentified as leptons.

- Non-prompt leptons are real genuine leptons but they do not originate from the primary $pp$ hard-scattering interactions.

- Charge mis-identified electrons (Q-MisID) are usually poorly reconstructed electrons which have undergone a sign flip for electric charge.

In the subsequent discussion, the term 'fake' will be used in reference to both fake leptons and non-prompt leptons.

### 5.2.1  Charge Mis-identification

Processes, that produce opposite-sign dilepton pairs in which the electric charge of one lepton has been mis-reconstructed to the wrong charge, will meet the same-sign requirement. It is considered only for electrons. The probability of muon charge misidentification is negligibly small due to the low rate of bremsstrahlung radiation from muons as well as the more accurate charge identification from the combination of ID and MS measurements. There are two primary mechanisms by which the electron charge can be misidentified as described in Section 4.3.1.3, 'trident' process and mis-curvature.

In both $t\bar{t}H$ analysis (see Section 6.3) and $t\bar{t}t\bar{t}$ analysis (see Section 7.2), the data-driven method used to estimate the Q-MisID background relies on the probability of an electron to have its charge incorrectly reconstructed[158]. This probability is called the charge flip rate $\epsilon$ and depends on $|\eta|$, $p_T$ and other properties (i.e. the $m_{trk-trk,PV}$ and $m_{trk-trk,CV}$ introduced in Section 4.3.1.4) of the electrons.

The charge flip rate is estimated in a $Z \rightarrow ee$ enriched control sample, called 'Z-peak' sample. This sample is selected by a requirement on the invariant mass of a di-electron pair $m_{ee}$ to be between 81 GeV and 101 GeV, without any requirement on the charge of the two electron tracks. It is assumed that the charge flip rate varies, i.e., with $|\eta|$ of the electron cluster and with $p_T$, but is uncorrelated between the two electrons in each event. The charge flip rate in a given $(\eta, p_T)$ bin is obtained from the numbers of events where both electrons have the same and opposite electric

charges. With the assumption that electron pairs from Z boson decays are entirely true opposite-sign electron pairs, the number of measured same-sign events $N_{ss}^{ij}$, where one electron is in the $i$th $(|\eta|, p_T)$ bin and the other is $j$th bin, is expected to be:

$$N_{ss}^{ij} = N^{ij}(\epsilon_i(1 - \epsilon_j) + \epsilon_j(1 - \epsilon_i)), \tag{5.1}$$

where $N^{ij}$ is the total number of observed events with one electron in bin $i$ and the other one in bin $j$, regardless of electric charges. The value of $\epsilon$ in each $(|\eta|, p_T)$ bin is then extracted by maximizing the Poisson likelihood for the observed number of same-sign pairs in each $(|\eta|, p_T)$ bin to be consistent with the expectation from Equation 5.1. Equivalently, this can be achieved by minimizing the following negative-log-likelihood:

$$-\ln[L(\epsilon|\boldsymbol{N_{ss}}, \boldsymbol{N})] = \sum_{ij} \ln[N^{ij}(\epsilon_i(1-\epsilon_j) + \epsilon_j(1-\epsilon_i))]N_{ss}^{ij} - N^{ij}(\epsilon_i(1-\epsilon_j) + \epsilon_j(1-\epsilon_i)).$$
$$\tag{5.2}$$

where $\boldsymbol{N_{ss}}$ and $\boldsymbol{N}$ are the collections of the numbers of observed events with a same-sign electron pair, and with a electron pair without charge requirements, respectively. The values of $\boldsymbol{N_{ss}}$ and $\boldsymbol{N}$ in each bin are extracted from the Z-peak sample.

To determine the expected number of events from Q-MisID in signal regions[3], control regions[4] and validation regions[5], a sample is selected using the same criteria as for the analysis selection, except that an opposite-sign (i.e. $e^\pm e^\mp/e^\pm \mu^\mp$) rather than a same-sign ($e^\pm e^\pm/e^\pm \mu^\pm$) dilepton pair is required. The following weight is then applied to each event according the values of the charge flip rate of the leptons in the event:

$$w = \frac{\epsilon_1 + \epsilon_2 - 2\epsilon_1\epsilon_2}{1 - \epsilon_1 - \epsilon_2 + 2\epsilon_1\epsilon_2}, \tag{5.3}$$

where $\epsilon_1$ ($\epsilon_2$) stands for the charge mis-identification rate for the first (second) lepton. If the lepton is a muon, its charge flip rate is assumed to be zero. This weight can be interpreted as the probability for this opposite-sign dilepton event to be reconstructed as a same-sign dilepton event.

## 5.2.2 Fake Leptons

The origins of the fake leptons (include both fake and non-prompt leptons) are complex since the SSML final state is sensitive to various instrumental effects related to leptons. In both $t\bar{t}H$ analysis

---

[3]Signal regions are regions of phase space where the signal is preferred.

[4]Control regions are regions where there are high purities for particular background processes.

[5]Validation regions typically contain events whose kinematics are more similar to those in signal regions than those in control regions, while still maintaining orthogonality between the control regions and signal regions.

and $t\bar{t}t\bar{t}$ analysis, the main source of fake leptons is the muon or electron originating from the semi-leptonic decays of $b$- and $c$- hadrons, and those leptons are called as 'heavy flavors' (HF). Other types of fakes account for leptons from $J/\psi$ resonance decays, light flavored mesons ($\pi$, K. . . ) decays, $\tau$ leptonic decays (excluding $\tau$'s originating from gauge bosons, Higgs bosons, or a top quark, in which case the leptons are classified as prompt), and mis-identified jets. These fakes are called as 'light flavors' (LF). For electrons, apart from HF and LF, there is also a large fraction from photon conversions (described in Section 4.3.1.4). These photons can originate from either ISR/FSR or $\pi^0$ decays.

Fakes are difficult to simulate accurately because many complex processes (e.g. heavy flavor production, radiation, detector material simulations) are involved to predict fake lepton contributions. Data-driven approaches are typically used for estimating fakes. Several methods exist. Some, e.g matrix method, are highly data-driven, while others, e.g template fit method, are semi-data-driven. In the following, the matrix method and template fit method will be introduced.

### 5.2.2.1  Matrix Method

The matrix method is a data-driven technique for estimating the contamination of fakes which pass a given selection corresponding to the one used in the signal region selection. The matrix method relies on that fakes and prompt leptons respond quite differently to isolation requirements, and can be characterized by the definition of two levels of lepton selections:

- **Tight lepton (T)**: leptons passing all reconstruction, identification and isolation criteria used in the signal region selection.

- **Loose lepton (L)**: leptons passing the relaxed requirements of either or both identification and isolation.

The basic idea underlying the matrix method can be effectively outlined in a simplified scenario where only one lepton is taken into account. The number of events with a tight lepton, $N^T$, and with a lepton passing the loose but fail tight criteria (referred to as anti-tight, $\bar{T}$), $N^{\bar{T}}$, can be expressed in terms of efficiencies and inefficiencies for the loose lepton.

$$N^T = \varepsilon_r\, N^r + \varepsilon_f\, N^f \tag{5.4}$$
$$N^{\bar{T}} = \bar{\varepsilon}_r\, N^r + \bar{\varepsilon}_f\, N^f$$

or, in matrix form:

$$\begin{pmatrix} N^T \\ N^{\bar{T}} \end{pmatrix} = \begin{pmatrix} \varepsilon_r & \varepsilon_f \\ \bar{\varepsilon}_r & \bar{\varepsilon}_f \end{pmatrix} \begin{pmatrix} N^r \\ N^f \end{pmatrix}, \tag{5.5}$$

where $\varepsilon_r$ ($\varepsilon_f$) represents the efficiency for a prompt (fake) loose lepton to pass the tight selection, and $\not{\varepsilon}_r \equiv (1 - \varepsilon_r)$ ($\not{\varepsilon}_f \equiv (1 - \varepsilon_f)$) represents the probability for a prompt (fake) loose lepton to fail the tight selection. $N^f$ ($N^r$) represents the number of events with a fake (prompt) lepton passing loose criteria, and is the unknown number to be determined. By inverting this equation, one can relate the $N^f$ and $N^r$ to a set of observable and measurable quantities, i.e., the number of tight and anti-tight leptons and the efficiencies to pass the tight selection. Both prompt and fake lepton efficiencies can be measured in data, as described in details later on.

In the case of two leptons, the equations can be casted into a matrix form shown below. Depending on whether or not each loose lepton passes the tight selection, each $i$-th event can be categorized into any of the four orthogonal regions:

- $TT$ : events with both leptons passing the tight selection;

- $T\not{T}$ : events with the leading lepton passing the tight selection and the subleading lepton failing the tight selection;

- $\not{T}T$ : events with the leading lepton failing the tight selection and the subleading lepton passing the tight selection;

- $\not{T}\not{T}$ : events with both leptons failing the tight selection.

A $4 \times 4$ efficiency matrix can be defined to map the total number of such events into the total number of events in four dileptonic regions characterized by different prompt and fake lepton compositions, namely:

- $rr$ : events with both leptons being prompt;

- $rf$ : events with the leading lepton being prompt and the subleading lepton being fake;

- $fr$ : events with the leading lepton being fake and the subleading lepton being prompt;

- $ff$ : events with both leptons being fake.

The $4 \times 4$ matrix equation can be written as:

$$
\begin{pmatrix} N^{TT} \\ N^{T\not{T}} \\ N^{\not{T}T} \\ N^{\not{T}\not{T}} \end{pmatrix} = \begin{pmatrix} \varepsilon_{r,1}\varepsilon_{r,2} & \varepsilon_{r,1}\varepsilon_{f,2} & \varepsilon_{f,1}\varepsilon_{r,2} & \varepsilon_{f,1}\varepsilon_{f,2} \\ \varepsilon_{r,1}\not{\varepsilon}_{r,2} & \varepsilon_{r,1}\not{\varepsilon}_{f,2} & \varepsilon_{f,1}\not{\varepsilon}_{r,2} & \varepsilon_{f,1}\not{\varepsilon}_{f,2} \\ \not{\varepsilon}_{r,1}\varepsilon_{r,2} & \not{\varepsilon}_{r,1}\varepsilon_{f,2} & \not{\varepsilon}_{f,1}\varepsilon_{r,2} & \not{\varepsilon}_{f,1}\varepsilon_{f,2} \\ \not{\varepsilon}_{r,1}\not{\varepsilon}_{r,2} & \not{\varepsilon}_{r,1}\not{\varepsilon}_{f,2} & \not{\varepsilon}_{f,1}\not{\varepsilon}_{r,2} & \not{\varepsilon}_{f,1}\not{\varepsilon}_{f,2} \end{pmatrix} \begin{pmatrix} N^{rr} \\ N^{rf} \\ N^{fr} \\ N^{ff} \end{pmatrix} ,
\tag{5.6}
$$

To obtain the number of fakes in signal region as a function of observables, the $4 \times 4$ matrix can be inverted:

$$
\begin{pmatrix} N^{rr} \\ N^{rf} \\ N^{fr} \\ N^{ff} \end{pmatrix} = \begin{pmatrix} \varepsilon_{r,1}\varepsilon_{r,2} & \varepsilon_{r,1}\varepsilon_{f,2} & \varepsilon_{f,1}\varepsilon_{r,2} & \varepsilon_{f,1}\varepsilon_{f,2} \\ \varepsilon_{r,1}\not\varepsilon_{r,2} & \varepsilon_{r,1}\not\varepsilon_{f,2} & \varepsilon_{f,1}\not\varepsilon_{r,2} & \varepsilon_{f,1}\not\varepsilon_{f,2} \\ \not\varepsilon_{r,1}\varepsilon_{r,2} & \not\varepsilon_{r,1}\varepsilon_{f,2} & \not\varepsilon_{f,1}\varepsilon_{r,2} & \not\varepsilon_{f,1}\varepsilon_{f,2} \\ \not\varepsilon_{r,1}\not\varepsilon_{r,2} & \not\varepsilon_{r,1}\not\varepsilon_{f,2} & \not\varepsilon_{f,1}\not\varepsilon_{r,2} & \not\varepsilon_{f,1}\not\varepsilon_{f,2} \end{pmatrix}^{-1} \begin{pmatrix} N^{TT} \\ N^{T\not T} \\ N^{\not T T} \\ N^{\not T \not T} \end{pmatrix}, \tag{5.7}
$$

and the final number of fakes in the signal region $N^{f}_{TT}$, i.e. the total number of $TT$ events with at least one fake lepton, can be obtained from the definition:

$$
N^{f}_{TT} = N^{rf}_{TT} + N^{fr}_{TT} + N^{ff}_{TT} = \varepsilon_{r,1}\varepsilon_{f,2}N^{rf} + \varepsilon_{r,2}\varepsilon_{f,1}N^{fr} + \varepsilon_{f,1}\varepsilon_{f,2}N^{ff}. \tag{5.8}
$$

By plugging the matrix equation (5.7) into this formula, one can finally obtain:

$$
\begin{aligned}
N^{f}_{TT} &= \\
&= \sum_{i} \left(\varepsilon_{r,1}\varepsilon_{f,2}\, rf\right)_i + \left(\varepsilon_{r,2}\varepsilon_{f,1}\, fr\right)_i + \left(\varepsilon_{f,1}\varepsilon_{f,2}\, ff\right)_i = \\
&= \sum_{i}^{\{TT\}} \left(w^{MM}_{TT}\, TT\right)_i + \sum_{i}^{\{T\not T\}} \left(w^{MM}_{T\not T}\, T\not T\right)_i + \sum_{i}^{\{\not T T\}} \left(w^{MM}_{\not T T}\, \not T T\right)_i + \sum_{i}^{\{\not T \not T\}} \left(w^{MM}_{\not T \not T}\, \not T \not T\right)_i
\end{aligned} \tag{5.9}
$$

where:

$$
\begin{aligned}
w^{MM}_{TT}{}_i &= \left(1 - \beta\varepsilon_{r,1}\varepsilon_{r,2}\not\varepsilon_{f,1}\not\varepsilon_{f,2}\right)_i \\
w^{MM}_{T\not T}{}_i &= \left(\beta\varepsilon_{r,1}\varepsilon_{r,2}\varepsilon_{f,2}\not\varepsilon_{f,1}\right)_i \\
w^{MM}_{\not T T}{}_i &= \left(\beta\varepsilon_{r,1}\varepsilon_{r,2}\varepsilon_{f,1}\not\varepsilon_{f,2}\right)_i \\
w^{MM}_{\not T \not T}{}_i &= -\left(\beta\varepsilon_{r,1}\varepsilon_{r,2}\varepsilon_{f,1}\varepsilon_{f,2}\right)_i \\
\beta_i &= \frac{1}{\left(\varepsilon_{r,1_i} - \varepsilon_{f,1_i}\right)\left(\varepsilon_{r,2_i} - \varepsilon_{f,2_i}\right)}
\end{aligned} \tag{5.10}
$$

Clearly, each $i$-th event will contribute to only one of the four terms on the right-hand-side of the Equation 5.9.

To get prompt and fake lepton efficiencies in data, dedicated control regions are built. The prompt efficiency, defined as the ratio of prompt leptons passing the tight selection over those passing the loose selection $\varepsilon_r = N^{r}_{T}/N^{r}_{L}$, can be measured in data through tag-and-probe methods[101]

with a sample of events enriched in $t\bar{t}$ dileptonic decays. Similarly, the fake efficiency is defined as the ratio of tight leptons over loose leptons for fake lepton candidates $\varepsilon_f = N_T^f/N_L^f$. However finding a control region for fake leptons can be difficult. Different types of fakes may react quite differently to the isolation requirements, and the composition for fakes in the control region can be different from that in the signal region. As a result, fake efficiency measured in the control region may not represent that in the signal region, and the estimation of fakes may be biased. For example, in the $t\bar{t}H$ analysis (see Section 6.3) where matrix method is used as a cross-check, events with the same sign dilepton and 2 or 3 jets are used to measure the fake efficiency. As shown in Figure 5.2, compositions are quite different between regions with low jet multiplicities ($N_j \leq 3$) and regions with high jet multiplicities ($N_j > 3$). Things might also get complicated when calculating fake ef-
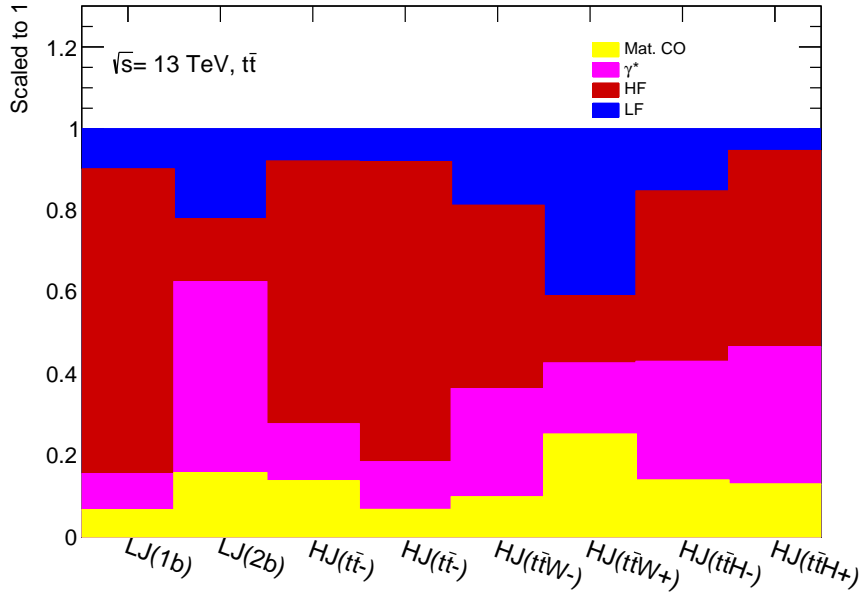


Figure 5.2: Fake compositions in different regions in the $t\bar{t}H$ analysis are estimated from the $t\bar{t}$ MC simulation. The first two bins (LJ(1b) and LJ(2b)) show compositions in two control regions with $\ell^\pm\ell^\pm$ and 2 or 3 jets, and the other bins reflect the corresponding compositions in signal regions and other control regions with at least 4 jets used in the analysis.

ficiency in the control region. There might be non-negligible contributions from the SM processes (e.g. the $t\bar{t}W$ process) which need to be subtracted in order to get the number of fake leptons passing the tight and loose selections. In this circumstance, variations of contributions from the SM processes, e.g. the $t\bar{t}W$ process, will impact the fake efficiency calculation, and it is non-trivial to deal with the correlation between $t\bar{t}W$ variation and fake contributions in the matrix method. For these reasons, the matrix method may fail in some analyses. However, another semi-data-driven method, template fit method, can be more flexible for multi-source fakes and is capable of dealing

with correlations between the SM processes (i.e. the $t\bar{t}W$ process) and fakes.

### 5.2.2.2 Template Fit Method

A template fit method has been developed for the $t\bar{t}H$ analysis (see Section 6.3) to deal with multi-source fakes. It is a semi-data-driven method which relies on MC simulation to define different types of fake/non-prompt leptons and to describe kinematics for different sources of fakes. In this method, the Normalization Factors (NFs)[6] of the different fake lepton contributions are allowed to float in a fit to data, and those NFs are used to correct the fakes estimated from MC simulations in the signal regions.

Based on the truth classification of events containing a fake/non-prompt lepton, following main contributions are distinguished and a free-floating NF is assigned to each of them:

- $NF^{Mat.CO}$: NF applied to events with one non-prompt electron from material photon conversion;

- $NF_e^{HF}$: NF applied to events with one non-prompt electron from $b/c$ hadron decays;

- $NF_\mu^{HF}$: NF applied to events with one non-prompt muon from $b/c$ hadron decays;

- $NF^{Int.CO}$: NF applied to events with one electron from QED processes $\gamma^* \rightarrow e^+e^-$.

For both the $t\bar{t}H$ analysis (see Section 6.3) and the $t\bar{t}t\bar{t}$ analysis (see Section 7.2), because of large contribution from the $t\bar{t}W$ process and poor description given by the current MC simulation, NF for $t\bar{t}W$ process is free-floating in the fit to data.

In order to measure and constrain NF for $t\bar{t}W$ and fakes, dedicated control regions have been developed. Moreover, validation regions are used to assess modeling of the main backgrounds. The ways to build control regions and validation regions vary from analysis to analysis, and details about how to setup these regions are discussed in Section 6.3 and 7.2 for the $t\bar{t}H$ analysis and the $t\bar{t}t\bar{t}$ analysis, respectively.

The template fit method is based heavily on MC simulations for describing kinematics of the processes, so complex systematic treatments are required to deal with possible bias of the kinematic distributions and the treatment differs from analysis to analysis. The commonly used systematics will be discussed in Section 5.3.2, and distinct ones will be discussed in Section 6.3 and 7.2 for the $t\bar{t}H$ analysis and the $t\bar{t}t\bar{t}$ analysis, respectively.

---

[6]A scale factor applied on top of the theory predictions or MC simulation.

# 5.3  Systematic Uncertainties

The extent to which a physics process can be understood is limited by both statistical and systematic uncertainties. Systematic uncertainties may arise from the lack of thorough understanding of many sources of mis-measurements for the physics objects as well as pertinent theoretical uncertainties. This section describes the sources of systematic uncertainties considered in analyses presented in Chapter 6 and 7. These uncertainties can be divided into three groups: experimental uncertainties, modeling uncertainties related to the background processes, and theoretical uncertainties on the signal processes. The experimental uncertainties and some modeling uncertainties related to the background processes that are common in both analyses are discussed in this section, while systematics that are unique in each analysis will be discussed in Chapter 6 and 7, separately.

## 5.3.1  Experimental Uncertainties

Experimental uncertainties are related to the trigger efficiency, reconstruction and identification of the physics objects described in Chapter 4 and the global event activities.

### 5.3.1.1  Event-wide Uncertainties

Event-wide uncertainties are process-independent and affect the overall normalization of the processes related to both luminosity and pileup measurements. The uncertainty in the combined 2015-2017 (2015-2018) integrated luminosity is 2% (1.78%) used in the $t\bar{t}H$ analysis (the $t\bar{t}t\bar{t}$ analysis). It is derived from the calibration of the luminosity scale using $x$-$y$ beam-separation scans, following a methodology similar to that detailed in Ref. [159], and using the LUCID-2 detector for the baseline luminosity measurements [160]. The luminosity uncertainty is applied to each process simulated using MC. To account for the difference in pile-up distributions between data and MC simulations, an uncertainty related to the MC scale factors is applied.

### 5.3.1.2  Lepton Uncertainties

For electrons and muons, the reconstruction, identification, isolation and trigger performances differ between data and MC. To correct these differences, scale factors for each are applied. They are estimated using the tag-and-probe method[101, 104]. The associated systematic uncertainties are then propagated to the final distributions used in the analyses. Additional uncertainties related to the lepton kinematics due to the resolution and scale of the electron energy (muon momentum) measurement are also considered.

### 5.3.1.3 Jet Uncertainties

Systematic uncertainties on the reconstructed jet objects are related to the JVT, JES and *Jet Energy Resolusion* (JER).

JVT systematic uncertainties is obtained by varying up and down the JVT cut with the JetVertexTaggerTool [113]. This uncertainty accounts for the remaining contamination from pile-up jets after applying pile-up suppression and the MC generator choice. The modeling of the JVT is tested in $Z(\rightarrow \mu\mu)$+jets events as well as semileptonic $t\bar{t}$ events.

There are many sources of uncertainties related to the JES and JER, each related to a specific part of the JES and JERcalibration measurements, as described in Section 4.4. They arise from the techniques and corrections derived in MC, including statistical, detector, modeling effects, jet flavor compositions, pileup corrections, and $\eta$-dependence effects. The JES and JER uncertainties have more dominant effects on the final results presented in this dissertation.

To determine the JES and its associated uncertainties, information from test-beam data, LHC collision data and simulation have been used, as described in Ref. [161]. A globally reduced uncertainty set, provided by the JetEtMiss group for Run II [162] searches, is used. The uncertainties are in a set of 30 (27) components used in analysis described in Chapter 7 (6), with an up/down variation for each component, and they can have different jet $p_T$ and $\eta$ dependencies.

The JER has been measured separately for data and MC using *in situ* techniques, similar to Ref. [163]. The expected fractional jet $p_{\rm T}$ resolution is obtained using the *JERSmearingTool* as a function of the $p_{\rm T}$ and rapidity of the given jet. A systematic uncertainty is defined as the quadratic difference between the jet energy resolutions for data and MC simulation. In the $t\bar{t}H$ analysis, one effective uncertainty is used to account for all the effects related to the JER, however in the $t\bar{t}t\bar{t}$ analysis, nine independent systematics are chosen.

### 5.3.1.4 Flavor Tagging Uncertainties

There are uncertainties related to the $b$-tagging efficiencies and the $c$- and light-jet mis-tagging efficiencies. They are mixtures of statistical, experimental, and modeling uncertainties incurred in the flavor tagging calibration procedures. The uncertainties affect the analyses through their impact on the scale factors, described in Section 4.4.1. Given the importance of $b$-tagged jets in the final states of the $t\bar{t}t\bar{t}$ signal process, these uncertainties have a large impact on the results of the $t\bar{t}t\bar{t}$ analysis. However, in the $t\bar{t}H$ analysis, as fewer $b$-jets are required in the signal region, the related uncertainties have a smaller impact on the result. A more complex systematic treatment is employed in the $t\bar{t}t\bar{t}$ analysis with a total of 85 independent systematic variations. The systematics are obtained after diagonalization of the error matrix across all pairs of kinematic bins, which are used to derive heavy-flavor efficiencies corrections[114]. The obtained eigenvectors corresponding

to independent variations[7] are included by constructing the proper correlations across different kinematic regions.

### 5.3.1.5 Missing Transverse Energy

Systematic variations of the $E_T^{\text{miss}}$ are incurred as a result of the systematic variations associated with the objects (jets and leptons) provided as input to the $E_T^{\text{miss}}$ calculation. Additional uncertainties related to the scale and resolution of soft-term in the $E_T^{\text{miss}}$ calculation are also considered. The uncertainty is estimated using events without real $E_T^{\text{miss}}$, namely $Z \rightarrow \ell\ell$ [164]. In that case, the soft term should be balanced against the object-based term to meet the no $E_T^{\text{miss}}$ requirements, but resolution effects spoil the equality between soft and hard term. This non-compensation between soft and hard term is measured in data and compared with the MC simulation. The difference is considered to be the uncertainty.

## 5.3.2 Background Uncertainties

Modeling uncertainties associated with the background processes need to be considered. These include variations in normalizations or kinematics (shape). Normalization uncertainties include cross-section uncertainties from theoretical calculations or from other measurements. Shape uncertainties are typically assessed with data-driven methods or through MC comparisons. By comparing the nominal MC simulation for the process with an alternative MC simulation in which theoretical or phenomenological parameters are varied, the impact of the underlying assumptions made in the MC simulation can be estimated.

### 5.3.2.1 $t\bar{t}W$ Production

Due to the importance of the $t\bar{t}W$ production for both analyses described in the Chapter 6 and 7, special care has been taken in the definition of modeling uncertainties for the $t\bar{t}W$ background. The lack of higher order corrections and tensions observed between data and MC simulation for the $t\bar{t}W$ process lead to a new strategy for the modeling of this process.

The systematic uncertainties associated with the $t\bar{t}W$ process are:

- the uncertainty related to the comparison of the AMC@NLO+PYTHIA8(0j@NLO) with SHERPA2.2.1(0j@NLO), both inclusive NLO setups, referred to as generator uncertainties;

---

[7]Strictly speaking, this eigenvector approach, which is an application of the more general Principal Component Analysis (PCA), remove *linear* correlations only. Since these eigenvector variations are linear combinations of physics-related uncertainties, their physics origin cannot be easily identified.

- the renormalization and factorization scale variations of the SHERPA2.2.1 multileg NLO (0,1j@NLo+2j@LO) sample by varying both scales by a factor 2 and $1/2$;

The variations for $t\bar{t}W$ as a function of jet multiplicities are shown in Figure 5.3.



<center>(a)                                                                           (b)</center>
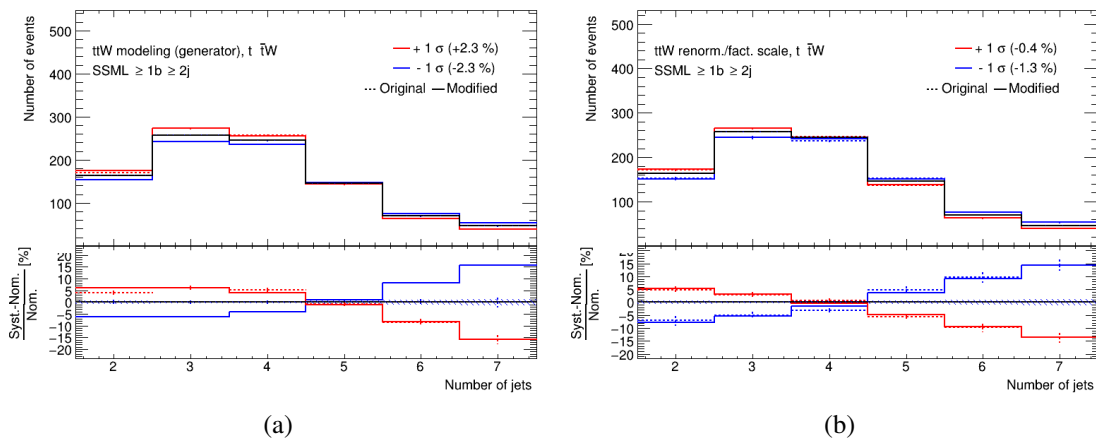
Figure 5.3: (a) The generator uncertainties and (b) the renormalization and factorization scale variations for $t\bar{t}W$ process as a function of jet multiplicities in the same sign dilepton and multilepton final states with at least 1 b-jets and at least 2 jets.

Data-driven systematics are also assessed for the $t\bar{t}W$ process to account for disagreement observed between data and MC simulation in both the $t\bar{t}H$ analysis and the $t\bar{t}t\bar{t}$ analysis, and these systematics will be presented in Section 6.3 and 7.2, respectively.

### 5.3.2.2   Uncertainties Related to Fakes

The template fit method is used as the nominal method in both the $t\bar{t}H$ analysis and the $t\bar{t}t\bar{t}$ analysis to estimate contributions from fake leptons. Uncertainties related to the template fit is discussed in this section.

Shape systematic uncertainties are considered for each of the fakes templates in both the $t\bar{t}H$ analysis and the $t\bar{t}t\bar{t}$ analysis, and are derived as follows. By inverting the lepton isolation requirements, regions with dominating fake contributions are obtained. As an example, Figure 5.4 shows the region for heavy flavor electron in the $t\bar{t}H$ analysis. After subtracting other prompt backgrounds from data in this inverted isolation regions, the fake contribution is calculated. A systematic uncertainty for fake templates (especially for heavy flavor electrons and heavy flavor muons) is derived by comparing the calculated fake contribution with the MC simulation in all bins used in the template fit.

A special $Z \to \mu^+\mu^-\gamma^*(\to e^+e^-)$ sample, defined by requiring two opposite-charge muons and one electron, is selected to validate the template fit results on conversions shown in Figure 5.5.
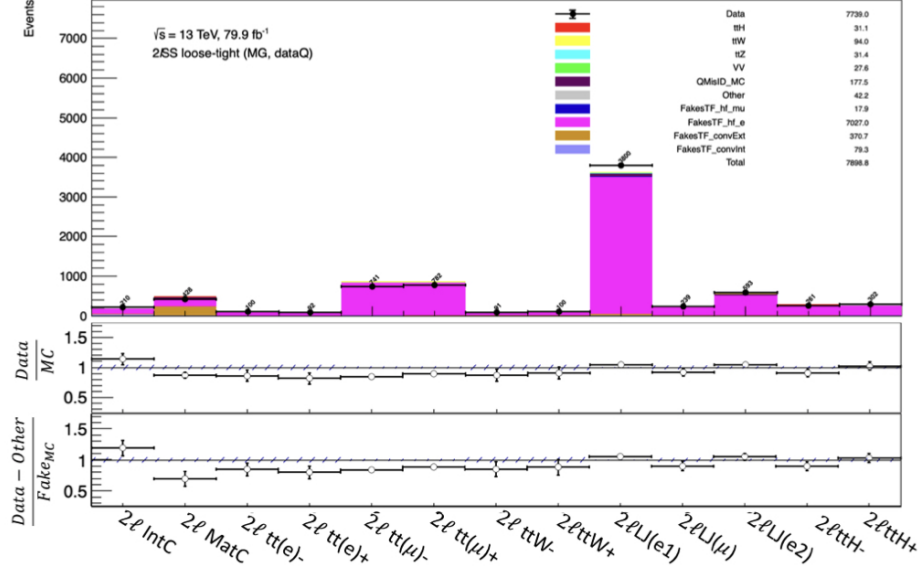
Figure 5.4: The summary plot for all control and signal regions with relaxed isolation criteria for heavy flavor electron templates in same sign dilepton channel in $t\bar{t}H$ analysis. Second ratio plots show the ratio of data fakes (after subtracting all non-fake MC background) to template fit fakes used to derive the HF systematic uncertainties.

Uncertainties for the internal and material conversions are obtained by comparing the data and the
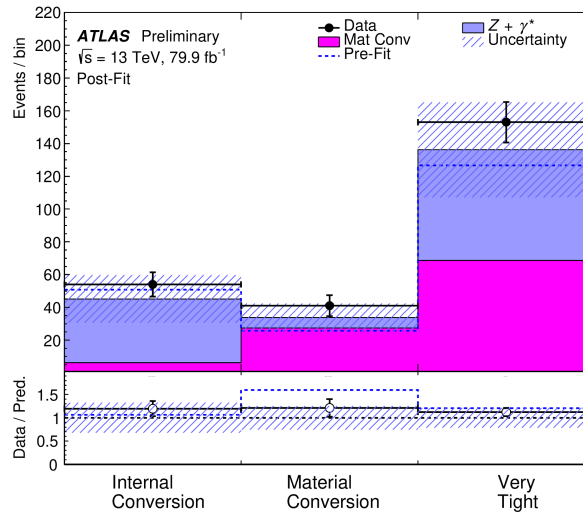


Figure 5.5: Comparison between data and prediction for the event yields in the trilepton validation region enriched in $Z \to \mu^+\mu^-\gamma^*(\to e^+e^-)$ candidate events, divided into three categories depending on the requirements satisfied by the electron: internal conversion, material conversion, or very tight.

POWHEG+PYTHIA8 simulation of $Z(\to \mu^+\mu^-)$+jets production.

Other modeling uncertainties might also be considered depending on the impact of the systematics, such as modeling of additional QCD radiation (see Section 6.3), uncertainties for LF contributions (see Section 6.3) and uncertainties for additional heavy flavor jets (see Section 7.2).

### 5.3.2.3   Charge Mis-identification

The systematic uncertainty on the Q-MisID background is estimated by applying a variation $\Delta w$ on the weight of Equation 5.3 described in Section 5.2.1 using the following formula:

$$\Delta w = \frac{\sqrt{(1 - 2\epsilon_1)^2 \Delta\epsilon_2^2 + (1 - 2\epsilon_2)^2 \Delta\epsilon_1^2 + (1 - 2\epsilon_1)(1 - 2\epsilon_2)\rho_{12}\Delta\epsilon_1\Delta\epsilon_2}}{(1 - \epsilon_1 - \epsilon_2 + 2\epsilon_1\epsilon_2)^2}, \tag{5.11}$$

where $\Delta\epsilon_1$ and $\Delta\epsilon_2$ stand for the uncertainties on the charge flip rates of the first and the second electron, and the $\rho_{12}$ stands for the correlation between $\epsilon_1$ and $\epsilon_2$.

Three sources of systematic uncertainties on the charge flip rates are considered in both the $t\bar{t}H$ analysis and the $t\bar{t}t\bar{t}$ analysis:

- the statistical uncertainties from the likelihood fit,

- the difference between the rate extracted by the likelihood method and the truth-matching method on the simulated $Z \to ee$ events,

- the systematic uncertainties from the variation of the dielectron invariant mass window used to define the $Z$ region.

## 5.3.3   Signal Uncertainties

Uncertainties on the signal modeling are assessed in both analyses presented in Chapter 6 and 7. The uncertainties arise from the variations in the $\mu_F$ and $\mu_R$ scales, as well as the PDF choice. They are assessed in exactly the same manner as for the SM backgrounds described in Section 5.3.2.

# 5.4   Statistical Method

The statistical analysis of the data is often treated as a final subsidiary step to experimental physics results, but it is a crucial element in physics analysis. Understanding the requirements of a robust statistical statement is an efficient way to design or formulate an analysis strategy. This section introduces the statistical method used in this dissertation.

## 5.4.1 Statistical Modeling

### 5.4.1.1 Parameterization

Parameters ($\alpha$) in physics analysis in this dissertation can be separated into two groups, the *Parameter of Interest* (POI) denoted as $\mu$ and Nuisance Parameters (NPs) denote as $\theta$ hereafter, thus $\alpha = (\mu, \theta)$.

Theories can provide probability models that predict the distributions of the observable quantities. The parameter of interest $\mu$ stands for the quantity that the analysis is aiming to measure. For example, the POI can be cross section of the signal process or the signal-strength modifier, defined as the cross section ratio between observation and theory prediction for the signal process.

The distribution of experimental data is the result of convolution of the distribution of underlying physics processes with the effect of experimental response - detector's finite resolution, mis-calibrations, the presence of background, etc. The detector response itself can be described by a probability model that depends on unknown parameters. Those additional unknown parameters are called nuisance parameters $\theta$. Imperfect knowledge of NPs lead to systematic uncertainties, described in Section 5.3.2. Those systematics can be estimated from dedicated auxiliary measurements, such as control regions, sidebands, data-driven background estimates and calibration measurements.

The auxiliary measurements[165] for a parameter $p$, which can be described by the probability density function $f_{aux}(D_{aux}|\alpha_p, \boldsymbol{\alpha_{other}})$ where $D_{aux}$ represents the observed events and $\boldsymbol{\alpha_{other}}$ is the set the other parameters related to the auxiliary measurement, provides $a_p$, a maximum likelihood estimates for $\alpha_p$ and $\sigma_p$, a standard error. Thus, the probability model for an auxiliary measurement $f(a_p|\alpha_p, \sigma_p)$ referred to as constraint term hereafter, can often be approximately modeled using a Gaussian function:

$$
\begin{aligned}
f(a_p|\alpha_p, \sigma_p) &= Gauss(a_p|\alpha_p, \sigma_p) \\
&= \frac{1}{\sqrt{2\pi\sigma_p^2}} \exp\left[\frac{(a_p - \alpha_p)^2}{\sigma_p^2}\right]
\end{aligned}
\tag{5.12}
$$

However, for an intrinsically non-negative parameter, such as event yields, energy scale uncertainties and uncertainties related to cross sections, the Gaussian function does not apply. In these cases, the constraint term can take the form of the log-normal distribution, which is given by

$$
f(a_p|\alpha_p, \sigma_p) = \frac{1}{\sqrt{2\pi}a_p \ln\kappa} \exp\left[-\frac{(\ln(\alpha_p/a_p))^2}{2(\ln\kappa)^2}\right]
\tag{5.13}
$$

where $\kappa = 1 + \sigma_p/a_p$.

The distributions for Gaussian and log-norm distribution with the same $a_p$ and $\sigma_p$ are shown in

Figure 5.6. When $a_p \gg \sigma_p$, the two distributions are similar (as shown in Figure 5.6b).



<div align="center">(a)</div>



<div align="center">(b)</div>
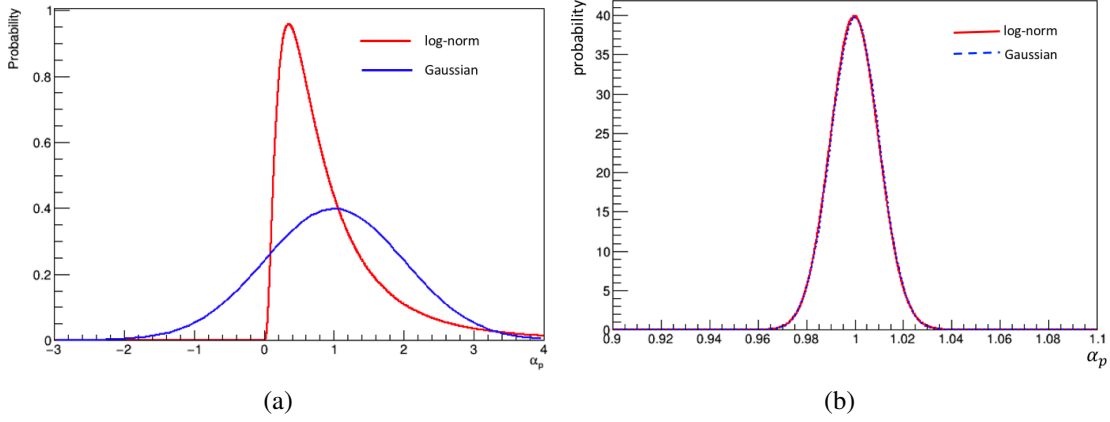
Figure 5.6: Comparison for Gaussian and log-norm distribution with the same (a) $a_p = 1$ and $\sigma_p = 1$ and (b) $a_p = 1$ and $\sigma_p = 0.01$.

## 5.4.2 Likelihood Construction

For analysis based on so-called 'counting/binned experiments' such as the $t\bar{t}H$ analysis and the $t\bar{t}t\bar{t}$ analysis described in Chapter 6 and Chapter 7, only the numbers of events, from data, the background estimations and expected signal, are used as input. These numbers are taken from all relevant regions (the control regions and signal regions) or bins in the analysis. The expected number of events populating each region is given by the following:

$$N_r^{exp}(\alpha_{sig}, \alpha_{bkg}) = N_r^{exp}(\mu_{sig}, \boldsymbol{\mu}_{bkg}, \boldsymbol{\theta}) = \mu_{sig} \cdot N_{r,sig}^{exp}(\boldsymbol{\theta}) + \sum_{b \in bkg} \mu_b \cdot N_{r,b}^{exp}(\boldsymbol{\theta}) \qquad (5.14)$$

where $\boldsymbol{\mu}_{bkg}$ is the collection of NFs associated with backgrounds, $\mu_b$ is the NF associated with the background '$b$', $\mu_{sig}$ is the signal-strength modifier associated with the signal hypothesis, usually also treated as POI, and $N_{r,sig}^{exp}$ and $N_{r,b}^{exp}$ are the predicted signal and background yields in region '$r$'. The predicted number of events for each process, signal or background, depends on the $\boldsymbol{\theta}$ parameter vector since systematic variations can adjust the overall normalization of a given process or change the acceptance of given process in the phase space provided by the region '$r$'.

The observed data yields in each region of the analysis are expected to obey Poisson statistics. Therefore, the likelihood function $L(\mu_{sig}, \boldsymbol{\mu}_{bkg}, \boldsymbol{\theta})$ is constructed as a product of Poisson probabil-

ity terms:

$$L_0(\mu_{sig}, \boldsymbol{\mu}_{bkg}, \boldsymbol{\theta}) = \prod_{r \in regions} \frac{N_r^{exp}(\mu_{sig}, \boldsymbol{\mu}_{bkg}, \boldsymbol{\theta})^{N_r^{obs}}}{N_r^{obs}!} \exp\left[-N_r^{exp}(\mu_{sig}, \boldsymbol{\mu}_{bkg}, \boldsymbol{\theta})\right], \qquad (5.15)$$

where $N_r^{obs}$ is the observed data yield in region 'r'.

In order to construct the full likelihood, the constraint terms for the NP are multiplied to the Equation 5.15, thus the full model can be written as:

$$L_{(\mu_{sig}, \boldsymbol{\mu}_{bkg}, \boldsymbol{\theta})} = L_0(\mu_{sig}, \boldsymbol{\mu}_{bkg}, \boldsymbol{\theta}) \cdot \prod_{p \in S} f(a_p | \alpha_p, \sigma_p) \qquad (5.16)$$

where the set of NPs constrained by auxiliary measurements is denoted as $S$ and a set of estimates of those parameters, also referred to as global observables, is denoted as $G = a_p$ with $p \in S$.

### 5.4.3 Statistical Approach

A test statistic can be a gauge to distinguish the null[8] from the alternative hypothesis[9] in statistical hypothesis testing. The profile likelihood ratio test statistic [166] is used to derive confidence intervals or upper limit on a measured quantity, and to obtain levels of compatibility between two hypotheses. The test statistic is defined such that larger values imply increasing level of disagreement, which can be quantified in terms of $p-$value

$$p(\mu) = \int_{t_{\mu,obs}}^{+\infty} f(t_\mu | \mu) dt_\mu, \qquad (5.17)$$

which is calculated by integrating the corresponding distribution of the test statistic $f(t_\mu | \mu)$ above the observed value of the test statistic in data, $t_{\mu,obs}$. The distribution of the test statistic, $f(t_\mu | \mu)$ can be obtained by the ensemble from MC pseudo-experiments. In case of the profiled likelihood ratio test statistic with sizable statistics in data, $f(t_\mu | \mu)$ can be well approximated by explicit formula[166], which will be discussed in more details later in this section. This approximation method is used in the dissertation.

In particle physics, the $p$-value can be converted into an equivalent significance $Z$, defined as

$$Z = \Phi^{-1}(1 - p) \qquad (5.18)$$

---

[8]In particle physics, the null hypothesis is often referred as the background-only hypothesis
[9]In particle physics, the alternative hypothesis is typically referred as the signal-plus-background hypothesis

where $\Phi^{-1}$ is the quantile of the standard Gaussian function[10]. In search for new physics, to constitute a discovery in particle physics, a significance of at least $Z = 5\sigma$ is needed to reject the null hypothesis. This corresponds to a $p$-value of $2.87 \times 10^{-7}$. A statistical significance of $Z = 3\sigma$ indicates evidence for new physics. This corresponds to a $p$-value of $0.13\%$.

For a measurement, the confidence level (CL) intervals or contours of the measured quantities are defined such that the boundaries of $100(1 - \beta)\%$ CL intervals $[\mu_1, \mu_2]$ satisfy $P(\mu_1) = 1 - \beta/2$ and $P(\mu_2) = \beta/2$.

### 5.4.3.1 Profile Likelihood Ratio

The test statistic defined for the analyses to be presented is based on the following profile likelihood ratio,

$$\lambda(\mu_{sig}) = \frac{L_{(\mu_{sig}, \hat{\hat{\boldsymbol{\mu}}}_{bkg}, \hat{\hat{\boldsymbol{\theta}}})}}{L_{(\hat{\mu}_{sig}, \hat{\boldsymbol{\mu}}_{bkg}, \hat{\boldsymbol{\theta}})}}, \tag{5.19}$$

where $\hat{\mu}_{sig}$, $\hat{\boldsymbol{\mu}}_{bkg}$ and $\hat{\boldsymbol{\theta}}$ are the maximum likelihood estimates (MLEs) for the POI, NFs of backgrounds and nuisance parameters respectively, and are the values of the parameters that maximize the likelihood function $L_{(\mu_{sig}, \boldsymbol{\mu}_{bkg}, \boldsymbol{\theta})}$. $\hat{\hat{\boldsymbol{\mu}}}_{bkg}$ and $\hat{\hat{\boldsymbol{\theta}}}$ are the conditional maximum likelihood estimates of $\boldsymbol{\mu}_{bkg}$ and $\boldsymbol{\theta}$, and maximize the likelihood function with POI fixed to a certain value. By definition $\lambda$ is between 0 and 1. A large $\lambda$ value indicates good agreement between the data and the hypothesized value of $\mu_{sig}$, and a small $\lambda$ indicates large disagreement between the two.

A modified profile likelihood ratio is also defined for scenarios in case the POI $\mu_{sig}$ is physically non-negative, $\mu_{sig} \geq 0$, and it is defined as:

$$\tilde{\lambda} = \begin{cases} \frac{L_{(\mu_{sig}, \hat{\hat{\boldsymbol{\mu}}}_{bkg}, \hat{\hat{\boldsymbol{\theta}}})}}{L_{(\hat{\mu}_{sig}, \hat{\boldsymbol{\mu}}_{bkg}, \hat{\boldsymbol{\theta}})}} & \hat{\mu}_{sig} \geq 0 \\ \frac{L_{(\mu_{sig}, \hat{\hat{\boldsymbol{\mu}}}_{bkg}, \hat{\hat{\boldsymbol{\theta}}})}}{L_{(0, \hat{\boldsymbol{\mu}}_{bkg}, \hat{\boldsymbol{\theta}})}} & \hat{\mu}_{sig} < 0 \end{cases} \tag{5.20}$$

### 5.4.3.2 Test Statistic $t_{\mu_{sig}}$

The profile likelihood test statistic is defined as

$$t_{\mu_{sig}} = -2 \ln \lambda(\mu_{sig}), \tag{5.21}$$

to measure the level of disagreement between the data and hypothesized value of $\mu_{sig}$. The sampling distribution of $t_{\mu_{sig}}$ can be well approximated by a $\chi^2$ distribution with $n$ degrees of freedom $\chi_n^2(t_{\mu_{sig}})$[166]:

$$f(t_{\mu_{sig}} | \mu_{sig}) \approx \chi_n^2(t_{\mu_{sig}}), \tag{5.22}$$

---

[10]The quantile function is also called the percent-point function or inverse cumulative distribution function.

where $n$ is number of POIs. The value of $t_{\mu_{sig}}$ close to 0 means the agreement between data and the hypothesized value of $\mu_{sig}$, while larger values imply increasing level of disagreement, which can be quantified in terms of the $p$-value defined in Equation 5.17:

$$p(\mu_{sig}) = \int_{t_{\mu_{sig},obs}}^{\infty} \chi_n^2(t_{\mu_{sig}}) dt_{t_{\mu_{sig}}}. \tag{5.23}$$

The p-value can be converted to the corresponding Gaussian significance using Equation 5.18. For one degree of freedom $n = 1$, 68.1% ($Z = 1\sigma$), 95.4% ($Z = 2\sigma$) and 99.7% ($Z = 3\sigma$) CL intervals are given by the values of $\mu_{sig}$ which satisfy $t_{\mu_{sig}} = 1.0, 4.0, 9.0$, respectively.

In the case for a positive signal, the statistic defined as

$$q_0 = \begin{cases} -2 \ln \lambda(0) & \hat{\mu}_{sig} \geq 0 \\ 0 & \hat{\mu}_{sig} < 0 \end{cases} \tag{5.24}$$

can be used to quantify the significance of the POI. The sampling distribution of $q_0$ can be approximated by:

$$f(q_0|0) \approx \frac{1}{2}\delta(q_0) + \frac{1}{2\sqrt{2\pi q_0}} e^{-q_0/2} \tag{5.25}$$

Therefore, the $p$-value to quantify the compatibility with background-only hypothesis is calculated using the equation:

$$p(\mu_{sig}) = 1 - \Phi(\sqrt{q_0}) \tag{5.26}$$

where $\Phi$ represents the cumulative distribution function of the standard Gaussian distribution. The corresponding signal significance can be calculated by:

$$Z(\mu) = \sqrt{q_0} \tag{5.27}$$

# CHAPTER 6

# Search for the Associated Production of a Higgs Boson with a Top Quark Pair in the Same-sign Dilepton and Multilepton Final States

This chapter discribes a search for $t\bar{t}H$ production in the multilepton final states using 80 fb$^{-1}$ of the data collected with the ATLAS detector at $\sqrt{s} = 13$ TeV during 2015-17. This search uses six final states, as shown in Figure 6.1, distinguished by the number and the flavor of leptons: two
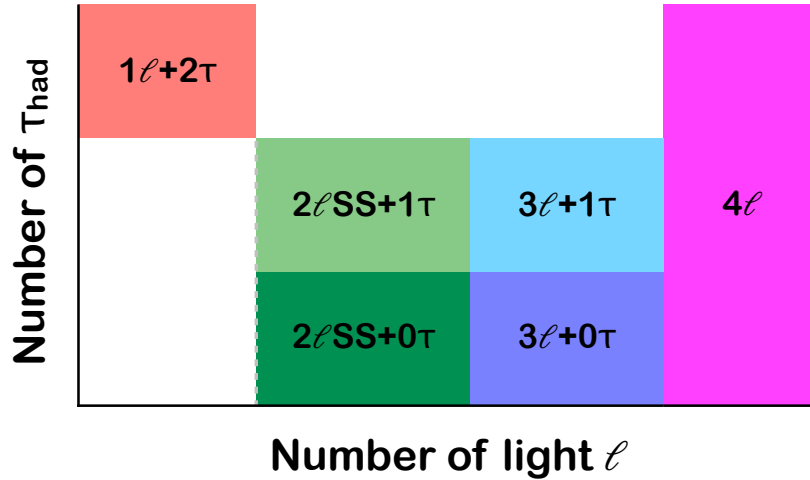
Figure 6.1: $t\bar{t}H$ multilepton channels in terms of light lepton multiplicity and $\tau_\text{had}$ multiplicity.

same-charge light leptons ($e$ or $\mu$) and no hadronically-decaying $\tau$ lepton candidates (2$\ell$SS); two same-charge light leptons and one hadronically-decaying $\tau$ lepton candidate (2$\ell$SS+1$\tau_\text{had}$); three

light leptons and no hadronically-decaying $\tau$ lepton candidates ($3\ell$); four light leptons ($4\ell$); three light leptons and one hadronically-decaying $\tau$ lepton candidate ($3\ell+1\tau_{\mathrm{had}}$); one light lepton and two hadronically-decaying $\tau$ lepton candidates ($1\ell+2\tau_{\mathrm{had}}$). These signatures are primarily sensitive to $H \to WW^*$ (with subsequent decay to $\ell\nu\ell\nu$ or $\ell\nu jj$) and $H \to \tau\tau$ decays. Feynman diagrams for the signal processes are presented in Figure 6.2. Backgrounds are estimated with a combination of
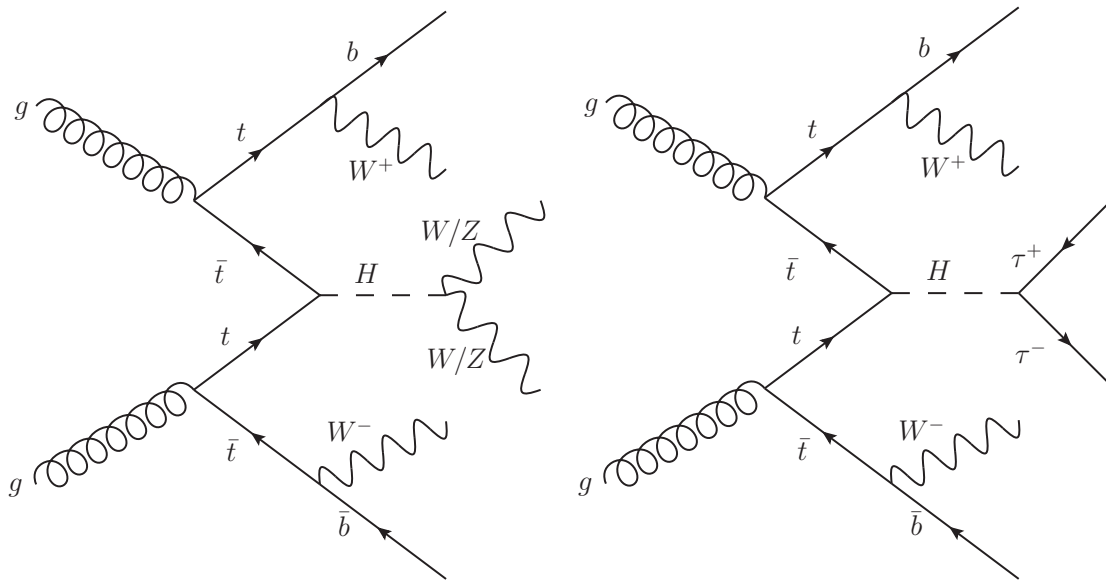


Figure 6.2: Examples of tree-level Feynman diagrams for the production of the Higgs boson in association with a pair of top quarks. Higgs boson decays to $WW/ZZ$ (left) or $\tau\tau$ (right) are shown.

simulation and data-driven techniques, and a global fit in all final states is used to extract the best estimate for the cross section of the $t\bar{t}H$ production.

This chapter focuses on the $2\ell$SS and $3\ell$ channels, and is organized as follows. The selection criteria of the physics objects are discussed in Section 6.1. The event selection and categorization are explained in Section 6.2. The methods used to estimate the backgrounds is described in Section 6.3. Theoretical and experimental systematic uncertainties are described in Section 6.4. Finally, the results obtained are presented in Section 6.5.

## 6.1   Object Selection

This section describes the selections applied to the reconstructed physics objects introduced in Chapter 4. Physics objects are required to satisfy certain kinematic criteria to ensure the quality of these objects, to pass the trigger requirements, and to possibly improve the sensitivity of the analysis. Discussion of the WPs for lepton reconstruction and identification is given in Section 4.3.

That of jets is presented in Section 4.4 and Section 4.4.1 for jets and b-tagged jets, respectively. Lepton isolation requirements as well as the kinematic criteria for both leptons and jets will be discussed in this section. For the newly introduced object - hadronically decay $\tau$-lepton - which is only used in this analysis, their reconstruction and identification will be discussed in this section. Finally, the overlap removal procedure is discussed.

### 6.1.1 Light Leptons

There can be large contributions from instrumental backgrounds. In order to reject as much instrumental backgrounds as possible, several tools described in Section 4.3 are used. 'Non-prompt lepton BDT' is applied to electrons and muons to reject non-prompt leptons originating from $b$-/$c$- decays, along with the 'FixCutLoose' isolation WP (see Section 4.3.3). The corresponding rejection factor against muons (electrons) from the decays of $b$-/$c$-hadrons is about 3.5 (10). The Q-MisID are rejected using the Q-MisID BDT described in Section 4.3.1.3. To further suppress conversions, photon conversion tagger is employed together with additional requirements on the associated track $p_T$ and on the ratio of the electron's calorimeter energy and the track momentum. With the photon conversion tagger, electrons passing the isolation and the Q-MisID BDT criteria are further split into three categories: 'material conversions', 'internal conversions', and 'very tight' as described in Section 4.3.1.4.

The efficiencies at the chosen WP for muons and electrons satisfying very tight (T*) criteria are presented in Figure 6.3 and 6.4.
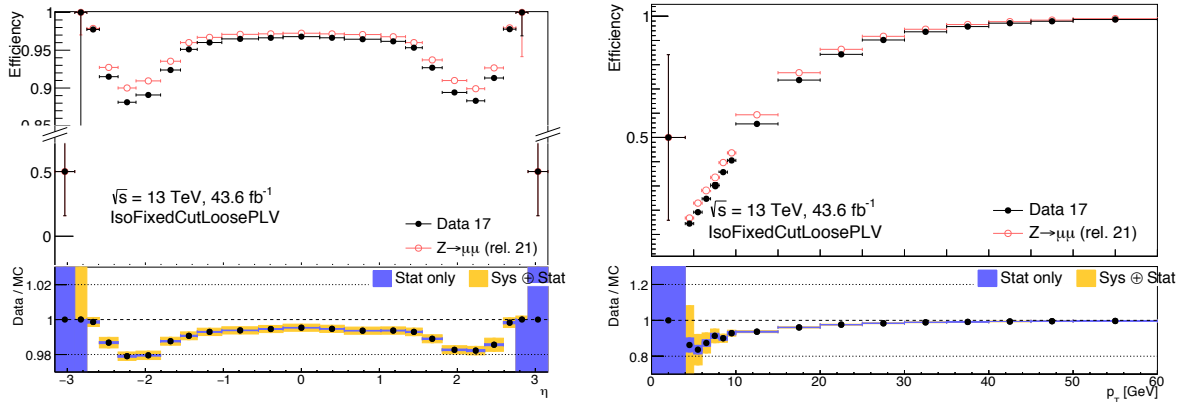


Figure 6.3: Selection efficiency of the combined tight isolation working point as a function of $\eta$ (left) and $p_T$ (right) in the muon channel. The ratio plot presents the data/MC agreement.

The different light-lepton selections used in the analysis are summarized in Table 6.1.
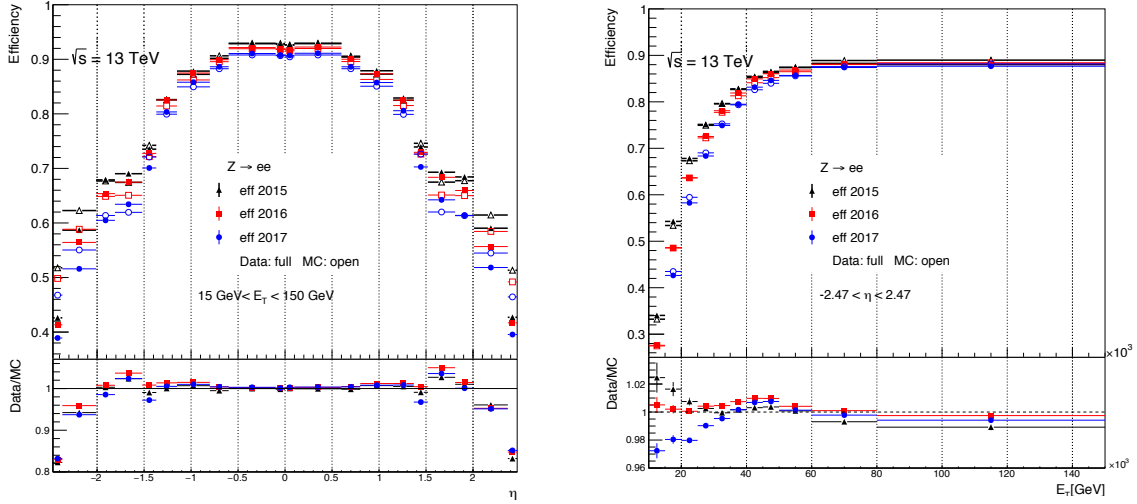
Figure 6.4: Selection efficiency of the combined tight isolation working point, including the electron charge misidentification MVA cut, as a function of $\eta$ (left) and $E_T$ (right) in the electron channel. The ratio plot presents the data/MC agreement.

Table 6.1: The requirements applied to select loose (L), loose and minimally-isolated (L*), tight (T) and very tight (T*) light leptons.

| | $e$ | | | | $\mu$ | | |
|---|---|---|---|---|---|---|---|
| | L | L* | T | T* | L | L* | T/T* |
| Identification | Loose | | Tight | | Loose | | Medium |
| Isolation (FixCutLoose WP) | No | Yes | | | No | Yes | |
| Non-prompt lepton veto | No | | Yes | | No | | Yes |
| Charge misidentification veto | No | | Yes | | N/A | | |
| Material/internal conversion veto | No | | Yes | | N/A | | |
| Lepton $|\eta|$ | $< 1.37$ or $1.52 - 2.47$ | | $< 1.37$ or $1.52 - 2$ | | $< 2.5$ | | |
| Lepton $p_T$ | $> 10$ GeV | | | | $> 10$ GeV | | |
| $|d_0|/\sigma_{d_0}$ | $< 5$ | | | | $< 3$ | | |
| $|z_0 \sin\theta|$ | $< 0.5$ mm | | | | | | |

## 6.1.2 Jets

Jets are required to satisfy $p_\mathrm{T} > 25$ GeV and $|\eta| < 2.5$.

Jets containing $b$-hadrons are identified ($b$-tagged) using MV2c10 which has a 70% efficiency for $b$-jets in the simulated $t\bar{t}$ events.

### 6.1.3   Hadronically Decay $\tau$-leptons

Hadronically decaying $\tau$-lepton candidates ($\tau_{\text{had}}$) are reconstructed from clusters in the calorimeters and associated inner detector tracks [167]. They are required to have either one or three associated tracks, with a total charge of $\pm 1$. Candidates must have transverse momentum $p_{\text{T}} > 25$ GeV and $|\eta| < 2.5$, excluding the EM calorimeter's transition region, and should originate from the primary vertex. A BDT discriminant using calorimeter- and tracking-based variables is used to identify $\tau_{\text{had}}$ candidates and reject jet backgrounds [168]. The medium WP has a target efficiency of 55% (40%) for one- (three-)prong $\tau_{\text{had}}$ decays, while the tight working point has an efficiency of 40% (30%) for one- (three-)prong $\tau_{\text{had}}$ decays. Electrons that are reconstructed as one-prong $\tau_{\text{had}}$ candidates are removed using a BDT with the rejection factor against electrons reconstructed as $\tau_{\text{had}}$ around 3 and the efficiency for real $\tau_{\text{had}}$ candidates around 95%. Any $\tau_{\text{had}}$ candidate that is also $b$-tagged is rejected.

### 6.1.4   Overlap Removal

To avoid double counting objects and to remove leptons likely from hadron decays, ambiguities are resolved with the following procedures. Muons are required to be separated by $\Delta R > \min(0.4, 0.04 + (10 \text{ GeV})/p_{\text{T},\mu})$ from any selected jets. If two electrons are closer than $\Delta R = 0.1$, only the one with the higher $p_{\text{T}}$ is considered. An electron lying within $\Delta R = 0.1$ of a selected muon is rejected. Any jets within $\Delta R = 0.3$ of a selected electron or a hadronically decaying $\tau$-lepton candidates are rejected. $\tau_{\text{had}}$ candidates are required to be separated by $\Delta R > 0.2$ from any selected electron or muon candidates.

## 6.2   Event Selection and Categorization

Six final states, termed channels, are analyzed (as shown in Figure 6.1). Certain channels are further split into categories to improve sensitivity. The selection criteria are orthogonal such that each event can only contribute to a single channel.

Events in channels containing at least two light leptons are required to have been selected by dilepton triggers. For the dielectron triggers the $p_{\text{T}}$ thresholds on the two electrons were 12 GeV in 2015, 17 GeV in 2016, and 24 GeV in 2017, while for the dimuon triggers the $p_{\text{T}}$ thresholds on the leading (sub-leading) muon were 18 GeV (8 GeV) in 2015, and 22 GeV (8 GeV) in 2016 and 2017. For the electron+muon triggers, the $p_{\text{T}}$ thresholds on the electron (muon) were 17 GeV (14 GeV) for all datasets. Events in the $1\ell + 2\tau_{\text{had}}$ channel are required to have been selected by a single-electron (single-muon) trigger with $p_{\text{T}} > 24$ (20) GeV in 2015, while for 2016 and 2017, the lepton $p_{\text{T}}$ threshold was raised to 26 GeV. Selected electrons or muons are required to match, with

$\Delta R < 0.15$, the corresponding leptons reconstructed by the trigger and to have a $p_{\mathrm{T}}$ exceeding the trigger $p_{\mathrm{T}}$ threshold by 1 GeV or 2 GeV (depending on the lepton trigger and data-taking conditions).

The trigger requirement has an efficiency of 80% to 99%, depending on the channel and the dataset, for signal events passing the final selections.

Table 6.2: Offline selection criteria applied to the channels. The common selection criteria for all channels are listed in the first line under the title "Common". Same-charge (opposite-charge) lepton pairs are also referred to as same-sign (opposite-sign) with abbreviation SS (OS). Same-flavor (SF), OS lepton pairs are referred to as SFOS pairs. In the categories for conversions the selection requirements on one of the leptons are loosened as discussed in Section 6.1.

| Channel | Selection criteria |
|---|---|
| Common | $N_{\mathrm{jets}} \geq 2$ and $N_{b-\mathrm{jets}} \geq 1$ |
| $2\ell$SS | Two SS very tight (T*) leptons, $p_{\mathrm{T}} > 20$ GeV |
| | No $\tau_{\mathrm{had}}$ candidates |
| | $m(\ell\ell) > 12$ GeV |
| | **13 categories**: enriched with $t\bar{t}H$ , $t\bar{t}W$ , $t\bar{t}$ , mat. conv, int. conv., |
| | split by lepton flavor, charge, jet and $b$-jet multiplicity |
| $3\ell$ | Three loose (L) leptons with $p_{\mathrm{T}} > 10$ GeV; sum of light-lepton charges $= \pm 1$ |
| | Two SS very tight (T*) leptons, $p_{\mathrm{T}} > 15$ GeV |
| | One OS (w.r.t the SS pair) loose-isolated (L*) lepton, $p_{\mathrm{T}} > 10$ GeV |
| | No $\tau_{\mathrm{had}}$ candidates |
| | $m(\ell^+\ell^-) > 12$ GeV and $|m(\ell^+\ell^-) - 91.2\,\mathrm{GeV}| > 10$ GeV for all SFOS pairs |
| | $|m(3\ell) - 91.2\,\mathrm{GeV}| > 10$ GeV |
| | **7 categories**: enriched with $t\bar{t}H$ , $t\bar{t}W$ , $t\bar{t}Z$ , $VV$ , $t\bar{t}$ , mat. conv, int. conv |
| $4\ell$ | Four loose-isolated (L*) leptons; sum of light lepton charges $= 0$ |
| | $m(\ell^+\ell^-) > 12$ GeV and $|m(\ell^+\ell^-) - 91.2\,\mathrm{GeV}| > 10$ GeV for all SFOS pairs |
| | $m(4\ell) < 115$ GeV or $m(4\ell) > 130$ GeV |
| | **2 categories**: Zenr ($Z$-enriched;1 or 2 SFOS pairs) or Zdep ($Z$-depleted; 0 SFOS pairs) |
| $1\ell+2\tau_{\mathrm{had}}$ | One tight (T) lepton, $p_{\mathrm{T}} > 27$ GeV |
| | Two OS $\tau_{\mathrm{had}}$ candidates |
| | At least one tight $\tau_{\mathrm{had}}$ candidate |
| | $N_{\mathrm{jets}} \geq 3$ |
| $2\ell$SS+$1\tau_{\mathrm{had}}$ | $2\ell$SS selection, except: One medium $\tau_{\mathrm{had}}$ candidate |
| | $N_{\mathrm{jets}} \geq 4$ |
| $3\ell+1\tau_{\mathrm{had}}$ | $3\ell$ selection, except: |
| | One medium $\tau_{\mathrm{had}}$ candidate, of opposite charge to the total charge of the light leptons |
| | Two SS tight (T) leptons |

The selection requirements for each channel are summarized in Table 6.2, and Table 6.3 shows the basic characteristics and strategies of the six analysis channels. The separation of the $t\bar{t}H$ signal from the background is achieved using multivariate techniques in the $2\ell$SS , $3\ell$ and $1\ell+2\tau_{\mathrm{had}}$ channels, and additional selection criteria in the $4\ell$ channel. No further event selection is applied in the

Table 6.3: Summary of basic characteristics and strategies of the six analysis channels. In lepton selection, $T$ stands for Tight lepton definition as defined in Tables 6.1, $L$ stands for Loose lepton definition, and $L^*$ stands for Loose lepton definition with an additional requirement to pass "Fixed-CutLoose" isolation. For the fake lepton and $\tau_{\text{had}}$ background estimations, $DD$ means data-driven, from which $TF$ is the template fit method and $SF$ refers to the fake scale factor method.

| | Non-tau channels | | | Tau channels | | |
|---|---|---|---|---|---|---|
| | $2\ell$SS | $3\ell$ | $4\ell$ | $1\ell+2\tau_{\text{had}}$ | $2\ell$SS+$1\tau_{\text{had}}$ | $3\ell+1\tau_{\text{had}}$ |
| Light lepton | 2T* | 1L*, 2T* | 4L* | 1L* | 2T* | 1L*, 2T |
| $\tau_{\text{had}}$ | 0M | 0M | - | $\geq$1T | 1M | 1M |
| $N_{\text{jets}}$ , $N_{b-\text{jets}}$ | $\geq 2, \geq 1$ | $\geq 2, \geq 1$ | $\geq 2, \geq 1$ | $\geq 3, \geq 1$ | $\geq 4, \geq 1$ | $\geq 2, \geq 1$ |
| Non-prompt lepton strategy | semi-DD | semi-DD | semi-DD | MC | semi-DD | MC |
| | (TF) | (TF) | (SF) | | (TF) | |
| Fake tau strategy | – | – | – | DD | semi-DD | semi-DD |
| | | | | (SS data) | (SF) | (SF) |
| BDT trained against | Fakes and $t\bar{t}V$ | $t\bar{t}$ , $t\bar{t}W$ , $t\bar{t}Z$ , VV | $t\bar{t}Z$ / - | $t\bar{t}$ | - | - |
| Discriminant in SRs | 2D BDT | 5D BDT | Event count | BDT | Event count | Event count |
| Number of bins in SRs | 3 / 3 | 3 | 1 / 1 | 3 | 1 | 1 |
| Number of CRs | 11 | 6 | - | - | - | - |

$2\ell$SS+$1\tau_{\text{had}}$ and $3\ell+1\tau_{\text{had}}$ channels. The categories used in $2\ell$SS and $3\ell$ are shown in Figure 6.5 and
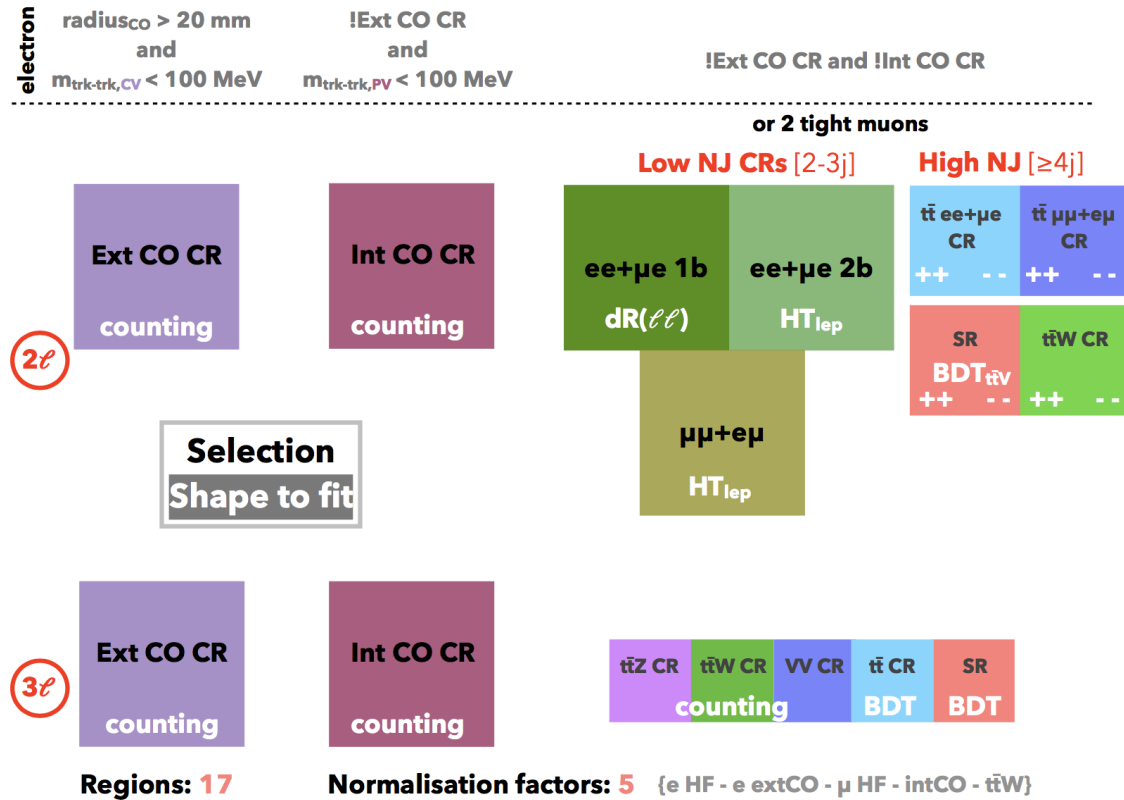


Figure 6.5: Categories in the $2\ell$SS and $3\ell$ channels.

will be discussed later in details in Section 6.2.1 and Section 6.2.2 correspondingly. Further details about how some of these categories are used to estimate the background (also denoted as "control regions") are provided in Section 6.3. Section 6.5 discusses the distributions exploited by the fit in each category. The TMVA package [108] is used to train BDTs in the $2\ell$SS and $1\ell+2\tau_{\text{had}}$ channels, while XGBoost [169] is used in the $3\ell$ channel. Depending on the channels, between 7 and 26 variables are used as inputs to the BDTs. In total, 877 events are selected in the data, distributed over the 25 event categories considered in the analysis. Different categories have signal-to-background ($S/B$) ratios ranging from 0.3% to 104%, as shown in Figure 6.6. The total expected number of reconstructed SM $t\bar{t}H$ events summed over all categories is 170, corresponding to 0.42% of all produced $t\bar{t}H$ events.
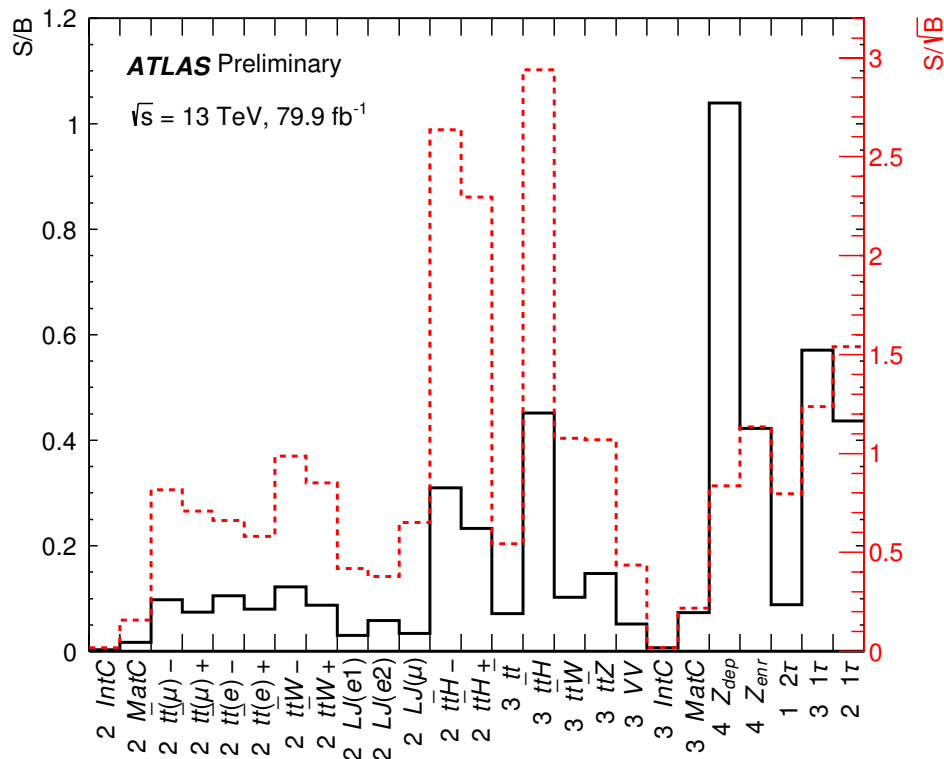


Figure 6.6: Pre-fit $S/B$ (black line) and $S/\sqrt{B}$ (red dashed line) ratios for each analysis category. The background prediction methods are described in Section 6.3.

### 6.2.1 $2\ell$SS Channel

#### 6.2.1.1 Multivariate Analysis

In the region with four or more jets (denoted as pre-MVA region), BDTs are used to categorize events as well as to increase separation between signal and backgrounds. Two independent BDTs are trained: one to separate $t\bar{t}H$ from $t\bar{t}$ (i.e. non-prompt background), denoted as $t\bar{t}$ BDT, and the other denoted as $t\bar{t}V$ BDT which is used to separate $t\bar{t}H$ from $t\bar{t}V$ (dominated by $t\bar{t}W$ ). Both BDTs include the same nine input variables:

- Number of jets, $N_{jets}$;

- Number of $b$-jets, $N_{b-jets}$;

- Leptonic flavor,$ee$, $e\mu$, $\mu e$ and $\mu\mu$ where the first lepton corresponds to the one with the larger $p_T$;

- Distance between the leading lepton and its closest jet, $\Delta R(\ell_0, j)$;

- Distance between the sub-leading lepton and its closest jet, $\Delta R(\ell_1, j)$;

- Maximum between lepton $|\eta_{\ell_0}|$ and $|\eta_{\ell_1}|$, $\text{Max}(|\eta_\ell|)$;

- Sub-leading lepton $p_T$, $p_T(\ell_1)$;

- $E_T^{\text{miss}}$ ;

- Distance between the two same-sign leptons, $\Delta R(\ell_0, \ell_1)$.

The input variables that have the highest separation power are $N_{jets}$, $\Delta R(\ell_0, jet)$ and $p_T(\ell_1)$ for $t\bar{t}$ BDT, and $N_{jets}$, $\Delta R(\ell_0, j)$, and $\Delta R(\ell_1, j)$ for $t\bar{t}V$ BDT. Figure 6.7 shows the distributions of the nine input variables for data and signal-plus-background prediction in the pre-MVA region, where fakes, $t\bar{t}W$, and internal conversions have been scaled with the measured NFs from the template fit (see Section 6.3).

A good data modeling can be observed in all distributions.

Both $t\bar{t}V$ and $t\bar{t}$ BDT trainings use simulation inputs scaled by the template-fit NFs. Distributions of signal and background BDT response for training and test are shown in Figure 6.8. A better signal-to-background separation is obtained for $t\bar{t}$ BDT compared to $t\bar{t}V$ BDT, as the result of the more distinguished kinematics between $t\bar{t}$ and $t\bar{t}H$ compared to that between $t\bar{t}V$ and $t\bar{t}H$ . The good agreement between the training sample and the test sample demonstrates that there is no apparent over-training. Figure 6.9 shows the post-fit distributions of the two output BDTs for data and signal-plus-background prediction. A fairly good data modeling is observed for the two BDT outputs.
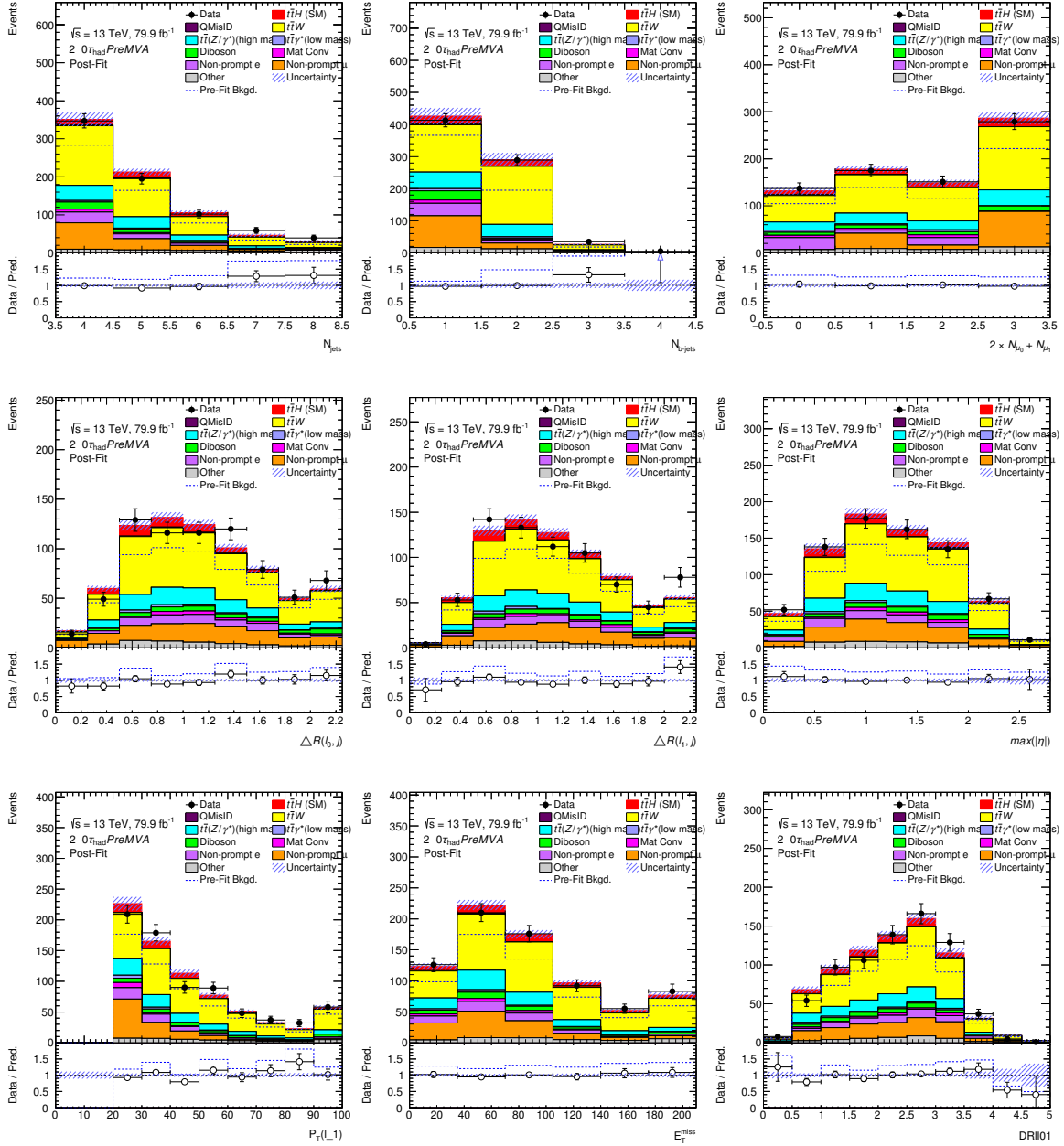
Figure 6.7: Distributions of 9 input variables for the BDTs in the $2\ell$SS channel. The background contributions after the likelihood fit ("Post-Fit") are shown as filled histograms. The total signal-plus-background prediction before the fit ("Pre-Fit") is shown as a dashed blue histogram. The $t\bar{t}H$ signal, scaled according to the results of the fit, is shown as a filled red histogram added to the post-fit background. The size of the combined statistical and systematic uncertainty in the signal-plus-background prediction is indicated by the blue hatched band. The ratios of the data to the total post-fit predictions are shown in the lower panel. The last bin in each figure contains the overflow.
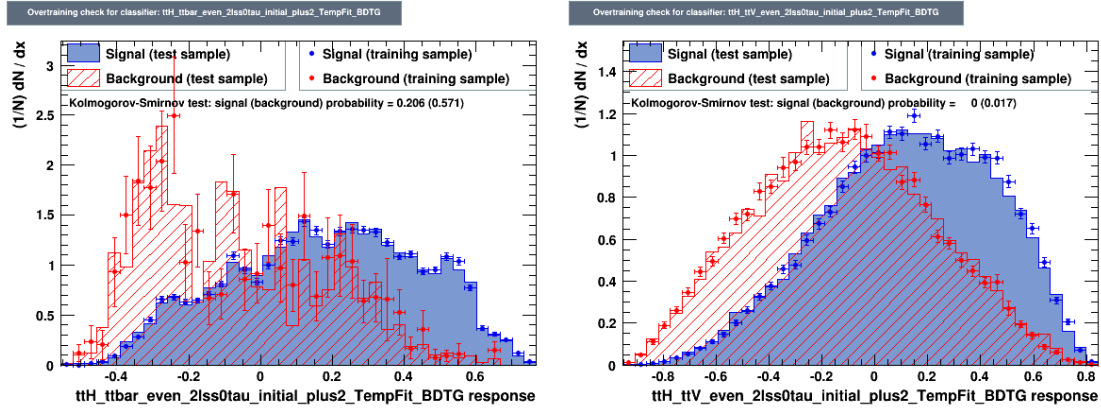
Figure 6.8: Distribution of the $t\bar{t}$ BDT response (left) and the $t\bar{t}V$ BDT response (right) in the $2\ell$SS channel.
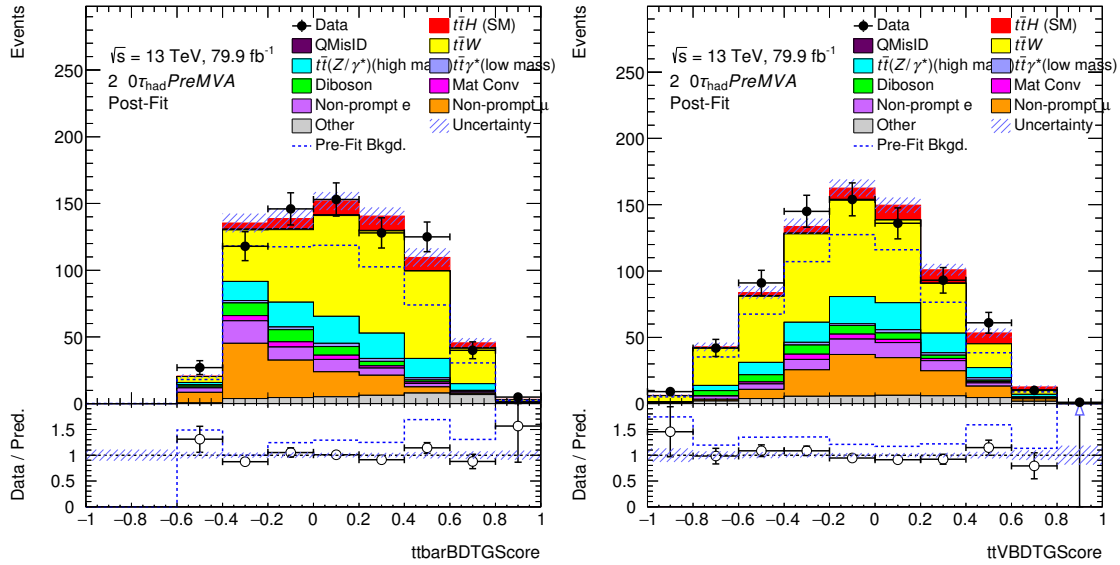


Figure 6.9: Distributions of the two separate BDTs trained to separate $t\bar{t}V$ and $t\bar{t}$ background from $t\bar{t}H$. The background contributions after the likelihood fit ("Post-Fit") are shown as filled histograms. The total signal-plus-background prediction before the fit ("Pre-Fit") is shown as a dashed blue histogram. The $t\bar{t}H$ signal, scaled according to the results of the fit, is shown as a filled red histogram added to the post-fit background. The size of the combined statistical and systematic uncertainty in the signal-plus-background prediction is indicated by the blue hatched band. The ratios of the data to the total post-fit predictions are shown in the lower panel. The last bin in each figure contains the overflow.

## 6.2.1.2 Categorization

In total, there are 13 categories in the $2\ell$SS channel (as shown in Figure 6.5). Five event categories are defined for the background determination. Two of these categories are defined by requiring the presence of an electron from either an internal conversion ($2\ell$IntC ) or a material conversion ($2\ell$MatC ) as defined in Section 6.1. The remaining three categories are required to contain either two or three reconstructed jets and are referred to as "low jet multiplicity (LJ)" categories. Events in these three categories are grouped according to the flavor of the sub-leading lepton as ee+$\mu$e and e$\mu$+$\mu\mu$, and those with a sub-leading electron are split into those containing one or two $b$-jets ($2\ell$LJ($e1$), $2\ell$LJ($e2$), and $2\ell$LJ($\mu$)). The categorization according to the flavor of the sub-leading lepton is motivated by the fact that this lepton is more likely to be non-prompt.

For events with four or more jets, a categorization procedure has been developed in order to maximize the discrimination against the $t\bar{t}W$ and $t\bar{t}$ background in the two dimensional BDT plane. Figure 6.10 shows the $t\bar{t}$, $t\bar{t}W$ and $t\bar{t}H$ events distributed in the two dimensional BDT plane, separately for ee+e$\mu$ (with electron being most likely a fake) and e$\mu$+$\mu\mu$ (where muon is most likely a fake). Categories enriched in $t\bar{t}H$, $t\bar{t}W$ and $t\bar{t}$ events are defined by two dimensional cuts on the BDT outputs. The $t\bar{t}$ category is split according to the flavor of the sub-leading leptons. Events in pre-MVA region are further split into categories according to the lepton charge to exploit the charge asymmetry of the $t\bar{t}W$ background. This results in six additional background categories ($2\ell$ttW+, $2\ell$ttW−, $2\ell$tt($e$)+, $2\ell$tt($e$)−, $2\ell$tt($\mu$)+, and $2\ell$tt($\mu$)−) and two categories for the signal
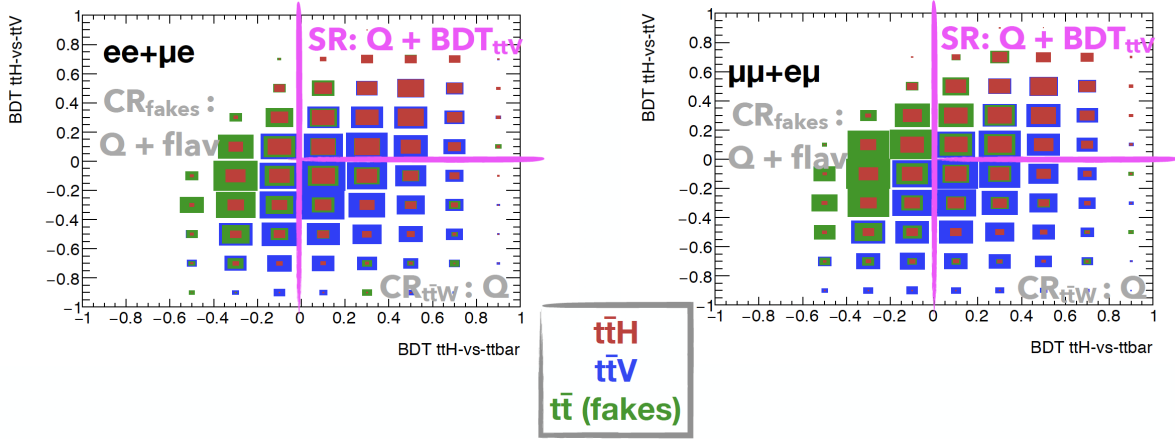


Figure 6.10: Fit categories in the pre-MVA $2\ell$SS region defined in the 2-dimensional space formed by the BDT ($t\bar{t}H$ vs $t\bar{t}V$) in the y-axis and the BDT ($t\bar{t}H$ vs $t\bar{t}$) in the x-axis. Signal-depleted regions are marked as "CR" and signal-enriched regions are marked as "SR". Only the $t\bar{t}$ CR is split in lepton flavors (flav), as shown in the plot. All regions are split in terms of the total charge of the event into "++" and "−−" (Q). The distribution of $t\bar{t}H$ (red), $t\bar{t}V$ (blue) and $t\bar{t}$ (green) MC events in these categories is shown.

(2ℓttH+, 2ℓttH−). These eight categories are referred to as "high jet multiplicity (HJ)" categories.

## 6.2.2   $3\ell$ **Channel**

The $3\ell$ channel uses a five-dimensional multinomial BDT with the following five classification targets: $t\bar{t}H$ , $t\bar{t}W$, $t\bar{t}Z$, $t\bar{t}$ and diboson. In total, the following 26 variables are used based on topological aspects of the events:

- Number of $b$-jets, $n_b$;

- Number of jets, $n_j$;

- Transverse momentum of the leptons: $p_T^{\ell_0}$, $p_T^{\ell_1}$ and $p_T^{\ell_2}$;

- Transverse momentum of the leading $b$-jet: $p_T^{b_0}$;

- Minimum angular separation between the leptons and the nearest jet (light or heavy flavor), $\min(\Delta R(\ell_0, j)$, $\min(\Delta R(\ell_1, j)$ and $\min(\Delta R(\ell_2, j)$ and the minimum of all leptons and all light jets, $\min(\Delta R(\ell, j)$;

- Minimum angular separation between the leptons and the nearest $b$-jet, $\min(\Delta R(\ell_0, b)$, $\min(\Delta R(\ell_1, b)$ and $\min(\Delta R(\ell_2, b)$;

- Angular separation between lepton pairs: $\Delta R(\ell_0, \ell_1)$ and $\Delta R(\ell_0, \ell_2)$;

- Scalar sum of the transverse momentum of the jets: $H_T^{\text{jets}}$;

- Invariant mass of the leptons, $m_{\ell_0\ell_1\ell_2}$ and the lepton pairs: $m_{\ell_1\ell_2}$, $m_{\ell_0\ell_1}$ and $m_{\ell_0\ell_2}$;

- Flavor and charge of the leptons: $\text{id}(\ell_0)$, $\text{id}(\ell_1)$ and $\text{id}(\ell_2)$;

- Transverse momentum of the sub-leading jet, $p_T^{j_1}$;

- Azimuthal separation between the leading jet and the transverse missing energy, $\Delta\phi(j_0, MET)$;

- Angular separation between the opposite sign lepton and the leading jet, $\Delta R(\ell_0, j_0)$.

Figure 6.11 shows the modeling of the six highest ranked input variables for all events passing the pre-selection. Overall, good agreement is observed.
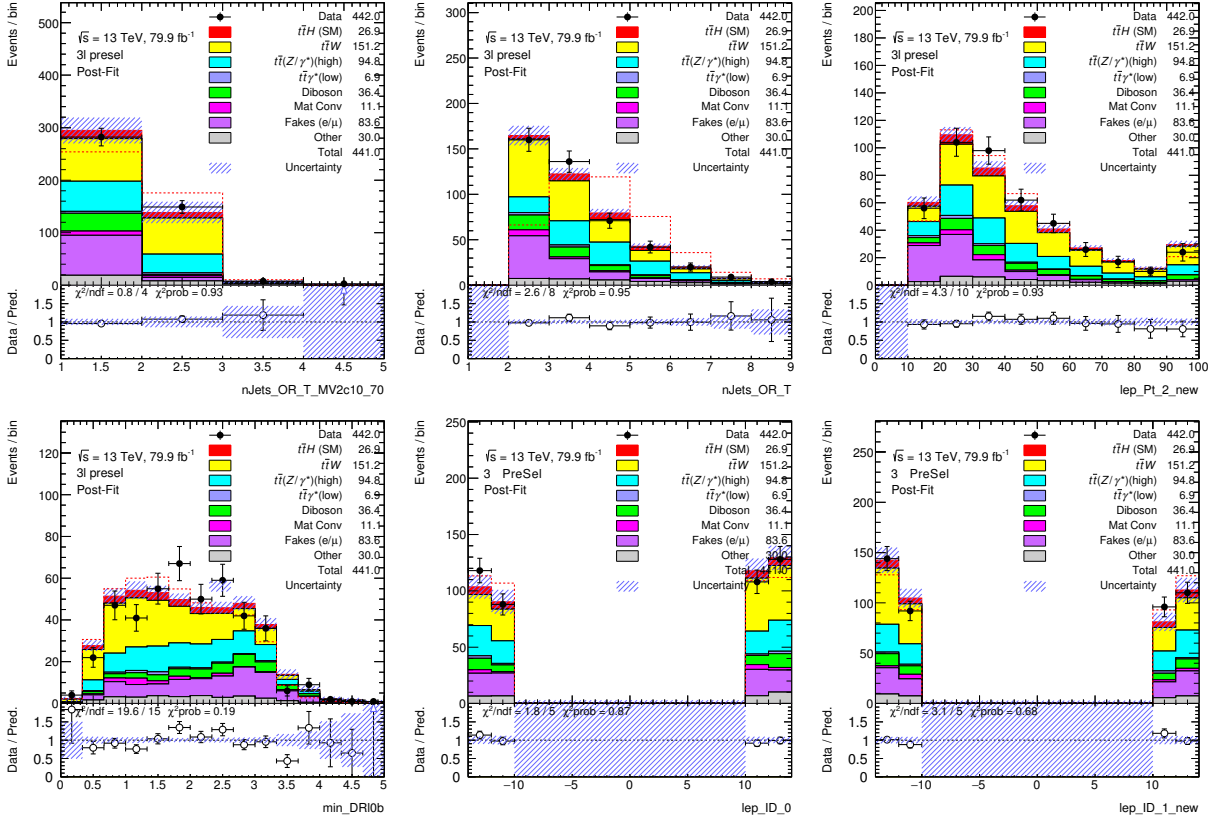
Figure 6.11: Comparison of the highly ranked six variables used in the training of the $3\ell$ multiclass BDT between data and prediction for all events passing the BDT pre-selection. The background contributions after the likelihood fit ("Post-Fit") are shown as filled histograms. The $t\bar{t}H$ signal, scaled to total background yield, is shown as a dashed red histogram. The $t\bar{t}H$ signal, scaled according to the results of the fit, is shown as a filled red histogram added to the post-fit background. The size of the combined statistical and systematic uncertainty in the signal-plus-background prediction is indicated by the blue hatched band. The ratios of the data to the total post-fit predictions are shown in the lower panel. The last bin in each figure contains the overflow.

A simultaneous training of a multi-class $BDT$ of $t\bar{t}H$ signal against the dominant backgrounds ($t\bar{t}W$, $t\bar{t}Z$, $t\bar{t}$ and diboson) is performed. The procedure, illustrated in Figure 6.12, is as follows:

The original set of MC samples is split into 10 folds. An iterative process taking always 9 out of the 10 folds forms consecutively 10 sub-samples. Each sub-sample then uses cross-validation[170] to esimate the optimal number and is split into 10 sub-folds with 10 BDTs trained always leaving 1 of the 10 sub-folds out. At the end, 100 BDTs are trained and averaged, and for each BDT, the training samples are uniquely defined. In this way one can avoid over-training.

A 5 dimensional multi-class discriminant is formed with 5 different BDT scores for different classes. Figure 6.13 shows the modeling of the 5 BDTs. These 5 BDTs classify events into 5
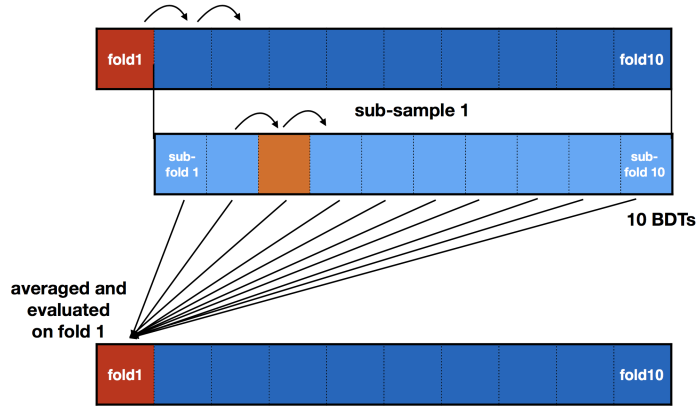
Figure 6.12: Illustration of the $3\ell$ BDT training procedure.
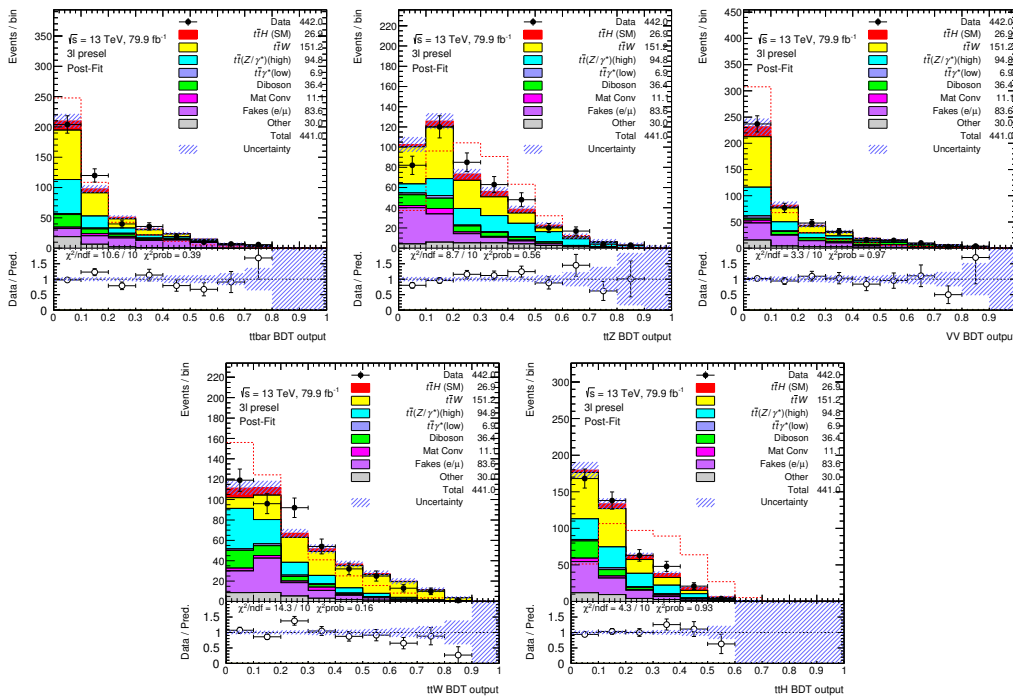


Figure 6.13: Comparison of the five BDT output scores of the $3\ell$ multiclass BDT between data and prediction for all events passing the BDT pre-selection. The background contributions after the likelihood fit ("Post-Fit") are shown as filled histograms. The $t\bar{t}H$ signal, scaled to total background yield, is shown as a dashed red histogram. The $t\bar{t}H$ signal, scaled according to the results of the fit, is shown as a filled red histogram added to the post-fit background. The size of the combined statistical and systematic uncertainty in the signal-plus-background prediction is indicated by the blue hatched band. The ratios of the data to the total post-fit predictions are shown in the lower panel. The last bin in each figure contains the overflow.

categories (3ℓttH, 3ℓttW, 3ℓttZ, 3ℓtt, and 3ℓVV) in which each of the trained processes has the highest purity (the "rest" category is merged with 3ℓtt due to similarity in composition). The result of categorization is presented in Figure 6.14. As for the 2ℓSS channel, two additional categories are defined for conversions (3ℓIntC and 3ℓMatC) by loosening the requirements on one electron following Section 6.1. In total seven categories are defined.
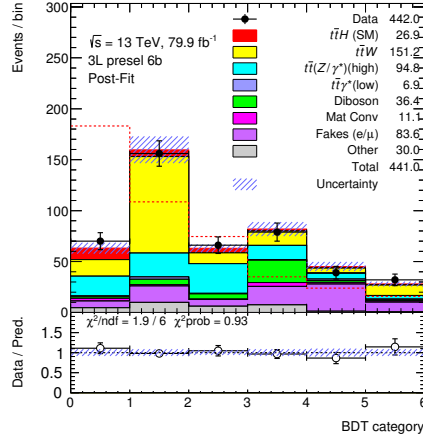


Figure 6.14: The category distribution in the $3\ell$ pre-selection region. The background contributions after the likelihood fit ("Post-Fit") are shown as filled histograms. The $t\bar{t}H$ signal, scaled to total background yield, is shown as a dashed red histogram. The $t\bar{t}H$ signal, scaled according to the results of the fit, is shown as a filled red histogram added to the post-fit background. The size of the combined statistical and systematic uncertainty in the signal-plus-background prediction is indicated by the blue hatched band. The ratios of the data to the total post-fit predictions are shown in the lower panel.

## 6.3  Background Estimation

Backgrounds are categorized into irreducible and reducible backgrounds.

Irreducible backgrounds (Section 6.3.1) have all selected leptons as prompt, i.e. produced in the $W/Z$ boson decays, in the $\tau$-lepton leptonic decays, or the internal conversions. Reducible backgrounds have prompt leptons with mis-assigned charge (labeled as "Q-MisID"), at least one non-prompt light lepton (Section 6.3.2.2), or jets misidentified as $\tau_\mathrm{had}$ candidates (fake $\tau_\mathrm{had}$). The Q-MisID and fake $\tau_\mathrm{had}$ backgrounds are estimated using data-driven techniques, and the $t\bar{t}W$ and non-prompt-lepton backgrounds are estimated with the template fit method (discussed in Section 5.2.2.2) where NFs of those processes are determined simultaneously with the $t\bar{t}H$ cross section by performing a likelihood fit to the data across all categories. All other backgrounds are estimated using the simulation.

The fractional contributions of various backgrounds to the predicted total background in each of the categories described in Section 6.2 are shown in Figure 6.15.
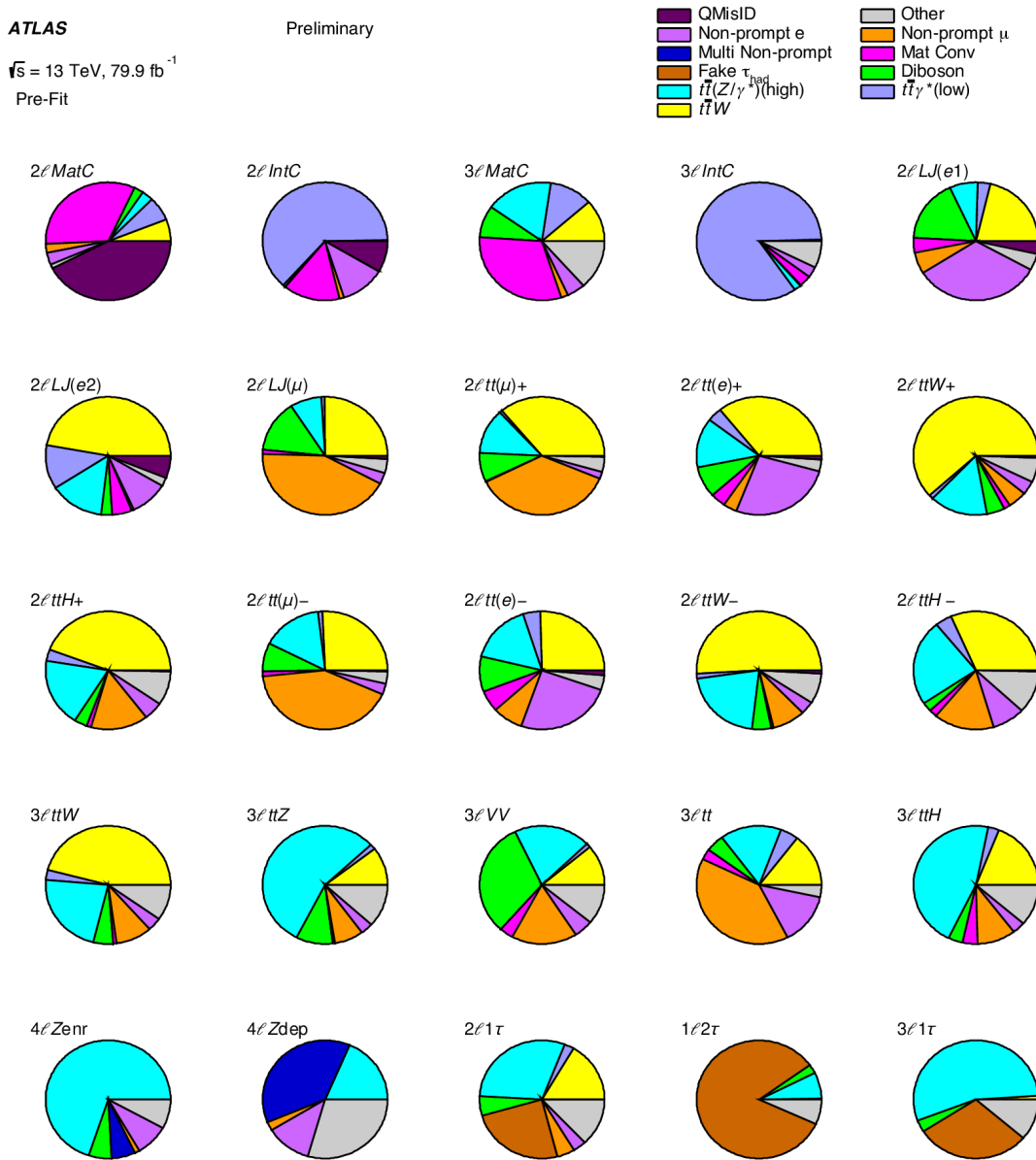


Figure 6.15: The fractional contributions of the various backgrounds to the total predicted background in each of the 25 event categories. The background estimation methods are described in Section 6.3. "Non-prompt $(e/\mu)$", "Mat Conv", and "QMisID" refer to the data-driven background estimates (largely $t\bar{t}$ but also include other electroweak processes), and rare processes ($tZ$, $tWZ$, $t\bar{t}WW$, $VVV$, $t\bar{t}t$, $t\bar{t}t\bar{t}$, and $tH$) are labelled as "Other".

### 6.3.1 Irreducible Backgrounds

Background contributions with prompt leptons originate from a wide range of physics processes with the relative importance of individual processes varying by channel. The main irreducible backgrounds originate from $t\bar{t}W$ and $t\bar{t}Z/\gamma^*$ production, followed by $VV$ (in particular $W^\pm Z$ ) production, and have final states and kinematic properties similar to the $t\bar{t}H$ signal. Smaller contributions originate from the following rare processes: $tZ$, $tWZ$, $t\bar{t}WW$, $VVV$, $t\bar{t}t$, and $t\bar{t}t\bar{t}$ production. The associated production of single top quarks with a Higgs boson, $tH$, contributes at most 2% in any signal region and other Higgs boson production mechanisms contribute negligibly ($<0.2\%$) in any signal region; therefore, they are treated as background processes and fixed to the SM predictions. Backgrounds with prompt leptons are estimated from simulation using the samples described in Section 5.1.

#### 6.3.1.1 $t\bar{t}W$ Background

The $t\bar{t}W$ background represents the dominant background particularly in the $2\ell$SS and $3\ell$ channels across multiple event categories, which span a wide range of kinematic regimes. Despite the use of the state-of-art simulations, the accurate modeling of additional QCD radiation in $t\bar{t}W$ production remains challenging. Categories sensitive to the $t\bar{t}W$ background have been introduced to the analysis to study and constrain this background. The jet multiplicity distributions in the $2\ell$SS and $3\ell$ channels after event selection are shown in Figure 6.16. Disagreements between the data and the total signal-plus-background prediction before the fit (denoted as 'Pre-Fit' prediction) from the simulation are observed. To minimize the dependence of the $t\bar{t}H$ signal extraction on the $t\bar{t}W$ prediction and to allow changes of kinematic behaviors in different channels and different jet multiplicity regions, three independent NFs for the $t\bar{t}W$ background are considered in the template fit: two corresponding to the LJ and HJ categories of the $2\ell$SS channel, and one corresponding to the $3\ell$ channel categories. The measured NFs are: $\hat{\lambda}_{t\bar{t}W}^{2\ell LJ} = 1.56_{-0.28}^{+0.30}$, $\hat{\lambda}_{t\bar{t}W}^{2\ell HJ} = 1.26_{-0.18}^{+0.19}$, and $\hat{\lambda}_{t\bar{t}W}^{3\ell} = 1.68_{-0.28}^{+0.30}$. The agreement between data and the expectation is improved after the application of the background corrections resulting from the template fit, particularly with the above $t\bar{t}W$ NFs. Additional uncertainties associated with the modeling of the $b$-jet multiplicity and $W$-boson charge asymmetry in the $t\bar{t}W$ background are introduced to account for observed discrepancies in the shape of these distributions between data and pre-fit background predictions in the $2\ell$SS and $3\ell$ channels (see Figure 6.17). The $W$-boson charge asymmetry is studied via the distribution of the sign of the sum of lepton charges (referred to as "total charge"). These uncertainties are constructed to affect only the shape of the $b$-jet multiplicity and total charge distributions, thus preserving the normalization of the $t\bar{t}W$ background after event selection. The uncertainty associated with the modeling of the $b$-jet multiplicity distribution is $\pm 25\%$ ($\mp 35\%$) for events with
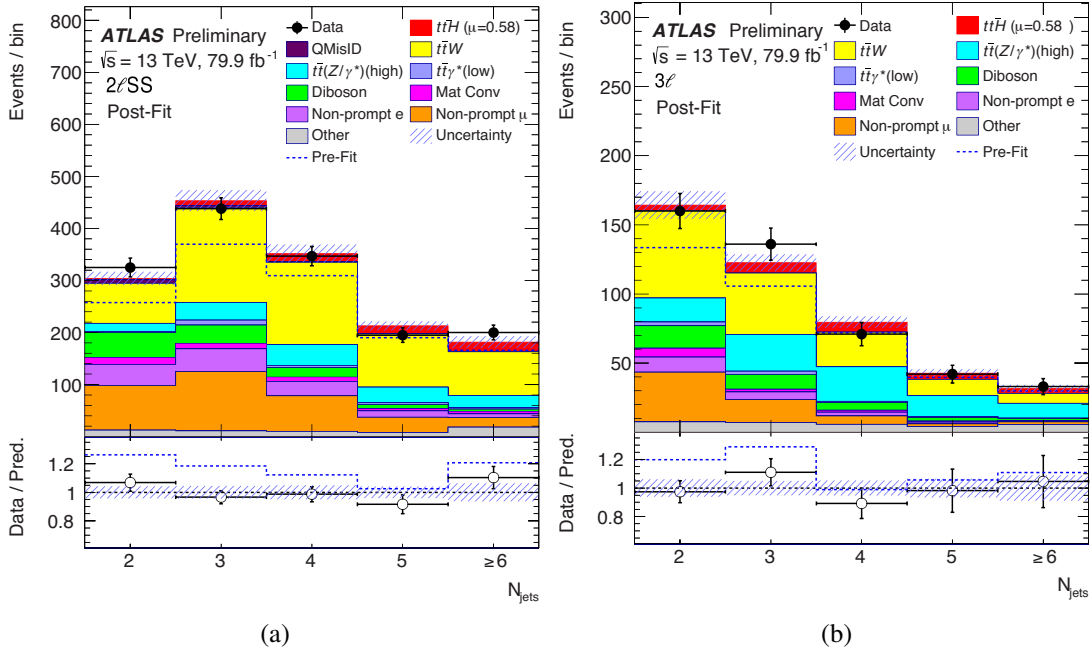
Figure 6.16: Comparison between data and signal-plus-background prediction for the distribution of jet multiplicity in (a) the $2\ell$SS channel and (b) the $3\ell$ channel after event selection and before further event categorization (see Section 6.2). The background contributions after the likelihood fit ("Post-Fit") are shown as filled histograms. The total signal-plus-background prediction before the fit ("Pre-Fit") is shown as a dashed blue histogram. The $t\bar{t}H$ signal, scaled according to the results of the fit, is shown as a filled red histogram added to the post-fit background. The size of the combined statistical and systematic uncertainty in the signal-plus-background prediction is indicated by the blue hatched band. The ratios of the data to the total pre- and post-fit predictions are shown in the lower panel. The last bin in each figure contains the overflow.

exactly one (at least two) $b$-jets. The uncertainty associated with the modeling of the total charge distribution is $\pm 20\%$ ($\mp 35\%$) for events with positive (negative) total charge. These additional uncertainties are treated as uncorrelated between the $2\ell$SS and $3\ell$ channels and are referred to as "extrapolation" uncertainties. In total, there are 41 uncertainties that are included in the statistical model to describe the $t\bar{t}W$ background. Further details of the impact of the $t\bar{t}W$ model is provided in Section 6.5.

### 6.3.1.2 Other Irreducible Backgrounds

The total yields in the $3\ell$ttZ and $3\ell$VV control regions are used in the likelihood fit to improve the estimation of the background contribution from the $t\bar{t}Z/\gamma^*$ and $VV$ processes. The rate of the background from internal conversions with $m(e^+e^-) < 1$ GeV is estimated using the two dedicated control regions ($2\ell$IntC and $3\ell$IntC). The total yield in each category is used in the likelihood fit
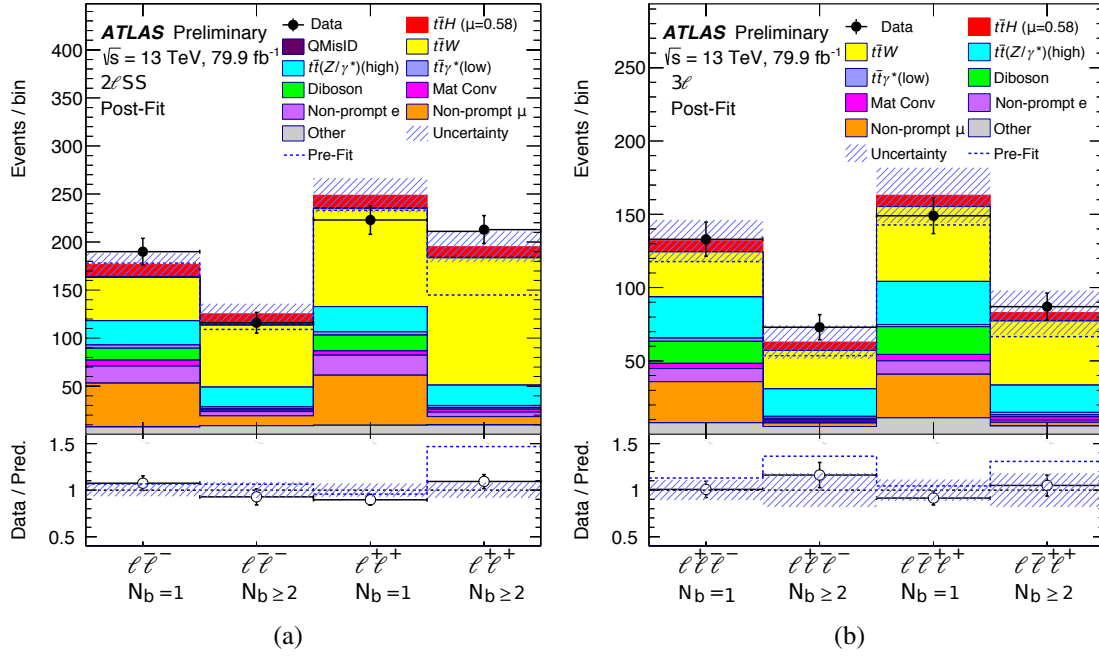
Figure 6.17: Comparison between data and signal-plus-background prediction for the event yields in (a) the $2\ell$SS channel and (b) the $3\ell$ channel after event selection and before further event categorization (see Section 6.2), split in four separate categories depending on the total charge and $b$-jet multiplicity. The background contributions after the likelihood fit ("Post-Fit") are shown as filled histograms. The total signal-plus-background prediction before the fit ("Pre-Fit") is shown as a dashed blue histogram. The $t\bar{t}H$ signal, scaled according to the results of the fit, is shown as a filled red histogram added to the post-fit background. The size of the combined statistical and systematic uncertainty in the signal-plus-background prediction is indicated by the blue hatched band. The ratios of the data to the total pre- and post-fit predictions are shown in the lower panel. The last bin in each figure contains the overflow.

to determine the following NF: $\hat{\lambda}_e^{\mathrm{IntC}} = 0.83 \pm 0.32$, where the uncertainty is dominated by the statistical uncertainty. As described in Section 5.3.2.2, a 25% systematic uncertainty is assigned to internal conversions based the level of agreement found between observed and predicted yields in $Z \to \mu^+\mu^-\gamma^*(\to e^+e^-)$ region (see first bin of distribution in Figure 5.5), and is an uncertainty associated with the extrapolation of the estimation from the internal conversion control regions to the other event categories.

## 6.3.2 Reducible Backgrounds

### 6.3.2.1 Charge Misassignment

Backgrounds with leptons with the charge incorrectly assigned affect primarily the $2\ell$SS and $2\ell$SS+$1\tau_{\mathrm{had}}$ channels and predominantly arise from $t\bar{t}$ production. The data-driven method used to measure Q-MisID is introduced in Section 5.2.1. The charge misassignment rate is measured separately for the three types of tight electrons ('internal conversion', 'material conversion', and 'very tight') and parameterized as a function of electron $p_{\mathrm{T}}$ and $|\eta|$ as shown in Figure 6.18.
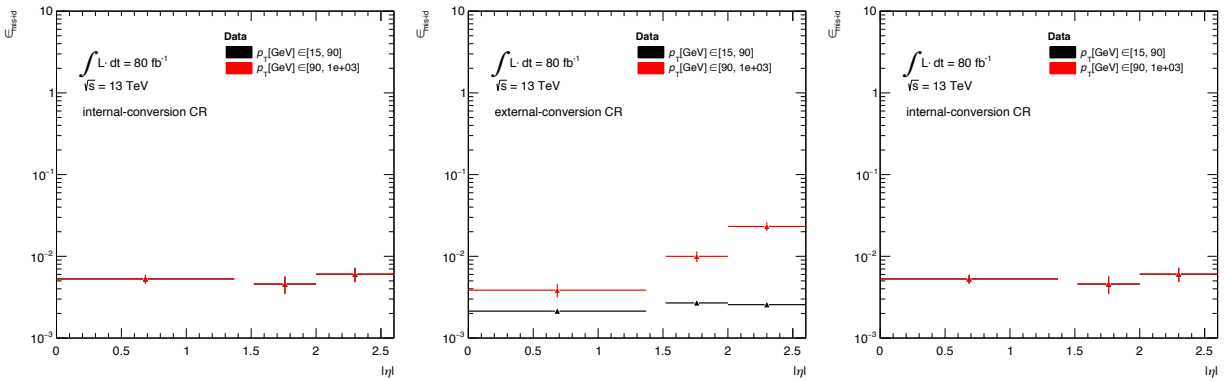


Figure 6.18: Electron charge-flip rates derived from the data with the likelihood method. The rates are presented as a function of $|\eta|$, parameterized in $p_{\mathrm{T}}$ for (a) internal conversion (b) external conversion and (c) very tight electrons.

The total systematic uncertainty in the charge misassignment background estimations for electrons based on the discription in Section 5.3.2.3 is about 30%, with the dominant contribution at low $p_{\mathrm{T}}$ originating from the closure tests and at high $p_{\mathrm{T}}$ from the statistical uncertainty.

### 6.3.2.2 Non-prompt Light Leptons

As discussed in Section 5.2.2, non-prompt leptons originate from material conversions, HF, or LF, with an admixture strongly depending on the lepton quality requirements and varying across event categories. The main contribution to the non-prompt-lepton background is from $t\bar{t}$ production, followed by much smaller contributions from $V$+jets and single-top-quark processes. This background is estimated with the template fit method, in the $2\ell$SS, $3\ell$ and $2\ell$SS+$1\tau_{\mathrm{had}}$ channels.

The non-prompt light leptons in the simulated $t\bar{t}$ sample are labeled according to whether they originate from HF or LF, or from a material conversion candidate (MatC). Simulated $t\bar{t}$ background events with a selected lepton with mismeasured charge are excluded because the Q-MisID background is estimated from data, as described in Section 6.3.2.1.

103

Several regions introduced in Section 6.2 are used to estimate the non-prompt lepton background. These control regions were designed to be enriched in specific processes, as shown in Figure 6.15. The $2\ell$MatC and $3\ell$MatC control regions are enriched in electrons from material conversions. There are eight control regions enriched in contributions from HF non-prompt leptons in $t\bar{t}$ events: seven in the $2\ell$SS channel and one in the $3\ell$ channel. Kinematic distributions are used in four control regions to optimize the sensitivity to the HF non-prompt electron and muon contributions. The distribution of the scalar sum of the lepton $p_T$ ($H_{\mathrm{T,\,lep}}$), which provides separation against $t\bar{t}W$ (see Figure 6.19c and 6.19b), is used in the $2\ell$LJ($\mu$) and $2\ell$LJ(e2) control regions. In the $2\ell$LJ(e1) control region, the $\Delta R(\ell, \ell)$ distribution is used as it provides separation against internal conversions (see Figure 6.19a), which are characterized by lower values of $\Delta R(\ell, \ell)$ since the virtual photon is usually radiated by one of the reconstructed leptons. The $3\ell$tt control region uses the output of the BDT corresponding to the $t\bar{t}$ category (see Figure 6.19d). The total event yield is used in all other control regions.

NFs for three non-prompt-lepton background contributions are estimated from the template fit method (see Section 5.2.2.2). The measured three NFs are: $\hat{\lambda}_e^{\mathrm{MatC}} = 1.61 \pm 0.48$ for material conversions, $\hat{\lambda}_e^{\mathrm{had}} = 1.12 \pm 0.38$ for HF non-prompt electrons , and $\hat{\lambda}_\mu^{\mathrm{had}} = 1.20 \pm 0.18$ for HF non-prompt muons, where the uncertainties are dominated by the statistical uncertainty.

The systematic uncertainties considered are discussed in the following, although they have a negligible impact on the final result. As described in Section 5.3.2.2, a shape uncertainty of up to 15% (6%) is assigned to the HF non-prompt electron (muon) background component from a comparison between data and simulation in the inverted isolation regions, and a 25% uncertainty on material conversions, derived using a $Z \to \mu^+\mu^-\gamma^*(\to e^+e^-)$ sample, is applied to all categories except for $2\ell$MatC and $3\ell$MatC acting as an extrapolation uncertainty. Besides, the uncertainty in the modeling of additional QCD radiation is assigned and assessed with two alternative samples generated with settings that increase or decrease the amount of radiation, because the background estimation procedure for non-prompt light leptons relies on the simulation to predict the kinematic distributions of the $t\bar{t}$ process. As the contribution from LF non-prompt leptons is small, about 10% percent of the contribution from HF non-prompt leptons, it is derived from the agreement between data and simulation in a LF enriched region at low values of the 'non-prompt lepton BDT'. The resulting uncertainty is 100%, and is taken to be uncorrelated between the categories enriched in internal and material conversions, and the rest of event categories. An additional uncertainty of 22% is assigned to the non-prompt light lepton background estimate in the $2\ell$SS+$1\tau_{\mathrm{had}}$ channel from the comparison with an alternative data-driven estimation based on the fake factor method [171]. Among the uncertainties associated with the non-prompt-lepton background estimation, the NF $\lambda_\mu^{\mathrm{had}}$ has the largest impact on the $t\bar{t}H$ cross section measurement.

Several studies were performed to validate the non-prompt-lepton background estimates and to
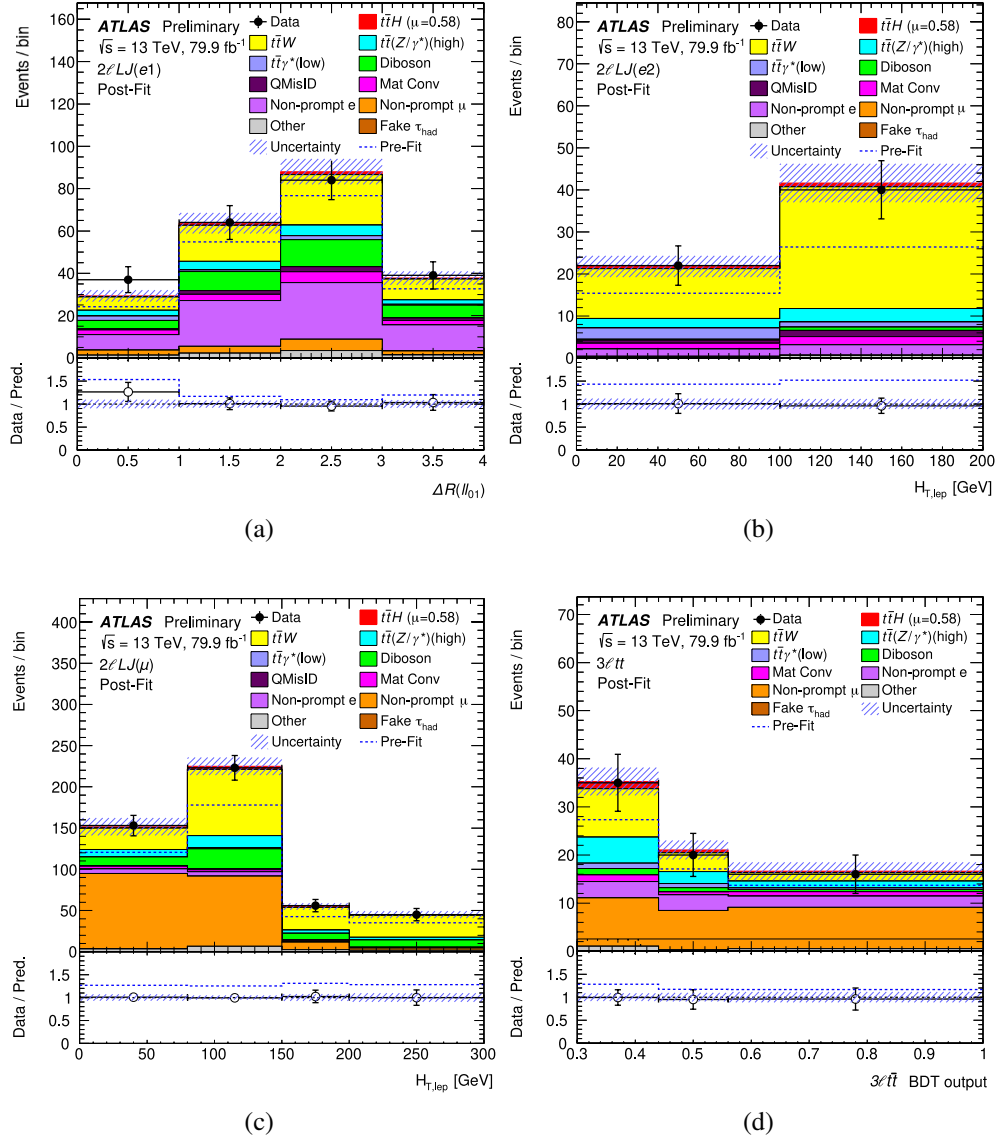
Figure 6.19: The distributions of the kinematic variables used in the four binned control regions: (a) $\Delta R(\ell, \ell)$ in the $2\ell$LJ(e1) control region, (b) scalar sum of the lepton $p_T$ ($H_{T,\,lep}$) in the $2\ell$LJ(e2) control region, (c) the scalar sum of the lepton $p_T$ ($H_{T,\,lep}$) in the $2\ell$SS $t\bar{t}$ control region at low jet multiplicity with a sub-leading muon, and (d) BDT score for the $t\bar{t}$ category in the $3\ell$tt control region. The background contributions after the likelihood fit ("Post-Fit") are shown as filled histograms. The total background before the fit ("Pre-Fit") is shown as a dashed blue histogram. The $t\bar{t}H$ ($t\bar{t}W$) signal, scaled according to the results of the fit, is shown as a filled red (yellow) histogram added to the post-fit background. The size of the combined statistical and systematic uncertainty in the total signal-plus-background prediction is indicated by the blue hatched band. The ratio of the data to the total post-fit prediction is shown in the lower panel. The last bin in each figure contains the overflow.

confirm that the data excess observed in several event categories is not because this background is mismodeled. In Section 6.5, it will be shown that this excess is assigned by the fit to $t\bar{t}W$-related fit parameters. A comparison of the data to the total predicted background was made in different event categories of the $2\ell$SS channel, split by the flavor of the sub-leading lepton, which has a higher probability to be non-prompt, and the $b$-jet multiplicity (see Figure 6.20a). There is good
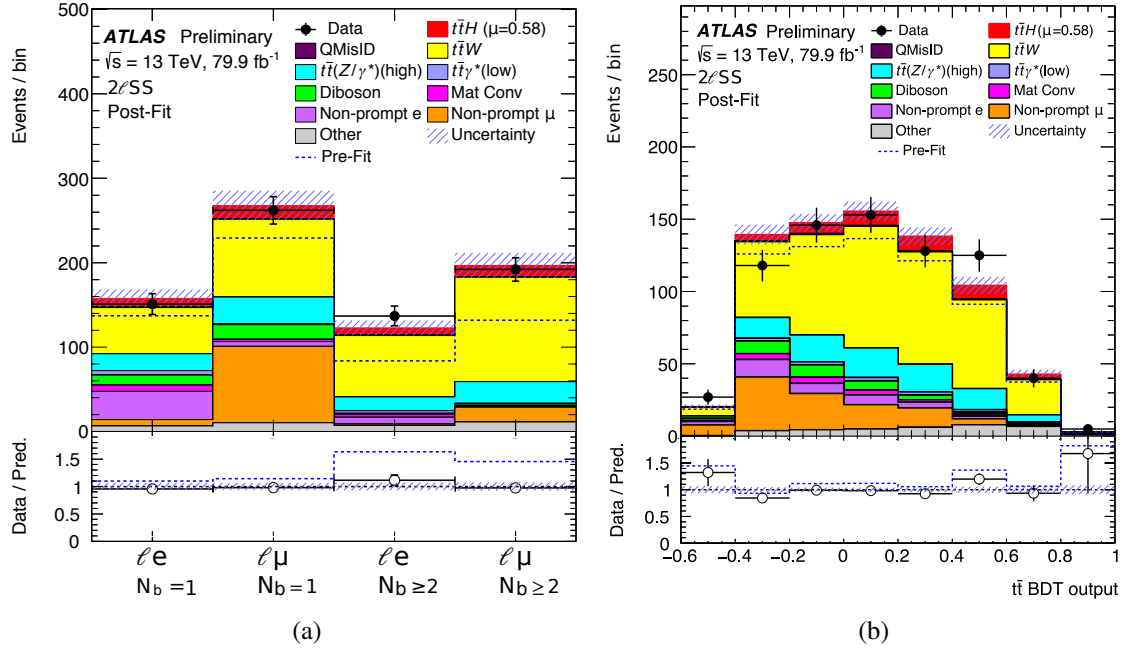


Figure 6.20: Comparison between data and signal-plus-background prediction in the $2\ell$SS channel after event selection for (a) the event yield, split in four separate categories depending on the flavor of the sub-leading lepton and the $b$-jet multiplicity, and (b) the score of the BDT trained to discriminate $t\bar{t}H$ signal from $t\bar{t}$ background. The background contributions after the likelihood fit ("Post-Fit") are shown as filled histograms. The total background before the fit ("Pre-Fit") is shown as a dashed blue histogram. The $t\bar{t}H$ signal, scaled according to the results of the fit, is shown as a filled red histogram added to the post-fit background. The size of the combined statistical and systematic uncertainty in the signal-plus-background prediction is indicated by the blue hatched band. The ratio of the data to the total post-fit prediction is shown in the lower panel.

agreement with the pre-fit background prediction for events with exactly one $b$-jet, but a significant data excess in events with at least two $b$-jets as shown with the dashed blue curve. The excess is shown to be independent of the flavor of the sub-leading lepton and hence uncorrelated with the fractional size of the non-prompt-lepton background. In addition, the $b$-jet multiplicity in a region strongly enriched in non-prompt leptons, obtained by relaxing the lepton selection requirements, is found to be well modeled. Finally, the score of the BDT which discriminates the $t\bar{t}H$ signal from the $t\bar{t}$ background is well-modeled in the non-prompt-lepton background-dominated region (see Figure 6.20b). This BDT is one of the main discriminators between non-prompt leptons and other

backgrounds. In general, regions with large non-prompt backgrounds appear to be well-modeled, however regions with large contributions from the $t\bar{t}W$ background and small contributions from non-prompt leptons, show significant discrepancies between data and the background prediction both in normalization and in shape.

Cross-checks with the matrix method (see Section 5.2.2) are also performed in the $2\ell$SS channel. Comparison between data and predictions from the matrix method for $t\bar{t}$ BDT distribution in $2\ell$SS pre-MVA region with dimuon events is shown in Figure 6.21a, and good agreement is observed. Comparison for $t\bar{t}$ BDT distribution between non-prompt leptons estimated from the matrix method and the template fit method are shown in Figure 6.21b. Estimations from both methods are similar in terms of total yields and of modeling of the main distributions used in the analysis.
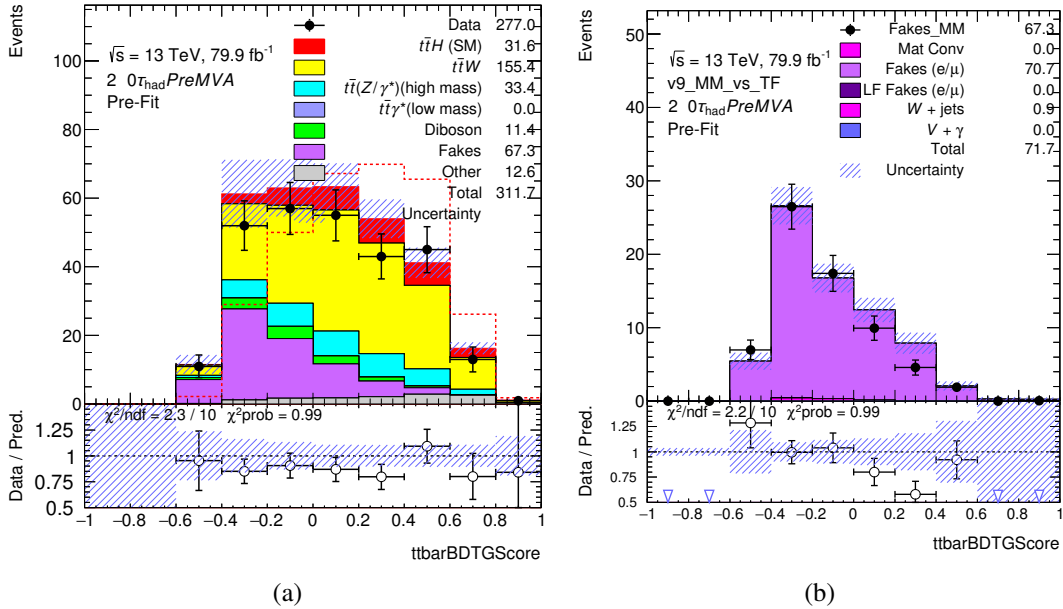


Figure 6.21: (a)Comparison between data and predictions from matrix method for $t\bar{t}$ BDT distribution in the $2\ell$SS pre-MVA region with dimuon events. The total background with non-prompt leptons estimated from matrix method and $t\bar{t}W$ scaled according to the results of fit in Section 6.5 are shown as filled histograms. The size of the statistical uncertainty in the signal-plus-background prediction is indicated by the blue hatched band. The ratio of the data to the total signal-plus-background prediction is shown in the lower panel. (b) Comparison for $t\bar{t}$ BDT distribution between non-prompts leptons estimated from matrix method and template fit method in $2\ell$SS pre-MVA region with dimuon events.

## 6.4   Systematic Uncertainties

A summary of systematic uncertainties is given in this section, mainly covering experimental systematics, signal and background modeling theoretical systematics. An overview can be found in Table 6.4. Experimental systemtaics are discussed in Section 5.3.1. Systematics for signal and background modeling will be discussed in this section.

Table 6.4: Sources of systematic uncertainty considered in the analysis. "(N)" means that the uncertainty is taken as normalization-only for all processes and channels affected. All other uncertainties also affect the shape of the fitted distributions and/or the acceptance in the fit categories. Some of the systematic uncertainties are split into several components, as indicated by the number in the rightmost column.

| Systematic uncertainty | Components | | Systematic uncertainty | Components |
|---|---|---|---|---|
| Luminosity (N) | 1 | | $t\bar{t}H$ **modeling** | |
| Pile-Up reweighting | 1 | | Renormalization and facterization scales | 1 |
| **Physics Objects** | | | Parton shower and hadronization model | 1 |
| Electron | 8 | | Shower tune | 1 |
| Muon | 11 | | PDF | 32 |
| Jet energy scale and resolution | 28 | | $t\bar{t}W$ **modeling** | |
| Jet vertex fraction | 1 | | Radiation | 1 |
| Jet flavor tagging | 17 | | Generator | 1 |
| $E_T^{\text{miss}}$ | 3 | | PDF | 32 |
| Total (Experimental) | 77 | | Extrapolation | 4 |
| **Data-driven background estimates** | | | $t\bar{t}Z/\gamma^*$ **modeling** | |
| Electron charge misassignment | 2 | | Cross section | 2 |
| Non-prompt light-lepton estimates ($3\ell$ ,$3\ell+1\tau_{\text{had}}$ ) | 1 | | Renormalization and factorization scales | 1 |
| Fake $\tau_{\text{had}}$ estimation | 6 | | Generator | 1 |
| Total(Data-driven reducible background) | 9 | | Shower tune | 1 |
| **Template Fit uncertainties** | | | $t\bar{t}$ **modeling** | |
| Material conversions | 1 | | Radiation | 1 |
| Internal conversions | 1 | | **Diboson modeling** | |
| HF non-prompt leptons | 2 | | Subprocesses | 4 |
| LF non-prompt leptons | 2 | | **Other background modeling** | |
| Total (reducible background) | 6 | | Cross section (N) | 22 |
| | | | Total (Signal and background modeling) | 118 |
| | | | Total (Overall) | 210 |

## 6.4.1   Signal and Background Modeling Systematics

This sub-section is devoted to modeling theoretical systematics. Background systematics from the template fit method and data-driven method have been discussed in Section 5.3.2 and 6.3: commonly used systematics for the SSML analyses are described in Section 5.3.2, while the unique systematics used in this analysis are described in Section 6.3. Table 6.5 provides a summary on uncertainties of cross-section, parton-shower and generator variations for main backgrounds relying on MC predictions. More details on the $t\bar{t}W$ systematics are given in Section 5.3.2 and 6.3. For the $t\bar{t}Z/\gamma*$ sample, the uncertainties affecting the modeling of the acceptance and event

Table 6.5: Summary of theoretical uncertainties for $t\bar{t}H$, $t\bar{t}Z/\gamma*$, and $t\bar{t}W$ MC predictions.

| Process (default) | X-section [%] | Generator (alternative) | Parton Shower (alternative) |
|---|---|---|---|
| $t\bar{t}H$ (Powheg+Pythia8) | QCD Scale: $^{+5.8}_{-9.2}$ <br> PDF$(+\alpha_S)$: $\pm 3.6$ | – (aMC@NLO+Pythia8) | (A14 shower tune) |
| $t\bar{t}Z$ (aMC@NLO+Pythia8) | QCD Scale: $^{+9.6}_{-11.3}$ <br> PDF$(+\alpha_S)$: $\pm 4$ | (Sherpa) | – (A14 shower tune) |
| $t\bar{t}W$ (Shepa NLO multileg) | - | aMC@NLO+Pythia8(0j@NLO) vs. Sherpa2.2.1(0j@NLO) | |

kinematics include the QCD scale and tune variations and the comparison to an alternative sample (see Table 6.5). For diboson backgrounds, a 50% normalization uncertainty is assigned and treated as uncorrelated among different subprocesses ($WZ$+light-jets, $WZ+\geq1c$, $WZ+\geq1b$, and $ZZ$+jets). "Rare" background contributions ($tZ$, $t\bar{t}t\bar{t}$, $ttWW$, $WtZ$, $VVV$, $t\bar{t}$, $tHjb$ and $WtH$) are assigned with an overall 50% normalization uncertainty.

### 6.4.1.1  $t\bar{t}H$ Modeling Uncertainties

Uncertainties impacting the $t\bar{t}H$ cross section include $^{+5.8\%}_{-9.2\%}$ estimated by varying the QCD factorization and renormalization scales and $\pm3.6\%$ due to uncertainties on the PDFs and the strong coupling constant $\alpha_s$. These uncertainties will not impact the measured $t\bar{t}H$ cross section nor the significance $Z$ (see Section 5.4.3), but will affect the measured $\mu$, the signal-strength modifier introduced in Section 5.4.1.1.

Uncertainties affecting the modeling of the acceptance and event kinematics include variations in the QCD factorization and renormalization scales, the choice of parton shower and hadronization model, the modeling of ISR, and PDF uncertainties. The theoretical uncertainties due to the QCD scale choice are estimated by varying the renormalization and factorization scale independently by a factor of 0.5 and 2.0 with respect to the central value. The largest variation is obtained when varying both scales simultaneously in the same direction. Figure 6.22 shows the effect of the renormalization and factorization scale variations on the $t\bar{t}H$ yields in bins of all categories. Uncertainties due to the choice of parton shower and hadronization model are estimated by comparing the nominal prediction with that obtained using an alternative sample generated with POWHEG-BOX interfaced to HERWIG7 (described in Section 5.1). The corresponding effect on the $t\bar{t}H$ yields is shown in Figure 6.23. The uncertainty associated with the modeling of ISR is estimated by considering the Var3c A14 tune variation [143], which corresponds to a variation of $\alpha_s$ in the A14 tune, and its effect is shown in Figure 6.24. The uncertainty due to the choice of PDF set is evaluated using the PDF4LHC15 prescription [172], utilizing 32 eigenvector shifts derived from fits to multiple NNLO PDF sets. Finally, the uncertainties associated with the predicted
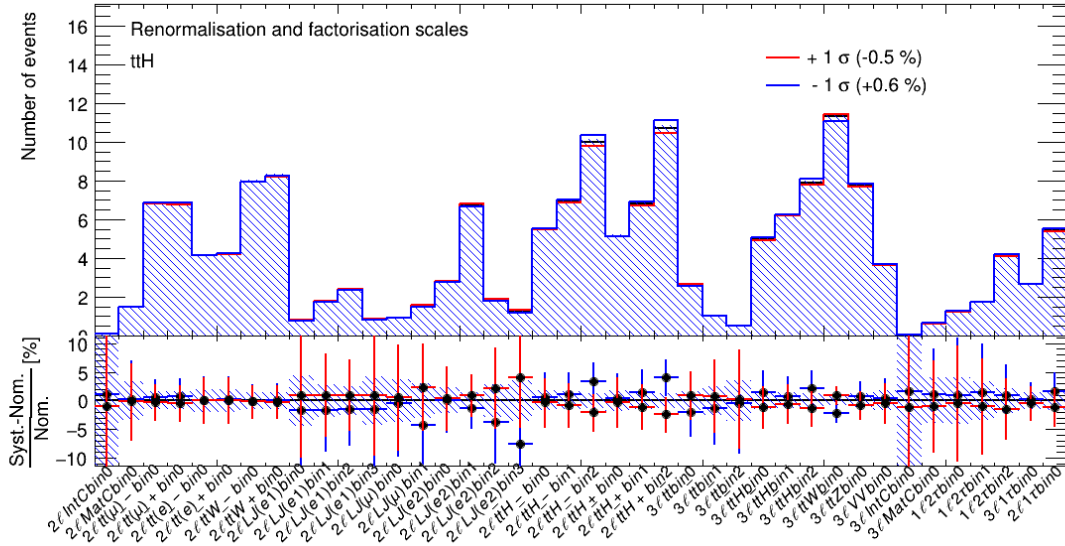
Figure 6.22: Effect of the renormalization and factorization scale variation on the $t\bar{t}H$ yields in bins of all categories.
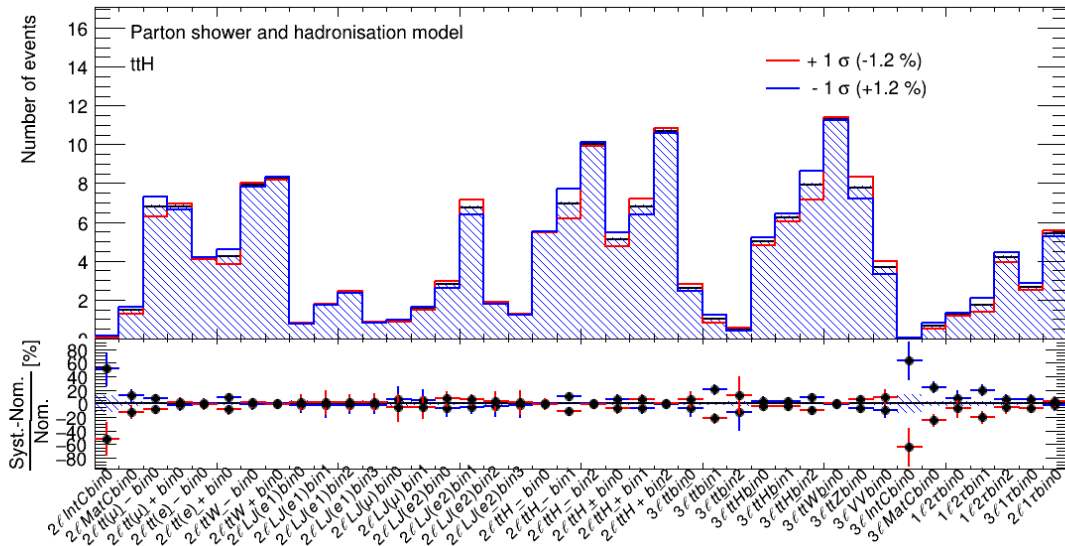


Figure 6.23: Effect of different parton shower and hadronization model choice on the $t\bar{t}H$ yields in bins of all categories.

Higgs-boson branching ratios [48] are also considered.
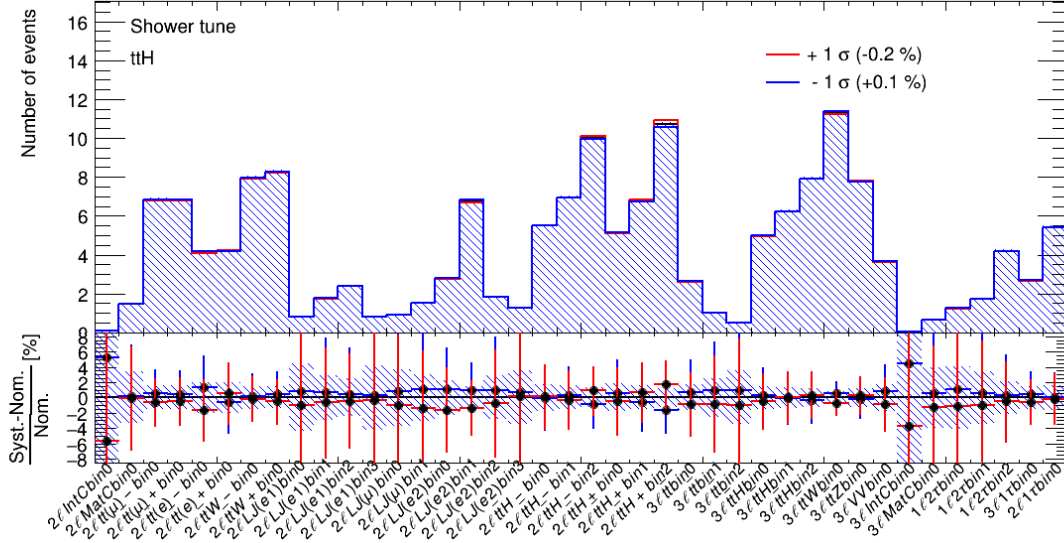
Figure 6.24: Effect of the Var3c A14 tune variation on the $t\bar{t}H$ yields in bins of all categories.

## 6.5 Results

A maximum-likelihood fit with profiled likelihood ratio (see Section 5.4) is performed on all bins in the 25 event categories defined in Section 6.2 to determine the $t\bar{t}H$ cross section and the normalization factors of the $t\bar{t}W$ process and other backgrounds. The $t\bar{t}H$ acceptance in each category is predicted by the simulation assuming the SM. Seventeen categories from the $2\ell$SS and $3\ell$ channels are used as control regions to either determine or constrain different backgrounds (material conversions, internal conversions, $t\bar{t}$ with non-prompt electrons and muons, $t\bar{t}W$, $t\bar{t}Z$, and $VV$). In thirteen of the total control regions, the total event yield (i.e. a single bin) is used, but in the remaining four control regions different kinematic variables are used to discriminate between $t\bar{t}$ and $t\bar{t}W$ backgrounds (see Section 6.3). The remaining eight regions are used as signal regions to measure the $t\bar{t}H$ cross section. In the $t\bar{t}H$ categories of the $2\ell$SS, $3\ell$ and $1\ell+2\tau_{\mathrm{had}}$ channels, a BDT discriminant is used, and the total event yield is used in the remaining four signal regions. Figures 6.25a and 6.25b compare the data to the yields after the predictions were adjusted by the fit in the 25 event categories considered. In all categories, the observed yields agree with the fitted prediction within uncertainties. The background before the fit is shown as a dashed blue histogram. Differences between the data and the prediction are observed before the fit, but resolved after the fit. Figure 6.26 shows the distributions of the BDT discriminants used in selected categories with the bins used in the fit. In the remaining categories, only the event yields are used in the fit.

Figure 6.27 shows the data, background and $t\bar{t}H$ signal yields, where the final-discriminant bins in all event categories are combined into bins of $\log_{10}(S/B)$, where $S$ is the expected $t\bar{t}H$ signal yield and $B$ the fitted background yield. The total background before the fit is shown as a

111

dashed blue histogram. The significance of the observed (expected) excess above the background-only expectation ($\mu = 0$) is $1.8$ $(3.1)$ standard deviations. The best-fit value of $\mu$ is:

$$\hat{\mu} = 0.58^{+0.26}_{-0.25} \text{ (stat.)}^{+0.19}_{-0.15} \text{ (exp.)}^{+0.13}_{-0.11} \text{ (bkg. th.)}^{+0.08}_{-0.07} \text{ (sig. th.)} = 0.58^{+0.36}_{-0.33}. \qquad (6.1)$$

The best-fit value of $\mu$ for each individual channel and the combination of all channels are shown in Figure 6.28. The individual channel results are extracted from the full fit but with a separate parameter of interest for each channel. The probability that the six fitted signal strengths are compatible with a single value is $98\%$.

Normalization factors for several important irreducible and reducible backgrounds are determined by the fit (see Section 6.3). Of particular interest are the three measured normalization factors for the $t\bar{t}W$ background in the $2\ell$SS and $3\ell$ event categories: $\hat{\lambda}^{2\ell\text{LJ}}_{t\bar{t}W} = 1.56^{+0.30}_{-0.28}$, $\hat{\lambda}^{2\ell\text{HJ}}_{t\bar{t}W} = 1.26^{+0.19}_{-0.18}$, and $\hat{\lambda}^{3\ell}_{t\bar{t}W} = 1.68^{+0.30}_{-0.28}$. They are consistent with each other and systematically above unity, indicating a preference of the data for a higher value of the $t\bar{t}W$ cross section than the updated $t\bar{t}W$ theoretical cross section (see Section 5.1). Because the $t\bar{t}W$ modeling uncertainties are constructed to only affect the shapes of distributions while the total yield is fixed, the normal-
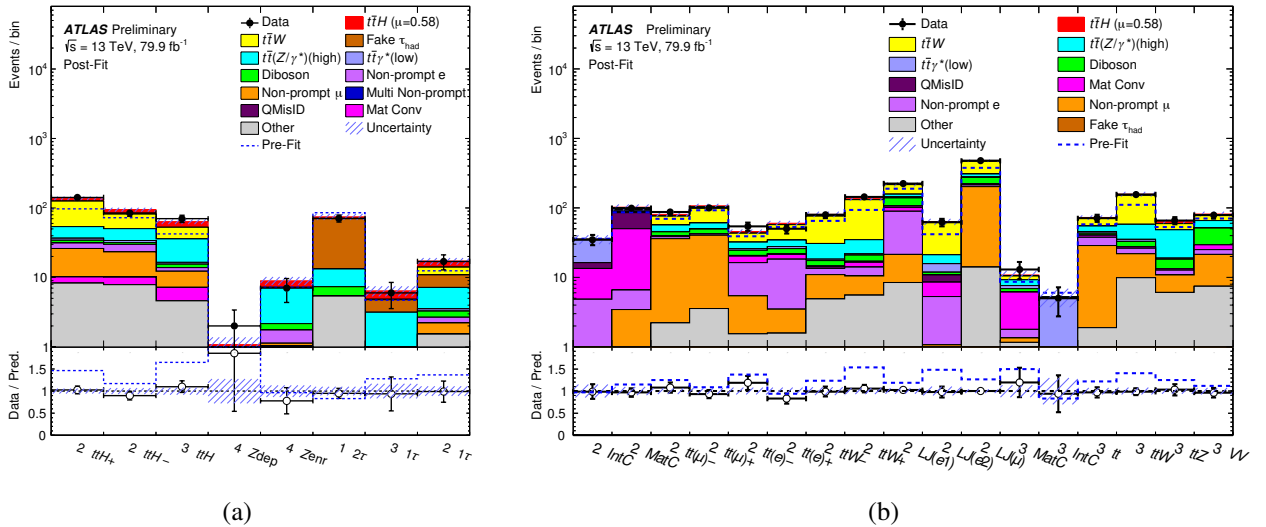


Figure 6.25: Comparison between data and prediction for the event yields in (a) the eight $t\bar{t}H$ categories and (b) the 17 control-region categories. The background contributions after the likelihood fit ("Post-Fit") are shown as filled histograms. The total background before the fit ("Pre-Fit") is shown as a dashed blue histogram. The $t\bar{t}H$ signal, scaled according to the results of the fit, is shown as a filled red histogram added to the post-fit background. The size of the combined statistical and systematic uncertainty in the total signal-plus-background prediction is indicated by the blue hatched band. The ratio of the data to the total post-fit prediction is shown in the lower panel.
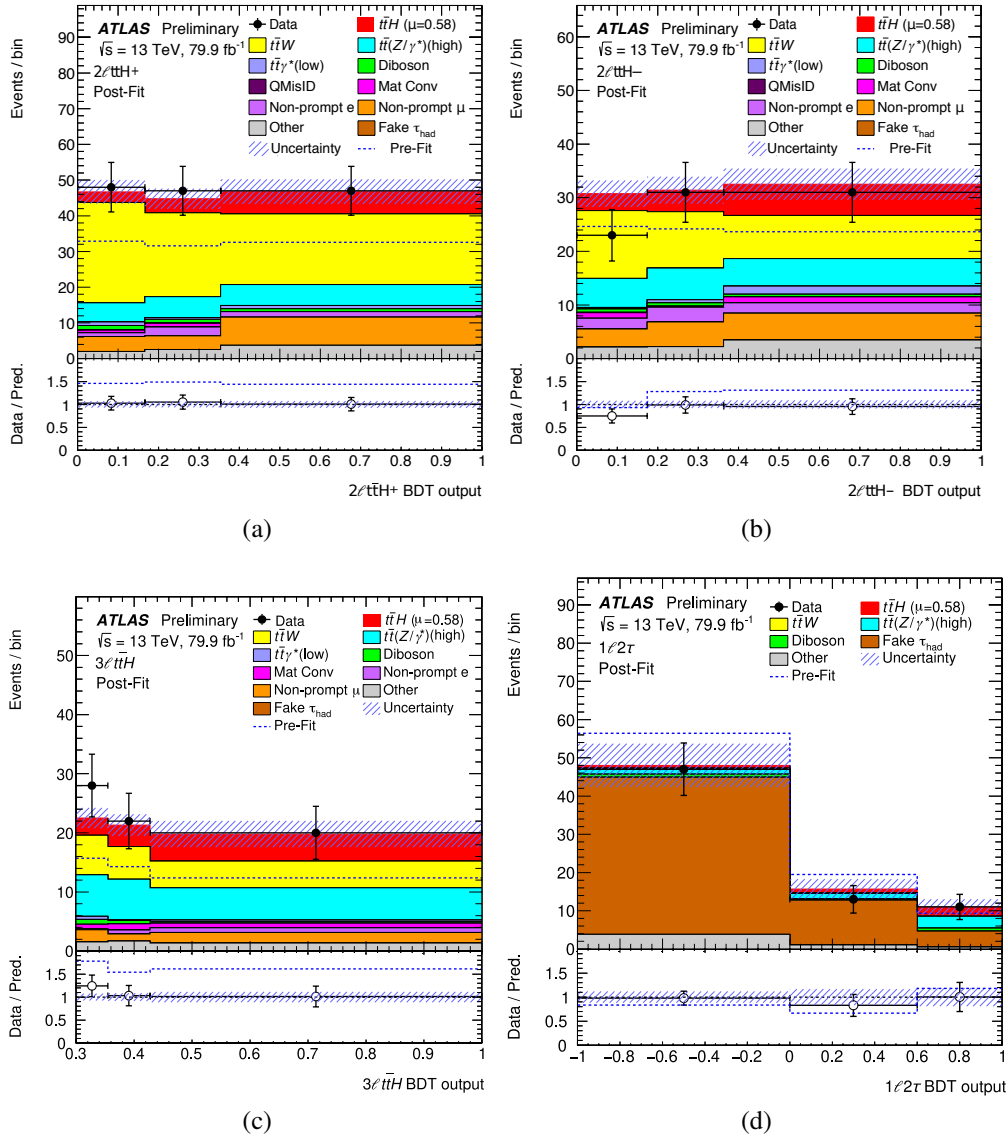
Figure 6.26: Comparison between data and prediction for the BDT discriminants used in different $t\bar{t}H$ categories: (a) 2$\ell$ttH+, (b) 2$\ell$ttH−, (c) 3$\ell$ttH and (d) $\ell$+2$\tau_{\mathrm{had}}$. The background contributions after the likelihood fit ("Post-Fit") are shown as filled histograms. The total background before the fit is shown as a dashed blue histogram. The total background before the fit ("Pre-Fit") is shown as a dashed blue histogram. The $t\bar{t}H$ signal, scaled according to the results of the fit, is shown as a filled red histogram added to the post-fit background. The size of the combined statistical and systematic uncertainty in the total signal-plus-background prediction is indicated by the blue hatched band. The ratio of the data to the total post-fit prediction is shown in the lower panel.

ization factors represent a scaling factor for $t\bar{t}W$ events selected in this analysis. Uncertainties to extrapolate the $t\bar{t}W$ scaling factor to the inclusive phase space are not included.

Contributions from the different sources of uncertainty on the measured signal strength are
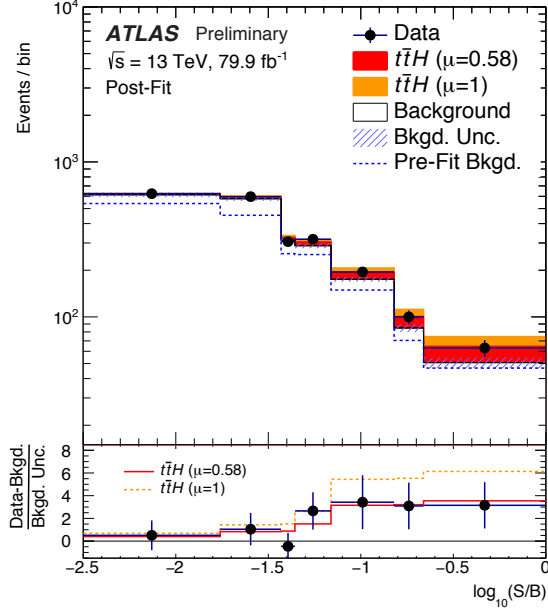
Figure 6.27: Event yields as a function of $\log_{10}(S/B)$ for data, background and a Higgs boson signal with $m_H = 125$ GeV. The discriminant bins in all categories are combined into bins of $\log_{10}(S/B)$, where $S$ is the expected $t\bar{t}H$ signal yield and $B$ the background yield from the unconditional fit. The background yields are shown as the fitted values, while the $t\bar{t}H$ signal yields are shown for the fitted value ($\mu = 0.58$) and the SM prediction ($\mu = 1$). The total background before the fit is shown as a dashed blue histogram. The size of the combined statistical and systematic uncertainty in the background prediction is indicated by the blue hatched band. The pull (residual divided by its uncertainty) of the data relative to the background-only prediction is shown in the lower panel, where the full red line (dashed orange line) indicates the pull of the prediction for signal with $\mu = 0.58$ ($\mu = 1$) and background relative to the background-only prediction.

shown in Table 6.6. The leading systematic uncertainty is in the jet energy scale and resolution. The most important systematic uncertainties arising from theoretical predictions are in the modeling of $t\bar{t}W$ production and the normalization of the $t\bar{t}Z/\gamma^*$ background. The uncertainty associated with the $\tau_{\mathrm{had}}$ background estimate is also significant. Only few nuisance parameters in the fit showed significant adjustments and/or constraints (see Figure 6.29). Among them are the NPs associated with the $b$-jet multiplicity and total charge extrapolation uncertainties on the $t\bar{t}W$ background in the $2\ell$SS channel. They were adjusted by $+0.33$ and $+0.75$ pre-fit standard deviations, respectively, and their uncertainties was reduced by factors of 3 and 2, respectively. The NP associated with the uncertainty in the closure test of the non-prompt lepton estimate in $1\ell+2\tau_{\mathrm{had}}$ channel was adjusted by $-0.56$ pre-fit standard deviations and its uncertainty was reduced by a factor of 1.7; however, this uncertainty does not significantly impact the $t\bar{t}H$ cross section measurement.

An extrapolation to the inclusive phase space, assuming the SM $t\bar{t}H$ kinematics, is made. The efficiency for the $t\bar{t}H$ signal selected in this analysis is $0.42\%$ and the measured $t\bar{t}H$ production
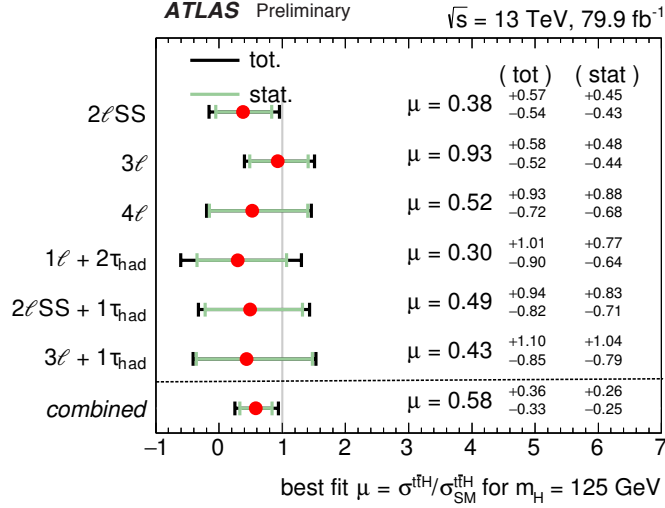
Figure 6.28: The observed best-fit values of the $t\bar{t}H$ signal strength $\mu$ and their uncertainties by analysis channel and combined. The individual $\mu$ values for the channels are obtained from a simultaneous fit with the signal-strength parameter for each channel floating independently. The SM prediction corresponds to $\mu$=1.

cross section is:

$$\hat{\sigma}(t\bar{t}H) = 294^{+132}_{-127} \text{ (stat.)}^{+94}_{-74} \text{ (exp.)}^{+73}_{-56} \text{ (bkg. th.)}^{+41}_{-39} \text{ (sig. th.) fb} = 294^{+182}_{-162} \text{ fb.} \qquad (6.2)$$

The predicted SM cross section is $\sigma(t\bar{t}H) = 507^{+35}_{-50}$ fb computed at NLO in QCD and electroweak couplings for the Higgs boson mass of 125 GeV [48]. The measured cross section is consistent with the SM prediction within uncertainties.

## 6.5.1 Cross-checks

A number of cross-checks of the assumptions in the statistical model were performed. The measured signal strength was found to be robust under these cross-checks, provided that the $t\bar{t}W$ normalization was not fixed. Here six key cross-checks are presented to test the robustness of the model and the consistency of the results with other analyses.

A comparison was made between the results from the combination of the $2\ell$SS and $3\ell$ categories in the nominal multivariate analysis and those in the cross-check cut-and-count analysis. Offline selection criteria applied to the $2\ell$SS and $3\ell$ channels in the cut-and-count analysis and the event categories are shown in Table 6.7. This analysis included the same $t\bar{t}W$ control regions as the nominal analysis. Comparison between data and prediction for the event yields in the categories in the $2\ell$SS and $3\ell$ channels are shown in Figure 6.30. The cut-and-count analysis has lower ex-

Table 6.6: Breakdown of the contributions to the uncertainties in $\hat{\mu}$. The contribution of the different sources of uncertainty is evaluated after the fit described in Section 6.5. The total statistical uncertainty is evaluated, as described in the text, by fixing all the nuisance parameters in the fit except for the free-floating background normalization factors. The contribution from the uncertainty in those normalization factors is then included in the quoted total statistical uncertainty rather than in the systematic uncertainty component. The statistical uncertainty evaluated after also fixing the background normalization factors is then indicated as "intrinsic statistical uncertainty". Statistical uncertainties from data-driven background estimates are included within the experimental uncertainties. The other quoted numbers are obtained by repeating the fit after having fixed a certain set of nuisance parameters corresponding to a group of systematic uncertainty sources, and subtracting in quadrature the resulting total uncertainty of $\mu$ from the uncertainty from the full fit. The same procedure is followed for quoting the individual effects of background normalization factors. Due to rounding effects and small correlations between the different sources of uncertainty, the total systematic uncertainty is different from the sum in quadrature of the individual sources.

| Uncertainty source | $\Delta\hat{\mu}$ | |
|---|---|---|
| Jet energy scale and resolution | +0.13 | −0.13 |
| $t\bar{t}Z/\gamma^*$ (high mass) modeling | +0.09 | −0.09 |
| $t\bar{t}W$ modeling (radiation, generator, PDF) | +0.08 | −0.08 |
| Fake $\tau_{\text{had}}$ background estimate | +0.07 | −0.07 |
| $t\bar{t}W$ modeling (extrapolation) | +0.05 | −0.05 |
| $t\bar{t}H$ cross section | +0.05 | −0.05 |
| Simulation sample size | +0.05 | −0.05 |
| $t\bar{t}H$ modeling | +0.04 | −0.04 |
| Other background modeling | +0.04 | −0.04 |
| Jet flavour tagging and $\tau_{\text{had}}$ identification | +0.04 | −0.04 |
| Other experimental uncertainties | +0.03 | −0.03 |
| Luminosity | +0.03 | −0.03 |
| Diboson modeling | +0.01 | −0.01 |
| $t\bar{t}\gamma^*$ (low mass) modeling | +0.01 | −0.01 |
| Charge misassignment | +0.01 | −0.01 |
| Template fit (non-prompt leptons) | +0.01 | −0.01 |
| Total systematic uncertainty | +0.25 | −0.22 |
| Intrinsic statistical uncertainty | +0.23 | −0.22 |
| $t\bar{t}W$ normalization factors | +0.10 | −0.10 |
| Non-prompt leptons normalization factors (HF, material conversions) | +0.05 | −0.05 |
| Total statistical uncertainty | +0.26 | −0.25 |
| Total uncertainty | +0.36 | −0.33 |

pected sensitivity relative to the background-only hypothesis compared with nominal multivariate analysis (1.4 vs 2.4 standard deviations). The resulting best-fit signal strengths were found to be $\hat{\mu} = 0.67^{+0.44}_{-0.41}$ and $\hat{\mu} = 0.43^{+0.66}_{-0.65}$ for the 2$\ell$SS and 3$\ell$ categories in the nominal and the cut-and-
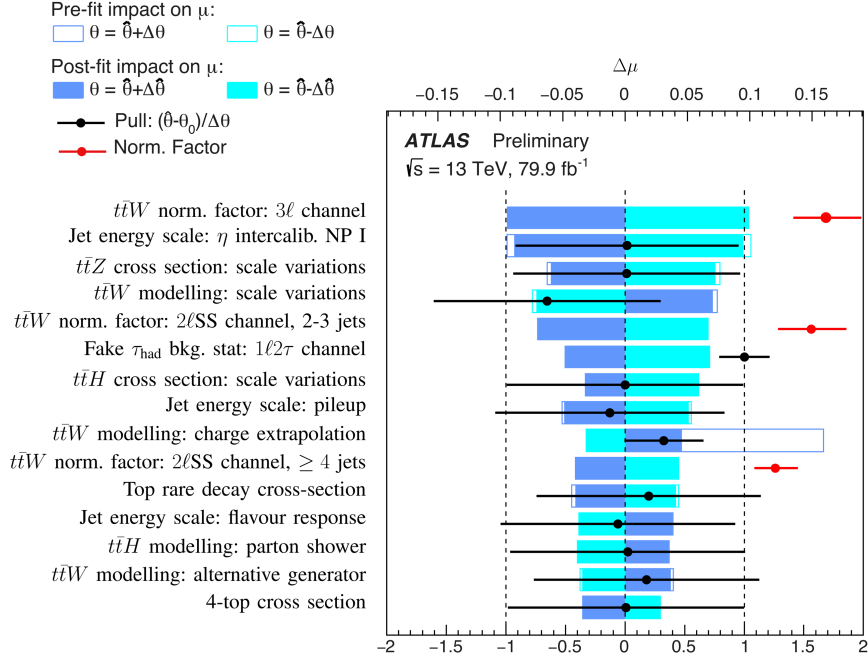
Figure 6.29: Ranking of the parameters included in the fit according to their impact on the signal strength $\mu$. Only the 15 most highly ranked parameters are shown. The empty blue rectangles correspond to the pre-fit impact on $\mu$ and the filled blue ones to the post-fit impact on $\mu$, both referring to the upper $x$-axis scale. The impact of each nuisance parameter (NP), $\Delta\mu$, is computed by comparing the nominal best-fit value of $\mu$ with the result of the fit when fixing the considered NP to its best-fit value, $\hat{\theta}$, shifted by its pre-fit (post-fit) uncertainties $\pm\Delta\theta$ ($\pm\Delta\hat{\theta}$). The black points show the pulls of the NPs relative to their nominal values, $\theta_0$. The nominal value for all NPs is $\theta_0 = 0$, with the exception of the NP associated with the limited sample size in the estimation of the fake $\tau_{\mathrm{had}}$ background in the $1\ell+2\tau_{\mathrm{had}}$ channel, for which the nominal value is $\theta_0 = 1$. These pulls and their relative post-fit errors, $\Delta\hat{\theta}/\Delta\theta$, refer to the lower $x$-axis scale. The $t\bar{t}W$ normalization factors (red points) also refer to the lower $x$-axis scale, and correspond to the floating normalizations of the $t\bar{t}W$ background, for which the pre-fit impact on $\mu$ is not defined. The nominal value of the $t\bar{t}W$ normalization factors is 1, which corresponds to the $t\bar{t}W$ prediction based on the "updated theoretical cross section" discussed in Section 5.1. For experimental uncertainties that are decomposed into several independent sources, "NP I" corresponds to the first nuisance parameter, ordered by its impact on $\mu$.

count analyses, respectively. In both cases the best-fit $t\bar{t}W$ normalization factors were found to be high and consistent with those from the nominal analysis.

The combined fit was performed separately on the 2015–2016 dataset (36 fb$^{-1}$) and the 2017 dataset (44 fb$^{-1}$), which were recorded under different pileup conditions (average number of $pp$ interactions per crossing of 25 and 38, respectively). The resulting best-fit signal strengths were found to be consistent between both datasets: $\hat{\mu} = 0.68^{+0.50}_{-0.45}$ and $\hat{\mu} = 0.52^{+0.45}_{-0.40}$, respectively.

Table 6.7: Offline selection criteria applied to the $2\ell$SS and $3\ell$ channels in the cut-and-count analysis, together with the event categories defined. The common selection criteria for all channels are listed in the first line under the title "Common". Same-charge (opposite-charge) lepton pairs are also referred to as same-sign (opposite-sign) with abbreviation SS (OS). In the $2\ell$SS channel the leading and trailing (in $p_{\rm T}$) SS leptons are denoted as $\ell_0$ and $\ell_1$ respectively. In the $3\ell$ channel, the OS lepton (w.r.t the SS pair) is denoted as $\ell_0$, but is not necessarily the one with highest $p_{\rm T}$; the remaining SS leptons are denoted as $\ell_1$ (closest in $\Delta R$ to $\ell_0$) and $\ell_2$ (the remaining one). Same-flavor (SF), OS lepton pairs are referred to as SFOS pairs.

| Channel | Selection criteria | |
|---|---|---|
| Common | $N_{\rm jets} \geq 2$ and $N_{b-\rm jets} \geq 1$ | |
| $2\ell$SS | Two SS very tight (T*) leptons, $p_{\rm T} > 20$ GeV | |
| | No $\tau_{\rm had}$ candidates | |
| | $m(\ell_0\ell_1) > 12$ GeV | |
| | **12 categories** based on the following criteria: | |
| | · Number of jets: $N_{\rm jets} = 4$ or $N_{\rm jets} > 4$ | |
| | · Number of b-tagged jets: $N_{b-\rm jets} = 1$ or $N_{b-\rm jets} > 1$ | |
| | · Flavour of SS leptons: $ee$, $\mu\mu$ or opposite flavour (OF) | |
| $3\ell$ | Three light (L) leptons with $p_{\rm T} > 10$ GeV; sum of light-lepton charges $= \pm1$ | |
| | Two SS very tight (T*) leptons, $p_{\rm T} > 15$ GeV | |
| | One OS (w.r.t the SS pair) loose-isolated (L*) lepton, $p_{\rm T} > 10$ GeV | |
| | No $\tau_{\rm had}$ candidates | |
| | $m(\ell^+\ell^-) > 12$ GeV for all SFOS pairs | |
| | $\|m(3\ell) - 91.2\,\text{GeV}\| > 10$ GeV | |
| | **12 categories** based on the following criteria: | |
| | LjZPeak | $3 \leq N_{\rm jets} \leq 5$; 1 SFOS pair, $m(\ell^+\ell^-) \in Z_{\rm win}$ |
| | HjZPeak | $N_{\rm jets} \geq 6$; 1 SFOS pair, $m(\ell^+\ell^-) \in Z_{\rm win}$ |
| | LjHmZenr | $3 \leq N_{\rm jets} \leq 5$; $m(\ell_0\ell_1) > 70$ GeV; 1 SFOS pair, $m(\ell^+\ell^-) \notin Z_{\rm win}$ |
| | HjHmZenr | $N_{\rm jets} \geq 6$; $m(\ell_0\ell_1) > 70$ GeV; 1 SFOS pair, $m(\ell^+\ell^-) \notin Z_{\rm win}$ |
| | LjHmZdep_pp | $3 \leq N_{\rm jets} \leq 5$; $m(\ell_0\ell_1) > 70$ GeV; 0 SFOS pair; $\ell_1$ and $\ell_2$ positively charged |
| | LjHmZdep_mm | $3 \leq N_{\rm jets} \leq 5$; $m(\ell_0\ell_1) > 70$ GeV; 0 SFOS pair; $\ell_1$ and $\ell_2$ negatively charged |
| | LjLm1bZenr | $3 \leq N_{\rm jets} \leq 5$; $N_{b-\rm jets} = 1$; $m(\ell_0\ell_1) < 70$ GeV; 1 SFOS pair, $m(\ell^+\ell^-) \notin Z_{\rm win}$ |
| | LjLm1bZdep | $3 \leq N_{\rm jets} \leq 5$; $N_{b-\rm jets} = 1$; $m(\ell_0\ell_1) < 70$ GeV; 0 SFOS pair |
| | LjLm2bZenr | $3 \leq N_{\rm jets} \leq 5$; $N_{b-\rm jets} \geq 2$; $m(\ell_0\ell_1) < 70$ GeV; 1 SFOS pair, $m(\ell^+\ell^-) \notin Z_{\rm win}$ |
| | LjLm2bZdep | $3 \leq N_{\rm jets} \leq 5$; $N_{b-\rm jets} \geq 2$; $m(\ell_0\ell_1) < 70$ GeV; 0 SFOS pair |
| | HjLmZenr | $N_{\rm jets} \geq 6$; $m(\ell_0\ell_1) < 70$ GeV; 1 SFOS pair, $m(\ell^+\ell^-) \notin Z_{\rm win}$ |
| | HjLmZdep | $N_{\rm jets} \geq 6$; $m(\ell_0\ell_1) < 70$ GeV; 0 SFOS pair |

[1] $Z_{\rm win} = [M_Z \pm 10\,\text{GeV}]$, where $M_Z$ denotes the $Z$-boson pole mass.

Similarly, the best-fit $t\bar{t}W$ normalization factors were found to be high and consistent between both datasets.

An alternative scenario with a single $t\bar{t}W$ normalization factor instead of three was tested. In this case the best-fit values obtained are $\hat{\mu} = 0.70^{+0.36}_{-0.33}$ and $\hat{\lambda}_{t\bar{t}W} = 1.39^{+0.17}_{-0.16}$, with only minor changes to the rest of the fitted parameters. The compatibility of this alternative fit with the nominal one is 28%, corresponding to 0.59 standard deviations.

The value of $\hat{\mu}$ obtained by this analysis was compared to that published using 36 fb$^{-1}$ of
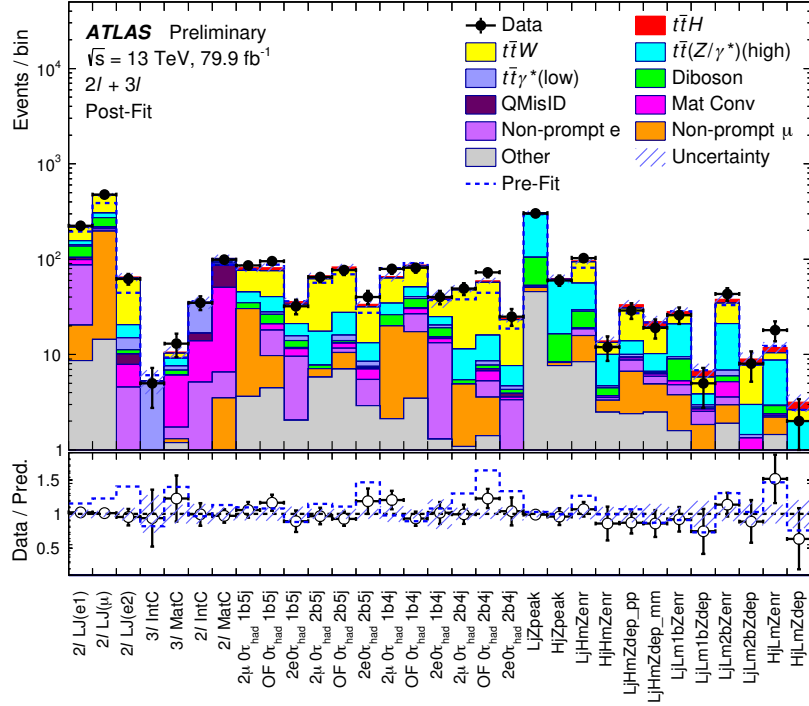
Figure 6.30: Comparison between data and prediction for the event yields in the categories in the $2\ell$SS and $3\ell$ channels from the cut-and-count cross-check analysis. The background contributions after the likelihood fit in the cut-and-count analysis ("Post-Fit") are shown as filled histograms. The total background before the fit ("Pre-Fit") is shown as a dashed blue histogram. The $t\bar{t}H$ signal, scaled according to the results of the fit, is shown as a filled red histogram added to the post-fit background. The size of the combined statistical and systematic uncertainty in the total signal-plus-background prediction is indicated by the blue hatched band. The ratio of the data to the total post-fit prediction is shown in the lower panel.

data [173], which was obtained with the $t\bar{t}W$ normalization constrained within uncertainties to its NLO QCD+EW theoretical cross section [48]. When the fit is performed in the current analysis with the $t\bar{t}W$ normalization forced to the same theoretical prediction, and without additional extrapolation uncertainties, a value of $\hat{\mu} = 1.5^{+0.5}_{-0.5}$ consistent with that of Ref. [173], $\hat{\mu}_{\text{HIGG-2017-02}} = 1.6^{+0.5}_{-0.4}$, is obtained on the same dataset. Compared to Ref. [173], this analysis has a factor of three improvements in the $t\bar{t}W$ sensitivity, as a result of the reduced non-prompt-lepton background, the improved event categorization, and the higher integrated luminosity used. This allows fewer assumptions in the background estimates to be made in the statistical analysis, and a larger value for the fitted $t\bar{t}W$ normalization is obtained.

Validation studies of the non-prompt-lepton background estimate (see Section 6.3) disfavor mismodeling of this background being the explanation for the enhanced $t\bar{t}W$ normalization factors. These studies, along with the preference of the fit model to assign the observed data excess to $t\bar{t}W$-

related fit parameters, are consistent with the data requiring a larger $t\bar{t}W$ normalization compared to theoretical predictions and the current estimate of the non-prompt-lepton background.

The value of $\hat{\lambda}_{t\bar{t}W}$ obtained by this analysis in the alternative scenario of a single $t\bar{t}W$ normalization factor (see above) was compared with that obtained by a previous measurement of the $t\bar{t}W$ cross section using 36 fb$^{-1}$ of data [174]. Such measurement yielded $\hat{\lambda}_{t\bar{t}W} = 1.19 \pm 0.26$ with respect to the updated $t\bar{t}W$ theoretical cross section (see Section 5.1).[1] While both results are similar, a detailed assessment of their compatibility is beyond the scope of this study.

---

[1]The number reported has been obtained by dividing the result of Ref. [174] by a factor of 1.21.

# CHAPTER 7

# Evidence for $t\bar{t}t\bar{t}$ Production in the Same-sign Dilepton and Multilepton Final States

This chapter introduces a search for $t\bar{t}t\bar{t}$ production in the same-sign leptons and multilepton final state (SSML) using 139 fb$^{-1}$ of data collected with the ATLAS detector at $\sqrt{s} = 13$ TeV during 2015-18. This analysis has been publish[79], declaring the evidence for $t\bar{t}t\bar{t}$ production. In the SM, the top quark is expected to decay into a $W$ boson and a $b$-quark with a branching fraction of approximately 100%. Thus, the $t\bar{t}t\bar{t}$ process will give rise to $W^+W^-W^+W^-b\bar{b}b\bar{b}$ events which then produce different final states depending on the hadronic or leptonic decay mode of the $W$ bosons. The $t\bar{t}t\bar{t}$ topology is then characterized by high jet and $b$-jet multiplicities and high overall energy that can be quantified as a large value for the scalar sum of the object transverse momenta in the event. The different branching fractions for the four $W$ bosons decays are shown in Figure 7.1. Events considered are that contain exactly two isolated leptons with the same electric
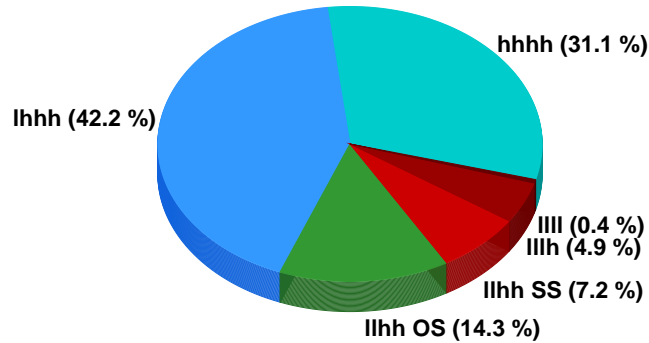


Figure 7.1: Branching fraction for the decays of four $W$ bosons. Here 'l' denotes an electron or a muon (electrons and muons from $\tau$ decays are included in the totals shown) and 'h' an hadronic decay. 'OS' stands for 'Opposite Sign' and 'SS" for 'Same Sign'.

charge (2LSS) or that with at least three isolated light leptons (3L), having a branching fraction of 7% and 5%, respectively. Although this channel has a small branching fraction, it benefits from low levels of background.

With the similar phase space as the $t\bar{t}H$ analysis presented in Chapter 6, this analysis has similar strategy as the $t\bar{t}H$ analysis. In the analysis, signal events are separated from background events using a multivariate discriminant. A fit is then performed on the distribution of the multivariate discriminant in the signal-enriched region. Background-enriched regions are also added to the fit to determine the normalizations of the $t\bar{t}W$ and some sources of the fake/non-prompt contributions.

This chapter is organized as follows. The selection criteria of the physics objects and the event selection are discussed in Section 7.1. Backgrounds are estimated with a combination of simulation and data-driven techniques which are described in Section 7.2. Section 7.3 discusses the BDT used to extract the $t\bar{t}t\bar{t}$ signal. The list of systematic uncertainties which impact the background prediction are described in Section 7.4. Finally, Section 7.5 discusses the global fit used to extract the best estimate of the $t\bar{t}t\bar{t}$ production cross section.


## 7.1   Object and Event Selection

This section describes the selections applied on the reconstructed physics objects introduced in Chapter 4. A brief summary of the main reconstruction and identification criteria applied for each of these physics objects is given in Table 7.1. Discussion of the working points for lepton identification and isolation is given in Section 4.3. That of jets is found in Section 4.4 and Section 4.4.1 for jets and b-tagged jets, respectively. Compared with the $t\bar{t}H$ analysis (see Section 6.1), looser isolation requirements are used and a tighter $b$-tagging WP is chosen.

Table 7.1: Summary of the object identification and definitions.

| | Electrons | Muons | Jets | $b$-jets |
|---|---|---|---|---|
| $p_T$ [GeV] | $> 28$ | $> 28$ | $> 25$ | $> 25$ |
| $|\eta|$ | $< 1.37$ or $1.52 - 2.47$ | $< 2.5$ | $< 2.5$ | $< 2.5$ |
| ID quality | Tight | Medium | JVT | MV2c10 77% |
| | ECIDS ($ee$, $e\mu$) | | | |
| Isolation | FCTight | FCTightTrackOnly | | |
| Track vertex : | | | | |
| $\quad - |d_0/\sigma_{d_0}|$ | $< 5$ | $< 3$ | | |
| $\quad - |z_0 \sin\theta|$ [mm] | $< 0.5$ | $< 0.5$ | | |

A sequential overlap removal procedure is applied to avoid the same calorimeter energy deposit or the same track to be reconstructed as two different objects. As a first step, electrons sharing their

track with a muon candidate are removed. Next, the closest jet within $\Delta R = 0.2$ of an electron is removed. Then, the electrons within $\Delta R = 0.4$ of a remaining jet are removed since they likely arise from $b$- or $c$-decays. After that, the jets with less than three associated tracks that are within $\Delta R = 0.2$ of a muon are removed. Finally, muons are removed if their tracks are within $\Delta R = 0.4 + 10\text{GeV}/p_T^\mu$ of any remaining jets as they also likely arise from $b$- or $c$-decays.

Events are required to have one same-sign lepton pair or at least three leptons without the charge requirement. Each event must have at least one reconstructed lepton that matches the lepton that fired the trigger.

Events with two same-sign electrons are required to have the di-electron invariant mass $m_{ee} >$ 15 GeV and $|m_{ee} - 91\,\text{GeV}| > 10$ GeV to reduce the charge misassignment background coming from low mass resonances and $Z$-boson. For events with at least three leptons, all the opposite-sign same-flavor lepton pairs are required to satisfy $|m_{\ell\ell} - 91\,\text{GeV}| > 10$ GeV to reduce contamination from the $Z$-boson decays.

Events arising from $t\bar{t}t\bar{t}$ production are selected by exploiting the high multiplicities of both light-jets and $b$-tagged jets as well as large overall event activities. This last property is probed by the scalar sum of the transverse momentum of the isolated leptons and jets in the event, referred to as $H_T$ . The inclusive signal region (SR) is defined by requiring at least six jets, at least two $b$-tagged jets and $H_T$ above $500\,\text{GeV}$.

## 7.2   Background Estimate

Similar to the $t\bar{t}H$ analysis (see Section 6.3), backgrounds in the SSML channel can be categorized into irreducible and reducible backgrounds. The irreducible backgrounds mainly originate from the $t\bar{t}W$+jets, $t\bar{t}H$+jets and $t\bar{t}H$+jets processes where jets refer to both light jets and $b$-jets. The smaller backgrounds include diboson or triboson production, $VH$ production in association with jets, and rare processes ($t\bar{t}WW$, $tWZ$, $tZq$, $t\bar{t}t$). These backgrounds are evaluated using MC simulations described in Section 5.1 normalized to their SM cross sections, except for $t\bar{t}W$ for which the normalization is corrected using data in a dedicated control region.

The reducible backgrounds originate mainly from $t\bar{t}$+jets and $tW$+jets production with prompt leptons with misassigned charge (QMis-ID) or fake/non-prompt leptons. This fake/non-prompt background, together with $t\bar{t}W$, is evaluated using the template fit method (see Section 5.2.2.2). The charge misassignment background is defined for the 2LSS channels only and predominantly arises from the $t\bar{t}$+jets events. This background is evaluated using a data-driven method introduced in Section 5.2.1.

The estimated yield of each source of background can be found in Section 7.5 and the fractional contributions of various backgrounds to the predicted total background in the SR and control re-

gions (defined in Section 7.2.1) are shown in Figure 7.2.
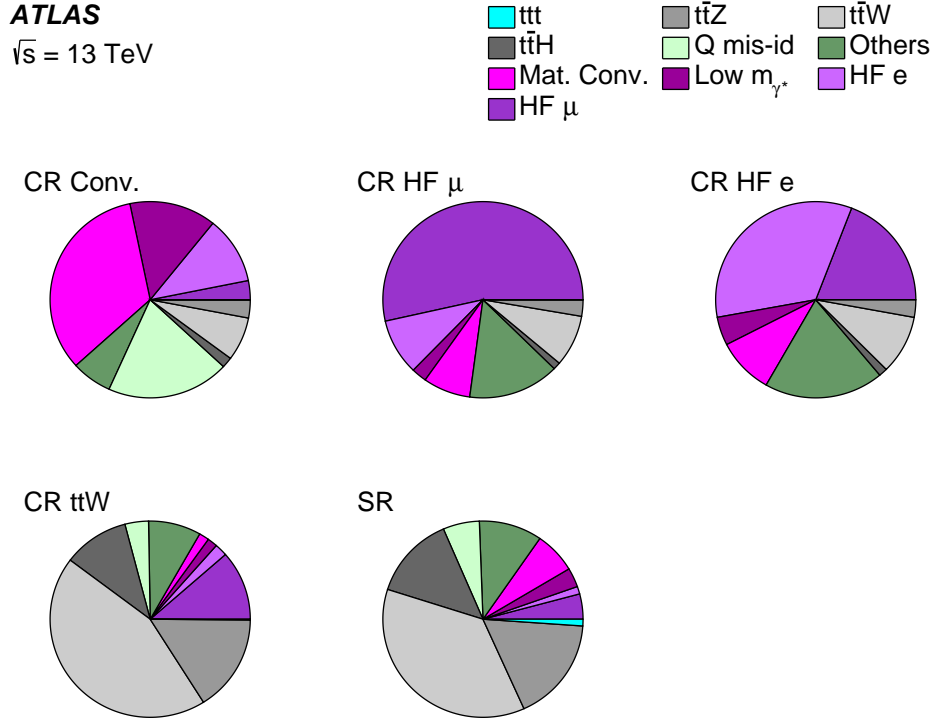


Figure 7.2: Post-fit pie chart for the background composition in each of the analysis regions.

## 7.2.1 Fake/non-prompt Lepton Background and $t\bar{t}W$ Production

The template fit method used to estimate the fake/non-prompt background relies on the simulation to model the kinematic distributions of background processes arising from fake and non-prompt leptons and on control regions to determine their normalizations simultaneously with the $t\bar{t}t\bar{t}$ signal. Five normalization factors are considered: $\text{NF}_{\text{HFe}}$ ($\text{NF}_{\text{HF}\mu}$) for the non-prompt electron (muon) background from heavy-flavour decays, $\text{NF}_{\text{Mat. Conv.}}$ for the background from detector material conversions, $\text{NF}_{\text{Low M}_{ee}}$ for the contribution of internal conversions, denoted as $\gamma^*$ processes here, and $\text{NF}_{t\bar{t}W}$ for the $t\bar{t}W$ contribution.

Several control regions are defined to determine the normalizations of various components of the fake/non-prompt background from data. In order to minimize the degeneracy between the normalizations of different background sources, each region must have a dominating component or a variable with good discriminating power between different components. Since events arising from $t\bar{t}W$ production represent a large contribution in all control and signal regions, its normalization is also determined simultaneously with the $t\bar{t}t\bar{t}$ signal using a dedicated control region. In total,

Table 7.2: Summary of the control regions used in the template fit. $M_{ee}$@CV ($M_{ee}$@PV) is defined as the invariant mass of the system formed by the track associated with the electron and the closest track at the conversion (primary) vertex. $H_T$ is defined as the scalar sum of the transverse momentum of the isolated leptons and jets.

| Region | Channel | $N_j$ | $N_b$ | Other requirements | Fitted variable |
|---|---|---|---|---|---|
| CRttbarCO2l | $e^\pm e^\pm \| \| e^\pm \mu^\pm$ | $4 \leq N_j < 6$ | $\geq 1$ | $M_{ee}$@CV $\in [0, 0.1$ GeV$]$ <br> $200 < H_T < 500$ GeV | $M_{ee}$@PV |
| CR1b3Le | $eee \| \| ee\mu$ | - | $= 1$ | $100 < H_T < 250$ GeV | counting |
| CR1b3Lm | $e\mu\mu \| \| \mu\mu\mu$ | - | $= 1$ | $100 < H_T < 250$ GeV | counting |
| CRttW2l | $e^\pm\mu^\pm \| \| \mu^\pm\mu^\pm$ | $\geq 4$ | $\geq 2$ | $M_{ee}$@CV $\notin [0, 0.1$ GeV$]$, $\|\eta(e)\| < 1.5$ <br> for $N_b = 2$, $H_T < 500$ GeV or $N_j < 6$ <br> for $N_b \geq 3$, $H_T < 500$ GeV | $\Sigma p_T{}^\ell$ |

four control regions with different discriminating variables are used in the analysis. These control regions are summarized in Table 7.2 and are defined below:

- CRttbarCO2l is enriched in background events arising from both material conversions and $\gamma^*$ processes. This region is obtained by selecting events with $m_{trk-trk,CV}$, denoted as $M_{ee}$@CV (introduced in Section 4.3.1.4). In order to separate the material conversion and the $\gamma^*$, $m_{trk-trk,PV}$ (also denoted as $M_{ee}$@PV as introduced in Section 4.3.1.4) is used for the fit. Virtual photons lead to a lepton pair originating from the primary vertex, having $M_{ee}$@PV$\sim m_{\gamma^*}$ which peeks roughly at 0 GeV, while material conversions happen further away from the primary vertex and the track extrapolation induces a larger invariant mass. According to the MC simulation, the background arising from both $\gamma^*$ and material conversion accounts for around 45% of the events in the control region (See Figure 7.2).

- CR1b3Le (CR1b3Lm ) is enriched in background events with an electron (muon) coming from heavy-flavor decay. This region is defined by selecting events with three leptons, namely $eee$ and $ee\mu$ ($\mu\mu\mu$ and $\mu\mu e$) for CR1b3Le (CR1b3Lm ), and exactly one identified $b$-jet. This selection targets $t\bar{t}$ dileptonic decays with an extra non-prompt lepton in events with low $H_T$. The number of events in the region is used in the maximum likelihood fit. According to the MC simulation, the background with an electron (muon) coming from heavy flavor decay accounts for around 40% (50%) of the events in the CR1b3Le (CR1b3Lm ) control region (See Figure 7.2).

- CRttW2l is enriched in $t\bar{t}W$ events. This region is obtained by selecting $e\mu$ and $\mu\mu$ events with at least four jets and two $b$-jets, and it is required to be orthogonal to the signal region and other control regions. Events containing electrons with $|\eta| > 1.5$ and $ee$ final states are not considered in order to reduce the contamination arising from charge misassignment background. The sum of the lepton $p_T$ provides a good discrimination against other processes and

is used in the maximum likelihood fit. According to the MC simulation, the $t\bar{t}W$ background accounts for around $45\%$ of the events in the control region (See Figure 7.2).

The normalization factors of different background sources determined from the fit are shown on Table 7.3.

Table 7.3: Normalization factors for various backgrounds determined from the fit to the control regions. The uncertainties include both statistical and systematic contributions.

| Parameter | $\mathrm{NF}_{t\bar{t}W}$ | $\mathrm{NF}_{\mathrm{Mat.\ Conv.}}$ | $\mathrm{NF}_{\mathrm{Low\ M_{ee}}}$ | $\mathrm{NF}_{\mathrm{HFe}}$ | $\mathrm{NF}_{\mathrm{HF}\mu}$ |
|-----------|--------------------------|--------------------------------------|--------------------------------------|------------------------------|--------------------------------|
| Value | $1.6 \pm 0.3$ | $1.6 \pm 0.5$ | $0.9 \pm 0.4$ | $0.8 \pm 0.4$ | $1.0 \pm 0.4$ |
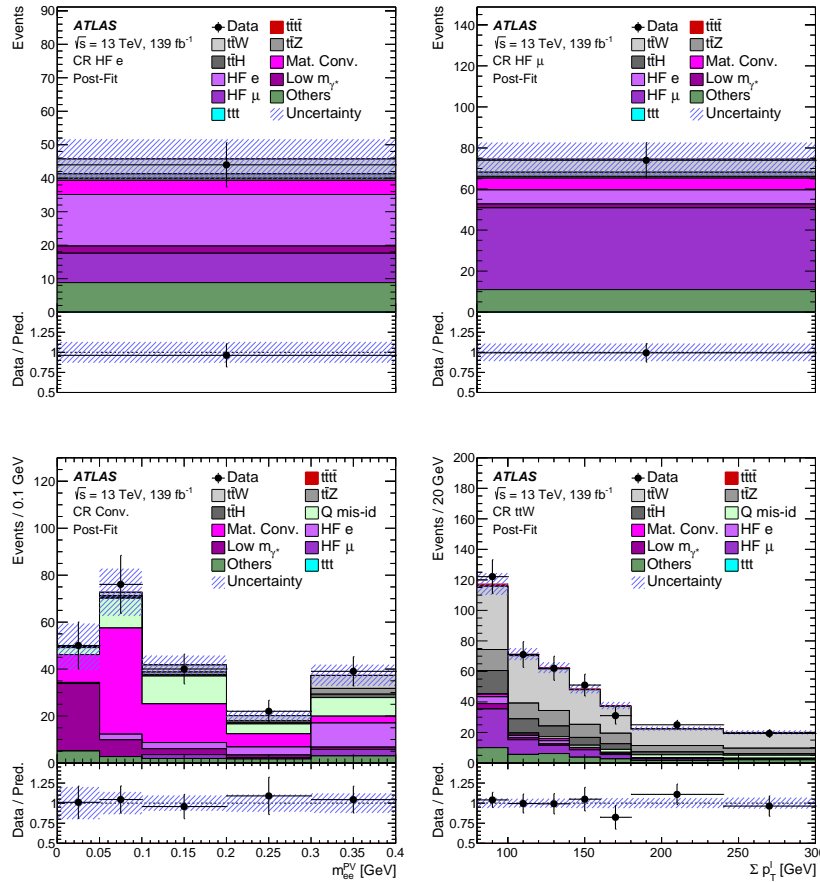


Figure 7.3: Comparison between data and prediction after the fit ("Post-Fit") for the distributions of the variables used in the fit in each control region (see Table 7.2). The band includes the total uncertainty on the post-fit computation. The ratio of the data to the total post-fit computation is shown in the lower panel. The first and last bins contain underflow and overflow events, respectively.

Figure 7.3 shows the yields or the discriminating variable distributions used in the fit in each control region. Good agreement is observed between the data and the post-fit prediction. The

normalization factor for the $t\bar{t}W$ background is compatible with the observation from the $t\bar{t}H$ multilepton analysis (see Section 6.3).

In order to assess the $t\bar{t}W$ background modeling, a validation region is defined based on the fact that the $t\bar{t}W$ process is charge asymmetric. The difference between the number of events with a positive sum and the number of events with a negative sum of the charges of the selected leptons is built in the region with at least four jets and at least two $b$-tagged jets. Such procedure removes the charge symmetric processes and allows to construct distributions where $t\bar{t}W$ events dominate. The BDT score distribution is displayed in Figure 7.4a which shows a good agreement between data and post-fit predictions. The jet multiplicity distribution is shown in Figure 7.4b, and a data excess is observed for the high jet multiplicities. An additional $125\%$ ($300\%$) uncertainty is added for $t\bar{t}W$ production with 7 (8 or more) jets.
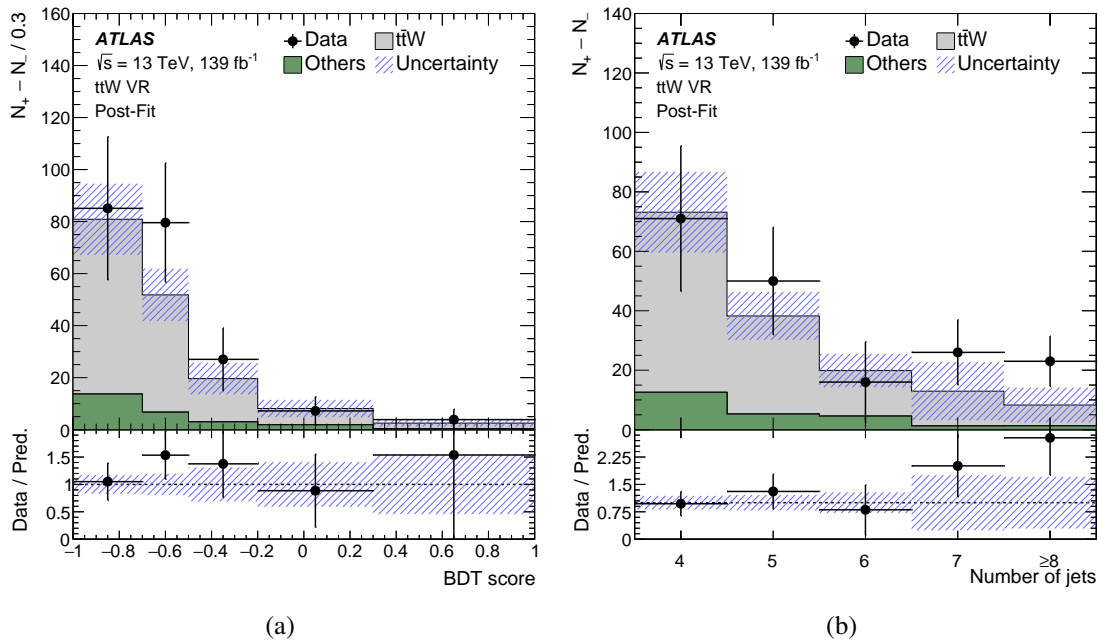


Figure 7.4: Post-fit comparison between data and prediction in the $t\bar{t}W$ validation region for the BDT score (left) and the multiplicity of jets (right). The y-axis label $N_+ - N_-$ represents the difference between the number of events with a positive sum and the number of events with a negative sum of the charges of the selected leptons. The band includes the total uncertainty on the post-fit computation. The ratio of the data to the total post-fit computation is shown in the lower panel. The first and last bins contain underflow and overflow events, respectively.

# 7.3 Signal Discrimination

The background composition of the SR is largely dominated by the production of top-quark pair in association with additional jets and/or bosons. To separate signal from background events, a multivariate discriminant is built in the SR combining several input observables into a BDT. In total, 12 observables are selected based on topological aspects of the events:

- **Jet activity:**

    - the leading jet $p_T$, $p_T(j_0)$,

    - the subleading jet $p_T$, $p_T(j_1)$,

    - the $6^{th}$ jet $p_T$, $p_T(j_5)$: the $6^{th}$ jet in backgrounds mainly comes from ISR or FSR which is softer compared with that in the $t\bar{t}t\bar{t}$ process,

    - $H_T$ (noleadjet) using all reconstructed objects in the event but the leading jet;

- $b$-**tagging information:**

    - Sum of $b$-tag scores: the pseudo-continuous $b$-tagging discriminant score (as described in Section 4.4.1) summed over all the jets in the event,

    - $p_T$ of the leading MV2c10 $b$-tagged jets;

- **Angular variables:**

    - $\min(\Delta R(\ell, \ell))$: the closest distance between any lepton pair,

    - $\max(\Delta R(\ell, b))$: the maximum distance between leptons and $b$-tagged jets,

    - $\min(\Delta R(j, b))$: the minimum distance between jets and $b$-tagged jets,

    - $\text{sum}\Delta R(\ell, \ell)$: sum of the distance between leading and sub-leading leptons in SS or any leptons pairs in 3L;

- **Event variables and lepton information:**

    - missing transverse energy, MET,

    - leading lepton $p_T$, $p_T(\ell_0)$.

Figure 7.5 shows the modeling of these input variables. Overall, good agreements are observed. Among them, sum of $b$-tag scores is the best discriminating variable due to the four $b$-jets produced mainly in signal events. The BDT training is performed inclusively, both in lepton flavor and lepton multiplicity for events passing the SR requirements. A set of BDT hyperparameters are
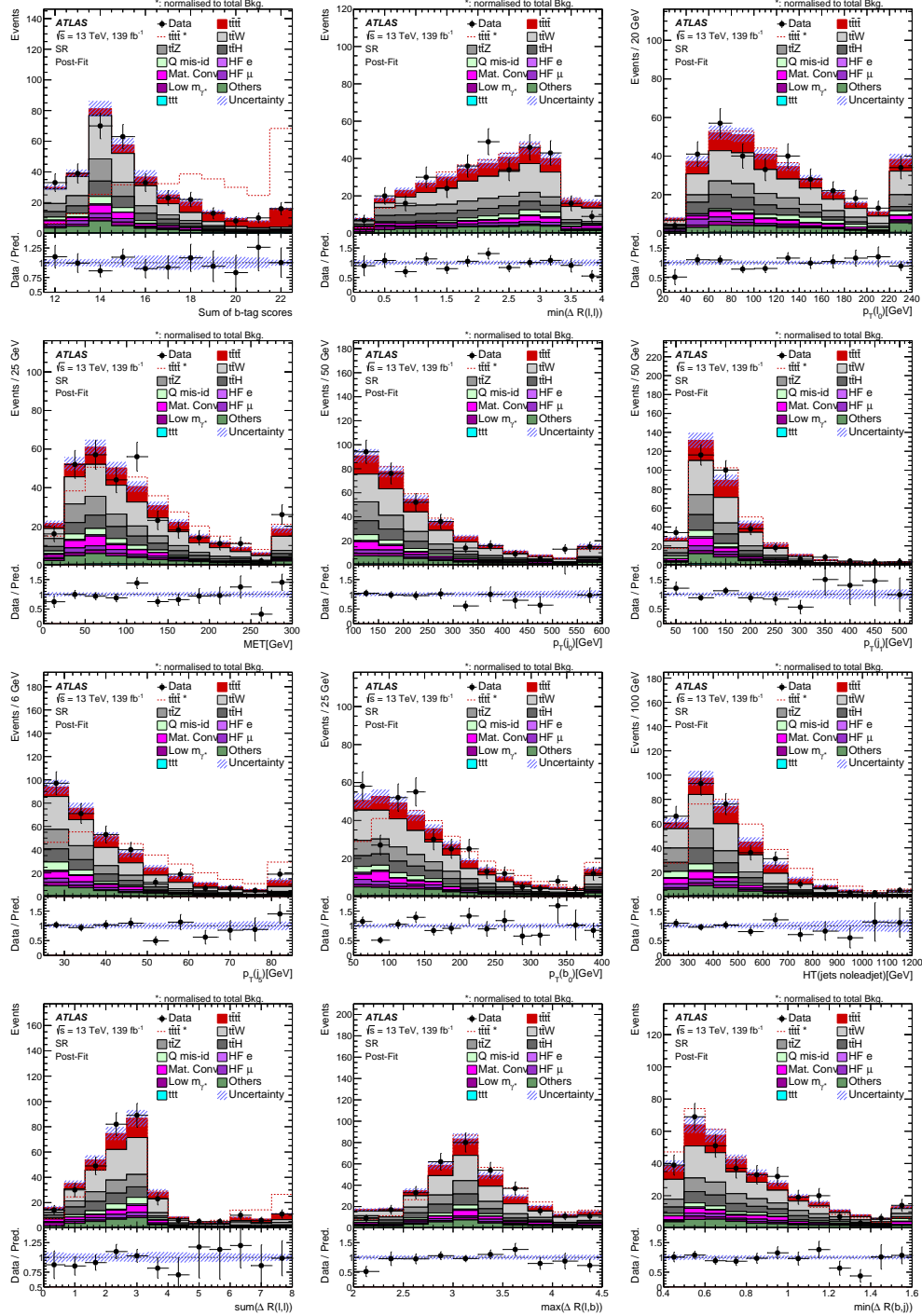
Figure 7.5: Post-fit comparison between data and prediction in the signal region for the variables used to train the multivariate discriminant. The ratio of the data to the total post-fit computation is shown in the lower panel. The dashed red histogram represents the signal scaled to the total number of background events. The first and last bins contain underflow and overflow events, respectively.

optimized to maximize the integral under the Receiver-Operator-Characteristics (ROC)[175] curve of the BDT. To check the performance of the BDT with the chosen input variables and the BDT hyperparameters, training-testing-validation method are used. Signal and background samples are split into three subsets: training, testing and validation. For $t\bar{t}t\bar{t}$ signal samples, LO sample is used for training, 80% of NLO sample is used for testing and the remaining 20% of the NLO sample is used in validation. For background samples, 20% is used for validation, 40% is used for training and the remaining 40% is used for testing. A schematic summary of the strategy described here is shown in Figure 7.6. Distributions of the signal and background BDT responses for training,
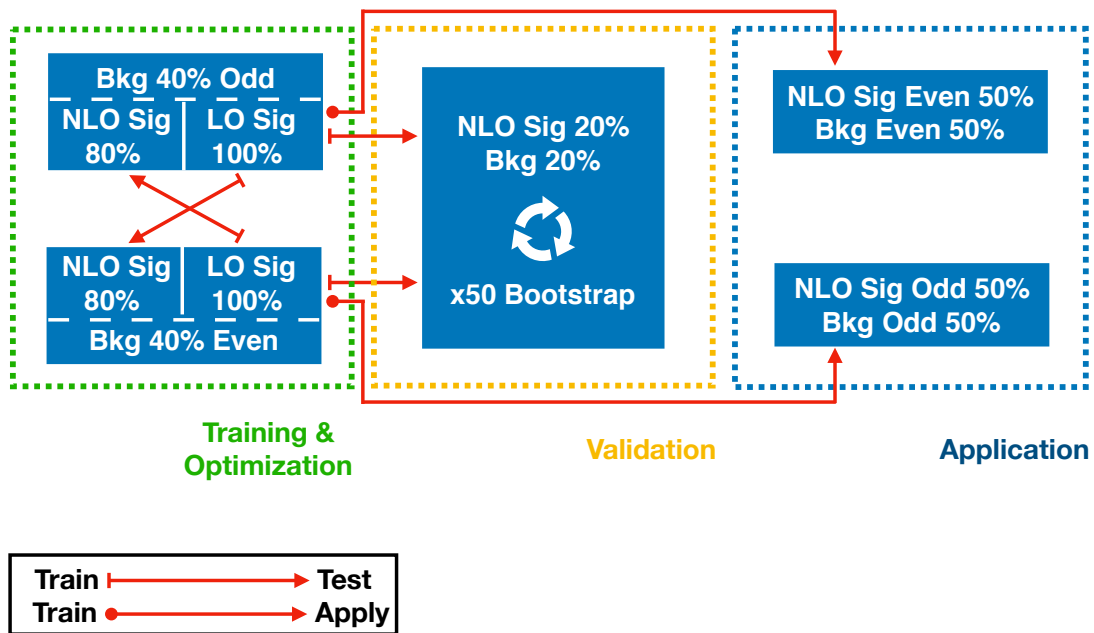


Figure 7.6: The schematic representation of sample fractions and training-testing-validation method.

testing and validation are shown in Figure 7.7a and 7.7b. The good agreement among training, testing and validation samples demonstrate that there is no over-training. Figure 7.8 shows the final BDT distribution and the corresponding background composition for data and signal-plus-background predication. A fairly good data modeling is observed.
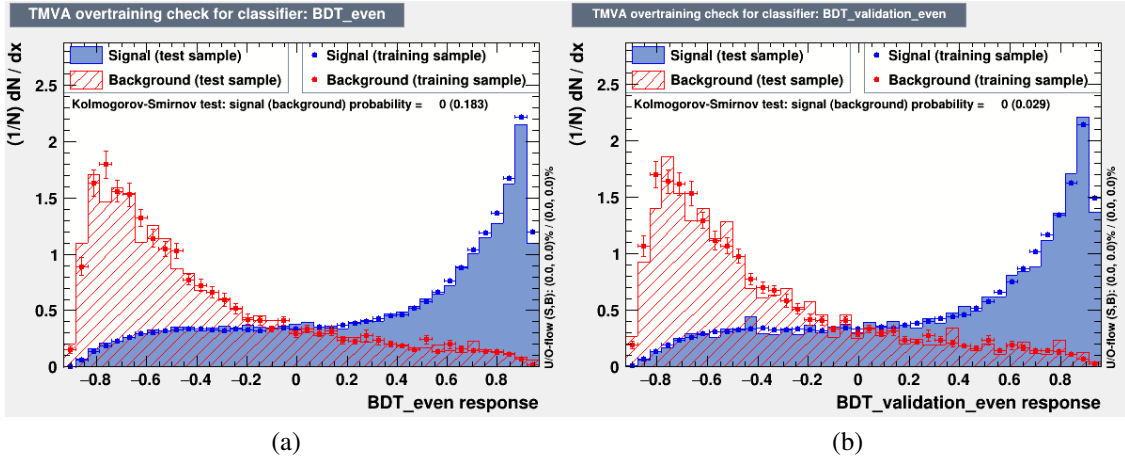
Figure 7.7: (a)Distribution of BDT response for training and testing samples and (b) Distribution of BDT response for training and validation samples.
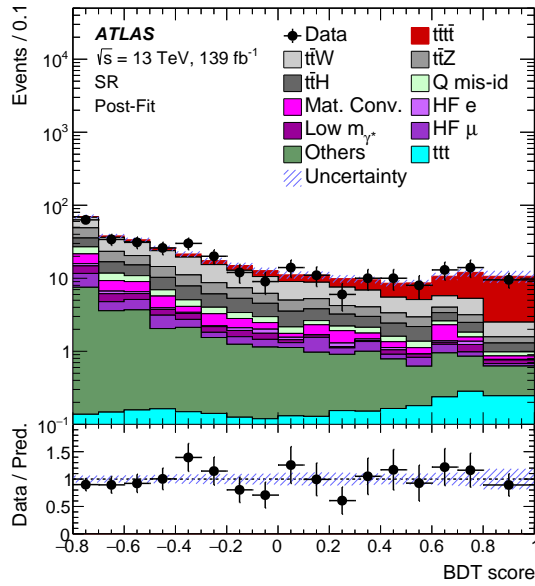


Figure 7.8: Comparison between data and prediction after the fit ("Post-Fit") for the distribution of the BDT score in the SR. The band includes the total uncertainty on the post-fit computation. The ratio of the data to the total post-fit computation is shown in the lower panel.

## 7.4 Systematic Uncertainties

A summary of systematic uncertainties is given in this section, mainly covering experimental systematics, signal and background modeling theoretical systematics. An overview of systematics relevant to the $t\bar{t}t\bar{t}$ analysis can be found in Table 7.4. Experimental systematics are discussed in Section 5.3. Systematics for signal and background modeling will be discussed in this section.

Table 7.4: Sources of systematic uncertainty considered in the analysis. "(N)" means that the uncertainty is taken as normalization-only for all processes and regions affected. All other uncertainties also affect the shape of the fitted distributions and/or the acceptance in the fit regions. Some of the systematic uncertainties are split into several Components, as indicated by the number in the rightmost column.

| Systematic uncertainty | Components |
| --- | --- |
| Luminosity (N) | 1 |
| Pile-Up reweighting | 1 |
| **Physics Objects** | |
| Electron | 7 |
| Muon | 12 |
| Jet energy scale and resolution | 39 |
| Jet vertex fraction | 1 |
| Jet flavor tagging | 85 |
| $E_T^{\text{miss}}$ | 3 |
| Total (Experimental) | 144 |
| Electron charge misassignment | 2 |
| **Template Fit uncertainties** | |
| Material conversions | 1 |
| Internal conversions | 1 |
| HF non-prompt leptons | 2 |
| Other fake leptons | 2 |
| Additional heavy flavor jets | 2 |
| Total (reducible background) | 10 |

| Systematic uncertainty | Components |
| --- | --- |
| $t\bar{t}t\bar{t}$ **modeling** | |
| Cross section (N) | 1 |
| Renormalization and factorization scales | 1 |
| Parton shower and hadronization model | 1 |
| PDF | 1 |
| $t\bar{t}H$ **modeling** | |
| Cross section (N) | 1 |
| Renormalization and factorization scales | 1 |
| Parton shower and hadronization model | 1 |
| PDF | 1 |
| Additional heavy flavor jets | 2 |
| $t\bar{t}W$ **modeling** | |
| Renormalization and factorization scales | 1 |
| Generator | 1 |
| Jets multiplicity modeling | 2 |
| Additional heavy flavor jets | 2 |
| $t\bar{t}Z$ **modeling** | |
| Cross section (N) | 1 |
| Renormalization and factorization scales | 1 |
| Generator | 1 |
| PDF | 1 |
| Additional heavy flavor jets | 2 |
| **Other background modeling** | |
| Cross section (N) | 5 |
| Additional heavy flavor jets | 3 |
| Total (Signal and background modeling) | 30 |
| Total (Overall) | 189 |

### 7.4.1 Signal and Background Modeling Systematics

#### 7.4.1.1 Signal Modeling Uncertainties

Several sources of modeling uncertainties are considered for the $t\bar{t}t\bar{t}$ signal. The uncertainty due to the missing higher-order QCD corrections is determined by varying the renormalization and the factorization scales simultaneously by a factor 2.0 and 0.5 with respect to their central values. The uncertainty related to the choices of the parton shower and hadronization model is estimated by comparing the nominal prediction with that obtained using an alternative sample generated with MADGRAPH5_AMC@NLO interfaced to HERWIG7(see Section 5.1). The PDF uncertainty in the signal MC prediction is calculated as the RMS of the 100 replicas of the NNPDF30_nlo_as_0118 PDF set following the PDF4LHC prescription [176]. The PDF uncertainty shape variations are very small and therefore are neglected. A flat uncertainty of 1% is assigned.

#### 7.4.1.2 Uncertainties for $t\bar{t}W$ , $t\bar{t}Z$ and $t\bar{t}H$ Processes

Modeling uncertainties for the $t\bar{t}Z$ and $t\bar{t}H$ processes are evaluated in a similar way and include the uncertainty due to the missing higher-order QCD corrections determined by varying the renormalization and the factorization scales simultaneously by a factor 2.0 and 0.5 with respect to their central value and a comparison with alternative generators. For the $t\bar{t}Z$ process, the nominal MC prediction is compared to an NLO SHERPA sample simulated with no additional jets, while for the $t\bar{t}H$ process the nominal simulation is compared to an NLO MADGRAPH5_AMC@NLO sample (described in Section 5.1). A 1% PDF uncertainty is assigned to both the $t\bar{t}Z$ and $t\bar{t}H$ processes. An uncertainty of $15\%$ ($20\%$) is applied to the $t\bar{t}Z$ ($t\bar{t}H$) total cross section [48, 177].

For the $t\bar{t}W$ process, discussions on the modeling systematics are given in Section 5.3 and 7.2.1.

The $t\bar{t}W$ , $t\bar{t}Z$ and $t\bar{t}H$ background processes enter the $t\bar{t}t\bar{t}$ signal region if they have additional heavy flavor jets. Such processes are difficult to model with the MC simulation. To account for this, an uncertainty of 50% is assigned to the events with three truth $b$-jets and a separate 50% uncertainty to the events with four or more truth $b$-jets. These uncertainties are based on the measurement of the $t\bar{t}$ production with additional heavy-flavor jets [178] and on the comparison between data and prediction in $t\bar{t}\,\gamma$ events with three and four $b$-tagged jets (shown in Figure 7.9).

#### 7.4.1.3 Uncertainties for Fake/Non-prompt Backgrounds

Systematic uncertainties for fake/non-prompt background are discussed in the following, although they have a negligible impact on the final result. Since the main source of the reducible background is $t\bar{t}$+jets production, the systematic uncertainty in the modeling of its heavy-flavor content can
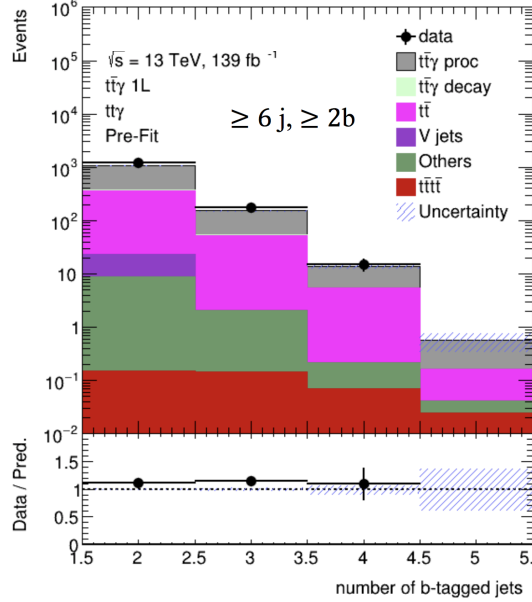
Figure 7.9: Comparison for $b$-tagged jet multiplicities between the data and the prediction in the $t\bar{t}\gamma$ events. The ratio of the data to the total post-fit computation is shown in the lower panel.

affect the shape of the template distributions used in the fit. To account for this effect an uncertainty of 30%, based on the measurement of the $t\bar{t}$ production with additional heavy-flavor jets [178], is assigned to the events with three truth $b$-jets and a separate 30% uncertainty to events with four or more truth $b$-jets. The uncertainty on the shape of the distributions for the heavy-flavor non-prompt lepton background is estimated by comparing the data to the background prediction, normalized to data, for a loose lepton selection with the isolation requirements dropped and relaxed identification criteria (see Section 5.3). An additional 25% uncertainty is applied to the material conversions and the $\gamma*$ processes, based on the comparison between data and simulation in a validation region of selected $Z \to \mu^+\mu^-\gamma^*(\to e^+e^-)$ candidate events.

### 7.4.1.4 Uncertainties for Other Backgrounds

The $t\bar{t}t$ production has similar event kinematics as the $t\bar{t}t\bar{t}$ signal, though the rate is expected to be much smaller. It is however currently unexplored experimentally. Thus a large ad-hoc uncertainty of 100% is assigned to its cross section and an additional 50% uncertainty is applied to $t\bar{t}t$ events with four truth $b$-jets.

The uncertainty on the $tZ$ and $tWZ$ single top-quark cross section is set to 30% [157, 179] and that for the $t\bar{t}WW$, $t\bar{t}ZZ$, $t\bar{t}WZ$,$t\bar{t}HH$ and $t\bar{t}WH$ cross sections to 50% [75]. The cross section uncertainty on the diboson production is set to 40% based on studies of the $WZ + b$ process. For each of the other small background processes, a large ad-hoc cross section uncertainty of 50% is

applied. For all small backgrounds except $t\bar{t}t$ , an additional 50% uncertainty is assigned to the events with three truth $b$-jets and separately a 50% uncertainty is applied to events with four or more truth $b$-jets.

## 7.5 Results

The $t\bar{t}t\bar{t}$ production cross section is measured via a binned likelihood fit of the BDT score distribution in the signal region and of the discriminating variables in the four control regions listed in Table 7.2. The fit determines the best value of the signal strength $\mu$, defined as a ratio of the $t\bar{t}t\bar{t}$ cross section to the SM expectation, its uncertainty, and five normalization factors. An uncertainty of 20% is assigned to the $t\bar{t}t\bar{t}$ cross section predicted by the SM.

The best-fit value of $\mu$ is:

$$\mu = 2.0\,^{+0.4}_{-0.4}(\text{stat})\,^{+0.7}_{-0.5}(\text{syst}) = 2.0\,^{+0.8}_{-0.6}. \tag{7.1}$$

After converting the fitted signal strength into an inclusive cross section using the SM $t\bar{t}t\bar{t}$ predicted cross section of $\sigma_{t\bar{t}t\bar{t}} = 12 \pm 2$ fb computed at NLO in QCD and electroweak corrections [63] for a top-quark mass of $172.5$ GeV, the measured $t\bar{t}t\bar{t}$ production cross section is:

$$\sigma_{t\bar{t}t\bar{t}} = 24\,^{+5}_{-5}(\text{stat})\,^{+5}_{-4}(\text{syst})\,\text{fb} = 24\,^{+7}_{-6}\,\text{fb}. \tag{7.2}$$

The $p$-value of the background-only hypothesis is derived using a profile-likelihood ratio (see Section 5.4). The negative log-likelihood (NLL) distribution for the $t\bar{t}t\bar{t}$ cross section is shown
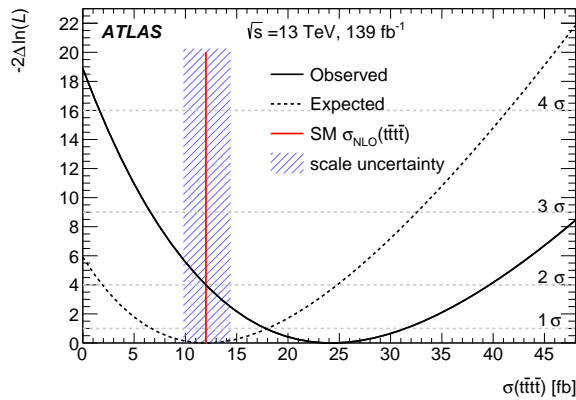


Figure 7.10: The negative log-likelihood (NLL) distribution for the cross section. The plain line represents the observed likelihood while the dashed line corresponds to the expected one. The red line shows the SM theory cross section [63] with its scale uncertainties (dashed region).

in Figure 7.10. From this, the significance of the observed signal is found to be 4.3 standard deviations, while the expected significance is 2.4 standard deviations. The measured cross section is consistent within 1.7 standard deviations with the SM prediction.

Table 7.5: Post-fit background and signal yields in the full signal region and requiring in addition the BDT score to be greater than 0. The total systematic uncertainty differs from the sum in quadrature of the different uncertainties due to correlations. Q Mis-ID refers to the charge misassignment background. Mat. Conv. and Low $M_{ee}$ refer respectively to events with one non-prompt electron originating from photon conversion taking place in the detector material and to events with a virtual photon leading to an $e^{\pm}e^{\pm}$ pair. HF e (HF $\mu$) refers to events with one non-prompt electron (muon) from heavy-flavor decay, and LF refers to events with a lepton originating from light-meson decay.

|  | SR | SR and BDT$> 0$ |
|---|---|---|
| $t\bar{t}W$ | $102 \pm 26$ | $23 \pm 10$ |
| $t\bar{t}WW$ | $7 \pm 4$ | $2 \pm 1$ |
| $t\bar{t}Z$ | $48 \pm 9$ | $9 \pm 2$ |
| $t\bar{t}H$ | $38 \pm 9$ | $8 \pm 2$ |
| Q mis-id | $16 \pm 1$ | $2.7 \pm 0.2$ |
| Mat. Conv. | $19 \pm 6$ | $3 \pm 1$ |
| Low $M_{ee}$ | $9 \pm 4$ | $0.9 \pm 0.5$ |
| HF e | $3 \pm 3$ | $1 \pm 1$ |
| HF $\mu$ | $12 \pm 6$ | $3 \pm 2$ |
| LF | $4 \pm 5$ | $1 \pm 1$ |
| other fake | $6 \pm 2$ | $2 \pm 1$ |
| other t($\bar{t}$)X | $5 \pm 2$ | $1.0 \pm 0.4$ |
| VV | $3 \pm 2$ | $0.2 \pm 0.2$ |
| others | $4 \pm 3$ | $1 \pm 1$ |
| $t\bar{t}t$ | $3 \pm 3$ | $2 \pm 2$ |
| Total bkg | $278 \pm 22$ | $59 \pm 10$ |
| $t\bar{t}t\bar{t}$ | $60 \pm 17$ | $44 \pm 12$ |
| Total | $337 \pm 18$ | $103 \pm 10$ |
| Data | $330$ | $105$ |

The post-fit background and signal yields are shown on Table 7.5. The distributions for some of the key analysis variables are shown in Figure 7.11 for the events in the signal region and in Figure 7.12 for events in a signal-enriched region with a BDT score above zero. Good agreement is observed.

The uncertainties impacting $\mu$ are summarized in Table 7.6. Apart from the theoretical uncer-
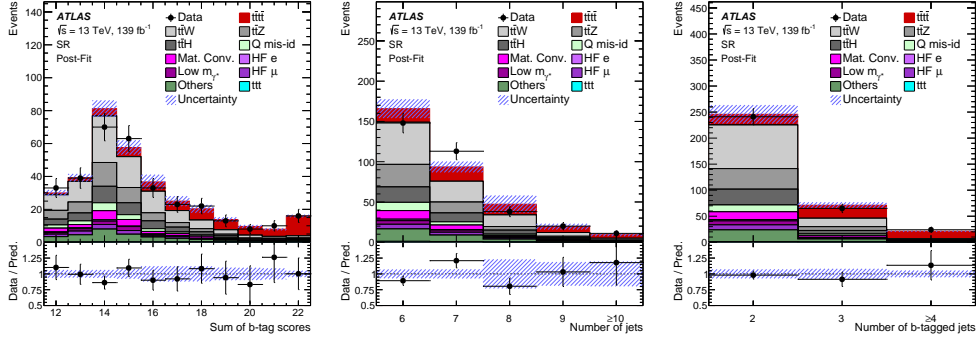
Figure 7.11: Post-fit comparison between data and prediction for signal region events for the distributions of: the sum of $b$-tagging pseudo-continuous scores of the jets in the event (left), the multiplicity of jets (middle) and the the multiplicity of $b$-tag jets (right). The band includes the total uncertainty on the post-fit computation. The ratio of the data to the total post-fit computation is shown in the lower panel. The first and last bins contain underflow and overflow events, respectively.
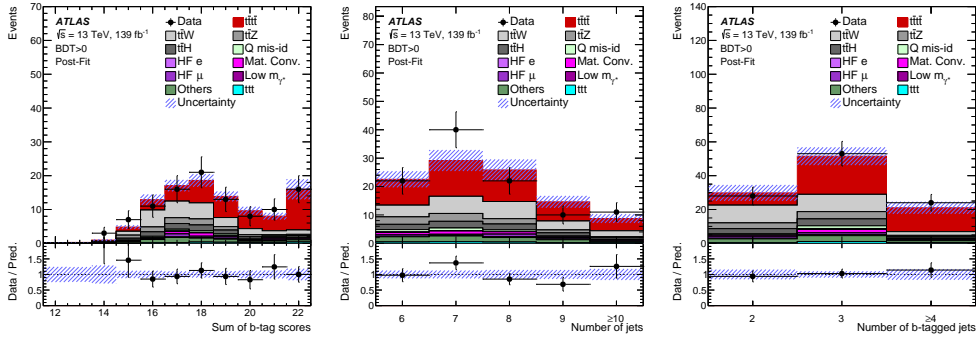


Figure 7.12: Post-fit comparison between data and prediction for signal region events with a BDT score greater than zero for the distributions of: the sum of $b$-tagging pseudo-continuous scores of the jets in the event (left), the multiplicity of jets (middle) and the the multiplicity of $b$-tag jets (right). The band includes the total uncertainty on the post-fit computation. The ratio of the data to the total post-fit computation is shown in the lower panel. The first and last bins contain underflow and overflow events, respectively.

tainty on the signal cross section, the largest systematic uncertainty is coming from the modeling of the $t\bar{t}W$ process. Within the uncertainties on the background modeling, the impact of the uncertainty on $t\bar{t}t$ production is also significant. The expected cross section of this process is only of the order of 10% of $\sigma_{t\bar{t}t\bar{t}}$. However the shape of the BDT score distribution for $t\bar{t}t$ production is similar to the one from the signal, thus leading to a sizable impact of this uncertainty on $\mu$. In order to test the sensitivity of the $t\bar{t}t\bar{t}$ measurement to the value of the $t\bar{t}t$ cross section, the fit has been also performed assuming a $t\bar{t}t$ cross section 5 times larger than the expected SM cross section. In that case the $t\bar{t}t\bar{t}$ signal strength $\mu$ decreases by 10% while the fitted background normalization

Table 7.6: List of the uncertainties on the signal strength $\mu$, grouped in categories.

| Uncertainty source | $\Delta\mu$ | |
|---|---|---|
| Signal modeling | | |
| $t\bar{t}t\bar{t}$ cross section | $+0.56$ | $-0.31$ |
| $t\bar{t}t\bar{t}$ modeling | $+0.15$ | $-0.09$ |
| Background modeling | | |
| $t\bar{t}W$ modeling | $+0.26$ | $-0.27$ |
| $t\bar{t}t$ modeling | $+0.10$ | $-0.07$ |
| Non-prompt leptons modeling | $+0.05$ | $-0.04$ |
| $t\bar{t}H$ modeling | $+0.04$ | $-0.01$ |
| $t\bar{t}Z$ modeling | $+0.02$ | $-0.04$ |
| Charge misassignment | $+0.01$ | $-0.02$ |
| Instrumental | | |
| Jet uncertainties | $+0.12$ | $-0.08$ |
| Jet flavor tagging (light-jets) | $+0.11$ | $-0.06$ |
| Simulation sample size | $+0.06$ | $-0.06$ |
| Luminosity | $+0.05$ | $-0.03$ |
| Jet flavor tagging ($b$-jets) | $+0.04$ | $-0.02$ |
| Other experimental uncertainties | $+0.03$ | $-0.01$ |
| Jet flavor tagging ($c$-jets) | $+0.03$ | $-0.01$ |
| Total systematic uncertainty | $+0.69$ | $-0.46$ |
| Statistical | $+0.42$ | $-0.39$ |
| Non-prompt leptons normalization(HF, material conversions) | $+0.05$ | $-0.04$ |
| $t\bar{t}W$ normalization | $+0.04$ | $-0.04$ |
| Total uncertainty | $+0.82$ | $-0.62$ |

factors are mostly unaffected. Only few nuisance parameters in the fit show significant adjustments and/or constraints (see Figure 7.13). The post-fit value of the nuisance parameters associated to the systematic uncertainty on the $t\bar{t}W$ background with $N_{\text{jets}} = 7$ is $0.18^{+0.73}_{-0.61}$, corresponding to an increase of 22% for $t\bar{t}W$ events with 7 jets and with $N_{\text{jets}} \geq 8$ is $0.22^{+0.56}_{-0.42}$, corresponding to an increase of 65% on the $t\bar{t}W$ events with $\geq 8$ jets. As a result of these increases and of the $t\bar{t}W$ background normalization factor $\text{NF}_{t\bar{t}W}$ , the overall $t\bar{t}W$ background yield in the signal-enriched region with a BDT score above zero is increased from the $12.4\pm8.8$ events predicted to $23.2\pm10.1$ events after the fit to data.

The stability of the result has been checked with respect to many aspects. The measured signal strength was found to be robust under these cross checks.

A fit was performed with SR split according to same-sign dilepton events (denoted as 2LSS channel) and events with at least three leptons (denoted as 3L channel). The individual channel re-
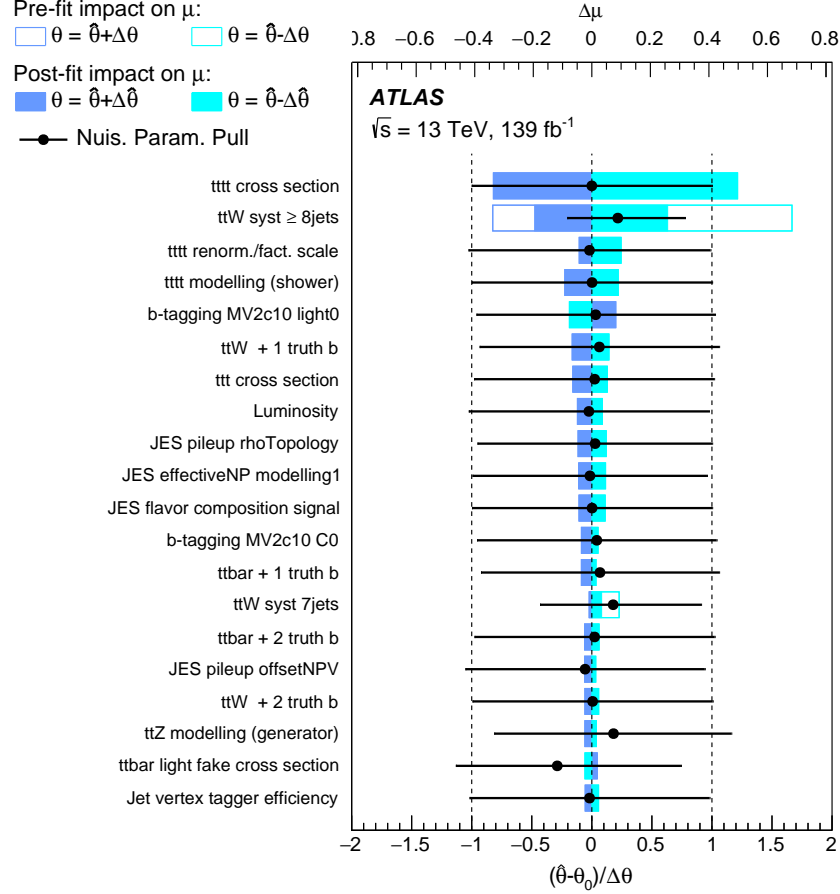
Figure 7.13: Ranking of the nuisance parameters included in the fit according to their impact on the signal strength $\mu$. Only the 20 highest ranked nuisance parameters are shown. The empty blue rectangles correspond to the pre-fit impact on $\mu$ and the filled blue ones to the post-fit impact on $\mu$, both referring to the upper $x$-axis scale. The impact of each nuisance parameter, $\Delta\mu$, is computed by comparing the nominal best-fit value of $\mu$ with the result of the fit when fixing the considered nuisance parameter to its best-fit value, $\hat{\theta}$, shifted by its pre-fit (post-fit) uncertainties $\pm\Delta\theta$ ($\pm\Delta\hat{\theta}$). The black points show the pulls of the parameter relative to their nominal values, $\theta_0$. The nominal value for all parameters is $\theta_0 = 0$. The pulls of the most impacting parameters and their relative post-fit errors, $\Delta\hat{\theta}/\Delta\theta$, refer to the lower $x$-axis scale.

sults are extracted from the fit with a separate parameter of interest for each channel. The resulting best-fit signal strengths were found to be $\mu_{2\text{LSS}} = 1.9^{+0.7}_{-0.7}$ and $\mu_{3\text{L}} = 1.9^{+1.0}_{-0.8}$ for 2LSS channel and 3L channel, respectively.

A fit was performed with the SR split according to the sign of the sum of the charges of the selected leptons in the event. The resulting best-fit signal strengths were found to be $\mu_+ = 2.7^{+0.9}_{-0.8}$ and $\mu_- = 1.6^{+0.7}_{-0.7}$ for events with a positive and negative sum of the charges of the selected leptons, respectively. They are consistent with the nominal result within 1 standard deviation.

A comparison was made between the results from nominal multivariate analysis and the cross-

check $H_T$ analysis. In the $H_T$ analysis, the SR is split into 5 regions according to the number of leptons and $b$-tagged jets and by fitting the $H_T$ distribution in each region. The selection criteria applied are shown in Table 7.7. This analysis share the same control regions as the nominal anal-

Table 7.7: Selection criteria applied in the $H_T$ analysis, together with the event categories defined. The common selection criteria for all signal regions are listed in the fist line under the title "Common".

| Channel | Selection criteria |
|---------|--------------------|
| Common | $N_j \geq 6$, $N_b \geq 2$ and $H_T > 500$ GeV |
| SR2b2l | SS events with $N_b = 2$ |
| SR2b3l | multilepton events with $N_b = 2$ |
| SR3b2l | SS events with $N_b = 3$ |
| SR3b3l | multilepton events with $N_b = 3$ |
| SR4b | events with $N_b \geq 4$ |

ysis. Comparison between data and prediction for the $H_T$ distribution are shown in Figure 7.14.
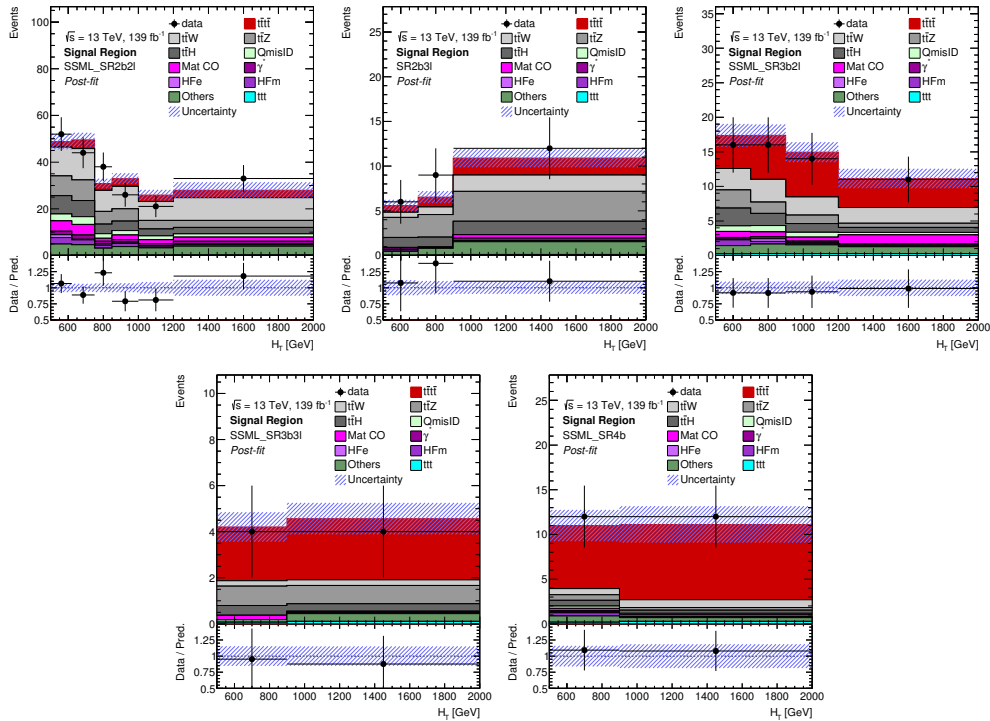


Figure 7.14: Comparison between data and prediction after the fit ("Post-Fit") for the distributions of the $H_T$ used in the fit in $H_T$ analysis. The band includes the total uncertainty on the post-fit computation. The ratio of the data to the total post-fit computation is shown in the lower panel. The first and last bins contain underflow and overflow events, respectively.

The observed (expected) significance is found to be $4.3$ $(2.1)$ and the signal strength is fitted to

$2.2^{+0.9}_{-0.6}$. This result is consistent with the result from the nominal fit.

The combined fit was performed separately on the 2015-2016 dataset (36 fb$^{-1}$), the 2017 dataset (44 fb$^{-1}$) and the 2018 dataset (59 fb$^{-1}$). The resulting best-fit signal strengths were found to be consistent among these three datasets: $\mu = 3.2^{+1.5}_{-1.0}$ for 2015-2016, $\mu = 1.2^{+1}_{-0.7}$ for 2017 and $\mu = 1.8^{+0.9}_{-0.7}$ for 2018.

# CHAPTER 8

# Summary and Outlook

In this dissertation, a search for the associated production of a Higgs boson with a top quark pair in the SSML final states and the evidence of $t\bar{t}t\bar{t}$ procution are presented. In these analyses, some excesses observed in data need to be better understood.

With 80 fb$^{-1}$ of $pp$ collision data at $\sqrt{s} = 13$ TeV collected in 2015-2017, the observed production cross section for $t\bar{t}H$ is $294^{+182}_{-162}$ fb, in agreement with the SM prediction of $507^{+35}_{-50}$ fb. The observed production rate of the $t\bar{t}W$ background process in the phase space selected by this analysis is $1.3-1.7$ times that of the SM expectation. Higher $t\bar{t}W$ production rate is also confirmed in other analyses and by the CMS experiment[180]. This points to the current limited understanding of the modeling of $t\bar{t}W$ production in the SSML phase space. BSM physics, e.g. the production of charged Higgs[181], might be hiding in this corner of phase space and more studies and scrutiny are needed to understand the observed high $t\bar{t}W$ production rate.

The evidence of $t\bar{t}t\bar{t}$ production is achieved with the 139 fb$^{-1}$ dataset. The $t\bar{t}t\bar{t}$ production cross section is measured to be $24^{+7}_{-6}$ fb, consistent within 1.7 standard deviation with the SM expectation of $\sigma_{t\bar{t}t\bar{t}} = 12.0 \pm 2.4$ fb. The slight excess of observed $t\bar{t}t\bar{t}$ production might point to possible BSM physics. Models like SUSY and 2HDM could enhance the $t\bar{t}t\bar{t}$ production. Further analysis of this excess and possible BSM interpretations are on-going.

As the LHC physics program continues, SSML final states remain to be interesting. On one hand, the observed excess in the current dataset needs to be confirmed and understood. On the other hand, the increased dataset will allow to study even more rarer processes.

# BIBLIOGRAPHY

[1] S. Tomonaga. On a Relativistically Invariant Formulation of the Quantum Theory of Wave Fields*. *Progress of Theoretical Physics*, 1(2):27–42, 08 1946.

[2] R. P. Feynman. Space-time approach to quantum electrodynamics. *Phys. Rev.*, 76:769–789, Sep 1949.

[3] R. P. Feynman. The theory of positrons. *Phys. Rev.*, 76:749–759, Sep 1949.

[4] R. P. Feynman. Mathematical formulation of the quantum theory of electromagnetic interaction. *Phys. Rev.*, 80:440–457, Nov 1950.

[5] Julian Schwinger. On quantum-electrodynamics and the magnetic moment of the electron. *Phys. Rev.*, 73:416–417, Feb 1948.

[6] Julian Schwinger. Quantum electrodynamics. i. a covariant formulation. *Phys. Rev.*, 74:1439–1461, Nov 1948.

[7] C. N. Yang and R. L. Mills. Conservation of isotopic spin and isotopic gauge invariance. *Phys. Rev.*, 96:191–195, Oct 1954.

[8] R. L. Mills and C. N. Yang. Treatment of Overlapping Divergences in the Photon Self-Energy function*. *Progress of Theoretical Physics Supplement*, 37-38:507–511, 03 1966.

[9] Peter W. Higgs. Broken symmetries and the masses of gauge bosons. *Phys. Rev. Lett.*, 13:508–509, Oct 1964.

[10] F. Englert and R. Brout. Broken symmetry and the mass of gauge vector mesons. *Phys. Rev. Lett.*, 13:321–323, Aug 1964.

[11] Peter Ware Higgs. Broken symmetries, massless particles and gauge fields. *Phys. Lett.*, 12:132–133, 1964.

[12] Yuval Ne'eman. Derivation of strong interactions from a gauge invariance. *Nucl. Phys.*, 26:222–229, 1961.

[13] Murray Gell-Mann. Symmetries of baryons and mesons. *Phys. Rev.*, 125:1067–1084, 1962.

[14] Murray Gell-Mann. A schematic model of baryons and mesons. *Phys. Lett.*, 8:214–215, 1964.

[15] G. Zweig. An su(3) model for strong interaction symmetry and its breaking. version 1. 1 1964.

[16] The UA2 Collaboration. Observation of single isolated electrons of high transverse momentum in events with missing transverse energy at the cern pp collider. *Physics Letters B*, 122(5):476 – 485, 1983.

[17] UA1 Collaboration. Experimental observation of isolated large transverse energy electrons with associated missing energy at s=540 gev. *Physics Letters B*, 122(1):103 – 116, 1983.

[18] P. Bagnaia et al. Evidence for $z^0 \rightarrow e^+ e^-$ at the cern $\bar{p}p$ collider. *Phys. Lett. B*, 129:130–140, 1983.

[19] G. Arnison et al. Experimental observation of lepton pairs of invariant mass around 95-GeV/c$^2$ at the cern sps collider. *Phys. Lett. B*, 126:398–410, 1983.

[20] Observation of the top quark. *Phys. Rev. Lett.*, 74:2632–2637, Apr 1995.

[21] Observation of top quark production in $\overline{p}p$ collisions with the collider detector at fermilab. *Phys. Rev. Lett.*, 74:2626–2631, Apr 1995.

[22] Observation of a new particle in the search for the standard model higgs boson with the atlas detector at the lhc. *Physics Letters B*, 716(1):1 – 29, 2012.

[23] Observation of a new boson at a mass of 125 gev with the cms experiment at the lhc. *Physics Letters B*, 716(1):30 – 61, 2012.

[24] R. Michael Barnett, John F. Gunion, and Howard E. Haber. Discovering supersymmetry with like-sign dileptons. *Physics Letters B*, 315(3-4):349354, Oct 1993.

[25] F.M.L. Almeida, Y.A. Coutinho, J.A. Martins Simes, P.P. Queiroz Filho, and C.M. Porto. Same-sign dileptons as a signature for heavy majorana neutrinos in hadron-hadron collisions. *Physics Letters B*, 400(3-4):331334, May 1997.

[26] J. A. Aguilar-Saavedra, R. Benbrik, S. Heinemeyer, and M. Pérez-Victoria. Handbook of vectorlike quarks: Mixing and single production. *Physical Review D*, 88(9), Nov 2013.

[27] Idir Boucheneb, Giacomo Cacciapaglia, Aldo Deandrea, and Benjamin Fuks. Revisiting monotop production at the lhc. *Journal of High Energy Physics*, 2015(1), Jan 2015.

[28] Robert. Oerter. The theory of almost everything: the standard model, the unsung triumph of modern physics. 2006.

[29] Wikipedia contributors. Standard model, 2004. Online; accessed 8-July-2020.

[30] Emmy Noether and M. A. Tavel. Invariant variation problems. 1971.

[31] Steven Weinberg. A model of leptons. *Phys. Rev. Lett.*, 19:1264–1266, Nov 1967.

[32] Sheldon L. Glashow. Partial-symmetries of weak interactions. *Nuclear Physics*, 22(4):579 – 588, 1961.

[33] Abdus Salam. Weak and Electromagnetic Interactions. *Conf. Proc. C*, 680519:367–377, 1968.

[34] M. Gell-Mann. The interpretation of the new particles as displaced charge multiplets. *Nuovo Cim.*, 4(S2):848–866, 1956.

[35] ATLAS Collaboration. Study of the spin and parity of the higgs boson in diboson decays with the atlas detector. *The European Physical Journal C*, 75(10), Oct 2015.

[36] ATLAS Collaboration. Test of cp invariance in vector-boson fusion production of the higgs boson using the optimal observable method in the ditau decay channel with the atlas detector. *The European Physical Journal C*, 76(12), Nov 2016.

[37] ATLAS Collaboration. Observation of higgs boson production in association with a top quark pair at the lhc with the atlas detector. *Physics Letters B*, 784:173–191, Sep 2018.

[38] ATLAS Collaboration. Observation of $h \rightarrow b\bar{b}$ decays and vh production with the atlas detector. *Physics Letters B*, 786:59–86, Nov 2018.

[39] ATLAS Collaboration. Measurements of the higgs boson production and decay rates and constraints on its couplings from a combined atlas and cms analysis of the lhc pp collision data at $\sqrt{s} = 7$ and 8 tev. *Journal of High Energy Physics*, 2016(8), Aug 2016.

[40] CMS Collaboration. Observation of $t\bar{t}h$ production. *Physical Review Letters*, 120(23), Jun 2018.

[41] CMS Collaboration. Observation of higgs boson decay to bottom quarks. *Physical Review Letters*, 121(12), Sep 2018.

[42] A combination of measurements of Higgs boson production and decay using up to $139\,\text{fb}^{-1}$ of proton–proton collision data at $\sqrt{s} = 13$ TeV collected with the ATLAS experiment. Technical Report ATLAS-CONF-2020-027, CERN, Geneva, Aug 2020.

[43] Standard Model Summary Plots Spring 2020. Technical Report ATL-PHYS-PUB-2020-010, CERN, Geneva, May 2020.

[44] Katherine Freese. Review of observational evidence for dark matter in the universe and in upcoming searches for dark stars. 2009.

[45] Evidence for oscillation of atmospheric neutrinos. *Phys. Rev. Lett.*, 81:1562–1567, Aug 1998.

[46] V.A. Kuzmin, V.A. Rubakov, and M.E. Shaposhnikov. On anomalous electroweak baryon-number non-conservation in the early universe. *Physics Letters B*, 155(1):36 – 42, 1985.

[47] Richard D. Ball, Valerio Bertone, Stefano Carrazza, Christopher S. Deans, Luigi Del Debbio, Stefano Forte, Alberto Guffanti, Nathan P. Hartland, José I. Latorre, and et al. Parton distributions for the lhc run ii. *Journal of High Energy Physics*, 2015(4), Apr 2015.

[48] D. de Florian et al. Handbook of LHC Higgs Cross Sections: 4. Deciphering the Nature of the Higgs Sector. 2/2017, 10 2016.

[49] Fedor Bezrukov and Mikhail Shaposhnikov. Why should we care about the top quark Yukawa coupling? *Z. Eksp. Teor. Fiz.*, 147(arXiv:1411.1923. CERN-PH-TH-2014-218. 3):389. 8 p, Nov 2014.

[50] S. Amor dos Santos, M.C.N. Fiolhais, R. Frederix, R. Gonçalo, E. Gouveia, R. Martins, A. Onofre, C.M. Pease, H. Peixoto, A. Reigoto, and et al. Probing the cp nature of the higgs coupling in $t\bar{t}h$ events at the lhc. *Physical Review D*, 96(1), Jul 2017.

[51] John Ellis, Dae Sung Hwang, Kazuki Sakurai, and Michihisa Takeuchi. Disentangling higgs-top couplings in associated production. *Journal of High Energy Physics*, 2014(4), Apr 2014.

[52] W. Beenakker, S. Dittmaier, M. Kramer, B. Plumper, M. Spira, and P. M. Zerwas. Higgs radiation off top quarks at the Tevatron and the LHC. *Phys. Rev. Lett.*, 87:201805, 2001.

[53] W. Beenakker, S. Dittmaier, M. Kramer, B. Plumper, M. Spira, and P. M. Zerwas. NLO QCD corrections to t anti-t H production in hadron collisions. *Nucl. Phys. B*, 653:151, 2003.

[54] S. Dawson, L. H. Orr, L. Reina, and D. Wackeroth. Associated top quark Higgs boson production at the LHC. *Phys. Rev. D*, 67:071503, 2003.

[55] S. Dawson, C. Jackson, L. H. Orr, L. Reina, and D. Wackeroth. Associated Higgs production with top quarks at the large hadron collider: NLO QCD corrections. *Phys. Rev. D*, 68:034022, 2003.

[56] Yu Zhang, Wen-Gan Ma, Ren-You Zhang, Chong Chen, and Lei Guo. QCD NLO and EW NLO corrections to $t\bar{t}H$ production with top quark decays at hadron collider. *Phys. Lett. B*, 738:1, 2014.

[57] S. Frixione, V. Hirschi, D. Pagani, H. S. Shao, and M. Zaro. Weak corrections to higgs hadroproduction in association with a top-quark pair. *JHEP*, 09:065, 2014.

[58] Ilaria Brivio and Michael Trott. The standard model as an effective field theory. *Physics Reports*, 793:1–98, Feb 2019.

[59] Steven Weinberg. Phenomenological lagrangians. *Physica A: Statistical Mechanics and its Applications*, 96(1):327 – 340, 1979.

[60] W. Buchmüller and D. Wyler. Effective lagrangian analysis of new interactions and flavour conservation. *Nuclear Physics B*, 268(3):621 – 653, 1986.

[61] John M. Campbell and R. Keith Ellis. $t\bar{t}W^{\pm}$ production and decay at NLO. *JHEP*, 07:052, 2012.

[62] S. Frixione, V. Hirschi, D. Pagani, H.-S. Shao, and M. Zaro. Electroweak and QCD corrections to top-pair hadroproduction in association with heavy bosons. *JHEP*, 06:184, 2015.

[63]   Rikkert Frederix, Davide Pagani, and Marco Zaro. Large NLO corrections in $t\bar{t}W^{\pm}$ and $t\bar{t}t\bar{t}$ hadroproduction from supposedly subleading EW contributions. *Journal of High Energy Physics*, 2018(2), Feb 2018.

[64]   Rikkert Frederix and Ioannis Tsinikos. Subleading ew corrections and spin-correlation effects in $t\bar{t}w$ multi-lepton signatures, 2020.

[65]   Giuseppe Bevilacqua, Huan-Yu Bi, Heribertus Bayu Hartanto, Manfred Kraus, and Malgorzata Worek. The simplest of them all: $t\bar{t}w^{\pm}$ at nlo accuracy in qcd. *Journal of High Energy Physics*, 2020(8), Aug 2020.

[66]   Qing-Hong Cao, Shao-Long Chen, and Yandong Liu. Probing higgs width and top quark yukawa coupling from $t\bar{t}h$ and $t\bar{t}t\bar{t}$ productions. *Physical Review D*, 95(5), Mar 2017.

[67]   Qing-Hong Cao, Shao-Long Chen, Yandong Liu, Rui Zhang, and Ya Zhang. Limiting top quark-higgs boson interaction and higgs-boson width from multitop productions. *Phys. Rev. D*, 99:113003, Jun 2019.

[68]   Hans Peter Nilles. Supersymmetry, Supergravity and Particle Physics. *Phys. Rept.*, 110:1–162, 1984.

[69]   Glennys R. Farrar and Pierre Fayet. Phenomenology of the production, decay, and detection of new hadronic states associated with supersymmetry. *Phys. Lett.*, 76B:575–579, 1978.

[70]   Tilman Plehn and Tim M. P. Tait. Seeking sgluons. *J. Phys.*, G36:075001, 2009.

[71]   Samuel Calvet, Benjamin Fuks, Philippe Gris, and Loic Valery. Searching for sgluons in multitop events at a center-of-mass energy of 8 tev. *JHEP*, 04:043, 2013.

[72]   D. Dicus, A. Stange, and S. Willenbrock. Higgs decay to top quarks at hadron colliders. *Phys. Lett.*, B333:126–131, 1994.

[73]   Nathaniel Craig, Francesco D'Eramo, Patrick Draper, Scott Thomas, and Hao Zhang. The hunt for the rest of the higgs bosons. *JHEP*, 06:137, 2015.

[74]   Nathaniel Craig, Jan Hajer, Ying-Ying Li, Tao Liu, and Hao Zhang. Heavy higgs bosons at low $\tan\beta$: from the lhc to 100 tev. *JHEP*, 01:018, 2017.

[75]   ATLAS Collaboration. Search for new phenomena in events with same-charge leptons and $b$-jets in $pp$ collisions at $\sqrt{s} = 13$ tev with the atlas detector. *JHEP*, 12:039, 2018.

[76]   ATLAS Collaboration. Search for four-top-quark production in the single-lepton and opposite-sign dilepton final states in pp collisions at $\sqrt{s} = 13$ tev with the atlas detector. *Phys. Rev. D*, 99(5):052009, 2019.

[77]   CMS Collaboration. Search for the production of four top quarks in the single-lepton and opposite-sign dilepton final states in proton-proton collisions at $\sqrt{s} = 13$ tev. *JHEP*, 11:082, 2019.

[78] CMS Collaboration. Search for production of four top quarks in final states with same-sign or multiple leptons in proton-proton collisions at $\sqrt{s} = 13$ tev. *Eur. Phys. J. C*, 80(2):75, 2020.

[79] Georges Aad et al. Evidence for $t\bar{t}t\bar{t}$ production in the multilepton final state in proton-proton collisions at $\sqrt{s}$=13 TeV with the ATLAS detector. 7 2020.

[80] Lyndon Evans and Philip Bryant. LHC machine. *Journal of Instrumentation*, 3(08):S08001–S08001, aug 2008.

[81] The ALICE Collaboration. The ALICE experiment at the CERN LHC. *Journal of Instrumentation*, 3(08):S08002–S08002, aug 2008.

[82] The ATLAS Collaboration. The ATLAS experiment at the CERN large hadron collider. *Journal of Instrumentation*, 3(08):S08003–S08003, aug 2008.

[83] The CMS Collaboration. The CMS experiment at the CERN LHC. *Journal of Instrumentation*, 3(08):S08004–S08004, aug 2008.

[84] The LHCb Collaboration. The LHCb detector at the LHC. *Journal of Instrumentation*, 3(08):S08005–S08005, aug 2008.

[85] Christiane Lefevre. The CERN accelerator complex. Technical report, Dec 2008.

[86] ATLAS Collaboration. Performance of pile-up mitigation techniques for jets in $pp$ collisions at $\sqrt{s} = 8$ tev using the atlas detector, Oct 2016.

[87] Luminosity determination in $pp$ collisions at $\sqrt{s} = 13$ TeV using the ATLAS detector at the LHC. Technical Report ATLAS-CONF-2019-021, CERN, Geneva, Jun 2019.

[88] S Haywood, L Rossi, R Nickerson, and A Romaniouk. *ATLAS inner detector: Technical Design Report, 2*. Technical Design Report ATLAS. CERN, Geneva, 1997.

[89] Ewa Stanecka. The atlas inner detector operation, data quality and tracking performance, 2013.

[90] Track Reconstruction Performance of the ATLAS Inner Detector at $\sqrt{s} = 13$ TeV. Technical Report ATL-PHYS-PUB-2015-018, CERN, Geneva, Jul 2015.

[91] M Capeans, G Darbo, K Einsweiller, M Elsing, T Flick, M Garcia-Sciveres, C Gemme, H Pernegger, O Rohne, and R Vuillermet. ATLAS Insertable B-Layer Technical Design Report. Technical Report CERN-LHCC-2010-013. ATLAS-TDR-19, Sep 2010.

[92] *ATLAS tile calorimeter: Technical Design Report*. Technical Design Report ATLAS. CERN, Geneva, 1996.

[93] *ATLAS liquid-argon calorimeter: Technical Design Report*. Technical Design Report ATLAS. CERN, Geneva, 1996.

[94] *ATLAS muon spectrometer: Technical Design Report*. Technical Design Report ATLAS. CERN, Geneva, 1997.

[95] ATLAS Outreach. ATLAS Fact Sheet : To raise awareness of the ATLAS detector and collaboration on the LHC. 2010.

[96] A Krasznahorkay and. The evolution of the trigger and data acquisition system in the AT-LAS experiment. *Journal of Physics: Conference Series*, 523:012019, jun 2014.

[97] Peter Jenni, Marzio Nessi, Markus Nordberg, and Kenway Smith. *ATLAS high-level trigger, data-acquisition and controls: Technical Design Report*. Technical Design Report ATLAS. CERN, Geneva, 2003.

[98] William Panduro Vazquez and ATLAS Collaboration. The ATLAS Data Acquisition system in LHC Run 2. Technical Report ATL-DAQ-PROC-2017-007. 3, CERN, Geneva, Feb 2017.

[99] *ATLAS Computing: technical design report*. Technical Design Report ATLAS. CERN, Geneva, 2005.

[100] T Cornelissen, M Elsing, S Fleischmann, W Liebig, E Moyse, and A Salzburger. Concepts, Design and Implementation of the ATLAS New Tracking (NEWT). Technical Report ATL-SOFT-PUB-2007-007. ATL-COM-SOFT-2007-002, CERN, Geneva, Mar 2007.

[101] ATLAS Collaboration. Muon reconstruction performance of the ATLAS detector in proton–proton collision data at $\sqrt{s} = 13$ TeV. *The European Physical Journal C*, 76(5), May 2016.

[102] ATLAS Collaboration. Reconstruction of primary vertices at the atlas experiment in run 1 proton–proton collisions at the lhc. *The European Physical Journal C*, 77(5), May 2017.

[103] Performance of primary vertex reconstruction in proton-proton collisions at $\sqrt{s} =$ 7 TeV in the ATLAS experiment. Technical Report ATLAS-CONF-2010-069, CERN, Geneva, Jul 2010.

[104] ATLAS Collaboration. Electron reconstruction and identification in the ATLAS experiment using the 2015 and 2016 LHC proton-proton collision data at $\sqrt{s} = 13$ TeV. *Eur. Phys. J. C*, 79(arXiv:1902.04655. 8):639. 40 p, Feb 2019.

[105] W Lampl, S Laplace, D Lelas, P Loch, H Ma, S Menke, S Rajagopalan, D Rousseau, S Snyder, and G Unal. Calorimeter Clustering Algorithms: Description and Performance. Technical Report ATL-LARG-PUB-2008-002. ATL-COM-LARG-2008-003, CERN, Geneva, Apr 2008.

[106] Improved electron reconstruction in ATLAS using the Gaussian Sum Filter-based model for bremsstrahlung. Technical Report ATLAS-CONF-2012-047, CERN, Geneva, May 2012.

[107] M. Aaboud, G. Aad, B. Abbott, O. Abdinov, B. Abeloos, D. K. Abhayasinghe, S. H. Abidi, O. S. AbouZeid, N. L. Abraham, and et al. Measurement of the photon identification efficiencies with the atlas detector using lhc run 2 data collected in 2015 and 2016. *The European Physical Journal C*, 79(3), Mar 2019.

[108] Andreas Hoecker, Peter Speckmayer, Joerg Stelzer, Jan Therhaag, Eckhard von Toerne, and Helge Voss. TMVA: Toolkit for Multivariate Data Analysis. *PoS*, ACAT:040, 2007.

[109] ATLAS Collaboration. Evidence for the associated production of the higgs boson and a top quark pair with the atlas detector. *Physical Review D*, 97(7), Apr 2018.

[110] Matteo Cacciari, Gavin P Salam, and Gregory Soyez. The anti-kt jet clustering algorithm. *Journal of High Energy Physics*, 2008(04):063–063, apr 2008.

[111] Jet energy scale measurements and their systematic uncertainties in proton-proton collisions at $\sqrt{s} = 13$ TeV with the atlas detector. *Phys. Rev. D*, 96:072002, Oct 2017.

[112] Topological cell clustering in the ATLAS calorimeters and its performance in LHC Run 1. *Eur. Phys. J. C*, 77(CERN-PH-EP-2015-304):490. 87 p, Mar 2016.

[113] ATLAS Collaboration. Tagging and suppression of pileup jets with the atlas detector. ATLAS-CONF-2014-018, 2014.

[114] Performance of b-jet identification in the ATLAS experiment. *Journal of Instrumentation*, 11(04):P04008–P04008, apr 2016.

[115] ATLAS b-jet identification performance and efficiency measurement with $t\bar{t}$ events in pp collisions at $\sqrt{s} = 13$ TeV. *Eur. Phys. J. C*, 79(11):970, 2019.

[116] Expected performance of missing transverse momentum reconstruction for the atlas detector at $\sqrt{s} = 13$ TeV. Technical Report ATL-PHYS-PUB-2015-023, CERN, Geneva, Jul 2015.

[117] J. M. Butterworth, J. R. Forshaw, and M. H. Seymour. Multiparton interactions in photoproduction at hera. *Zeitschrift für Physik C: Particles and Fields*, 72(4):637–646, Dec 1996.

[118] J. Alwall et al. The automated computation of tree-level and next-to-leading order differential cross sections, and their matching to parton shower simulations. *JHEP*, 07:079, 2014.

[119] Stefano Frixione, Paolo Nason, and Giovanni Ridolfi. A Positive-weight next-to-leading-order Monte Carlo for heavy flavour hadroproduction. *JHEP*, 09:126, 2007.

[120] Heribertus B. Hartanto, Barbara Jäger, Laura Reina, and Doreen Wackeroth. Higgs boson production in association with top quarks in the POWHEG BOX. *Phys. Rev. D*, 91:094003, 2015.

[121] Torbjorn Sjöstrand, Stephen Mrenna, and Peter Z. Skands. A brief introduction to PYTHIA 8.1. *Comput. Phys. Commun.*, 178:852, 2008.

[122] Johannes Bellm et al. Herwig 7.0/herwig++ 3.0 release note. *Eur. Phys. J. C*, 76:196, 2016.

[123] T. Gleisberg et al. Event generation with sherpa 1.1. *JHEP*, 02:007, 2009.

[124] Fabio Cascioli, Philipp Maierhofer, and Stefano Pozzorini. Scattering Amplitudes with Open Loops. *Phys. Rev. Lett.*, 108:111601, 2012.

[125] Tanju Gleisberg and Stefan Hoeche. Comix, a new matrix element generator. *JHEP*, 12:039, 2008.

[126] Steffen Schumann and Frank Krauss. A Parton shower algorithm based on Catani-Seymour dipole factorisation. *JHEP*, 03:038, 2008.

[127] Stefan Hoeche, Frank Krauss, Marek Schonherr, and Frank Siegert. QCD matrix elements + parton showers: The NLO case. *JHEP*, 04:027, 2013.

[128] S. Agostinelli et al. GEANT4: A Simulation toolkit. *Nucl. Instrum. Meth.*, A506:250–303, 2003.

[129] ATLAS Collaboration. The ATLAS Simulation Infrastructure. *Eur. Phys. J. C*, 70:823, 2010.

[130] T. Sjöstrand et al. High-energy-physics event generation with pythia 6.1. *Comput. Phys. Commun.*, 135:238, 2001.

[131] Torbjorn Sjöstrand, Stefan Ask, Jesper R. Christiansen, Richard Corke, Nishita Desai, Philip Ilten, Stephen Mrenna, Stefan Prestel, Christine O. Rasmussen, and Peter Z. Skands. An Introduction to PYTHIA 8.2. *Comput. Phys. Commun.*, 191:159, 2015.

[132] M. Bahr et al. Herwig++ physics and manual. *Eur. Phys. J. C*, 58:639, 2008.

[133] D. J. Lange. The evtgen particle decay simulation package. *Nucl. Instrum. Meth. Phys. Res. A*, 462:152, 2001.

[134] Piotr Golonka and Zbigniew Was. Photos monte carlo: A precision tool for qed corrections in $z$ and $w$ decays. *Eur. Phys. J.*, C45:97–107, 2006.

[135] Richard D. Ball, Valerio Bertone, Stefano Carrazza, Christopher S. Deans, Luigi Del Debbio, Stefano Forte, Alberto Guffanti, Nathan P. Hartland, José I. Latorre, Juan Rojo, and et al. Parton distributions with lhc data. *Nuclear Physics B*, 867(2):244–289, Feb 2013.

[136] L. A. Harland-Lang, A. D. Martin, P. Motylinski, and R. S. Thorne. Parton distributions in the lhc era: Mmht 2014 pdfs. *Eur. Phys. J. C*, 75:204, 2015.

[137] H.-L. Lai et al. New parton distributions for collider physics. *Phys. Rev. D*, 82:074024, 2010.

[138] J. Pumplin, D. R. Stump, J. Huston, H.-L. Lai, P. M. Nadolsky, and W. K. Tung. New generation of parton distributions with uncertainties from global qcd analysis. *JHEP*, 07:012, 2002.

[139] P. M. Nadolsky et al. Implications of cteq global analysis for collider observables. *Phys. Rev. D*, 78:013004, 2008.

[140] E. Re. Single-top wt-channel production matched with parton showers using the powheg method. *Eur. Phys. J. C*, 71:1547, 2011.

[141] S. Alioli, P. Nason, C. Oleari, and E. Re. Nlo single-top production matched with shower in powheg: $s-$ and $t-$channel contributions. *JHEP*, 09:111, 2009.

[142] Rikkert Frederix, Emanuele Re, and Paolo Torrielli. Single-top t-channel hadroproduction in the four-flavour scheme with POWHEG and aMC@NLO. *JHEP*, 09:130, 2012.

[143] ATLAS Collaboration. ATLAS Run 1 Pythia8 tunes. ATL-PHYS-PUB-2014-021, 2014.

[144] A. Djouadi, J. Kalinowski, and M. Spira. HDECAY: a program for Higgs boson decays in the Standard Model and its supersymmetric extension. *Comput. Phys. Commun.*, 108:56, 1998.

[145] Stefano Frixione, Eric Laenen, Patrick Motylinski, and Bryan R. Webber. Angular correlations of lepton pairs from vector boson and top quark decays in Monte Carlo simulations. *JHEP*, 0704:081, 2007.

[146] Pierre Artoisenet, Rikkert Frederix, Olivier Mattelaer, and Robbert Rietkerk. Automatic spin-entangled decays of heavy resonances in Monte Carlo simulations. *JHEP*, 1303:015, 2013.

[147] Rikkert Frederix and Stefano Frixione. Merging meets matching in MC@NLO. *JHEP*, 12:061, 2012.

[148] ATLAS Collaboration. Modelling of the $t\bar{t}h$ and $t\bar{t}v$ $(v = w, z)$ processes for $\sqrt{s}$ = 13 tev atlas analyses. (ATL-COM-PHYS-2015-1510), Dec 2015. ATL-PHYS-PUB-2016-005.

[149] ATLAS Collaboration. Multi-boson simulation for 13 tev atlas analyses. (ATL-COM-PHYS-2015-1499), Dec 2015. ATL-PHYS-PUB-2016-002.

[150] ATLAS Collaboration. Simulation of top quark production for the atlas experiment at $\sqrt{s}$ = 13 tev. (ATL-COM-PHYS-2015-1496), Dec 2015. ATL-PHYS-PUB-2016-004.

[151] ATLAS Collaboration. Studies on top-quark monte carlo modelling for top2016. ATL-PHYS-PUB-2016-020, 2016.

[152] Matteo Cacciari, Michal Czakon, Michelangelo Mangano, Alexander Mitov, and Paolo Nason. Top-pair production at hadron colliders with next-to-next-to-leading logarithmic soft-gluon resummation. *Phys. Lett. B*, 710:612, 2012.

[153] Peter Bärnreuther, Michal Czakon, and Alexander Mitov. Percent-level-precision physics at the tevatron: Next-to-next-to-leading order qcd corrections to $q\bar{q} \rightarrow t\bar{t} + x$. *Phys. Rev. Lett.*, 109:132001, 2012.

[154] Michal Czakon and Alexander Mitov. Nnlo corrections to top-pair production at hadron colliders: the all-fermionic scattering channels. *JHEP*, 12:054, 2012.

[155] Michal Czakon and Alexander Mitov. NNLO corrections to top pair production at hadron colliders: the quark-gluon reaction. *JHEP*, 01:080, 2013.

[156] Michal Czakon, Paul Fiedler, and Alexander Mitov. Total Top-Quark Pair-Production Cross Section at Hadron Colliders Through $\mathcal{O}(\alpha_S^4)$. *Phys. Rev. Lett.*, 110:252004, 2013.

[157] Olga Bessidskaia Bylund. Modelling wt and twz production at nlo for atlas analyses. In *Proceedings, 9th International Workshop on Top Quark Physics (TOP 2016): Olomouc, Czech Republic, September 19-23, 2016*, 2016.

[158] D Paredes and D Calvet. Estimation of the mis-identification rates of the electron charge at 8 tev. Technical Report ATL-COM-PHYS-2013-1622, CERN, Geneva, Dec 2013.

[159] ATLAS Collaboration. Luminosity determination in $pp$ collisions at $\sqrt{s} = 8$tev using the atlas detector at the lhc. *Eur. Phys. J. C*, 76:653, 2016.

[160] G. Avoni et al. The new lucid-2 detector for luminosity measurement and monitoring in atlas. *JINST*, 13(07):P07017, 2018.

[161] ATLAS Collaboration. Jet calibration and systematic uncertainties for jets reconstructed in the atlas detector at $\sqrt{s} = 13$ TeV. ATL-PHYS-PUB-2015-015, 2015.

[162] ATLAS Internal. JetEtMiss Recommendations R21, 2018.

[163] Georges Aad et al. Jet energy measurement with the atlas detector in proton-proton collisions at $\sqrt{s} = 7$ tev. *Eur. Phys. J.*, C73(3):2304.

[164] ATLAS Collaboration. $e_t^{\text{miss}}$ performance in the atlas detector using 2015–2016 lhc $pp$ collisions. ATLAS-CONF-2018-023, 2018.

[165] Combined search for the standard model higgs boson in $pp$ collisions at $\sqrt{s}$=7 TeV with the atlas detector. *Phys. Rev. D*, 86:032003, Aug 2012.

[166] Glen Cowan, Kyle Cranmer, Eilam Gross, and Ofer Vitells. Asymptotic formulae for likelihood-based tests of new physics. *The European Physical Journal C*, 71(2), Feb 2011.

[167] ATLAS Collaboration. Reconstruction, Energy Calibration, and Identification of Hadronically Decaying Tau Leptons in the ATLAS Experiment for Run-2 of the LHC. ATL-PHYS-PUB-2015-045, 2015.

[168] ATLAS Collaboration. Measurement of the tau lepton reconstruction and identification performance in the ATLAS experiment using $(pp)$ collisions at $\sqrt{s} = 13$ TeV. ATLAS-CONF-2017-029, 2017.

[169] Tianqi Chen and Carlos Guestrin. Xgboost: A scalable tree boosting system. *CoRR*, abs/1603.02754, 2016.

[170] Wikipedia contributors. Cross-validation, 2004. Online; accessed 5-Oct-2020.

[171] ATLAS Collaboration. Evidence for the associated production of the Higgs boson and a top quark pair with the ATLAS detector. *Phys. Rev. D*, 97:072003, 2018.

[172] Jon Butterworth et al. Pdf4lhc recommendations for lhc run ii. *J. Phys. G*, 43:023001, 2016.

[173] ATLAS Collaboration. Evidence for the associated production of the higgs boson and a top quark pair with the atlas detector. *Phys. Rev. D*, 97:072003, 2018.

[174] ATLAS Collaboration. Measurement of the $t\bar{t}z$ and $t\bar{t}w$ cross sections in proton-proton collisions at $\sqrt{s} = 13$ tev with the atlas detector. *Phys. Rev. D*, 99:072009, 2019.

[175] Wikipedia contributors. Standard model, 2004. Online; accessed 30-Sep-2020.

[176] Michiel Botje et al. The pdf4lhc working group interim recommendations. 2011.

[177] ATLAS Collaboration. Combined measurements of higgs boson production and decay using up to $80$ fb$^{-1}$ of proton-proton collision data at $\sqrt{s} = 13$ tev collected with the atlas experiment. *Phys. Rev. D*, 101(1):012002, 2020.

[178] ATLAS Collaboration. Measurements of inclusive and differential fiducial cross-sections of $t\bar{t}$ production with additional heavy-flavour jets in proton–proton collisions at $\sqrt{s} = 13$ TeV with the atlas detector. *JHEP*, 04:046, 2019.

[179] ATLAS Collaboration. Measurement of the production cross-section of a single top quark in association with a Z boson in proton-proton collisions at 13 TeV with the ATLAS detector. *Phys. Lett.*, B780:557–577, 2018.

[180] Higgs boson production in association with top quarks in final states with electrons, muons, and hadronically decaying tau leptons at $\sqrt{s} = 13$ TeV. Technical Report CMS-PAS-HIG-19-008, CERN, Geneva, 2020.

[181] Akeroyd, A. G., Aoki, M., Arhrib, A., Basso, L., Ginzburg, I. F., Guedes, R., Hernandez-Sanchez, J., Huitu, K., Hurth, T., Kadastik, M., Kanemura, S., Kannike, K., Khater, W., Krawczyk, M., Mahmoudi, F., Moretti, S., Najjari, S., Osland, P., Pruna, G. M., Purmohammadi, M., Racioppi, A., Raidal, M., Santos, R., Sharma, P., Sokolowska, D., Stål, O., Yagyu, K., and Yildirim, E. Prospects for charged higgs searches at the lhc. *Eur. Phys. J. C*, 77(5):276, 2017.